2011

Investigation of Antimicrobial Peptides in Lipid Membranes by Solid-State NMR

Yuan Zhang
Iowa State University

Investigation of Antimicrobial Peptides in Lipid Membranes by Solid-state NMR

by

Yuan Zhang

A dissertation submitted to the graduate faculty

In partial fulfillment of the requirements for the degree of

DOCTOR OF PHILOSOPHY

Major: Chemistry

Program of Study Committee:
Mei Hong, Co-Major Professor
Klaus Schmidt-Rohr, Co-Major Professor
Emily Smith
Xueyu Song
Surya Mallapragada

Iowa State University

Ames, Iowa

2011

Table of Contents

Acknowledgements

I am truly grateful to all people who helped me get through the past five years of study and research. The first and foremost people I want to thank are my thesis advisors Dr. Mei Hong and Dr. Klaus Schmidt-Rohr. They led me into the wonderful world of solid-state NMR. Mei is an excellent mentor who provides the lab a positive atmosphere for research and shapes me as a scientist. Every time when I feel my research is going toward the dead end, she will always be the person who provides me the enlightening advices and encourages me to open my mind. I am also thankful to Klaus for his deep and thorough theoretical lessons and helpful discussion.

I would like to thank my committee members, Dr. Emily Smith, Dr. Xueyu Song and Dr. Surya Mallapragada for offering their opinions and guidance on my scientific course of study. I would also like to thank my past and current group members not only for helping me through my scientific life but also for being really good friends for the past five years: Dr. Rajee Mani, Dr. Ming Tang, Dr. Wenbin Luo, Dr. Timorthy Doherty, Dr. Sarah Cady, Dr. Yongchao Su, Dr. Shenhui Li, Dr. Hongwei Yao, Fanghao Hu, Marilu Perez, Tuo Wang, Aaron Liao, Byungsu Kwon, Jonathan Williams, Keith Fritzsching and all the members of the Schimidt-Rohr group. Thanks to Dr. Wuyuan Lu and Dr. Jing Li at the Institute of Human Virology for supplying us with high quality peptide and kindly teaching me protein expression technique. I am also thankful to Dr. Jacek Lubkowski in the National Cancer Institute for teaching me crystallization skills. I greatly appreciate the assistance from many members of the Iowa State University Department of Chemistry staff – Dr. Shu Xu and Dr. Dave Scott in the NMR facility, Bev, Carlene, Renee, Lynette and Mary in the Chemistry Office.

I would like to express thanks to my friends here. To my chemistry peers, I would not forget the time when we worked hard together to live through the tough courses and exams in the first year. To my friends outside Gilman who are too numerous to name, thanks for sharing the countless wonderful time with me as well as providing me selfless help. You guys make Ames such a great place and I will definitely miss here in the future.

And thanks to my friends far away from Ames: Zilu Wang and Yiqing Wang. Thank you for being good friends with me for such a long time and helping me survive through those tough times.

Last but not least, I thank my beloved parents for their unconditional love and support through my life. Thanks to them, I realize that there is always a place where I can take a rest whenever I feel tired. To them I sincerely dedicate this thesis.

Abstract

Solid-state NMR spectroscopy is an important tool for studying the chemical and three-dimensional structures of organic and inorganic solids because of its intrinsic atomic-level structural information, nonperturbing nature, and the large range of dynamic time scales. It is especially powerful in studying insoluble and noncrystalline membrane proteins, which are difficult to analyze by traditional X-ray crystallography or solution NMR techniques. In this thesis, various NMR techniques are used to study the structure and dynamics of membrane proteins within lipid bilayers.

The main protein we are focusing on is human neutrophil peptide 1 (HNP-1). It is a small cysteine-rich cationic antimicrobial protein found in human neutrophils. It forms the first line of defense by the innate immune system of humans against pathogens. The antimicrobial activity of HNP-1 is believed to be caused by disruption of the microbial cell membrane and various models of HNP-membrane interaction have been proposed. However, none of these mechanistic models are based on structure information from the lipid bilayer. Therefore, understanding the peptide structure in the presence of membrane and its interaction with the lipids will shed light on the antimicrobial mechanism of HNP-1. As a first step, we have calculated the minimum-energy structures of uniformly ^{13}C, ^{15}N-labeled microcrystalline HNP-1 based on all NMR torsion angle and distance restraints determined by various 2D and 3D correlation techniques. The solid-state NMR structure has close similarity to the crystal structures of the HNP family. Then we reconstituted HNP-1 into DMPC/DMPG lipid bilayers. We confirmed that the protein is predominantly dimerized at high protein/lipid molar ratios by ^{19}F spin diffusion experiments. Various methods under magic-angle spinning (MAS) such as ^{13}C-^{31}P REDOR, ^{1}H spin diffusion and ^{13}C DIPSHIFT have been utilized to study the interaction of HNP-1 with lipid bilayers. The experimental results strongly support a “dimer pore” topology of HNP-1 in which the polar top of the dimer lines an aqueous pore while the hydrophobic bottom faces the lipid chains.

The second focus of this thesis is the oriented bicelle alignment , we have studied the alignment of bicelles with different lipids combinations, long- to short-chain lipid ratios, hydration levels and a phase diagram was generated. We also show that the orientation of a protein called HNP-1, which has 3 β-strands and dimerizes, can be simulated by predicting the correlation of the ^{15}N anisotropic chemical shift and the N-H dipolar coupling.

Chapter 1

Introduction

1.1 Antimicrobial Peptides

Antimicrobial peptides are small polypeptides that constitute part of the innate immune system of many plants and animals to rapidly kill invading microbial pathogens, such as Gram negative and Gram positive bacteria, mycobacteria, enveloped virus, fungi and even transformed or cancerous cells. They are divided into subgoups on the basis of the amino acid composition and structure. For instances, Dermcidins from humans are anionic peptides that are rich in glutamic and aspartic acids [1]; Cecropins from insects [2] and LL37 from humans [3] are linear cationic α-helical peptides that are characterized by a lack of cysteine; Tachyplesin from the horseshoe crab [4] and protegrin-1 in porcine leukocytes [5] are cationic peptides that are enriched in arginines and that contain cysteines to form disulfide bonds. Despite this structural diversity, all antimicrobial peptides contain hydrophilic amino acid residues aligned along one side and hydrophobic amino acid residues aligned along the opposite side, with the underlying structural principle that polar and non-polar regions in the molecule are spatially separated (‘amphiphathic’ structure) [6].

The modes of action by which antimicrobial peptides kill bacteria are varied. One way is to allow the AMPs to penetrate into the cell to bind intracellular molecules that are crucial to cell survival [7]. This model includes inhibition of cell wall synthesis, alternation of the cytoplasmic membrane, activation of autolysin, which is an enzyme that hydrolyzes the components of a biological cell, inhibition of DNA, RNA and protein synthesis, and inhibition of certain enzymes. Another way to kill the microbes is to disrupt their cell membranes. Various models have been proposed for this membrane disruption [8]. The first model, ‘barrel-stave’, involves several peptides forming a barrel to span the lipid bilayer. This model has been used to explain pore formation and step-wise conductivity increases in single-channel measurements of alamethicin [9]. The

second model is the 'carpet' model, in which peptides first assemble on the bilayer surface with the hydrophobic side embedded into the membrane, causing membrane thinning. Once a critical concentration is reached, the membrane is micellized and starts to leak. This model is proposed based on the observations of the antimicrobial peptide dermaseptin, revealed by a dissipation of diffusion potential and a release of entrapped calcein from SUV (small unilamellar vesicles) [10]. The third model is the toroidal pore model, in which peptide aggregation and lipid disorder lead to the formation of a stable channel. This model has been shown to occur for protegrin-1 [11,12]. The last model is the in-plane diffusion model, in which the peptides are bound to the surface of lipid membrane and diffuse around the bilayer normal, which cause areas of local negative curvature strain and sufficient disruption to form transient pores [13,14].

There are several factors that determine the selectivity of antimicrobial peptides. First, the microbial membranes have more anionic phospholipids, especially for the outer leaflet, while the host cell membranes consist of zwitterionic phospholipids. This makes the microbial membrane more negatively charged, thus it is more susceptible to antimicrobial peptides with cationic residues [15]. Second, cholesterol is normally widely distributed in the mammalian cell membranes but absent in bacterial cell membranes. People have observed the presence of cholesterol will generally reduce the activities of the antimicrobial peptides by either rigidifying the lipid bilayers or interacting with the peptides and therefore protect the cells from attack by the AMPs [16]. Besides, the more negative transmembrane potential of bacterial cells also facilitates the insertion of positively charged peptides into the membrane [17].

1.2 Defensins

Defensins are small (3-5 kDa), cysteine-rich, cationic proteins stabilized by several (usually three) disulfide bonds [18-20]. They are found in both vertebrates and invertebrates and are active against bacteria, fungi and many enveloped and non-enveloped viruses [21,22]. They are classified into three categories based on the disulfide-linkage patterns. In α-defensins, three disulfide bridges have the topology, Cys^{I}-Cys^{VI}, Cys^{II}-Cys^{IV}, Cys^{III}-Cys^{V} [23]. They are expressed primarily in neutrophils as well

as in NK cells and certain T-lymphocyte subsets. β-defensins are the most widely distributed, being secreted by leukocytes and epithelial cells of many kinds. The disulfide linkage arrangement of β-defensins is Cys^{I}-Cys^{V}, Cys^{II}-Cys^{IV}, Cys^{III}-Cys^{VI} [24]. θ-defensins are cyclic peptides and are found in some non-human primates, but not in human, gorilla, bonobo and chimpanzee [25-27]. So far, six α-defensins have been identified in humans. The first four defensins are often called neutrophile peptides (HNP1-4) [18,28,29] and defensins 5 and 6 are frequently referred to as intestinal defensins (HD5-6) [30,31]. HNP1-3 differs only by a single N-terminal residue [22]. The relative potencies of human α-defensins against Gram-negative bacterium *E. coli* are HNP4 > HNP2 > HNP1 = HNP3 [32].

The overall fold of the α-defensin monomer is attributed to the three β-strands arranged into antiparallel β-sheet, the long loop connecting β1 and β2 and the β-hairpin formed by β2 and β3. The structures of HNP1-3 are similar, which are dimerized in the crystal through intermolecular H-bonds between the two β2 strands, extending the triple-stranded β-sheet to a six-strand β-sheet. The dimer has a basket shape and is amphipathic, with a polar top and an apolar base [19,20].

It is generally believed that the killing of microorganisms by defensins is a consequence of disruption of the microbial membrane [33]. Many antimicrobial assays and lipid vesicle experiments have been reported to understand the mechanism of action [34,35], and a number of biochemical studies indicate pore formation by human α-defensins in anionic lipid membranes. For example, dye release and fluorescence spectroscopy experiments found that HNP1 caused both fusion and lysis of negatively charged lipid vesicles through electrostatic interactions [36]. Electron micrographs of human parasite *Trypanosoma cruzi* cells in the presence of micromolar concentration of HNP1 showed 25 nm sized pores in the cellular and flagellar membranes, through which HNP1 appears to enter the trypanosome cells, causing subsequent DNA fragmentation and cell destruction [37]. Vesicle leakage experiments also showed that HNP-induced pores increasing in number with the concentration of the anionic lipid [38].

Based on the crystal structure of HNP3, several models have been proposed to explain the antimicrobial mechanism of human α-defensins. The first model is called the wedge model [19], in which the dimer is inserted into the membrane either partly or completely, with its hydrophobic base embedded into the hydrocarbon region of the membrane. The second model is called the dimer pore model [19]. In this model, two dimers form a membrane-spanning pore with the hydrophobic base facing the lipids and the top view shows a basket shape. The general pore model [19] is similar to the dimer pore model, with the dimers rotated by 90º around the horizontal axis and its side view shows the basket shape of the dimer. A multimeric pore model was also proposed with six to eight HNP dimers forming a large pore with an inner diameter of 20 – 25 Å and the dimers are oriented so that the Arg residues are located in two rings parallel to the membrane surface [39].

To obtain high-resolution information about intermolecular interaction and dynamics of HNP-1 in the lipid membrane, solid-state NMR spectroscopy is an excellet technique because of its advantage in the amorphous and insoluble systems compared to solution NMR and X-ray diffraction. In order to distinguish which one of the models mentioned above explains the antimicrobial activity of HNP-1, the following aspects of the complex system consisting of HNP1 and lipid bilayers have to be investigated.

Depth of Insertion

For antimicrobial peptides, their depth of insertion into the lipid membrane often provides important clues to their mechanism of action. For example, in the carpet model and the in-plane diffusion model, the peptides reside on the membrane surface, while for the barrel-stave model and the toroidal pore model they insert all the way to the hydrophobic center of the lipid bilayer. In the case of HNP1, the measurement of depth of insertion can differentiate wedge model from the other models. Several NMR methods are developed to determine the depth of insertion of membrane proteins. A lipid-to-protein ^{1}H spin diffusion experiment is employed for immobilized membrane proteins such as PG-1 and TP-1 [40-43]. In this experiment, the intensity buildup of lipid chain-peptide cross peaks as a function of mixing times gives a semi-quantitative measurement

of the minimum distance separation between the protein and the hydrophobic core of the bilayers. For mobile membrane peptides that have similar mobility as the lipids, the Paramagnetic Relaxation Enhancement (PRE) effect is used to extract quantitative distance information. Since paramagnetic ions binding to the phosphate groups on the membrane surface can broaden the nuclear spin signals by enhancing their T_2 relaxation in a distance-dependent manner [44], the electron-nucleus distances can be measured semi-quantitatively by comparing the PRE effect of the peptide with that of the lipids. Our group has determined the penetratin position in the lipid bilayers using this method [45].

Site-Specific Quantitative Depth of Insertion

Revealing the contact between the peptide and the lipids helps to explain how the peptide binds the lipid bilayer. A well-established X-^{31}P (X=^{13}C, ^{15}N, etc.) REDOR technique can be carried out to measure residue specific and accurate depths of insertion [46]. Our group measured the depth of V6 ^{13}CO and G10 ^{13}CO in TP-I bound to DMPC/DMPG membranes by ^{13}C-^{31}P REDOR on trehalose-protected lipid membranes and found that TP-I lies at the interface between water and the hydrophobic chains, parallel to the membrane surface [14].

Oligomeric Structure of Membrane Proteins

Membrane-lytic peptides are thought to oligomerize to inflict maximal damage to the lipid membrane. It is thus important to determine the protein's quaternary structure in addition to the secondary and tertiary structures to understand the structural basis of membrane protein function. Previously our group developed a ^{19}F spin diffusion NMR technique based on the CODEX technique [47] to determine both the oligomeric number and long-range intermolecular distances in membrane protein assemblies. The fraction of magnetization residing on the initial spin without the orientational change is the inverse of the number of spins in the cluster [48,49]. The rate of the magnetization decay reflects the distance between the monomers [50]. For HNP1, it has been proposed that several dimers need to aggregate together to achieve pore formation on the lipid membrane

[19,39]. Therefore, understanding the oligomerization of HNP1 in the lipid bilayers should shed light on its antimicrobial mechanism.

Protein Dynamics

The hydrated lipid membranes are highly mobile systems. Lipids undergo fast lateral diffusion and uniaxial rotational diffusion, thus molecular motion for membrane proteins is very common and is often related to the function and lipid-interaction of proteins. The most robust solid-state NMR strategy for obtaining site-resolved dynamics information employs 2D chemical shift and dipolar correlation spectroscopy to measure heteronuclear X-H dipolar couplings (DIPSHIFT or 2D LG-CP) [51,52]. Since the distance of X-H bond is fixed, the dipolar coupling strength is also fixed in the absence of motion; thus any reduction from the rigid-limit value is indicative of motional averaging. Our group has measured C-H and N-H dipolar couplings in several membrane proteins and peptides to determine the amplitude of motion [41,53].

1.3 Protein Structure Determination by Solid State NMR

The main methods for high-resolution protein structure determination are X-ray crystallography and solution NMR. However, there is a wide variety of proteins that are insoluble in water, which makes the X-ray crystallography and solution NMR unsuitable. Over the past few years, there have been remarkable advances in solid-state NMR spectroscopy which make the structure characterization of insoluble proteins possible. Excellent NMR line widths can be achieved for microcrystalline proteins using magic angle spinning (MAS) methods. For instances, the ^{13}C line width of the microcrystallized ubiquitin can be as narrow as 0.5-0.6 ppm and the ^{15}N line widths are 0.3-0.5 ppm [54].

In recent years, solid-state NMR has accumulated a considerable track record with respect to *de novo*-structure determination of proteins, which are mostly on nano- or microcrystalline preparation of proteins and on protein fibrils. Oschkinat and coworkers determined the structure of SH3 domain with 286 carbon-carbon and 6 nitrogen-nitrogen inter-residue constraints and the Cα coordinates of this structure show a root mean square deviation of 1.6 Å [55]. Loquet et al. published a structure of the domain-swapped dimer

of the Crh domain with 1.33 Å RMSD by using 643 distance constraints, combining carbon-carbon and proton-proton distances [56]. Frank et al. determined the GB1 structure through 7826 distance constraints, resulting in a backbone RMSD of 0.31 Å [57]. Investigations of membrane protein systems are also making progress. The group of Baldus has published a number of interesting structural models of potassium channels derived from solid-state NMR, which enabled a deeper understanding of potassium channel activations and inhibition [58]. The group of Rienstra has published assignments of the membrane protein DsbB [59]. In general, the improvement in solid-state NMR methodology will lead to reasonably well determined structures that are useful to the scientific community.

The structure determination paradigm is overall robust. First, ^{13}C and ^{15}N chemical shifts were measured on uniformly ^{13}C, ^{15}N labeled proteins by well-defined solid-state NMR correlation experiments, such as NCACX and NCOCX, providing both inter- and intra-residue correlations [60-62]. Correlations between α-carbons have also proved to be of high value for sequential assignment. These chemical shift values provide information about the secondary structure of the protein.

With all the chemical shifts assigned, the next step is to obtain inter-residue distance constraints. Various methods have been developed for this purpose. The most frequently used method is DARR or PDSD with different mixing times [63]. Another type of experiment is CHHC, which has very short CP and ^{1}H-^{1}H exchange times, to obtain inter-strand distance constraints [64]. Griffin's group developed the PAR technique, which can obtain long range constraints more easily than DARR [65]. A 3D CCC technique was developed by our group in order to obtain both short range and long range correlations and improve the resolution by adding another dimension [66]. Different labeling schemes are also applied. Instead of uniformly labeled protein, 1,3- and 2-^{13}C-glycerol are used as carbon sources during the growth of the bacteria to generate partially labeled protein [55,67-69]. In this way, the spectra are less crowded, which is helpful for removing ambiguities and resolving resonance overlap. Another very promising approach is based on the clever use of paramagnetic centers, either present in the molecules or added to the sample [70]. Since these paramagnetic centers often cause

low intensities or pseudocontact shifts, by analyzing these effects, one can estimate the distance from various residues to the paramagnetic center and therefore obtain more distance constraints.

Torsion angle restraints can also be measured in proteins. Hong et al have developed a method to determine the torsion angle ϕ in peptides, based on the measurement of the relative orientation of the N-HN and Cα-Hα bonds [71]. And the ψ torsion angle can be measured by fitting the time-course of Cα-C' double-quantum coherence dephasing [72]. The group of Rienstra has demonstrated that relative orientations of molecular fragments can be determined from dipolar line shapes of proteins. By using vector angle restraints, they improved the backbone RMSD of GB1 from 1.01 Å to 0.31 Å [57].

1.4. Thesis Organization

This thesis is composed mainly of published journal papers on the structure and antimicrobial mechanism of the human neutrophil peptide 1. Some papers contains supplementary information that was only published in the online edition of the journal, and this data is located at the end of its respective chapter.

Chapter 2 describes the solid state NMR theory and techniques related to this work. Double quantum filter theory is brifly reviewed. Chapter 3 shows the determination of the three-dimensional structure of HNP-1 in a microcrystalline state outside the lipid membrane. A suite of 2D and 3D magic-angle spinning experiments were applied to complete the ^{13}C and ^{15}N chemical shift assignment. Combining the torsion angle constraints derived from chemical shifts and inter-residue distance constraints, a high resolution solid-state NMR structure of HNP-1 was determined.

Chapter 4 demonstrates a 3D ^{13}C-^{13}C-^{13}C (CCC) magic-angle spinning correlation technique for obtaining two orders of magnitude more long-range distance restraints. Combining these distance restraints and the chemical-shift-derived torsion angles, we obtained a *de novo* high-resolution NMR structure of HNP-1.

Chapter 5 determined the conformation, dynamics, oligomeric state and topology of HNP-1 in DMPC/DMPG lipid bilayers by various solid-state NMR techniques. The results strongly support a "dimer pore" topology of HNP-1 and thus provide the first glimpse into the membrane-bound structure and mechanism of action of human-α-defensins.

Chapter 6 shows the investigation of the alignment of bicelles with various conditions. We also show in this chapter that the orientation of HNP-1 can be determined in principle through 2D correlation spectra of ^{15}N anisotropic chemical shift and N-H dipolar coupling.

Finally, two appendices are located at the end of the thesis. Appendix A summarizes the protein expression, purification and crystallization of HNP-1 in detail. Appendix B gives the input code for protein structure determination by Xplor-NIH.

1.5 Copyright Permission

Chapter 3, 4, 5 are reprints of published papers. The copyright permissions do not require a license for re-use in a thesis or dissertation. Figure 2.3, Figure 5.5a and Figure 5.6a are reprints from the referenced paper. Permissions have been obtained from the following publishing groups.

Chapter 3 and 4: Elsevier, Inc.

Chapter 5: American Chemical Society

Figure 2.3: Springer, license number: 2738430062616

Figure 5.5a: Elsevier, Inc. license number: 2738400453944

Figure 5.6a: Elsevier, Inc. license number: 2738400676772

References

[1] Schittek, B.; Hipfel, R.; Sauer, B.; Bauer, J.; Kalbacher, H.; Stevanovic, S.; Schirle, M.; Schroeder, K.; Blin, N.; Meier, F.; Rassner, G.; Garbe, C., Dermcidin: a novel human antibiotic peptide secreted by sweat glands, Nature Immunology 2 (2001) 1133-1137.

[2] Wu, J.; Jan, P.; Yu, H.; Haung, H.; Fang, H.; Chang, Y.; Cheng, J.; Chen, H., Structure and function of a custom anticancer peptide, CB1a, Peptides 30 (2009) 839-848.

[3] Gudmundsson, G.; Agerberth, B.; Odeberg, J.; Bergman, T.; Olsson, B.; Salcedo, R., The human gene FALL39 and processing of the cathelin precursor to the antimicrobial peptide LL-37 in granulocytes, Eur. J. Biochem. 238 (1996) 325-332.

[4] Nakamura, T.; Furunaka, H.; Miyata, T.; Tokunaga, F.; Muta, T.; Iwanaga, S.; Niwa, M.; Takao, T.; Shimonishi, Y., Tachyplesin, a class of antimicrobial peptide from the hemocytes of the horseshoe crab (Tachypleus tridentatus). Isolation and chemical structure, J. Biol. Chem. 263 (1988) 16709-16713.

[5] Bellm, L.; Lehrer, R.; Ganz, T., Protegrins: new antibiotics of mammalian origin, Expert. Opin. Investig. Drugs. 9 (2000) 1731-1742.

[6] Yeaman, M.; Yount, N., Mechanisms of antimicrobial peptide action and resistance, Pharmacol. Rev. 55 (2003) 27-55.

[7] Brogden, K., Antimicrobial peptides: pore formers or metabolic inhibitors in bacteria?, Nat. Rev. Microbiol. 3 (2005) 238-250.

[8] Bechinger, B., The structure, dynamics and orientation of antimicrobial peptides in membranes by multidimensional solid-state NMR spectroscopy, Biochim. Biophys. Acta. 1462 (1999) 157-183.

[9] Baumman, G.; Mueller, P., A molecular model of membrane excitability, J. Supramol. Struct. 2 (1974) 538-557.

[10] Pouny, Y.; Rapaport, D.; Mor, A.; Nicolas, P.; Shai, Y., Interaction of antimicrobial dermaseptin and its fluorescently labeled analogues with phospholipid membranes, Biochemistry. 31 (1992) 12416-12423.

[11] Mani, R.; Cady, S.; Tang, M.; Waring, A.; Lehrer, R.; Hong, M., Membrane-dependent oligomeric structure and pore formation of a beta-hairpin antimicrobial peptide

in lipid bilayers from solid-state NMR, Proc. Natl. Acad. Sci. U S A. 103 (2006) 16242-16247.

[12] Tang, M.; Waring, A.; Hong, M., Phosphate-mediated arginine insertion into lipid membranes and pore formation by a cationic membrane peptide from solid-state NMR, J. Am. Chem. Soc. 129 (2007) 11438-11446.

[13] Doherty, T.; Waring, A.; Hong, M., Peptide-Lipid Interactions of the β-Hairpin Antimicrobial Peptide Tachyplesin and its Linear Derivatives from Solid-State NMR, Biochim. Biophys. Acta. 1758 (2006) 1285-1291.

[14] Doherty, T.; Waring, A.; Hong, M., Membrane-bound conformation and topology of Tachyplesin-1 by solid-state NMR spectroscopy, Biochemistry. 45 (2006) 13323-13330.

[15] Hancock, R.; Sahl, H., Antimicrobial and host-defense peptides as new anti-infective therapeutic strategies, Nat. Biotechnol. 24 (2006) 1551-1557.

[16] Zasloff, M., Antimicrobial peptides of multicellular organisms, Nature. 415 (2002) 389-395.

[17] Matsuzaki, K.; Sugishita, K.; Fujii, N.; Miyajima, K., Molecular basis for membrane selectivity of an antimicrobial peptide, magainin 2, Biochemistry. 34 (1995) 3423-3429.

[18] Ganz, T.; Selsted, M. E.; Szklarek, D.; Harwig, S. S.; Daher, K.; Bainton, D. F.; Lehrer, R. I., Defensins. Natural peptide antibiotics of human neutrophils, J. Clin. Invest. 76 (1985) 1427-1435.

[19] Hill, C. P.; Yee, J.; Selsted, M. E.; Eisenberg, D., Crystal structure of defensin HNP-3, an amphiphilic dimer: mechanisms of membrane permeabilization., Science 251 (1991) 1481-1485.

[20] Szyk, A.; Wu, Z.; Tucker, K.; Yang, D.; Lu, W.; Lubkowski, J., Crystal structures of human alpha-defensins HNP4, HD5, and HD6., Protein Sci. 15 (2006) 2749-2760.

[21] Ganz, T., Immunology:Versatile defensins, Science 298 (2002) 977-979.

[22] Lehrer, R. I.; Ganz, T., Defensins of vertebrate animals, Curr. Opin. Immunol. 14 (2002) 96-102.

[23] Selsted, M.; Harwig, S., Determination of the disulfide array in the human defensin HNP-2. A covalently cyclized peptide, J. Biol. Chem. 264 (1989) 4003-4007.

[24] Tang, Y.; Selsted, M., Characterization of the disulfide motif in BNBD-12, an antimicrobial beta-defensin peptide from bovine neutrophils, J. Biol. Chem. 268 (1993) 6649-6653.

[25] Cole, A.; Wang, W.; Waring, A.; Lehrer, R., Retrocyclins: using past as prologue, 2004 5 (2004) 373-381.

[26] Tang, Y.; Yuan, J.; Osapay, G.; Osapay, K.; Tran, D.; Miller, C.; Ouellette, A.; Selsted, M., A cyclic antimicrobial peptide produced in primate leukocytes by the ligation of two truncated alpha-defensins., Science. 286 (1999) 498-502.

[27] Leonova, L.; Kokyakov, V.; Aleshina, G.; Hong, T.; Nguyen, T.; Zhao, C.; Waring, A.; Lehrer, R., Circular minidefensins and posttranslational generation of molecular diversity, J. Leukoc. Biol. 70 (2001) 461-464.

[28] Lehrer, R.; Selsted, M.; Szklarek, D.; Fleischmann, J., Antibacterial activity of microbicidal cationic proteins 1 and 2, natural peptide antibiotics of rabbit lung macrophages, Infect. Immun. 42 (1983) 10-14.

[29] Selsted, M.; Szklarek, D.; Lehrer, R., Purification and antibacterial activity of antimicrobial peptides of rabbit granulocytes, Infect. Immun. 45 (1984) 150-154.

[30] Jones, D.; Bevins, C., Paneth cells of the human small intestine express an antimicrobial peptide gene, J. Biol. Chem. 267 (1992) 23216-23225.

[31] Jones, D.; Bevins, C., Defensin-6 mRNA in human Paneth cells: implications for antimicrobial peptides in host defense of the human bowel, FEBS. Lett. 315 (1993) 187-192.

[32] Ericksen, B.; Wu, Z.; Lu, W.; Lehrer, R., Antibacterial activity and specificity of the six human {alpha}-defensins, Antimicrob. Agents. Chemother. 49 (2005) 269-275.

[33] Lehrer, R. I.; Barton, A.; Daher, K. A.; Harwig, S. S.; Ganz, T.; Selsted, M. E., Interaction of human defensins with Escherichia coli. Mechanism of bactericidal activity, J. Clin. Invest. 84 (1989) 553-561.

[34] Ganz, T., Defensins: antimicrobial peptides of innate immunity, Nat. Rev. Immunol. 3 (2003) 710-720.

[35] Lehrer, R. I.; Lichtenstein, A. K.; Ganz, T., Defensins: antimicrobial and cytotoxic peptides of mammalian cells, Annu. Rev. Immunol. 11 (1993) 105-128.

[36] Fujii, G.; Selsted, M. E.; Eisenberg, D., Defensins promote fusion and lysis of negatively charged membranes., Prot. Sci. 2 (1993) 1301-1312.

[37] Madison, M. N.; Kleshchenko, Y. Y.; Nde, P. N.; Simmons, K. J.; Lima, M. F.; Villalta, F., Human Defensin alpha-1 Causes Trypanosoma cruzi Membrane Pore Formation and Induces DNA Fragmentation, Which Leads to Trypanosome Destruction, Infect. Immun. 75 (2007) 4780-4791.

[38] de Leeuw, E.; Li, C.; Zeng, P.; Li, C.; Diepeveen-de Buin, M.; Lu, W. Y.; Breukink, E.; Lu, W., Functional interaction of human neutrophil peptide-1 with the cell wall precursor lipid II, FEBS Lett. 584 (2010) 1543-1548.

[39] Wimley, W. C.; Selsted, M. E.; White, S. H., Interactions between human defensins and lipid bilayers: evidence for formation of multimeric pores, Protein Sci. 3 (1994) 1362-1373.

[40] Huster, D.; Yao, X. L.; Hong, M., Membrane protein topology probed by 1H spin diffusion from lipids using solid-state NMR spectroscopy, J. Am. Chem. Soc 124 (2002) 874-883.

[41] Buffy, J. J.; Waring, A. J.; Lehrer, R. I.; Hong, M., Immobilization and Aggregation of Antimicrobial Peptide Protegrin in Lipid Bilayers Investigated by Solid-State NMR, Biochemistry 42 (2003) 13725-13734.

[42] Mani, R.; Cady, S. D.; Tang, M.; Waring, A. J.; Lehrer, R. I.; Hong, M., Membrane-dependent oligomeric structure and pore formation of a b-hairpin antimicrobial peptide in lipid bilayers from solid-state NMR, Proc. Natl. Acad. Sci. USA 103 (2006) 16242-16247.

[43] Doherty, T.; Waring, A. J.; Hong, M., Membrane-bound conformation and topology of the antimicrobial peptide tachyplesin-I by solid-state NMR Biochemistry 45 (2006) 13323-13330.

[44] Buffy, J. J.; Hong, T.; Yamaguchi, S.; Waring, A.; Lehrer, R. I.; Hong, M., Solid-State NMR Investigation of the Depth of Insertion of Protegin-1 in Lipid Bilayers Using Paramagnetic Mn2+, Biophys. J. 85 (2003) 2363-2373.

[45] Su, Y.; Mani, R.; Hong, M., Asymmetric Insertion of Membrane Proteins in Lipid Bilayers by Solid-State NMR Paramagnetic Relaxation Enhancement: a Cell-Penetrating Peptide Example, J. Am. Chem. Soc. 130 (2008) 8856-8864.

[46] Gullion, T.; Schaefer, J., Rotational echo double resonance NMR, J. Magn. Reson. 81 (1989) 196-200.

[47] deAzevedo, E. R.; Bonagamba, T. J.; Hu, W.; Schmidt-Rohr, K., Centerband-only detection of exchange: efficient analysis of dynamics in solids by NMR, J. Am. Chem. Soc. 121 (1999) 8411-8412.

[48] Buffy, J. J.; Waring, A. J.; Hong, M., Determination of Peptide Oligomerization in Lipid Membranes with Magic-Angle Spinning Spin Diffusion NMR, Journal of the American Chemical Society 127 (2005) 4477-4483.

[49] Luo, W.; Hong, M., "Determination of the Oligomeric Number and Intermolecular Distances of Membrane Protein Assemblies by Anisotropic 1H-Driven Spin Diffusion NMR, J. Am. Chem. Soc. 128 (2006) 7242-7251.

[50] Luo, W.; Hong, M., Determination of the oligomeric number and intermolecular distances of membrane protein assemblies by anisotropic 1H-driven spin diffusion NMR spectroscopy, J. Am. Chem. Soc. 128 (2006) 7242-7251.

[51] Munowitz, M. G.; Griffin, R. G.; Bodenhausen, G.; Huang, T. H., Two-dimensional rotational spin-echo NMR in solids: correlation of chemical shift and dipolar interactions, J. Am. Chem. Soc. 103 (1981) 2529-2533.

[52] van Rossum, B.; de Groot, C.; Ladizhansky, V.; Vega, S.; de Groot, H., A Method for Measuring Heteronuclear (1H-13C) Distances in High Speed MAS NMR, J. Am. Chem. Soc. 122 (2000) 3465-3472.

[53] Huster, D.; Xiao, L. S.; Hong, M., Solid-State NMR Investigation of the dynamics of colicin Ia channel-forming domain, Biochemistry 40 (2001) 7662-7674.

[54] Igumenova, T.; Wand, A.; McDermott, A., Assignment of the backbone resonances for microcrystalline ubiquitin., J Am Chem Soc. 126 (2004) 5323-5331.

[55] Castellani, F. R., B.; Diehl, A.; Schubert, M.; Rehbein, K.; Oschkinat, H., Structure of a protein determined by solid-state magic-angle-spinning NMR spectroscopy, Nature 420 (2002) 98-102.

[56] Loquet, A.; Bardiaux, B.; Gardiennet, C.; Blanchet, C.; Baldus, M.; Nilges, M.; Malliavin, T.; Böckmann, A., 3D structure determination of the Crh protein from highly ambiguous solid-state NMR restraints, J. Am. Chem. Soc. 130 (2008) 3579-3589.

[57] Franks, W. T.; Wylie, B. J.; Schmidt, H. L.; Nieuwkoop, A. J.; Mayrhofer, R. M.; Shah, G. J.; Graesser, D. T.; Rienstra, C. M., Dipole tensor-based atomic-resolution structure determination of a nanocrystalline protein by solid-state NMR, Proc. Natl. Acad. Sci. U. S. A. 105 (2008) 4621-4626.

[58] Schneider, R.; Ader, C.; Lange, A.; Giller, K.; Hornig, S.; Pongs, O.; Becker, S.; Baldus, M., Solid-state NMR spectroscopy applied to a chimeric potassium channel in lipid bilayers, J. Am. Chem. Soc. 130 (2008) 7427-7435.

[59] Tang, M.; Sperling, L.; Berthold, D.; Nesbitt, A.; Gennis, R.; Rienstra, C. M., Solid-state NMR study of the charge-transfer complex between ubiquinone-8 and disulfide bond generating membrane protein DsbB, J. Am. Chem. Soc. 133 (2011) 4359-4366.

[60] Hong, M., Resonance Assignment of 13C/15N Labeled Proteins by Two- and Three-Dimensional Magic-Angle-Spinning NMR, Journal of Biomolecular NMR 15 (1999) 1-14.

[61] Rienstra, C. M.; Hohwy, M.; Hong, M.; Griffin, R. G., 2D and 3D 15N-13C-13C NMR chemical shift correlation spectroscopy of solids: assignment of MAS spectra of peptides., Journal of the American Chemical Society 122 (2000) 10979-10990.

[62] Straus, S.; Bremi, T.; Ernst, R., Experiments and strategies for the assignment of fully 13C/15N-labelled polypeptides by solid state NMR., J Biomol NMR 12 (1998) 39-50.

[63] Takegoshi, K.; Nakamura, S.; Terao, T., ^{13}C - ^{1}H dipolar-assisted rotational resonance in magic-angle spinning NMR Chem. Phys. Lett 344 (2001) 631-637.

[64] Lange, A.; Seidel, K.; Verdier, L.; Luca, S.; Baldus, M., Analysis of proton-proton transfer dynamics in rotating solids and their use for 3D structure determination, J. Am. Chem. Soc. 125 (2003) 12640-12648.

[65] De Paëpe, G.; Lewandowski, J.; Griffin, R. G., Spin dynamics in the modulation frame: application to homonuclear recoupling in magic angle spinning solid-state NMR, J. Chem. Phys. 128 (2008) 124503.

[66] Li, S.; Zhang, Y.; Hong, M., 3D 13C-13C-13C correlation NMR for de novo distance determination of solid proteins and application to a human alpha defensin, J. Magn. Reson. 202 (2010) 203-210.

[67] Lemaster, D.; Kushlan, D., Dynamical Mapping of E. coli Thioredoxin via 13C NMR Relaxation Analysis, J. Am. Chem. Soc. 118 (1996) 9255-9264.

[68] Zech, S.; Wand, A.; McDermott, A., Protein structure determination by high-resolution solid-state NMR spectroscopy: application to microcrystalline ubiquitin., J Am Chem Soc. 127 (2005) 8618-8626.

[69] Hong, M.; Jakes, K., Selective and Extensive 13C Labeling of a Membrane Protein for Solid-State NMR Investigation, J. Biomol. NMR. 14 (1999) 71-74.

[70] Nadaud, P.; Helmus, J.; Kall, S.; Jaroniec, C., Paramagnetic ions enable tuning of nuclear relaxation rates and provide long-range structural restraints in solid-state NMR of proteins, J. Am. Chem. Soc. 131 (2009) 8108-8120.

[71] Hong, M.; Gross, J. D.; Griffin, R. G., Site-resolved Determination of Peptide Torsion Angle Phi from the Relative Orientations of Backbone N-H and C-H Bonds by Solid-State NMR, J. Phys. Chem. 101 (1997) 5869-5874.

[72] Costa, P. R.; Gross, J. D.; Hong, M.; Griffin, R. G., A NCCN 2Q-HLF Experiment for Y Torsion Angle Measurements in Peptides, Chem. Phys. Lett. 280 (1997) 95-103.

Chapter 2

NMR Methodology

2.1 Protein Structure Determination by Solid-state NMR

2.1.1 Hetereonuclear Magnetization Transfer Method -- SPECIFIC CP

3D NCACX and NCOCX are two important experiments for ^{13}C and ^{15}N resonance assignment of protein by solid state NMR. In these experiments, the ^{15}N-^{13}C SPECIFIC CP is a crucial step. The cross-polarization experiment [1,2] is plagued by its extreme sensitivity to the exact match condition at one of the sidebands of the Hartman-Hahn condition $|\omega_{1S}| - |\omega_{1I}| = n|\omega_r|$ [3] under fast magic angle spinning (MAS). Here ω_{1S} and ω_{1I} denote the ^{13}C and ^{15}N RF field amplitudes and ω_r is the spinning (angular) frequency and n is a small integer. This condition must be met within the magnitude of the dipolar coupling frequency. Therefore, the chemical shift differences make it impossible to achieve exact match for all spin pairs simultaneously. However, this chemical shift differences can be utilized to achieve frequency specific transfer such as N –> CO or N-> CA.

Figure 2.1 shows the theory of SPECIFIC CP [4]. If the carrier is close to the CA chemical shift (~55 ppm), then $\omega_{eff, CA} \approx \omega_{1, CA}$. But for CO, since it has a large chemical shift difference from CA (18 kHz on a 600 MHz spectrometer and 12 kHz on a 400 MHz NMR), its $\omega_{eff, CO}$ can be calculated by the equation: $\omega^2_{eff, CO} = \omega^2_{1, CO} + \omega^2_r$. Therefore, if the $\omega_{eff, CA}$ matches the ^{15}N-^{13}C CP matching condition $|\omega_{eff, CA}| - |\omega_{eff, N}| = n|\omega_r|$, the $\omega_{eff, CO}$ cannot satisfy this condition. Thus we will obtain only the N->CA transfer and vice versa. The MLF spectra show that we can obtain clean NCA or NCO spectra using the correct condition.

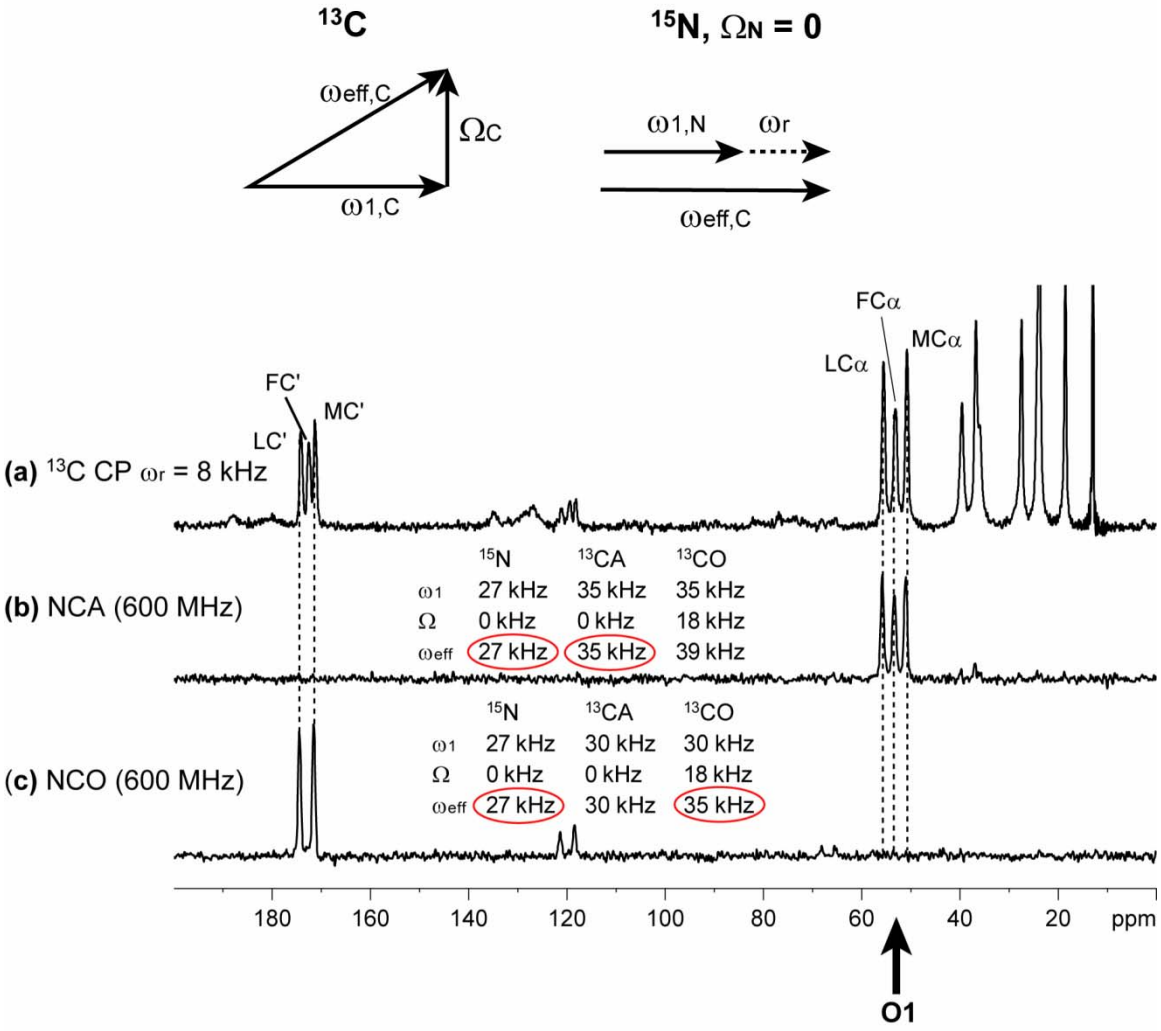

Figure 2.1. Spectra and experimental conditions for MLF SPECIFIC CP. (a) MLF ^{13}C CP. (b) MLF NCA. $\omega_{eff,CA} = \omega_{eff,N} + \omega_r$. (c) MLF NCO. $\omega_{eff,CO} = \omega_{eff,N} + \omega_r$.

It turns out that the SPECIFIC CP condition is quite sensitive that even a difference of 0.2 dB, which translates to ~2% difference in ω_1, difference can affect the intensity significantly. Usually the efficiency of SPECIFIC CP, as indicated by the percentage between the ^{13}C CP and the ^{13}C detected SPECIFIC CP, is ~30% for NCA and ~50% for NCO.

2.1.2 3D NCACX and NCOCX and Resonance Assignment

A 3D N-C-C correlation technique can be used to obtain the sequential ^{13}C and ^{15}N chemical shift assignment of a protein [5,6]. In this experiment, the magnetization was first transferred from ^{1}H to ^{15}N by a normal Hartman-Hahn ^{1}H-^{15}N CP with a 1 ms CP contact time. A ^{15}N t_1 evolution time was applied after the CP to give the F1 dimension. Then the magnetization was selectively transferred from ^{15}N to either ^{13}CA or ^{13}CO by SPECIFIC CP. The contact time is 3-4 ms, longer than ^{1}H-^{13}C CP, to give complete magnetization transfer. After the SPECIFIC CP, there is a ^{13}C t_2 evolution time to give the F2 dimension for ^{13}CA or ^{13}CO. A DARR (Dipolar Assisted Resonance Recoupling) block was implemented to drive the magnetization transfer from the backbone ^{13}C to the sidechain by ^{13}C-^{13}C dipolar coupling. The spin diffusion time is variable. Previous experiences have shown that 40-60 ms is enough for a microcrystalline sample. The membrane sample may need longer time (100 ms) because it has more mobility, which weakens the ^{13}C-^{13}C dipolar coupling and makes it more difficult to obtain ^{13}C-^{13}C correlation. The 1D test of NCACX and NCOCX shows it has 5-10% intensity of a normal ^{13}C CP experiment. The 3D experiment needs 4 days to one week to obtain a sufficient signal-to-noise ratio.

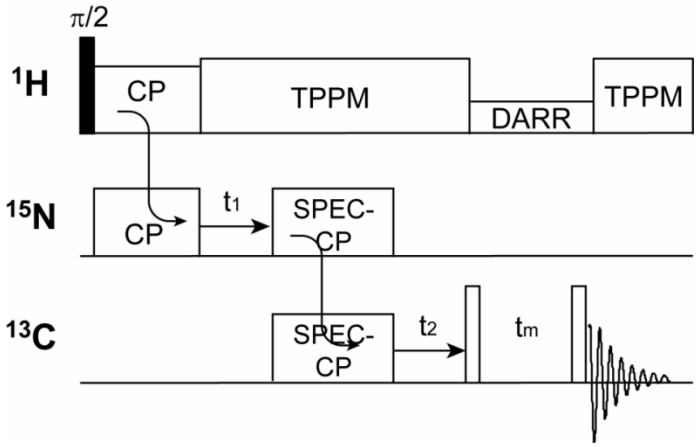

Figure 2.2. 3D NCACX and NCOCX pulse sequence.

Both 3D NCACX and NCOCX spectra are necessary for sequential chemical shift assignment of a protein. The NCACX gives intra-residue assignment and NCOCX gives inter-residue assignment. One can make a "backbone walk" by combining these two spectra. First, we need a residue which has a unique ^{13}C or ^{15}N chemical shift as a starting

point. For example, for the microcrystalline HNP-1 sample, its Ala2 residue has a NH_3 group and its ^{15}N chemical shift is ~41 ppm which is "folded" to ~110 ppm in the NCACX spectrum. So we found the Ala2 $^{13}C\alpha$, $^{13}C\beta$ and ^{13}CO in the 110 ppm ^{15}N plane of NCACX. Then we went to the NCOCX spectrum and found the ^{13}C chemical shifts of Ala2 in the correct ^{13}CO plane. Since the NCOCX gives $^{15}N_{i+1} - ^{13}CO_i - ^{13}CX_i$ correlation, the ^{15}N chemical shift of these peaks is assigned to the next residue, Cys3. After this, we returned to the NCACX spectrum, went to the Cys3 ^{15}N plane and found the chemical shifts of the Cys3 backbone and sidechain carbons. Same as the Ala2 residue, we then returned to the NCOCX spectrum again to find the ^{15}N chemical shift of Tyr4.

Although sequential assignment is obtained by "backbone walk" because it uses the backbone ^{15}N, ^{13}CO and $^{13}C\alpha$ chemical shifts, the sidechains of amino acids are very useful as well. There are a number of amino acids that have unique sidechain ^{13}C chemical shifts. For example, alanine, leucine and isoleucine can be easily identified by their distinct correlation patterns involving their isolated methyl group signals (16-20 ppm, isoleucine even has another methyl which gives a more upfield chemical shift: ~12 ppm). The characteristic $C\beta$-$C\alpha$ cross-peaks at the downfield end of the aliphatic region allow the identification of serines (65 ppm – 60 ppm) and threonines (70 ppm – 60 ppm). The glutamates and glutamines can be identified starting from their $C\delta$ chemical shifts, isolated at the downfield end of the spectrum (182 ppm for Glu and 177 ppm for Gln). Glycines can be recognized by their isolated ^{15}N-$C\alpha$ and ^{15}N-CO cross peaks (^{15}N: ~110 ppm, ^{13}CO: ~170 ppm, $^{13}C\alpha$: ~45 ppm) and cysteines can be identified by their isolated $^{13}C\alpha$-$^{13}C\beta$ (~40 ppm) correlations. Prolines can be recognized on the basis of their typical $C\alpha$ (62 ppm) and $C\delta$ (47 ppm) chemical shifts. They also have a downshield ^{15}N chemical shift of ~134 ppm. But since this ^{15}N doesn't have any ^{1}H attached, its signal is difficult to observe, which makes prolines "breaking point" in resonance assignment.

2.1.3 Torsion Angle Prediction by TALOS

The ^{13}C and ^{15}N chemical shifts allow us to determine the backbone (ϕ, ψ) torsion angles of a protein using the well-known empirical relation between N, $C\alpha$, $C\beta$ and CO

chemical shifts and protein secondary structure [7]. The TALOS program can be used for this purpose [8].

The idea behind TALOS is that if one can find some triplet of residues in a protein of known structure with similar secondary shifts and sequence to a triplet in the target protein, then the ϕ and ψ angles in the known structure will be useful predictors for the torsion angles in the target protein. This program is a database system for empirical prediction of ϕ and ψ backbone torsion angles using a combination of five chemical shifts (Hα, Cα, Cβ, CO, N) for a given protein sequence. During the prediction, it searches a high-resolution structure database for the 10 best matches to the secondary chemical shifts of a given residue in the target protein along with its two flanking residues (a triplet). If there is consensus of ϕ and ψ angles among the 10 best database matches, then it uses these database triplet structures to form a prediction of the backbone angles of the target residue. If the 10 best matches have mutually inconsistent values of ϕ and ψ, the matches are declared ambiguous and no prediction is made for the central residue. What is more, a prediction is considered "good" if at least 9 out of the 10 best database matches fell in the same well-populated region of the Ramachandran map as the ϕ and ψ values from the crystal structure. Conversely, a prediction was considered "bad" or incorrect if it greatly deviated from the observed ϕ or ψ angles from the crystal structure.

In 2009, the Bax group developed an enhanced version of the TALOS system named TALOS+ [9]. It adds an artificial neural network (ANN) classification scheme to this database mining approach. The neural network analyzes the chemical shifts and sequence to estimate the likelihood of a given residue being in a sheet, helix, or loop conformation. This ANN classification information is combined with the database mining results to increase the number of residues where useful backbone angle predictions can be made. As a result, the TALOS+ rules for defining consistent ("good") predictions are slightly stricter. Three conditions need to be satisfied: 1. All 10 best database matches fall in a "consistent" region of the Ramachandran map. 2. The confidence of the ANN 3-state ϕ/ψ distribution prediction for this residue (defined as the difference between the probabilities of the two most favored predicted states) must be above 0.6. 3. The order

parameter S^2 values predicted by the RCI method, which is based on chemical shift data to give a quantitative mapping of protein backbone mobility [10], is larger than 0.5.

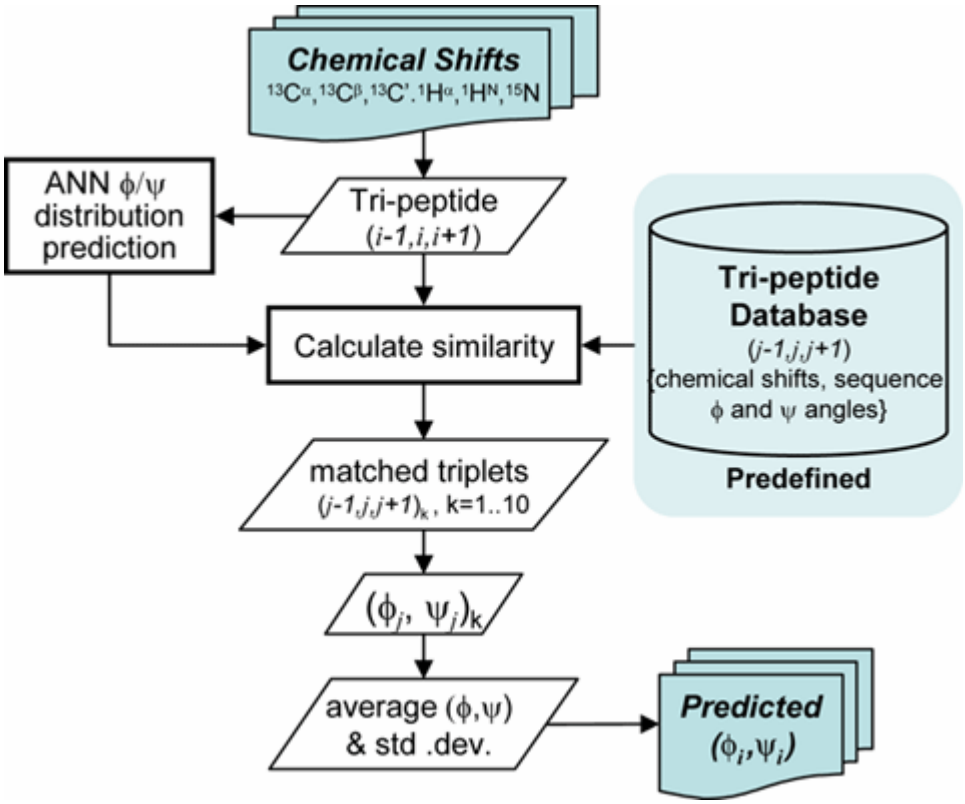

Figure 2.3. The flowchart of TALOS+ database search procedure [9].

2.1.4 XPLOR-NIH

Xplor-NIH is a generalized package for biomolecular structure determination from experimental NMR data combined with known geometric data [11,12]. This is achieved by seeking the minimum of a target function comprising terms from the experimental NMR restraints, covalent geometry and non-bonded contacts using a variety of minimization procedures including molecular dynamics in Cartesian and torsion angle space, Monte Carlo methods and conventional gradient-based minimization. The following potential energy terms are frequently used in NMR structure determination:

1. Covalent geometry. These terms ensure that fixed bond lengths, bond angles, planar atom groups and chiral centers are correct.

2. Non-bonded contacts. These terms include a repulsive quartic van der Waals term, which is used solely to prevent atoms from overlapping.

3. NMR observables. A number of potential energy terms are included in Xplor-NIH that correspond to NMR observables. For structure determination by solid state NMR, the most important terms are torsion angle restraints generated from chemical shifts and ^{13}C-^{13}C and ^{15}N-^{15}N distance restraints, which are derived from the long mixing time spin diffusion spectra. Sequential Cα–Cα distances are fixed by the peptide plane geometry to be 3.8 Å and are thus placed in the range of 3.5–4.1 Å. Sequential N–N distances depend on the ϕ torsion angle and fall within the range of 2.5–3.6 Å. In one representative retraints sorting method, all inter-residue peaks first observed in the 100-ms ^{13}C–^{13}C DARR spectrum were assigned to the range 2.5–5.4 Å, those first appearing in the 200-ms DARR spectrum were assigned to 2.5–6.3 Å, and those inter-residue peaks appearing in the 2D CHHC spectra were assigned to 2.5–7.5 Å [8]. In addition, the few interresidue correlations observed in the 40-ms ^{13}C–^{13}C DARR spectrum were assigned to the range 2.5– 4.8 Å. All non-sequential ^{15}N–^{15}N contacts were placed in the 3.0- to 6.0-Å range.

4. Knowledge-based potentials of mean force. These terms seek to bias conformational space sampling during simulated annealing to regions that are known to be physically realizable.

The structure calculations proceed in two stages. For the annealing process, an ensemble of 200 structures was calculated by performing molecular dynamics at 3500 K for 40 ps, followed by slow cooling from 3500 K to 25 K in 12.5 K increments, with 0.4 ps of dynamics at each temperature using a soft square NOE potential. In the second stage, each structure was refined by repeating the annealing protocol with 10 ps of initial annealing using a hard square NOE potential with the k_{NOE} force constant held at 30 kcal. After structure refinement, the ensemble of 10 lowest energy structures was selected to represent the final structure of HNP-1.

2.2 The Homonuclear Double Quantum Filter Experiment

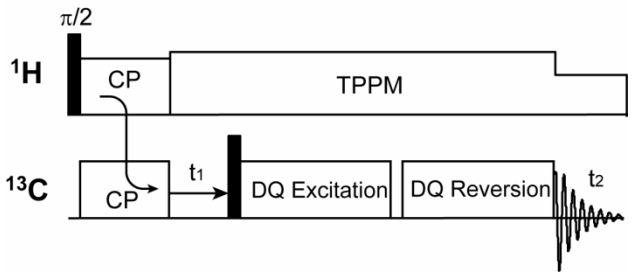

Figure 2.4. The format of double-quantum filtered experiment. Double-quantum coherence is excited then converted to observable single-quantum coherence.

In any system with strongly dipolar-coupled spin pairs, it is in principle possible to excite double-quantum coherences involving the pair of coupled spins. The experiments rely on the fact that excitation efficiency for the double-quantum coherences depends upon the strength of the dipolar coupling. Since we cannot observe double-quantum coherences directly, we convert any excited double-quantum coherence into observable, single-quantum coherence. This experiment is expressed as double-quantum filtered experiment. This kind of experiment can be applied to give directly-bonded carbon correlation and therefore suppress the overlapping lipid signals.

Most solid-state NMR experiments are run under magic-angle-spinning (MAS) for the purpose of high sensitivity and resolution. However, MAS also suppresses all dipolar coupling, which is essential for double-quantum coherence excitation. Therefore, 'dipolar recovery' methods are applied to reintroduce the dipolar coupling between the spins of interest. Here I will outline the theory behind the operation of these methods. The following treatment is referred to Solid-State NMR Spectroscopy by Duer [13] and Multidimensional Solid-State NMR and Polymers by Schmidt-Rohr and Spiess [14].

2.2.1 Dipolar Hamiltonian in Terms of Spherical Tensor Operators

The first-order average homonuclear dipolar Hamiltonian in terms of spherical tensor operators in the rotating frame of reference for dipolar coupling between two spins, I and J, is

$$\hat{H}_{dd} = -\Lambda_{20}\hat{T}_{20}.$$

Here the spin part of this Hamiltonian is given by $\hat{T}_{20} = \frac{1}{\sqrt{6}}(3I_zJ_z - \vec{I}\cdot\vec{J})$. The spatial part Λ_{20} is related with the dipolar coupling tensor in the laboratory frame via

$$\Lambda_{20} = \sum_{m'=-2}^{+2} D^2_{m'0}(\alpha_{PL},\beta_{PL},\gamma_{PL})\lambda_{2m'} = D^2_{00}(\alpha_{PL},\beta_{PL},\gamma_{PL})\lambda_{20} = \frac{1}{2}(3\cos^2\beta_{PL} - 1)\lambda_{20}$$

Here $D^2_{00}(\alpha_{PL},\beta_{PL},\gamma_{PL})$ is the Wigner rotation matrix with the Euler angles $(\alpha_{PL},\beta_{PL},\gamma_{PL})$ specifying the coordinate transformation from the principal axis frame (PAF) to the laboratory frame and has been already well defined. Generally, $D^L_{m'm}(\alpha,\beta,\gamma)$ is defined as $D^L_{m'm}(\alpha,\beta,\gamma) = d^L_{m'm}(\beta)e^{-im'\alpha}e^{-im\gamma}$. $d^L_{m'm}(\beta)$ is the 'reduced rotational matrix' element. Here $d^2_{00}(\beta)$ is defined as $d^2_{00}(\beta) = \frac{1}{2}(3\cos^2\beta - 1)$. λ_{20} is the dipolar coupling tensor in the principal axis frame (PAF), defined as $\lambda_{20} = -\sqrt{6}d$, where d is the dipolar coupling constant for the IS spin pair [15,16].

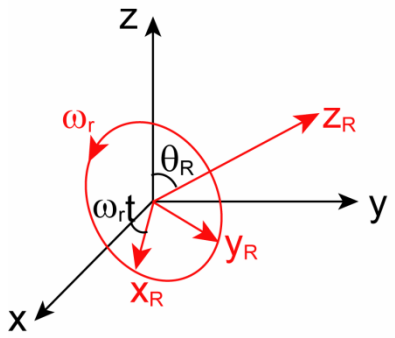

Figure 2.5. The relationship between the laboratory frame (x, y, z) and the magic-angle rotor frame (x_R, y_R, z_R). The z_R axis in the rotator frame is tilted by θ_R (54.7°) from the z axis of the laboratory frame. The x_R and y_R axis are precessing around the z_R axis with a frequency of ω_r.

We need to consider the effects of magic-angle spinning (MAS). To do this, we need to describe an extra coordinate frame, the rotor frame, which we designate (x_R, y_R, z_R). To express the dipolar-coupling tensor in the rotor frame, we first find the dipolar-

coupling tensor with respect to the rotor frame, which is given by $\Lambda_{2m}^{R}(R) = D_{0m}^{2}(\alpha_{PR}, \beta_{PR}, \gamma_{PR})\lambda_{20}$. Then we need to relate the tensor to the laboratory frame ($\alpha_{RL} = \omega_r t, \beta_{RL} = \theta_R, \gamma_{RL} = 0$), which can be found in a similar manner:

$$\begin{aligned}
\Lambda_{2m}^{R}(lab) &= \sum_{m'=-2}^{+2} D_{m'm}^{2}(\omega_r t, \theta_R, 0)\Lambda_{2m'}^{R} \\
&= \sum_{m'=-2}^{+2} D_{m'm}^{2}(\omega_r t, \theta_R, 0) D_{0m'}^{2}(\alpha_{PR}, \beta_{PR}, \gamma_{PR})\lambda_{20} \\
&= \sum_{m'=-2}^{+2} \exp(im\omega_r t) d_{m0}^{2}(\theta_R) D_{0m'}^{2}(\alpha_{PR}, \beta_{PR}, \gamma_{PR})\lambda_{20} \\
&= \sum_{m'=-2}^{+2} \exp(im\omega_r t)\omega_{IJ}^{(m)}
\end{aligned}$$

Here $\omega_{IJ}^{(m)} = \sum_{m=-2}^{+2} d_{m0}^{2}(\theta_R) D_{0m}^{2}(\alpha_{PR}, \beta_{PR}, \gamma_{PR})\lambda_{20}$. $d_{m0}^{2}(\theta_R)$ is a θ_R-dependent factor whose polynomial depends on the m value.

Thus the first-order average homonuclear dipolar Hamiltonian under magic-angle spinning in spherical tensor form (for a two-spin system) is

$$\hat{H}_{dd}(t) = \hat{T}_{20} \sum_{m=-2}^{+2} \exp(im\omega_r t)\omega_{IJ}^{(m)}$$

2.2.2 Analysis of the C7 Pulse Sequence

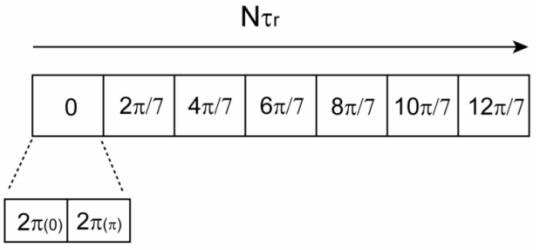

Figure 2.6. The C7 pulse sequence includes n rf pulse cycles and is timed to fit into N rotor periods [17].

The double-quantum C7 method is an efficient way for homonuclear dipolar recoupling. It has been used successfully for double-quantum excitation. The C7 pulse sequence [17] consists of a sequence of n rf pulse cycles C, which is timed to fit into N periods of the sample rotation exactly. Each rf pulse cycle consists of ($2\pi_p$ $2\pi_{-p}$) where the phase Φ_p is given by $\Phi_p = 2\pi p/n$ (p = 0, 1, 2, …, n-1) and the length of each cycle is $\tau_c = N\tau_r/n$ [18].

If the pulse sequence starts at time 0, and the pulse cycle C_p starts at time t_p^0, then a time τ into the cycle, the dipolar Hamiltonian is given by

$$\begin{aligned}\hat{H}_{dd}(t_p^0+\tau) &= \hat{T}_{20}\sum_{m=-2}^{+2}\exp(im\omega_r(t_p^0+\tau))\omega_{IS}^{(m)} \\ &= \hat{T}_{20}\sum_{m=-2}^{+2}\exp(im\omega_r Np\tau_r/n)\exp(im\omega_r\tau)\omega_{IS}^{(m)} \\ &= \hat{T}_{20}\sum_{m=-2}^{+2}\exp(i2\pi mNp/n)\exp(im\omega_r\tau)\omega_{IS}^{(m)}\end{aligned}$$

Where we have $t_p^0 = Np\tau_r/n$, since each cycle is of length $Np\tau_r/n$.

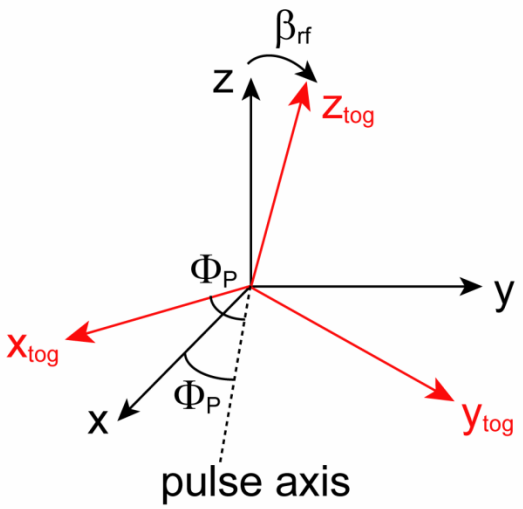

Figure 2.7. The relationship between the rotating frame (x, y, z) and the toggling frame (x_{tog}, y_{tog}, z_{tog}) employed in the analysis of the C7 pulse sequence. A rotation of $-(\pi/2 - \Phi_P)$ about z brings y into coincidence with the pulse axis in the rotating frame. A rotation of $-\beta_{rf}$ about the pulse axis

generates the z_{tog} of the toggling frame. Finally, a rotation of $(\pi/2 + \Phi_P)$ about z_{tog} generates the x_{tog} and y_{tog} axes of the toggling frame.

Now we transform the spin coordinates in the Hamiltonian describing the spin system to a toggling frame in which the effect of the rf pulse vanishes during the pulse cycle. This frame is one which is rotated from the normal rotating frame by $-\beta_{rf}(\tau)$ about the axis of the pulse, where β_{rf} is the nutation angle of the pulse, $\omega_1\tau$. The axis of the pulse is in the x-y plane of the rotating frame at an angle Φ_p from the x-axis. The rotating frame is therefore rotated into the toggling frame via the Euler angles $(-(\pi/2-\Phi_p), -\beta_{rf}(\tau), (\pi/2-_p))$. So the dipolar Hamiltonian at time τ into the pulse cycle expressed in the new toggling frame is $\hat{H}^*(t_p^0+\tau)$, given by

$$\hat{H}^*(t_p^0+\tau) = \hat{R}^{-1}(-(\pi/2-\Phi_p), -\beta_{rf}(\tau), (\pi/2-\Phi_p))\hat{H}_{dd}(t_p^0+\tau)$$
$$\times\hat{R}(-(\pi/2-\Phi_p), -\beta_{rf}(\tau), (\pi/2-\Phi_p))$$

The rotation operator R is the operator which rotates the spin coordinate rotating frame into the toggling frame [13]. It acts on the spin operators of the dipolar Hamiltonian. For this case

$$\hat{R}^{-1}\hat{T}_{20}\hat{R} = \sum_{q=-2}^{+2} D_{q0}^2(-(\pi/2-\Phi_p), -\beta_{rf}(\tau), (\pi/2-\Phi_p))\hat{T}_{2q}$$
$$= \sum_{q=-2}^{+2} \exp(iq(\pi/2-\Phi_p))d_{q0}^2(-\beta_{rf}(\tau))\hat{T}_{2q}$$
$$= \sum_{q=-2}^{+2} i^q \exp(iq2\pi p/n)d_{q0}^2(-\beta_{rf}(\tau))\hat{T}_{2q}$$

Thus, the Hamiltonian in the toggling frame can be rewritten as

$$\hat{H}^*(t_p^0+\tau) = \sum_{q=-2}^{+2}\sum_{m=-2}^{+2} \exp(i2\pi(Nm-q)p/n)\omega_{qm}(\tau)\hat{T}_{2q}$$

Where $\omega_{qm}(\tau)$ is given by

$$\omega_{qm}(\tau) = i^q \exp(im\omega_r\tau) d^2_{q0}(-\beta_{rf}(\tau))\omega^{(m)}_{IS}$$

The average Hamiltonian to first order over the *p*th pulse cycle can be formed:

$$\bar{H}^{(0)}_p = \sum_{q=-2}^{+2}\sum_{m=-2}^{+2} \exp(i2\pi(Nm-q)p/n)\bar{\omega}_{qm}\hat{T}_{2q}$$

Where

$$\bar{\omega}_{qm} = \frac{1}{\tau_c}\int_0^{\tau_c} \omega_{qm}(\tau)d\tau$$

The average Hamiltonian over the whole pulse sequence is then found by averaging the above equation over all the n cycles in the pulse sequence:

$$\begin{aligned}\bar{H}^{(0)} &= \frac{1}{n}\sum_p \bar{H}^{(0)}_p \\ &= \frac{1}{n}\sum_p \sum_{q=-2}^{+2}\sum_{m=-2}^{+2} \exp(i2\pi(Nm-q)p/n)\bar{\omega}^{IS}_{qm}\hat{T}^{IS}_{2q} \\ &= \sum_{q=-2}^{+2}\sum_{m=-2}^{+2} \bar{\omega}^{IS}_{qm}\hat{T}^{IS}_{2q}\delta(Nm-q=n\mu)\end{aligned}$$

Here μ is an integer. Therefore, to reintroduce the dipolar coupling interaction, $\delta(Nm-q=n\mu)$ needs to be 1, which means $Nm-q=n\mu$. And we also wish to 1) Excite double-quantum coherence with the pulse sequence. For that we need to retain $\hat{T}_{2\pm2}$ terms in the average Hamiltonian, which makes q = ±2. 2) Suppress all remaining chemical shift terms, then $q \neq \pm1$. 3) Each double-quantum term q is associated with one spatial component m. If we have (N, n) = (2, 4), then (m, q, μ) can be (1, 0, 2), (-1, -1, 2) etc. Since q = 2 couples to both m = 1 and m = -1, which does not satisfy condition 3), (N, n) = (2, 4) would not work. If (N, n) = (2, 5), then (m, q, μ) can be (1, 2, 0), (-1, -2, 0), (2, -1, 1) and (-2, 1, -1). Note here we have q = ±1, which means we still have the chemical shift terms. So this condition does not work as well. To satisfy all three conditions, it turns out the simplest sequence is n = 7 and N = 2, while with (m, q, μ) to be (1, 2, 0) and (-1, -2, 0). The C_7^2 sequence therefore generates double-quantum coherence in a dipolar coupled

spin pair. The pulse length of each 2π rf pulse in the cycle is $\frac{N\tau_r}{2n} = \frac{\tau_r}{7}$. Thus the field strength $\omega_1 = \frac{7 \cdot 2\pi}{\tau_r} = 7\omega_r$.

2.2.3 Analysis of the SPC-5 pulse sequence

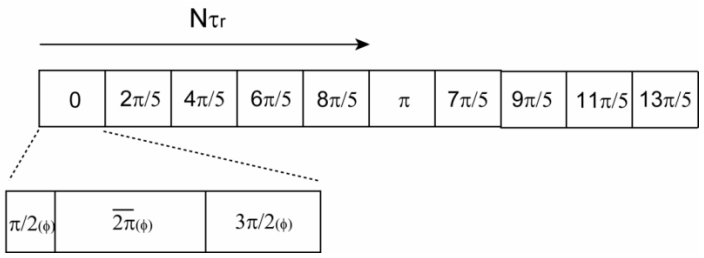

Figure 2.8. The SPC-5 pulse sequence.

The SPC-5 sequence consists of two C7 type cycles with an overall phase shift of Ψ[19]. The Euler angle between the rotating frame and the toggling frame of the second pulse cycle is (-(π/2 - Φ_p + Ψ), $\beta_{rf}(\tau)$, (π/2 - Φ_p + Ψ)). Thus the total Hamiltonian for each interaction (chemical shift, dipolar coupling, etc.) is

$$\bar{H}^{(0)} = \frac{1}{2n}\sum_{p=0}^{n-1}\sum_{q=-2}^{+2}\sum_{m=-2}^{+2}(1+\exp(-iq\Psi))\exp(i2\pi(Nm-q)p/n)\bar{\omega}_{qm}^{IS}\hat{T}_{2q}^{IS}$$

When Ψ = π and q = ±1, the (1 + exp(-*iq*Ψ)) term is zero, which means when Ψ = π, all the q = ±1 terms are eliminated. This provides a wider choice of the n and N number. For the C7 type cycles, when N = 2 and n = 5, there are 4 (q, m) combinations: (2, 1), (-2, -1), (-1, 2) and (1, -2). Since we want to suppress the q = ±1 terms, this combination does not work. But for the SPC-5 cycles, the q = ±1 terms are eliminated by the overall phase shift of π, which makes the N = 2 and n = 5 a good combination for double quantum excitation. As a result, the length of the 2π pulses in the SPC-5 sequence is $\frac{N\tau_r}{2n} = \frac{\tau_r}{5}$ and the field strength is $\omega_1 = \frac{5 \cdot 2\pi}{\tau_r} = 5\omega_r$. Therefore, if one is using 5 kHz MAS frequency, the radio frequency power needs to be 35 kHz for C7 sequence while for SPC-5 sequence, it only needs to

be 25 kHz. In the real condition, the optimized radio frequency power is ~2 dB softer than the calculated value.

2.3 Dipolar Correlation Experiments for Measuring Backbone (ϕ, ψ) Torsion Angles

In recent years solid-state nuclear magnetic resonance has proven crucial for investigating the structure of macroscopically disordered biological solids, especially for those inaccessible to the more traditional methods such as X-ray crystallography and solution NMR. While people are still trying to make progress to improve both the accuracy and range of the internuclear distance measuring techniques, some alternative experimental approaches can also be applied to increase structural resolution. For example, besides distance restraints, the (ϕ, ψ) torsion angles, which give secondary structure information, can also be used as a powerful approach for structure determination. People commonly use TALOS program to generate empirical (ϕ, ψ) angle prediction from chemical shifts. The direct measurement of the (ϕ, ψ) angles can increase the accuracy of this kind of restraints.

2.3.1 HNCH

The ϕ angles can be measured using the HNCH technique, which correlates the $^{1}H^{N}$-^{15}N and $^{13}C\alpha$-$^{1}H\alpha$ dipolar couplings. This experiment yields H^{N}-N-Cα-Hα angle (ϕ_H), which is related to the ϕ-angle according to $\phi = \phi_H + 60^o$ [20].

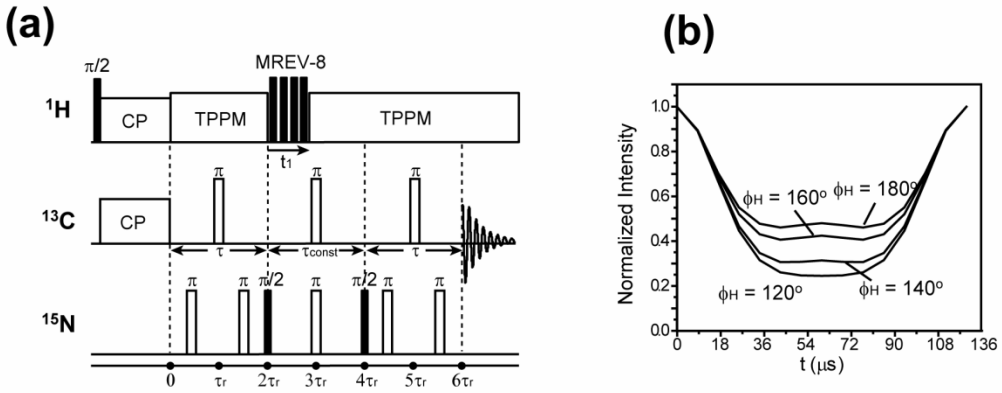

Figure 2.9. (a) HNCH pulse sequence. (b) Simulated HNCH dephasing curves for ϕ_H from 180º to 120º with $\omega_r/2\pi$ = 8 kHz.

Figure 2.8 shows the pulse sequence for HNCH. After the transverse ^{13}C magnetization is created by cross polarization, it evolves under the influence of the recoupled ^{15}N-^{13}C dipolar interaction for a period τ. A series of rotor-synchronized ^{15}N and ^{13}C 180º pulses was implemented after CP to recouple the N-C dipolar coupling. These pulses perturb MAS averaging of the anisotropic dipolar interaction so that antiphase magnetization C_yN_z is created. Then a ^{15}N 90º pulse converts C_yN_z into a combination of double- and zero-quantum coherences, C_yN_x. Next, the ^{1}H homonuclear dipolar coupling is removed by a MREV-8 pulse train, which defines the evolution time t_1, which has a maximum length of one rotor period. During this time, the magnetization evolves under the N-H and C-H dipolar coupling interaction. A pair of 180º pulses is placed at the center of this constant time period (τ_{const}) to refocus the ^{15}N and ^{13}C chemical shifts. At the end of the τ_{const}, a second ^{15}N 90º pulse and N-C recoupling period reconvert the N-C multiple-quantum coherences into observable ^{13}C magnetization, which is then detected. The transformations of the spin density operators under the pulse sequence are outlined below.

$$C_x \xrightarrow{\tau} C_yN_zf(\tau) \xrightarrow{90°_y{}^{15}N} C_yN_xf(\tau) \xrightarrow{t_1} C_yN_xf(\tau)\cos\left(\Psi_{CH}(t_1)\right)\cos\left(\Psi_{NH}(t_1)\right)$$
$$\xrightarrow{90°_{-y}{}^{15}N} C_yN_zf(\tau)\cos\left(\Psi_{CH}(t_1)\right)\cos\left(\Psi_{NH}(t_1)\right)$$
$$\xrightarrow{\tau} -C_xf^2(\tau)\cos\left(\Psi_{CH}(t_1)\right)\cos\left(\Psi_{NH}(t_1)\right)$$

Here $\Psi_{CH}(t_1)$ and $\Psi_{NH}(t_1)$ are the MAS phase angles accumulated during t_1 due to the C-H and N-H dipolar interactions. They depend on the relative orientations of the two dipolar coupling tensors, whose unique axes are along the Cα-Hα and N-H^N bonds and therefore reflect the torsion angle Φ_H.

2.3.2 NCCN

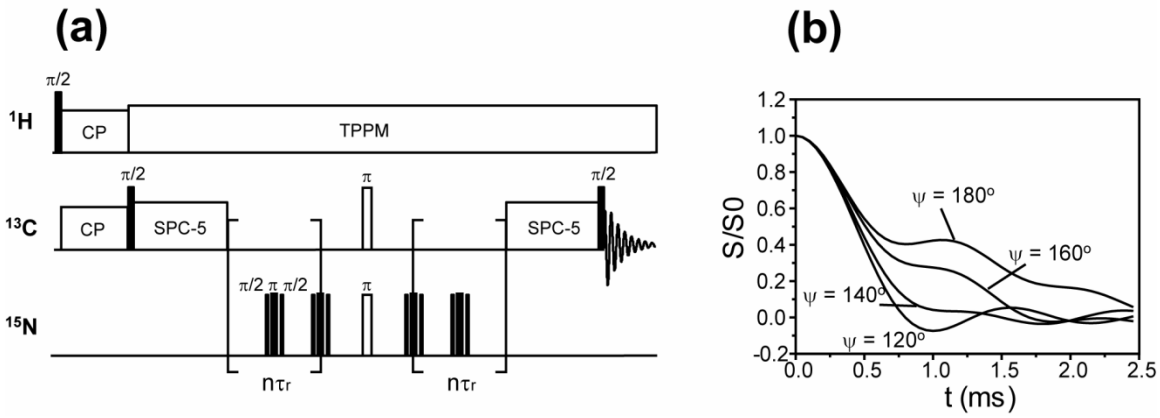

Figure 2.10. (a) NCCN pulse sequence. (b) Simulated NCCN dephasing curves for ψ from 180º to 120º.

NCCN is a robust method for measuring the backbone ψ torsion angles of proteins, which correlates the $^{15}N_i$-$^{13}C\alpha_i$ and $^{13}CO_i$-$^{15}N_{i+1}$ dipolar couplings to obtain the relative bond orientation [21,22]. $^{13}C\alpha$-^{13}CO double quantum coherence was excited using the SPC-5 sequence [23]. After that, the ^{15}N-^{13}C heteronuclear dipolar couplings were recoupled by a REDOR sequence [24], which yield a double quantum coherence dephasing curve whose shape provides information about the relative orientation of the ^{15}N-^{13}C internuclear vectors, and hence the ^{13}C-^{13}C torsion angle.

References

[1] Hediger, S.; Meier, B.; Kurur, N.; Bodenhausen, G.; Ernst, R., NMR cross polarization by adiabatic passage through the Hartmann—Hahn condition (APHH), Chem. Phys. Lett. 223 (1994) 283-288.

[2] Hediger, S.; Meier, B.; Ernst, R., Adiabatic passage Hartmann-Hahn cross polarization in NMR under magic angle sample spinning, Chem. Phys. Lett. 240 (1995) 449-456.

[3] Hartmann, S.; Hahn, E., Nuclear Double Resonance in the Rotating Frame, Phys. Rev. 128 (1962) 2042-2053.

[4] Baldus, M.; Geurts, D. G.; Hediger, S.; Meier, B. H., Efficient N-15-C-13 polarization transfer by adiabatic-passage Hartmann-Hahn cross polarization, J. Magn. Res. 118 (1996) 140-144.

[5] Hong, M., Resonance Assignment of 13C/15N Labeled Proteins by Two- and Three-Dimensional Magic-Angle-Spinning NMR, Journal of Biomolecular NMR 15 (1999) 1-14.

[6] Rienstra, C. M.; Hohwy, M.; Hong, M.; Griffin, R. G., 2D and 3D 15N-13C-13C NMR chemical shift correlation spectroscopy of solids: assignment of MAS spectra of peptides., Journal of the American Chemical Society 122 (2000) 10979-10990.

[7] Wishart, D. S.; Sykes, B. D.; Richards, F. M., Relationship between nuclear magnetic resonance chemical shift and protein secondary structure, J. Mol. Biol. 222 (1991) 311-333.

[8] Castellani, F. R., B.; Diehl, A.; Schubert, M.; Rehbein, K.; Oschkinat, H., Structure of a protein determined by solid-state magic-angle-spinning NMR spectroscopy, Nature 420 (2002) 98-102.

[9] Shen, Y.; Delagio, F.; Cornilescu, G.; Bax, A., TALOS+: A hybrid method for predicting protein backbone torsion angles from NMR chemical shifts, J. Biomol. NMR. 44 (2009) 213-223.

[10] Berjanskii, M. V.; Washart, D. S., A simple method to predict protein flexibility using secondary chemical shifts., J. Am. Chem. Soc. 127 (2005) 14970-14971.

[11] Schwieters, C.; Kuszewski, J.; Clore, G., Using Xplor-NIH for NMR molecular structure determination, Progr. NMR Spectroscopy 48 (2006) 47-62.

[12] Schwieters, C.; Kuszewski, J.; Tjandra, N.; Clore, G., The Xplor-NIH NMR Molecular Structure Determination Package, J. Magn. Res. 160 (2003) 66-74.

[13] Duer, M. Solid-State NMR Spectroscopy; Blackwell Publishing Ltd: Oxford, 2004.

[14] Schmidt-Rohr, K.; Spiess, H. W. Multidimensional Solid-State NMR and Polymers, 1994.

[15] Brink, D.; Satchler, G. Angular Momentum; Clarendon Press: Oxford, 1994.

[16] Zare, R. Angular Momentum; Wiley: New York, 1988.

[17] Brinkmann, A.; Eden, M.; Levitt, M. H., Synchronous helical pulse sequences in magic-angle spinning nuclear magnetic resonance: Double quantum recoupling of multiple-spin systems, J. Chem. Phys. 112 (2000) 8539-8554.

[18] Brinkman, A.; Eden, M.; Levitt, M., Synchronous helical pulse sequences in magic-angle spinning nuclear magnetic resonance: Double quantum recoupling of multiple-spin systems, J. Chem. Phys. 112 (2000) 8539-8554.

[19] Hohwy, M.; Rienstra, C. M.; Jaroniec, C. P.; Griffin, R. G., Fivefold symmetric homonuclear dipolar recoupling in rotating solids: Application to double quantum spectroscopy, Journal of Chemical Physics 110 (1999) 7983-7992.

[20] Hong, M.; Gross, J. D.; Griffin, R. G., Site-resolved determination of peptide torsion angle phi from the relative orientations of backbone N-H and C-H bonds by solid-state NMR, Journal of Physical Chemistry B 101 (1997) 5869-5874.

[21] Costa, P. R.; Gross, J. D.; Hong, M.; Griffin, R. G., Solid-State NMR Measurement of psi in Peptides: a NCCN 2Q-Heteronuclear Local Field Experiment, Chem. Phys. Lett. 280 (1997) 95-103.

[22] Feng, X.; Eden, M.; Brinkmann, A.; Luthman, H.; Eriksson, L.; Graslund, A.; Antzutkin, O. N.; Levitt, M. H., Direct determination of a peptide torsion angle psi by double-quantum solid-state NMR, Journal of the American Chemical Society 119 (1997) 12006-12007.

[23] Hohwy, M.; Jakobsen, H. J.; Eden, M.; Levitt, M. H.; Nielsen, N. C., Broadband dipolar recoupling in the nuclear magnetic resonance of rotating solids: a compensated C7 pulse sequence., Journal of Chemical Physics 108 (1998) 2686-2694.

[24] Gullion, T.; Schaefer, J., Rotational echo double resonance NMR, J. Magn. Reson. 81 (1989) 196-200.

Chapter 3

Resonance Assignment and Three-Dimensional Structure Determination of a Human Alpha-Defensin, HNP-1, by Solid-State NMR

A paper published in J. Mol. Biol.

2010, vol. 397, pp. 408-422

Yuan Zhang, Tim Doherty, Jing Li, Wuyuan Lu, Cyril Barinka, Jacek Lubkowski, and Mei Hong

Abstract

Human α-defensins (HNPs) are immune defense mini-proteins that act by disrupting microbial cell membranes. Elucidating the three-dimensional structures of HNPs in lipid membranes is important for understanding their mechanisms of action. Using solid-state NMR, we have determined the three-dimensional structure of HNP-1 in a microcrystalline state outside the lipid membrane, which provides benchmarks for structure determination and comparison with the membrane-bound state. From a suite of 2D and 3D magic-angle spinning experiments, ^{13}C and ^{15}N chemical shifts were obtained that yielded torsion angle constraints while inter-residue distances were obtained to restrain the three-dimensional fold. Together, these constraints led to the first high-resolution SSNMR structure of a human defensin. The SSNMR structure has close similarity to the crystal structures of the HNP family, with the exception of the loop region between the first and second β-strands. The difference, which is partially validated by direct torsion angle measurements of selected loop residues, suggests possible

conformational variation and flexibility of this segment of the protein, which may regulate HNP interaction with the phospholipid membrane of microbial cells.

Introduction

Antimicrobial peptides (AMPs) are small cationic peptides that constitute part of the innate immune system of many plants and animals to rapidly kill invading microbial pathogens. In mammals the two main classes of antimicrobial peptides are cathelicidins and defensins [1]. While most cathelicidins are α-helical in structure, defensins contain β-strands stabilized by three disulfide bonds [2-4]. Based on the disulfide-linkage patterns, three classes of defensins, α-, β-, and θ-defensins, are identified in vertebrates. Humans have six α-defensins that contain 29-32 residues. Four of these proteins are present in the azurophilic granules of neutrophils and are called human neutrophil peptides 1-4 (HNP 1-4) [2,5], and two are expressed in intestinal Paneth cells and are called HD-5 and HD-6 [6,7]. Except for HD-6, all five human α-defensins have wide-spectrum antimicrobial activities with LD_{50} in the μg/ml range [8,9]. Similar to most other AMPs, the main mechanism of action of HNPs is believed to be permeabilization of the microbial cell membrane [10,11].

The presence of three antiparallel disulfide-stabilized β-strands makes defensins larger and more complex proteins than most other AMPs. In particular, they are natural extensions of the two-stranded β-hairpin AMPs such as protegrins from porcine leukocytes and tachyplesins from horseshoe crabs, whose membrane-bound structure and lipid interaction have been characterized in detail by solid-state NMR recently [12-21]. Compared to these smaller β-sheet AMPs, HNPs have weaker antimicrobial activities. Moreover, although HNP 1-3 have nearly identical sequences, differing only in the N-terminus residue, their activities differ by as much as 4-fold [8]. Understanding the activity differences among human defensins requires structural investigations in the lipid membrane. However, so far most high-resolution structures of human defensins come from X-ray crystallography in the absence of any membrane-mimetic solvents [3,4]. A few biophysical studies that investigated the interactions of defensins with lipid

membranes have also been reported, but did not contain high-resolution structural information [22-24].

Solid-state NMR magic-angle spinning (MAS) NMR has been recently shown to be able to elucidate the atomic-resolution structure of ^{13}C, ^{15}N-labeled proteins in microcrystalline states [25-28], in fibrillar forms [29-31], and in lipid membranes [32,33]. A wide variety of 2D and 3D correlation techniques have been developed to obtain resonance assignment [34,35], torsion angles [36-38] and inter-atomic distances [39]. Therefore, the technology is now in place to determine the full structures of human α-defensins in lipid membranes to elucidate the mechanism of action of this important class of immune defense molecules.

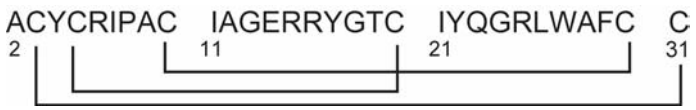

Figure 3.1. Amino acid sequence and disulfide bond connectivities of HNP-1.

In this work, we report the three-dimensional structure determination of recombinant HNP-1, whose sequence is shown in **Figure 3.1**, by SSNMR. We have carried out resonance assignment and internuclear distance measurements of HNP-1 in an ordered microcrystalline state, in preparation for structure determination of the protein bound to the lipid membrane, since membrane-bound proteins usually give lower-resolution spectra due to the disorder created by the lipid bilayer. The conformation of microcrystalline HNP-1 also represents the protein structure before binding to the lipid membrane, and is thus necessary for understanding potential conformational changes of HNPs induced by the lipid bilayer. We compare the SSNMR structure with various published crystal structures of HNPs [3,4,40].

Results

Preparation of microcrystalline HNP-1 samples for solid-state NMR experiments

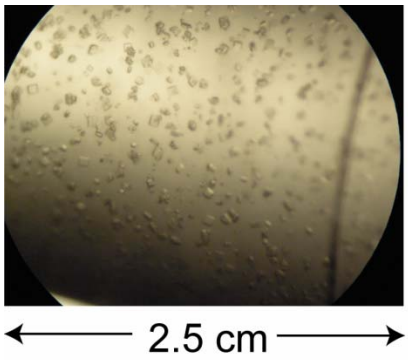

Figure 3.2. An image of microcrystalline HNP-1. The average size of the crystals is ~20 μm.

The solid-state NMR data presented here were obtained from microcrystalline samples of HNP-1 precipitated from a polyethylene glycol (PEG) solution. Two samples were prepared using different concentrations of the protein stock solution. The high-concentration stock solution (36 mg/ml) yielded microcrystals one hour after mixing with PEG, while the low-concentration stock solution (30 mg/ml) produced microcrystals gradually in a 4-day period, with ~80% of the protein eventually precipitating from the supernatant. The slower precipitation produced larger crystals of ~20 μm diameter compared to 2 μm for the rapidly precipitated sample. **Figure 3.2** shows an image of HNP-1 microcrystals obtained from the slower precipitation procedure.

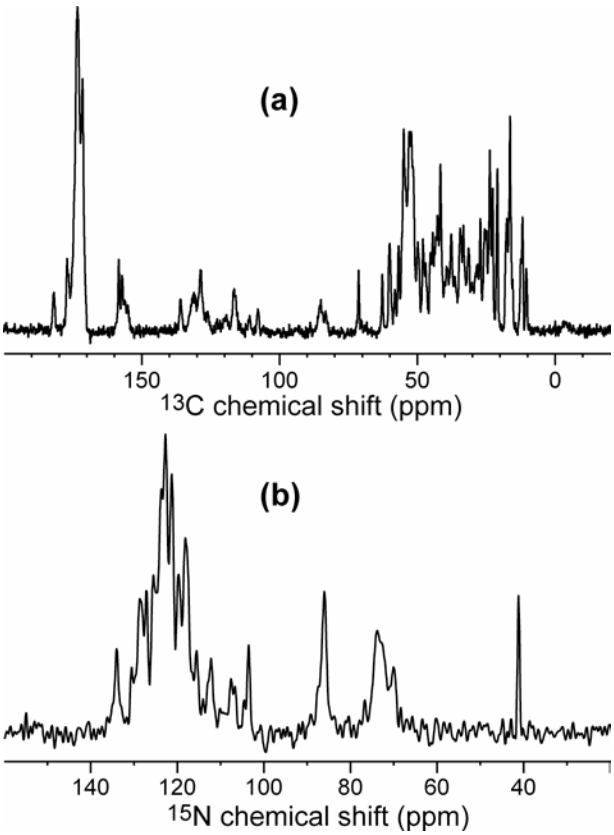

Figure 3.3. 1D CP-MAS spectra of microcrystalline U-^{13}C, ^{15}N-labeled HNP-1. (a) ^{13}C spectrum, measured at 258 K at a ^{13}C Larmor frequency of 225 MHz. (b) ^{15}N spectrum, measured at 268 K at a ^{15}N Larmor frequency of 60 MHz.

Both microcrystalline HNP-1 samples yielded well-resolved ^{13}C and ^{15}N MAS spectra, shown in **Figure 3.3**. For the rapidly precipitated sample in the 4 mm rotor, the ^{13}C full widths at half maxima were 0.6 – 1.0 ppm and the ^{15}N linewidths were 1.3 – 1.7 ppm. For the slowly precipitated sample in the 2.5 mm rotor, the linewidths improved to 0.4 – 0.8 ppm for ^{13}C and 1.0 – 1.5 ppm for ^{15}N. Faster spinning frequencies and stronger ^{1}H decoupling fields further contributed to the narrower linewidths of the 2.5 mm rotor sample.

Resonance assignment of HNP-1 by 2D and 3D SSNMR

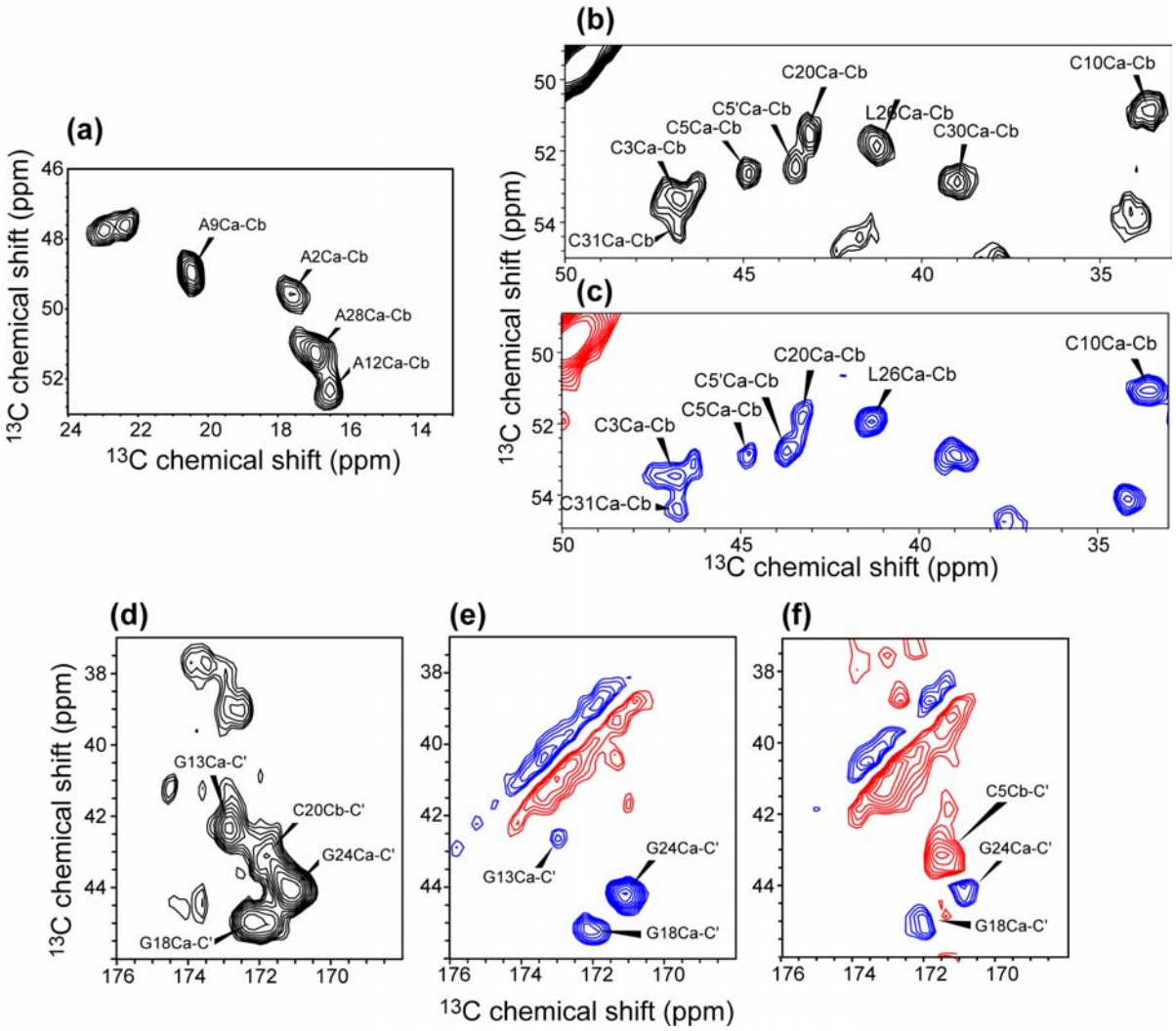

Figure 3.4. Representative regions of 2D ^{13}C-^{13}C correlation spectra of HNP-1. (a) Ala Cα-Cβ region from a 40 ms DARR spectrum. (b) Cys Cα-Cβ region from a 40 ms DARR spectrum. (c) Cys Cα-Cβ region from a 0.8 ms CM_5RR spectrum. Blue: positive intensities. Red: negative intensities. (d-f) CO-Cα/Cβ region. (d) 40 ms DARR spectrum, (e) 0.8 ms CM_5RR spectrum. (f) 1.5 ms CM_5RR. The sign of the cross peak intensities distinguishes the one-bond Gly CO-Cα peaks (red, indicating negative) from the two-bond Cys CO-Cβ peaks (blue, indicating positive).

We first assigned the amino acid spin systems of HNP-1 using 2D ^{13}C-^{13}C correlation experiments, including a DARR experiment with 40 ms mixing, and double-quantum (DQ)-filtered experiments using SPC5 [41] and CM_5RR sequences [42]. The 40 ms DARR spectrum allowed the assignment of most amino acid types (**Figure 3.4a, b, d**), including Cys, Ala, Ile, Arg, Leu, Pro, and Thr, which have distinct cross peak patterns.

The aromatic residues were assigned based on the Cα/Cβ cross peaks to the aromatic carbons. For example, the Cγ of the unique tryptophan W27 resonates at 107.8 ppm (**Figure S1**), which allowed the rest of the W27 spin system to be identified. For the unique glutamate E14 and glutamine Q23, the sidechain Cδ chemical shifts (181 ppm for E14 and 176 ppm for Q23) served as useful guides for identifying the chemical shifts of the other sidechain carbons.

The DQ-filtered 2D spectra confirmed the DARR assignment by exhibiting opposite intensities for one-bond and two-bond cross peaks. For example, Gly Cα and Cys Cβ, which both resonate at 40-45 ppm, are distinguished based on the negative intensities of the one-bond Gly Cα-CO peaks and the positive intensities of the two-bond Cys Cβ-CO peaks in the CM_5RR spectra **(Figure 3.4c, e, f)**. Similarly, while Q23 Cβ has similar chemical shifts to Arg Cγ in the DARR spectrum, in the DQ filtered spectra Q23 Cβ exhibits a positive one-bond Cα-Cβ cross peak, which is distinct from the negative two-bond Arg Cα-Cγ cross peaks. By comparing various 2D ^{13}C-^{13}C spectra, we assigned all amino acid spin systems except for one Arg.

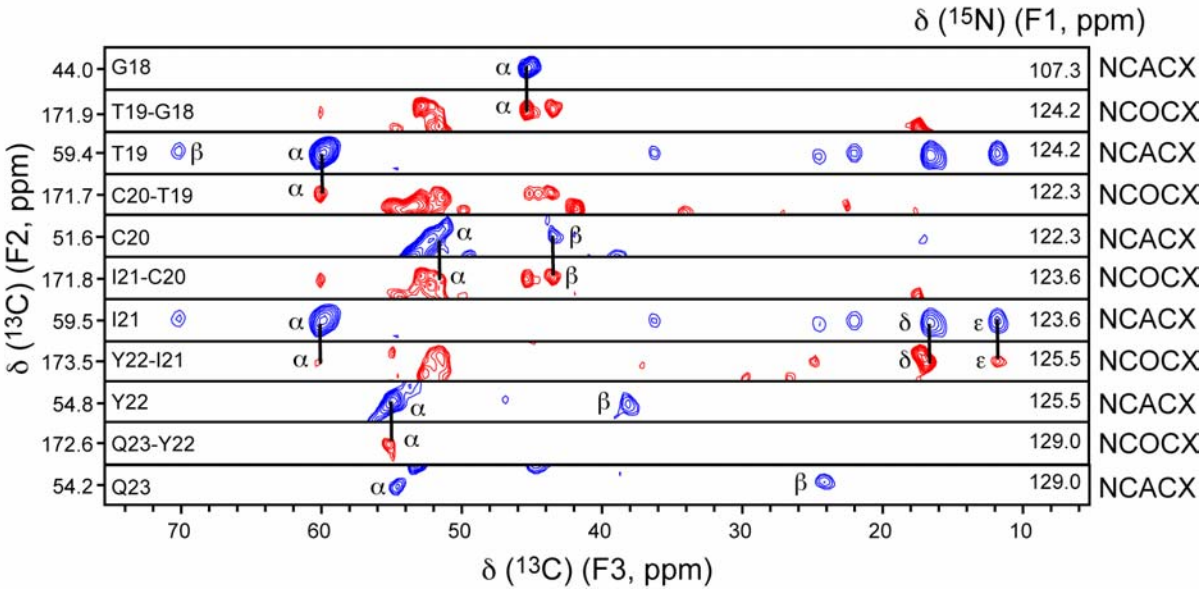

Figure 3.5. F2-F3 strips of 3D NCACX (blue) and NCOCX (red) spectra for residues G18 to Q23, illustrating sequential resonance assignment. The strip width for the F2 dimension is 2.3 ppm. The F1 ^{15}N chemical shifts for the strips are indicated on the right end of each strip.

Next, we obtained sequence-specific assignment from inter-residue NCOCX and intra-residue NCACX 3D experiments [34,35]. **Figure 3.5** shows a representative strip of F2-F3 planes of the two 3D experiments for residues G18-Q23. We first identified the ^{15}N chemical shift of residue *i* in the NCACX spectrum by comparing the ^{13}C chemical shifts with those obtained from the 2D CC spectra. The ^{15}N chemical shift of residue *i*+1 was then obtained from the NCOCX spectrum through its cross peaks with the ^{13}C chemical shifts of residue *i*. The ^{15}N plane of residue *i*+1 was then searched in the NCACX spectrum to identify the ^{13}C chemical shifts of residue *i*+1.

A2, A9, T19 and C30 are clear starting points for assigning a consecutive segment of residues. The N-terminal residue A2 has a distinct ^{15}N chemical shift of 41.7 ppm, which is folded to 106.9 ppm. Residue A9 has cross peaks with P8, which has characteristic ^{13}C chemical shifts. Residue T19 has characteristic Cα and Cβ chemical shifts.

The four Ala residues, which are well resolved in the 2D CC spectra, were sequentially assigned in the 3D spectra. For example, A9 was assigned based on its correlation with the unique P8 and with C10, and A12 was assigned based on its correlation with the well defined I11 and G13. For the three Gly residues, G24 was identified by inter-residue correlations Q23N-G24Cα and R25N-G24Cα in the 3D spectra and in the 100 ms DARR spectrum, while G18 was assigned based on the T19N-G18Cα correlations in the 3D spectrum.

The six Cys residues were resolved and assigned based on their cross peaks with their neighboring residues in the NCOCX spectrum. For example, C3 has characteristic cross peaks with A2 Cβ and Cα, and C5 has cross peaks with the Y4 spin system. Interestingly, C5 exhibits two Cβ chemical shifts differing by 0.9 ppm, suggesting the presence of two conformations at this site. C10 has a Cβ chemical shift of 33.4 ppm (on the TMS scale), which is slightly low for an oxidized cysteine. However, its assignment was corroborated by multiple sequential C10 – A9 cross peaks and I11 – C10 cross peaks. For example, C10N-A9C'-A9Cα/Cβ cross peaks were identified in the 3D NCOCX

spectrum, and sequential C10Cα-A9Cβ, C10Cβ-A9Cβ, and A9Cα-C10Cβ cross peaks were also detected in the 100 ms DARR spectrum (**Figure S2**).

Table 3.1. ^{13}C and ^{15}N chemical shifts of microcrystalline HNP-1 without lipids [a].

	N	Cα	Cβ	Cγ	Cδ	Cε	CO
A2	41.7	49.5	17.5				171.0
C3$^{(C31)}$[b]	117.8	53.0	46.6				171.4
Y4	117.6	54.8					172.6
C5 $^{(C20)}$	130.6	52.7	44.5/43.4				171.4
R6	123.1	53.9	33.7	26.7	41.5		173.6
I7	122.3	56.5	41.2	28.0	15.3	10.1	172.6
P8	134.4	62.2	32.9	23.1/22.1	47.5		172.7
A9	122.6	48.8	20.6				172.9
C10$^{(C30)}$	115.6	50.8	33.4				173.0
I11	115.4	57.9	37.5	23.8	15.9	12.2	173.0
A12	121.9	51.8	16.6				175.2
G13	109.6	42.6					
E14	121.3	52.2	31.4	34.4	181.8		173.6
R15	130.6	52.7					171.4
R16	122.8	54.5	28.1	27.0	42.4	157.1	175.3
Y17	128.1	56.3	38.5	131.5			173.5
G18	107.3	45.0					171.9
T19	124.2	59.4	69.6	21.7			171.7
C20$^{(C5)}$	122.3	51.6	43.0				171.8
I21	123.6	59.5	35.8	24.3	16.2	11.4	173.5
Y22	125.5	54.8	37.7				172.6
Q23	129.0	54.2	23.8	31.9	176.5		173.9
G24	103.4	44.0					170.3
R25	118.4	51.6	32.2	25.5	41.2		172.0
L26	120.2	51.6	41.2	25.4	23.2	22.4	174.4
W27	120.7	52.0	29.0				175.3
A28	127.1	51.0	16.9				172.8
F29	123.8	56.6	39.8	129.2			
C30$^{(C10)}$	121.9	53.0	38.6				172.7
C31$^{(C3)}$	121.1	55.3	47.0				177.5

[a] The ^{13}C chemical shifts are referenced to TMS. To convert to DSS-referenced chemical shifts, the ^{13}C frequencies in this table should be increased by 1.7 ppm. The ^{15}N chemical shifts are referenced to liquid ammonia.

[b] The partner cysteine involved in the disulfide bond is indicated in the bracket.

The complete ^{13}C and ^{15}N isotropic chemical shifts of HNP-1 are summarized in **Table 3.1**. Among the six cysteines, the C10 – C30 pair has relatively upfield Cβ chemical shifts. To further verify that C10 and C30 are indeed disulfide-bonded, we compared the Cα and Cβ chemical shifts of all HNP-1 cysteines with literature statistical analyses of the dependence of cysteine ^{13}C chemical shifts on the oxidation state and conformation [43,44]. On the DSS scale, the oxidized cysteines have Cβ chemical shifts of 33 - 51 ppm and Cα chemical shifts of 50 - 61 ppm. When the HNP-1 cysteine chemical shifts are also referenced to DSS (thus increasing the ^{13}C chemical shifts in **Table 3.1** by 1.7 ppm), we find that all six cysteines, including C10 and C30, lie in the oxidized range (**Figure S3**), thus confirming the disulfide-bonded nature of all three pairs.

Backbone dihedral angles and verification by dipolar correlation experiments

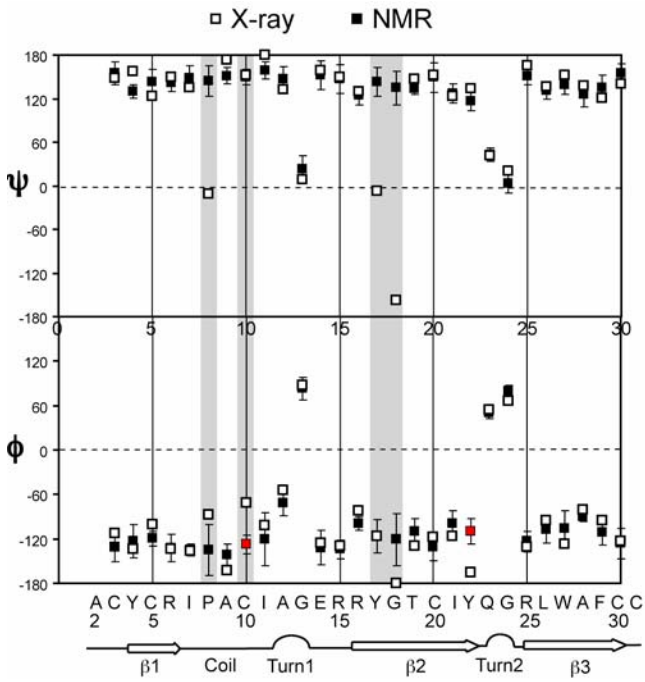

Figure 3.6. HNP-1 (ϕ, ψ) torsion angles determined from solid-state NMR ^{13}C and ^{15}N chemical shifts (filled squares). The torsion angles of HNP-3 are shown for comparison (open squares and ribbons) (PDB accession code: 1DFN). Residues with significantly different torsion angles from the crystal structure values of HNP-3 are shaded.

The ^{13}C and ^{15}N chemical shifts allowed us to determine the backbone (ϕ, ψ) torsion angles of HNP-1 using the well-known empirical relation between N, Cα, Cβ, CO chemical shifts and protein secondary structure [45]. We used the TALOS program [46] to predict the (ϕ, ψ) angles and compared them with the values found from the crystal structure of HNP-3 [3] (PDB code: 1DFN). The chemical-shift constrained torsion angles indicate three well-defined β-strands, β1, β2 and β3, separated by a type-II β-turn at A12-G13 and a type I' β-turn at Q23-G24 (**Figure 3.6**). These secondary structure motifs are consistent with those of the HNP-3 structure, although the boundaries of the loop or turn segments between β-strands differ slightly between HNP-3 and HNP-1.

Among the 28 (ϕ, ψ) pairs predicted by TALOS, excluding the terminal A2 and C31, 24 ϕ angles and 24 ψ angles agree well with the crystal structure values within the experimental uncertainty. Residues with large dihedral angle discrepancies are P8, C10, Y17, G18 and Y22 (**Figure 3.6** and **Table S1**). P8 and C10 both lie in the loop between β1 and β2 strands and might be expected to be dynamically disordered. However, the HNP-3 crystal structure shows well-defined positions for these residues, with B factors not higher than the average [3]. Direct measurement of C-H order parameters of the HNP-1 sample by NMR (see **Figure 3.11** below) also indicates that the loop region in HNP-1 is not dynamic.

To verify the torsion angle differences between TALOS and the crystal structure, we conducted the HNCH experiment to directly measure the ϕ angles of C10 and Y22. The experiment measures the ϕ_H angle (defined as H^N-N-Cα-Hα, which is related to ϕ by $\phi_H+60^\circ=\phi$) by correlating the N-H and Cα-Hα dipolar couplings [36,47], and is particularly sensitive to the β-sheet conformation, which has ϕ_H angles around 180°. To maximize the angular resolution, we implemented the N-H doubled version of the experiment [47]. In principle, a 3D experiment where two chemical shift dimensions provide site resolution while one dipolar dimension gives the angular information is the most desirable. However, the low sensitivity of the 3D experiment and the limited protein amount precluded its implementation. Thus, we used one ^{13}C chemical shift dimension for site resolution and measured the dipolar evolution at time 0 and half a rotor period.

Simulations have shown that the HNCH dipolar dephasing at the middle of the rotor period is the most sensitive to ϕ_H angle differences [48].

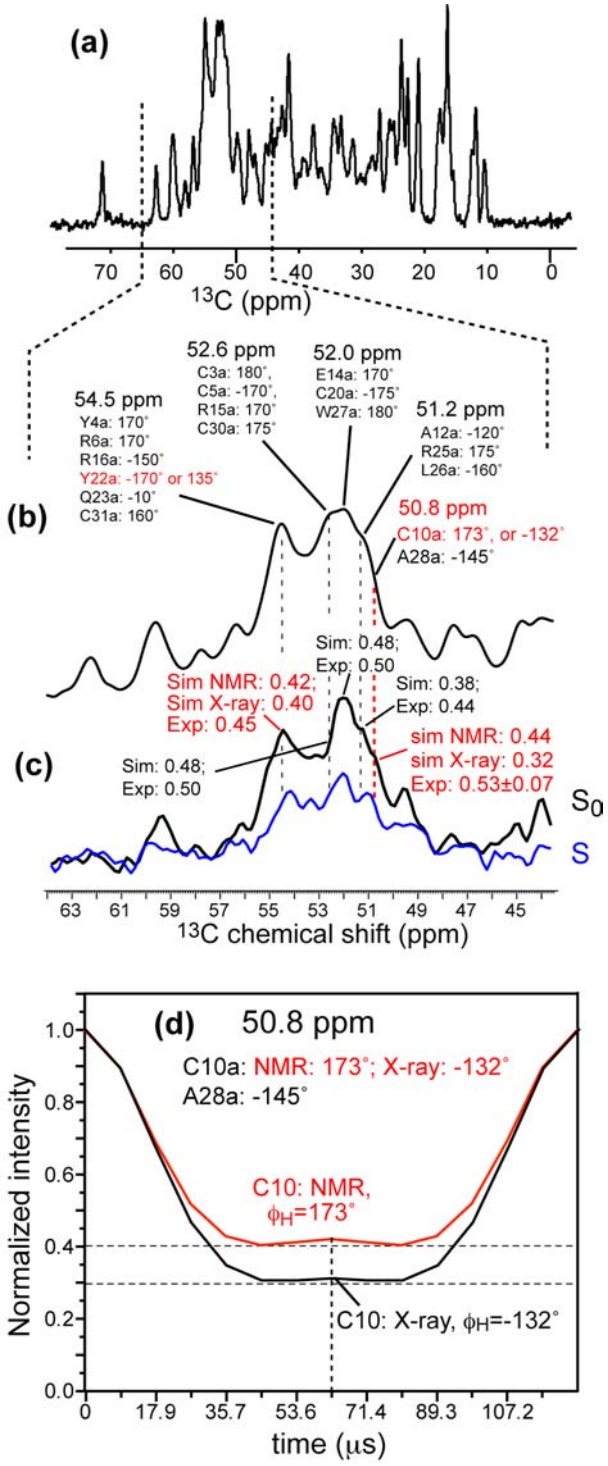

Figure 3.7. Direct measurement of ϕ torsion angles by HNCH. (a) Aliphatic region of the 1D ^{13}C spectrum. (b) Cα region (44-64 ppm) of the ^{13}C spectrum, indicating the assignment of the resolved peaks and the ϕ_H torsion angles (ϕ_H+60˚=ϕ) of each residue. For most residues the ϕ_H angles agree between TALOS and the crystal structure within ±10˚. But for C10 and Y22, significant deviations exist. (c) Measured HNCH spectra with dipolar evolution time of 0 (S_0) and half a rotor period (S, shown in blue). The measured S.S_0 values are indicated along with calculated values. The 50.8-ppm peak has an S/S_0 value that is consistent with the chemical shift derived ϕ angles and not the HNP-3 value. (d) Calculated HNCH curves for the 50.8 ppm C10/A28 Cα peak. The A28 ϕ_H angle is fixed while the C10 ϕ_H angle is either 173˚ or 132˚. The measured HNCH intensity at the middle of the rotor period is consistent with the TALOS ϕ_H angle but not the crystal structure value.

Figure 3.7c shows the Cα region of the ^{13}C spectra with 0 and half a rotor period of HNCH evolution. The peaks were assigned based on the 2D and 3D spectra above. Although single-site resolution is not available, most sites have consistent ϕ angles between the TALOS prediction and the crystal structure within ±10˚ (**Table S1**). The only uncertain residues are C10 and Y22, thus their ϕ_H angles can be extracted from the intensities. Specifically, the C10 Cα signal at 50.8 ppm overlaps with only one residue, A28, whose ϕ_H angle is -145˚±5˚, as indicated by both TALOS and the crystal structure (**Figure 3.7b**). Thus, the calculated HNCH curve for 50.8 ppm is very sensitive to the C10 ϕ_H angle (**Figure 3.7d**). The experimental intensity (0.53) is much more consistent with the TALOS prediction of a β-sheet like ϕ_H angle of about 180˚ rather than a low value of about -130˚ (**Figure S4**). Similarly, the measured HNCH intensity for the 54.5-ppm peak, which is a composite of Y22 Cα with five other Cα sites, is more consistent with the TALOS prediction than with the crystal structure, although the distinction between the two possibilities is smaller for this peak due to more resonances overlapping at this position.

For P8, both ϕ and ψ angles differ between the chemical shift prediction and the crystal structure (**Table S1**). The lack of H^N at Pro precludes direct measurement of its ϕ angle. In principle, the ψ angle can be measured using the NCCN technique [37]. At

present the protein amount is insufficient for this experiment, which requires ^{13}C double-quantum filtration in addition to ^{13}C-^{15}N REDOR. Thus, future experiments are necessary to clarify the conformational discrepancy at P8. Nevertheless, based on distance constraints involving this loop, we hypothesize that the difference may be real instead of due to inaccuracy of the NMR structure determination (see below).

The torsion angle difference for Y17-G18 is also noteworthy. TALOS predicted a relatively ideal β-strand ψ angle for Y17 whereas the crystal structure gives an unusual ψ angle near 0˚. On the other hand, the TALOS Y17 torsion angles have relatively large uncertainties ($\Delta\phi$=23˚, $\Delta\psi$=20˚) (**Table S1**). Among the 10 pairs of torsion angles predicted, seven pairs lie in the β-sheet region while three pairs lie near the α-helical region, with ψ angles of about -20˚, which are similar to the crystal structure ψ value. Thus, the ensemble of NMR torsion angles for Y17 encompasses the crystal structure value.

For G18, chemical shifts predicted a ϕ angle of -120˚ whereas the crystal structure shows a ϕ angle near 180˚. Since glycine residues have two Hα protons, the HNCH experiment is not ideal for measuring their ϕ angles. The TALOS uncertainties for G18 are ($\Delta\phi$=35˚, $\Delta\psi$=23˚) (**Table S1**), and three of the predicted pairs of angles lie in the right-handed α-helix region of the Ramachandran diagram. Thus, the conformation of this residue is not well predicted from the chemical shifts. On the other hand, G18 is strictly conserved in all human defensins. Based on comparisons of HNP-4, HD5 and HD6 crystal structures, it has been suggested that G18 may act as a hinge for the G18-L29 β-hairpin [4], which has significantly different orientations in various HNPs. Thus, it remains a possibility that the G18 torsion angle difference between the NMR and crystal structures may reflect real conformational variations at this residue.

Inter-residue distances

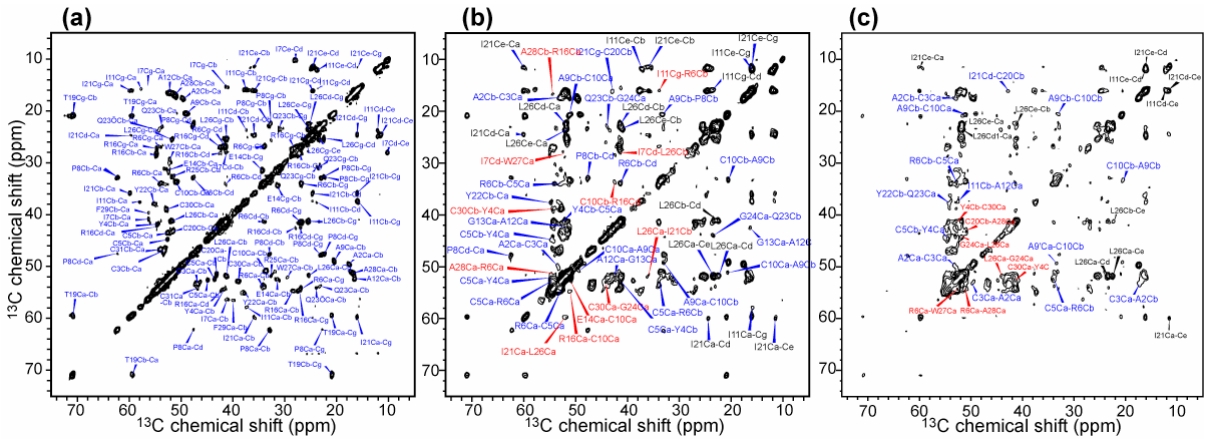

Figure 3.8. 2D ^{13}C-^{13}C DARR spectra of HNP-1 with mixing times (a) 40 ms, (b) 100 ms, and (c) 200 ms. In (a), all peaks are assigned. In (b) and (c), only inter-residue and intra-residue multiple-bond correlations not observed in (a) are assigned. Red: non-sequential inter-residue correlations; blue: sequential correlations; black: intra-residue multiple-bond correlations.

To constrain the three-dimensional fold of HNP-1, we measured distances between sequential and non-sequential residues using DARR experiments with long mixing times. Two spin diffusion mixing times, 100 ms and 200 ms, were chosen, which resulted in larger numbers of cross peaks that deteriorated the spectral resolution (**Figure 3.8**). To bypass this problem, we used a comparative strategy to identify the long-distance correlation peaks. For each inter-residue cross peak, we first found all possible assignments that agree with the peak position to ±0.2 ppm. We then measured the distances of these inter-residue pairs in the HNP-3 crystal structure [3], and selected the assignment with the shortest distance. For these inter-residue cross peaks, since distances between sequential residues are usually the shortest, where ambiguity arises, we gave preferences to sequential distances over medium or long-range distances.

Table 3.2. Non-sequential inter-residue distance restraints.

residues	spectrum	type of correlation	Distance (A)
C10Cα-E14Cβ	40 ms DARR	medium range: i – (i+4)	2.5 – 4.8
E14Cγ-C30Cα	40 ms DARR	long range	2.5 – 4.8
A2Cα-C30Cα	100 ms DARR	long range: β1 – β3	2.5 – 5.4

Y4Cα-C30Cβ	100 ms DARR	long range: β1 – β3	2.5 – 5.4
R6Cα-A28Cα	100 ms DARR	long range: β1 – β3	2.5 – 5.4
I7Cγ-L26Cβ	100 ms DARR	long range	2.5 – 5.4
I7Cγ-W27Cα	100 ms DARR	long range	2.5 – 5.4
C10Cβ-R16Cδ	100 ms DARR	long range	2.5 – 5.4
R16Cα-A28Cβ	100 ms DARR	long range: β2 – β3	2.5 – 5.4
I21Cα-L26Cα	100 ms DARR	long range: β2 – β3	2.5 – 5.4
R6Cδ-C30Cβ	200 ms DARR	long range: β1 – β3	2.5 – 6.3
R16Cβ-F29Cα	200 ms DARR	long range: β2 – β3	2.5 – 6.3
R6Cγ-A28Cα	200 μs CHHC	long range: β1 – β3	2.5 – 8.0
C5Cβ-F29Cβ	300 μs CHHC	long range: β1 – β3	2.5 – 8.0
Y4N-G13N	3 s ^{15}N PDSD	long range	3.0 – 6.0
C5N-T19N	3 s ^{15}N PDSD	long range: β1 – β2	3.0 – 6.0
P8N-Y22N	3 s ^{15}N PDSD	long range	3.0 – 6.0
P8N-W27N	3 s ^{15}N PDSD	long range	3.0 – 6.0
P8N-A28N	3 s ^{15}N PDSD	long range	3.0 – 6.0
C10N-G13N	3 s ^{15}N PDSD	medium range: i – (i+3)	3.0 – 6.0
Y17N-C30N	3 s ^{15}N PDSD	long range: β2 – β3	3.0 – 6.0
G18N-W27N	3 s ^{15}N PDSD	long range: β2 – β3	3.0 – 6.0
Y22N-R25N	3 s ^{15}N PDSD	medium range: β2 – β3	3.0 – 6.0
G24N-L26N	3 s ^{15}N PDSD	medium range: i – (i+2)	3.0 – 6.0

In this way, we identified 40 inter-residue CC correlations, among which 26 were sequential contacts, 1 was medium range ($1< |i-j| <4$), and 13 were long-range contacts ($|i-j| > 4$). Non-sequential correlations were observed for residues A2, Y4, R6, I7, C10, E14, R16, I21, L26, W27, F29 and C30 (**Table 3.2**). Six long-range correlation peaks were detected between β1 and β3 strands, and six contacts between β2 and β3 strands. These inter-strand correlations provided important restraints to the three-dimensional fold of the protein.

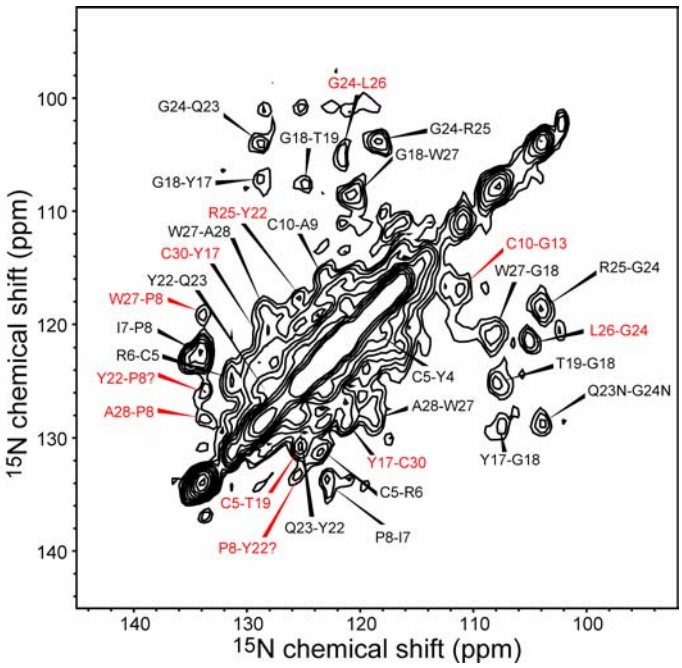

Figure 3.9. ^{15}N-^{15}N 2D PDSD spectrum with a mixing time of 3 s. Black and red assignments indicate sequential and non-sequential correlations, respectively.

We also measured a 2D ^{15}N-^{15}N correlation spectrum to obtain additional inter-residue distance restraints (**Figure 3.9**). The Gly region was the best resolved and provided many useful sequential and long-range cross peaks. P8 also gave well-resolved cross peaks due to its unique imine ^{15}N chemical shift. The 110 – 130 ppm region is more congested, thus we only assigned the intensity maxima and gave them tentative assignments in the same fashion as the CC constraints. The non-sequential NN contacts are included **Table 3.2**.

Since the above distance extraction strategy used the HNP-3 structure as partial input, potential differences of HNP-1 from HNP-3 can only be discerned based on missing correlations for HNP-1, and mis-assignment cannot be ruled out. To extract distance restraints in a *de novo* fashion, without input from the HNP-3 structure, we carried out further 3D ^{13}C-^{13}C-^{13}C correlation experiments, which removed the problem of resonance overlap. As we report in a separate publication, the 3D CCC experiment yielded 270 unique inter-residue distances, among which 129 were sequential, 45 were

medium range, and 96 were long-range constraints. These distances verified and refined the current structure, as we show below.

Three-dimensional structure of HNP-1

Table 3.3. Structure calculation summary of HNP-1.

Restraints	
Total inter-residue CC and NN restraints	60
Sequential (|i-j| = 1)	36
Medium range (1< |i-j| <4)	4
Long range (|i-j| > 4)	20
β1 – β3	6
β2 – β3	6
β1 – β2	1
CC Restraints in the class 2.5 – 4.8 Å	4
CC Restraints in the class 2.5 – 5.4 Å	18
CC Restraints in the class 2.5 – 6.3 Å	5
CC Restraints in the class 2.5 – 8.0 Å	7
NN restraints in the class 2.5 – 4.0 Å	10
NN restraints in the class 3.0 – 6.0 Å	10
Total (ϕ, ψ) torsional angle restraints	56
rms deviation of 11 lowest-energy structures from the crystal structure	
Backbone atoms:	2.7 Å
Heavy atoms:	3.8 Å
E_{global} (kcal mol^{-1})	264

Using the distance and angular restraints obtained from the above SSNMR experiments, we calculated the HNP-1 structure using the XPLOR-NIH program. We assigned the distance restraints to specific ranges based on the mixing times for the first appearance of cross peaks that correspond to well-defined secondary structures (**Table 3.3**). Sequential Cα-Cα distances are fixed by the peptide plane geometry to be 3.8 Å and

were thus placed in the range of 3.5-4.1 Å. Sequential N-N distances depend on the ψ torsion angle and fall within the range of 2.5 – 3.6 Å. All inter-residue peaks first observed in the 100 ms ^{13}C-^{13}C DARR spectrum were assigned to the range 2.5 – 5.4 Å, those first appearing in the 200 ms DARR spectrum assigned to 2.5 – 6.3 Å, and those inter-residue peaks appearing in the 2D CHHC spectra assigned to 2.5 – 7.5 Å. In addition, the few inter-residue correlations observed in the 40 ms ^{13}C-^{13}C DARR spectrum were assigned to the range 2.5 – 4.8 Å. All non-sequential ^{15}N-^{15}N contacts were placed in the 3.0 – 6.0 Å range.

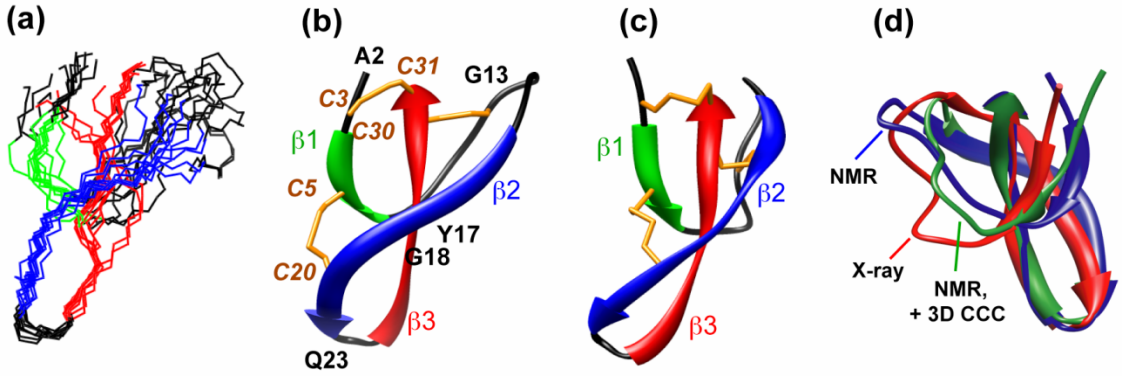

Figure 3.10. SSNMR structures of HNP-1 compared with the X-ray crystal structure of HNP-3. (a) Eleven minimum energy SSNMR structures of HNP-1. (b) Average structure of (a). (c) Crystal structure of HNP-3. The disulfide bonds are shown in orange. (d) Comparison of the β1-β2 loop conformation between the crystal structure (red), the current solid-state NMR structure (blue), and the NMR structure with the additional distance restraints from the 3D CCC experiment (green).

In total, we obtained 60 inter-residue distance restraints, 56 (ϕ, ψ) torsion angles, and three disulfide bond restraints, and subjected them to structure calculation by XPLOR-NIH. The 10 lowest-energy structures out of 200 calculated structures (**Figure 3.10a**) cluster closely. Compared to the crystal structure, the average NMR structure has a backbone atomic root-mean-square deviation (RMSD) of 2.7 Å and a heavy-atom RMSD of 3.8 Å. **Figure 3.10** compares the NMR structure ensemble with the X-ray structure of HNP-3. The NMR structure shows three well-defined β-strands connected by

a long loop between the β1 and β2 strands and a tight turn between the β2 and β3 strands. Both the HNP-1 NMR structure and the HNP-3 crystal structure have the same topology: the β3 strand is inserted between the β1 and β2 strands. Beyond these similarities, we found two main differences: the β1-β2 loop has a very different orientation to the rest of the protein in the two structures, and the β2 strand has a different twist and orientation. The origins of these differences will be discussed below.

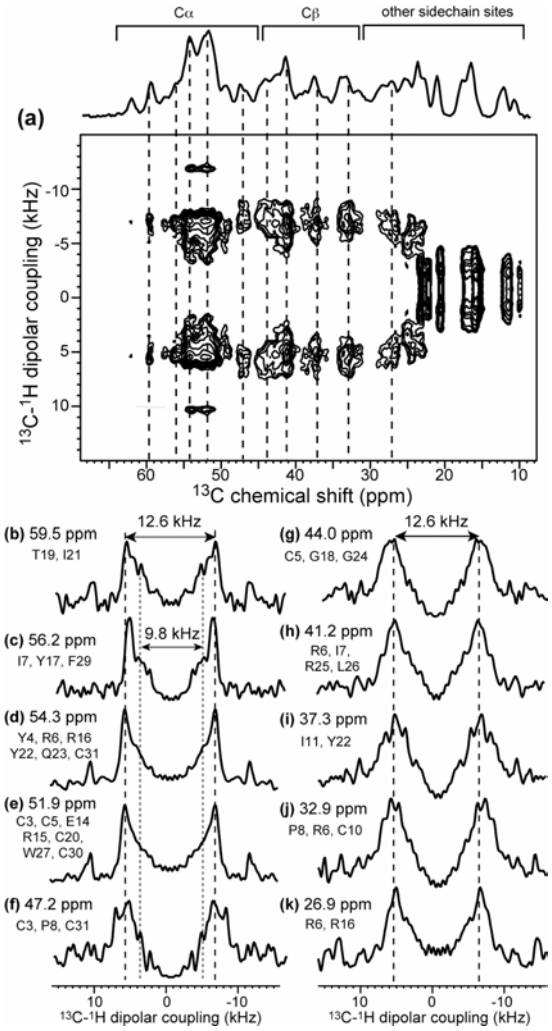

Figure 3.11. 2D ^{13}C-^{1}H LG-CP spectrum to determine the mobility of microcrystalline HNP-1. (a) 2D spectrum, measured under 11 kHz MAS and 293 K. (b-k) 1D dipolar cross sections at selected chemical shifts. Most Cα and Cβ cross sections show rigid-limit values (after taking into account the LG scaling factor of 0.577), except for the 56.2-ppm cross section (c), which has a second coupling that is smaller than the rest.

To ascertain whether large-amplitude motion exists in the HNP-1 backbone, we measured the ^{1}H-^{13}C one-bond dipolar couplings using a 2D LG-CP experiment (**Figure 3.11**). The spectrum shows that most backbone Cα sites have rigid-limit couplings of ~12.5 kHz after scaling by the homonuclear decoupling scaling factor. The only exception is the signal at 56 ppm, which shows a splitting of 9.8 kHz. This value corresponds to a smaller C-H order parameter of 0.78, consistent with moderate-amplitude dynamics of some of the Cα sites, including I7, Y17, and F29.

Discussion

HNP-1 conformational homogeneity and SSNMR structural quality

The microcrystalline HNP-1 samples are well ordered on the nanometer and micrometer scale. The ^{13}C linewidths of 0.4 – 0.8 ppm and ^{15}N linewidths 1.0-1.5 ppm are overall comparable to those observed in other microcrystalline proteins [49] and are better than some amyloid proteins [31]. The ^{15}N linewidths are particularly sensitive to the conformational heterogeneity. Compared to one of the well-studied globular proteins, ubiquitin [49], whose ^{15}N linewidths were reported as 0.3 – 0.5 ppm, the microcrystalline HNP-1 still has residual conformational heterogeneity. However, since the eventual goal is to study HNP-1 in the lipid membrane, whose thermal disorder generally promotes conformational heterogeneity in small proteins, it is not essential to produce HNP-1 with the highest conformational homogeneity.

Variable-temperature 1D ^{13}C and ^{15}N spectra showed quantitatively similar intensities and linewidths in the range of 293 – 253 K (**Figure S5**), indicating that the HNP-1 backbone is largely immobilized at room temperature and only small-amplitude segmental motions exist. This observation is supported by the 2D LG-CP spectrum, which exhibits near rigid-limit Cα - Hα dipolar couplings for most sites. The persistence of narrow linewidths at mild low temperatures is consistent with the behavior of other microcrystalline proteins but contrasts with that of membrane peptides, which manifest gel-phase-induced line broadening in the same temperature range.

The quality of the HNP-1 structure can be compared with the SSNMR structures of other recently studied globular proteins, such as the α-spectrin SH3 domain [25], ubiquitin [26], and GB1 [50]. In terms of agreement with the crystal structure, the SH3 domain and HNP-1 are comparable: the SH3 domain NMR structure has a backbone RMSD of 2.6 Å from the crystal structure for the β-strand segments, while the HNP-1 NMR structure has an all-segment backbone RMSD of 2.7 Å from the crystal structure of HNP-3. However, this similarity belies the difference that a larger number of restraints were obtained (292) for SH3, which corresponded to ~5 restraints per residue, and all constraints were independently extracted from NMR. In comparison, 116 restraints were obtained for HNP-1, thus about 4 restraints were available per residue. The HNP-1 structure constraints also contain a smaller number of medium and long-range distances (24) compared to SH3 (170 non-sequential restraints).

For ubiquitin, structure determination using a combination of uniformly ^{13}C-labeled protein and 2-^{13}C selectively labeled protein resulted in 336 inter-residue contacts for the 76-residue protein [49], among which 149 were sequential, 74 were medium range and 113 were long range. Combined with 122 torsion angle restraints, the high-resolution solid-state NMR structure had a ~1 Å RMSD for secondary structure elements compared to the crystal structure. For the 56-residue GB1, a very high resolution NMR structure was obtained from 888 unique distance restraints and dihedral angles, resulting in a backbone RMSD of 1.32 Å from one of the crystal structures [50].

Conformation of the inter-strand β1-β2 loop and comparison with other human α-defensins

Compared to the structures of other human α-defensins [4], the HNP-1 NMR structure has the same overall fold, with three antiparallel β-strands arranged into a β-sheet. A tight β-hairpin connects β2 and β3 strands while a loop connects the β1 and β2

strands, so that the N- and C-termini lie close together. This structural fold separates the charged and hydrophobic regions spatially, thus may facilitate the insertion of the protein into the phospholipid bilayer with the hydrophobic region buried in the membrane interior while the charged region interacting with the polar surface of the bilayer and with water [3].

Within the context of this general similarity, the SSNMR structure of HNP-1 shows two main differences from the crystal structures of various HNPs. First, the β2 strand in the NMR structure has less orientation change between the N- and C-terminal half compared to the crystal structure (**Figure 3.10b, c**), and the strand twist is also less significant. We attribute these differences largely to insufficient distance restraints between the β2 strand and the rest of the protein (9 distances for 7 residues). When the much larger number of inter-residue distances restraints from the 3D CCC experiment were used for structure calculation, the β2 strand was found to have a more similar twist and orientation to those of the HNP-3 structure. Thus, there appears to be no real conformational difference in the β2 strand of HNP-1 and HNP-3.

The second, more important, difference is the conformation of the loop between residues I7 and R15, which controls the relative orientation of the β1 and β2 strands. In the HNP-3 structure, the loop is bent at P8-A9 and protrudes significantly from the rest of the protein, while in the HNP-1 structure, the P8-A9 segment is extended and the loop is tugged closer to the β2 strand (**Figure 3.10d**). Several lines of evidence suggest that these are real conformational differences between HNP-1 and HNP-3, rather than artifacts due to insufficient constraints of the NMR structure. The structural inputs for the loop region include the chemical-shift based torsion angles (**Table S1**) and eleven inter-residue distances (**Table 3.2**). The P8 and C10 torsion angles were the main factor that determined the presence or absence of a turn at this position. Although we have not directly measured the P8 ψ torsion angle due to sensitivity limitations, the fact that the C10 ϕ angle is confirmed by HNCH experiments to have a regular β-strand value suggests that there is a significant possibility that the P8-C10 segment in HNP-1 does not adopt a turn conformation as in HNP-3. Second, eleven inter-residue distances

established close contacts between the N-terminal region of the loop (residues I7-P8) and the β3 strand (residues L26-W27), between residue C10 and residues G13-E14 within the loop, and between the end of the loop (residues E14-R15) and the β3 strand (residues F29-C30) (**Table 3.2**). Thus, this segment has a reasonable number of distance restraints. When the larger number of independently assigned restraints from 3D CCC experiments were inputted for structure calculation, the loop conformational difference largely remained (**Figure 3.10d**), supporting the hypothesis that the conformational difference is real.

It is noteworthy that a previous ^{1}H solution NMR structure of HNP-1 also concluded a different loop orientation [51]. Similar to the current result, the solution structure showed the HNP-1 loop to be well defined by itself but that its relation to the rest of the protein was different from that of HNP-3. Moreover, when the HNP-1 solution structure was compared with the structures of the related rabbit defensins NP-2 and NP-5, it was revealed that the loop conformation also differs among these three proteins. Thus, the solution NMR study suggested that the β1-β2 loop conformation may be highly sequence-specific and may play a systematic role in regulating the activities of different α-defensins.

What might be the origin of the loop conformation difference between HNP-1 and HNP-3? It cannot result from fast motion, since the 2D LG-CP spectrum (**Figure 3.11**) shows nearly rigid-limit C-H dipolar couplings and ^{13}C variable-temperature spectra (**Figure S5**) also indicate little temperature dependence. Thus, this conformational difference must be attributed to intrinsic structural differences caused either by the single-residue change at the N-terminus or by external environmental factors such as the ionic content, hydration level, and intermolecular packing. Since the loop conformation difference was also seen in the solution NMR structure [51] where there was no crystal packing effects or hydration problems, the single-residue difference at the N-terminus is likely the main reason for the loop conformational variability. The N-terminus residue is Ala in HNP-1, Asp in HNP-3, and absent in HNP-2, which thus starts its sequence with Cys. Thus, HNP-3 is more polar than HNP-1 or HNP-2 at the N-terminus.

Correspondingly, the antimicrobial activities of HNP-1 and HNP-2 are similar but the HNP-3 activity is distinct [2]. A recent study of HNP 1-3 against a panel of six bacteria of both Gram-positive and Gram-negative origins showed that the average LD_{50} of HNP-2 is 1.10 ±0.25 times that of HNP-1 [8], indicating very similar potencies, while the average LD_{50} of HNP-3 is 2.20 ± 1.10 that of HNP-1, indicating that HNP-3 is about 2-fold less active than HNP-1 [8]. Molecular dynamics simulations comparing the HNP 1-3 structures suggested that Asp_2 in HNP-3 may facilitate electrostatic interactions between the two monomers of the dimer, thus making the basket-shaped dimer more compact for HNP-3 than for HNP-1 and 2 [52]. This difference may in turn cause distinct interactions of HNPs with the lipid membrane.

Whatever the exact molecular reason for the loop conformation difference, given the tight structural constraints imposed by the disulfide bonds and the dominant β-strand motifs for these proteins, one would expect that it is precisely the non-strand residues, without backbone hydrogen bonds, that should modulate the interactions of these proteins with the lipid membrane and tune their antimicrobial activities. Indeed, preliminary spectra of membrane-bound HNP-1 containing site-specific isotopic labels showed that A12 in the loop undergoes an interesting chemical shift change between a more helical conformation and the conformation seen in the microcrystalline state (**Figure S6**). This data suggests that the β1-β2 loop conformation is sensitive to the environment, in addition to the sequence. Further comparative structural studies are necessary to fully understand the structure-activity relationship of the HNPs and elucidate the functionally relevant conformation of the β1-β2 loop. Solid-state NMR experiments that determine the conformation, orientation and depth of insertion of HNP-1 in lipid bilayers will be crucial for this purpose.

Materials and Methods

HNP-1 expression and microcrystalline sample preparation

Recombinant HNP-1, whose amino acid sequence is shown in **Figure 3.1**, was obtained as a cleavage product from its precursor protein, proHNP1, which was

expressed as a GST-fusion protein in *E. coli* and folded. Uniformly ^{13}C, ^{15}N-enriched media Spectra 9 (Cambridge Isotope Laboratories) was used to label the protein. Briefly, the fusion protein GST-proHNP1 was expressed in *E. coli* BL21 with IPTG induction. The insoluble inclusion bodies were denatured by 8 M urea and then folded in 2 M urea, 3 mM cysteine and 0.3 mM cystine. The folded fusion protein was dialyzed in a pH 7 buffer containing 20 mM Tris-HCl, 150 mM NaCl and 1.5 mM $CaCl_2$. The fusion protein was then cleaved by thrombin, producing proHNP1, which was purified by reversed-phase HPLC. ProHNP1 was further cleaved by cyanogen bromide to yield the correctly folded HNP-1. The crude HNP-1 was purified by reversed-phase HPLC and analyzed by electrospray ionization mass spectrometry to confirm the mass (3634 Da). The yield of HNP-1 was ~3 mg per liter culture. Antimicrobial assays confirmed the activity of the protein. For example, 100% killing of *S. aureus* is reached at 64 μg/ml HNP-1.

Microcrystalline HNP-1 was precipitated from a polyethylene glycol 400 (PEG-400) solution containing 30 mM cacodylate and 60 mM Li_2SO_4 at pH 6.5. The PEG-400 solution was added slowly to a protein stock solution to reach a final PEG-400 concentration of 30 wt%. Two protein stock solutions, at concentrations of 30 mg/ml and 36 mg/ml, were used. The protein precipitants were centrifuged in a sealed pipette tip, the supernatant removed, the pipette tip cut open, and the precipitant was centrifuged into a 4 mm MAS rotor. Two HNP-1 samples, one in a 4 mm MAS rotor containing ~4 mg protein and the other in a 2.5 mm MAS rotor (~2.7 mg protein) were used in this study.

Solid-state NMR spectroscopy

Most SSNMR experiments were carried out on a Bruker AVANCE-600 (14.1 Tesla) spectrometer (Karlsruhe, Germany) using triple-resonance MAS probes. Most spectra were measured at 253 – 268 K under MAS frequencies of 8 – 15 kHz. 2D CM_5RR spectra were acquired on a 900 MHz NMR spectrometer at the Harvard/MIT Center for Magnetic Resonance. The 900 MHz spectra were measured on a 2.5 mm MAS probe under 20 kHz MAS.

Typical radio-frequency (rf) pulse lengths were 3.5 μs for ^{13}C, 6.0 μs for ^{15}N, and 2.5-4.0 μs for ^{1}H. ^{1}H decoupling fields were typically 70 kHz on the 4 mm rotor sample and 100 kHz on the 2.5 mm rotor sample. ^{13}C chemical shifts were referenced externally to the α-Gly ^{13}CO signal at 176.49 ppm on the TMS scale, and ^{15}N chemical shifts were referenced to the ^{15}N signal of N-acetylvaline at 122.0 ppm on the liquid ammonia scale. The TMS scale differs from the DSS scale by 1.7 ppm, thus all ^{13}C chemical shift values reported here should be increased by 1.7 ppm before comparing with DSS-referenced solution NMR chemical shifts. For torsion angle prediction by the TALOS software, we converted the TMS-based chemical shifts to DSS-referenced values.

2D ^{13}C-^{13}C dipolar-assisted rotational resonance (DARR) experiments [53] were acquired under 8 kHz MAS on the 4 mm rotor sample and 10-15 kHz on the 2.5 mm rotor sample. Four spectra were acquired with mixing times of 20 ms, 40 ms, 100 ms, and 200 ms. For the 4 mm rotor sample, the maximum evolution time for the indirect dimension was 5.6 ms, corresponding to 300 t_1 points. The number of scans per t_1 slice was 96 and the recycle delay was 2 s, giving an experimental time of ~16 hour per 2D spectrum. For the 2.5 mm rotor sample, the maximum ^{13}C evolution time was increased to 7.2 – 7.4 ms due to the better homogeneity and spectral resolution of the sample. 380 t_1 points were measured for the 20 ms and 40 ms experiments and 580 t_1 points were measured for the 100 ms and 200 ms mixing times. The experimental time was 18 – 26 hours per 2D spectrum.

Sequence-specific ^{13}C and ^{15}N resonance assignment was carried out by 3D NCOCX and NCACX experiments [34,35,54] under 8 kHz MAS at 268 K. Magnetization transfer between ^{15}N and ^{13}CO or ^{15}N and $^{13}C\alpha$ was achieved using band-selective SPECIFIC-CP [55]. In the intra-residue NCACX experiment, the Cα magnetization was selected by a 17-kHz ^{15}N spin-lock field and a 25-kHz ^{13}C spin lock field on resonance with Cα. In the inter-residue NCOCX experiment, the spin-lock fields were 27 kHz for ^{15}N and 30 kHz for ^{13}C on resonance with Cα. In the latter case, since the CO offset was 18 kHz, the effective field of the CO resonances was ~35 kHz, thus satisfying the sideband matching condition with ^{15}N. After SPECIFIC-CP, ^{13}C-^{13}C

magnetization transfer occurred during a DARR mixing time, which was 40 ms for NCACX and 60 ms for NCOCX.

For the NCOCX experiment, the ^{15}N spectral width was 4 kHz and the maximum t_1 evolution time was 4.75 ms, corresponding to 38 t_1 points. The ^{13}CO spectral width was 2 kHz and the number of t_2 points was 22, giving a maximum t_2 of 5.56 ms. The experimental time was about 2.5 days. For the NCACX experiment, the ^{15}N spectral width was the same as that of NCOCX, while the $^{13}C\alpha$ (ω_2) spectral width was 4.5 kHz and the acquisition time was 5.56 ms, corresponding to 50 t_2 points. The experimental time was 2 days.

The 2D ^{15}N-^{15}N correlation experiment was conducted using ^{1}H-driven spin diffusion (PDSD) under 6 kHz MAS at 253 K. The mixing time was 3 s to obtain inter-residue ^{15}N-^{15}N correlation peaks. The indirect dimension has a spectral width of 16 kHz and an acquisition time of 6.88 ms, corresponding to 220 t_1 points. The number of scan per t_1 slice was 144 and the recycle delay was 1.5 s, giving an experimental time of 40 hours.

The N-H doubled HNCH experiment to determine ϕ torsion angles [36,47] were carried out on the 2.5 mm rotor sample under 8 kHz MAS at 263 K. ^{1}H homonuclear decoupling during the N-H and C-H evolution periods were achieved using the FSLG sequence [56]. The $C\alpha$ peaks of the chemical shift dimension were assigned based on the 2D and 3D correlation spectra. Although resonance overlap was unavoidable, most residues have consistent ϕ angles between the TALOS and the crystal structure results, thus allowing the residues of interest to be measured. For sensitivity reasons, only the intensities at 0 and half a rotor period of dipolar evolution times were measured. Simulations (**Figure S4**) indicate that the intensity at half a rotor period is the most sensitive to ϕ angle variations.

Structure calculation

The $^{13}C\alpha$, $^{13}C\beta$, ^{13}CO and ^{15}N chemical shifts were inputted into the TALOS program [46] to obtain (ϕ, ψ) torsion angles. Structure calculations were performed using the simulated annealing protocol of the XPLOR-NIH program [57,58]. Input constraints included 60 torsion angles, 9 distances associated with the disulfide bonds, 46 distances between sequential residues, and 24 non-sequential inter-residue distances. An ensemble of 200 structures were first calculated by performing molecular dynamics at 3500 K for 40 ps, followed by slow cooling from 3500 K to 25 K in 12.5 K steps. At each temperature 0.4 ps of dynamics was performed using a soft square NOE potential. Each structure was then refined with the same protocol but with 10 ps of initial annealing using a hard square potential with the k_{NOE} force constant held at 30 kcal. After refinement, the 10 lowest-energy structures were chosen to represent the final structure of HNP-1. All structures were visualized in Chimera (UCSF).

Accession numbers

The HNP-1 SSNMR structure coordinates have been deposited in the Protein Data Bank (PDB code: 2KHT). The chemical shifts and distance restraints have been deposited in the Biological Magnetic Resonance Bank (accession number: rcsb101138).

Acknowledgement

The authors thank Chih-Chia Su for assistance with microcrystal visualization, Professor Chad Rienstra for sharing the design of microcrystal transfer tools, Professor Robert Griffin, Dr. Jozef Lewandowski, Dr. Gaël De Paëpe and Dr. Tony Bielecki for assistance with the 900 MHz NMR experiments, and Dr. Andrew Severin and Dr. Shenhui Li for help with the XPLOR-NIH structure calculations.

This work is supported by the NIH grant GM66976 to M.H. and P41-EB-002026 for the 900 MHz NMR time at MIT.

References

[1] Selsted, M. E.; Ouellette, A. J., Mammalian defensins in the antimicrobial immune response, Nat. Immunol. 6 (2005) 551-557.

[2] Ganz, T.; Selsted, M. E.; Szklarek, D.; Harwig, S. S.; Daher, K.; Bainton, D. F.; Lehrer, R. I., Defensins. Natural peptide antibiotics of human neutrophils, J. Clin. Invest. 76 (1985) 1427-1435.

[3] Hill, C. P.; Yee, J.; Selsted, M. E.; Eisenberg, D., Crystal structure of defensin HNP-3, an amphiphilic dimer: mechanisms of membrane permeabilization., Science 251 (1991) 1481-1485.

[4] Szyk, A.; Wu, Z.; Tucker, K.; Yang, D.; Lu, W.; Lubkowski, J., Crystal structures of human alpha-defensins HNP4, HD5, and HD6., Protein Sci. 15 (2006) 2749-2760.

[5] Gabay, J. E.; Scott, R. W.; Campanelli, D.; Griffith, J.; Wilde, C.; Marra, M. N.; Seeger, M.; Nathan, C. F., Antibiotic proteins of human polymorphonuclear leukocytes, Proc. Natl. Acad. Sci. U. S. A. 86 (1989) 5610-5614.

[6] Jones, D. E.; Bevins, C. L., Defensin-6 mRNA in human Paneth cells: implications for antimicrobial peptides in host defense of the human bowel, FEBS Lett. 315 (1993) 187-192.

[7] Jones, D. E.; Bevins, C. L., Paneth cells of the human small intestine express an antimicrobial peptide gene, J. Biol. Chem. 267 (1992) 23216-23225.

[8] Ericksen, B.; Wu, Z.; Lu, W.; Lehrer, R. I., Antibacterial activity and specificity of the six human {alpha}-defensins, Antimicrob. Agents Chemother. 49 (2005) 269-275.

[9] Wu, Z.; Ericksen, B.; Tucker, K.; Lubkowski, J.; Lu, W., Synthesis and characterization of human alpha-defensins 4-6., J. Pept. Res. 64 (2004) 118-125.

[10] Lehrer, R. I.; Lichtenstein, A. K.; Ganz, T., Defensins: antimicrobial and cytotoxic peptides of mammalian cells, Annu. Rev. Immunol. 11 (1993) 105-128.

[11] Ganz, T., Defensins: antimicrobial peptides of innate immunity, Nat. Rev. Immunol. 3 (2003) 710-720.

[12] Hong, M., Structure, topology, and dynamics of membrane peptides and proteins from solid-state NMR spectroscopy, J. Phys. Chem. B. 111 (2007) 10340-10351.

[13] Doherty, T.; Waring, A. J.; Hong, M., Dynamic structure of disulfide-removed linear analogs of tachyplesin-I in the lipid bilayer from solid-state NMR, Biochemistry 47 (2008) 1105-1116.

[14] Doherty, T.; Waring, A. J.; Hong, M., Membrane-bound conformation and topology of the antimicrobial peptide tachyplesin-I by solid-state NMR Biochemistry 45 (2006) 13323-13330.

[15] Mani, R.; Cady, S. D.; Tang, M.; Waring, A. J.; Lehrer, R. I.; Hong, M., Membrane-dependent oligomeric structure and pore formation of a b-hairpin antimicrobial peptide in lipid bilayers from solid-state NMR, Proc. Natl. Acad. Sci. USA 103 (2006) 16242-16247.

[16] Mani, R.; Tang, M.; Wu, X.; Buffy, J. J.; Waring, A. J.; Sherman, M. A.; Hong, M., Membrane-bound dimer structure of a b-hairpin antimicrobial peptide from rotational-echo double-resonance solid-state NMR, Biochemistry 45 (2006) 8341-8349.

[17] Tang, M.; Waring, A. J.; Hong, M., Mechanism of Arg insertion into lipid membranes and pore formation by a cationic peptide, J. Am. Chem. Soc. 129 (2007) 11438-11446.

[18] Tang, M.; Waring, A. J.; Lehrer, R. I.; Hong, M., Effects of Guanidinium-Phosphate Hydrogen Bonding on the Membrane-Bound Structure and Activity of an Arginine-Rich Membrane Peptide from Solid-State NMR, Angew. Chem. Int. Ed. Engl. 47 (2008) 3202-3205.

[19] Tang, M.; Waring, A. J.; Lehrer, R. I.; Hong, M., Orientation of a b-hairpin Antimicrobial Peptide in Lipid Bilayers from 2D Dipolar Chemical-Shift Correlation NMR, Biophys. J. 90 (2006) 3616-3624.

[20] Buffy, J. J.; Hong, T.; Yamaguchi, S.; Waring, A.; Lehrer, R. I.; Hong, M., Solid-State NMR Investigation of the Depth of Insertion of Protegin-1 in Lipid Bilayers Using Paramagnetic Mn2+, Biophys. J. 85 (2003) 2363-2373.

[21] Buffy, J. J.; McCormick, M. J.; Wi, S.; Waring, A.; Lehrer, R. I.; Hong, M., Solid-State NMR Investigation of the Selective Perturbation of Lipid Bilayers by the Cyclic Antimicrobial Peptide RTD-1, Biochemistry 43 (2004) 9800-9812.

[22] Kagan, B. L.; Selsted, M. E.; Ganz, T.; Lehrer, R. I., Antimicrobial defensin peptides form voltage-dependent ion-permeable channels in planar lipid bilayer membranes, Proc. Natl. Acad. Sci. U. S. A. 87 (1990) 210-214.

[23] Wimley, W. C.; Selsted, M. E.; White, S. H., Interactions between human defensins and lipid bilayers: evidence for formation of multimeric pores, Protein Sci. 3 (1994) 1362-1373.

[24] Lohner, K.; Latal, A.; Lehrer, R. I.; Ganz, T., Differential scanning microcalorimetry indicates that human defensin, HNP-2, interacts specifically with biomembrane mimetic systems, Biochemistry 36 (1997) 1525-1531.

[25] Castellani, F. R., B.; Diehl, A.; Schubert, M.; Rehbein, K.; Oschkinat, H., Structure of a protein determined by solid-state magic-angle-spinning NMR spectroscopy, Nature 420 (2002) 98-102.

[26] Igumenova, T.; Wand, A.; McDermott, A., Assignment of the backbone resonances for microcrystalline ubiquitin., J Am Chem Soc. 126 (2004) 5323-5331.

[27] Franks, W.; Zhou, D.; Wylie, B.; Money, B.; Graesser, D.; Frericks, H.; Sahota, G.; Rienstra, C., Magic-angle spinning solid-state NMR spectroscopy of the beta1 immunoglobulin binding domain of protein G (GB1): 15N and 13C chemical shift assignments and conformational analysis., J. Am. Chem. Soc. 127 (2005) 12291-12305.

[28] Marulanda, D.; Tasayco, M.; Cataldi, M.; Arriaran, V.; Polenova, T., Resonance assignments and secondary structure analysis of E. coli thioredoxin by magic angle spinning solid-state NMR spectroscopy., J. Phys. Chem. B 109 (2005) 18135-18145.

[29] Petkova, A. T.; Ishii, Y.; Balbach, J. J.; Antzutkin, O. N.; Leapman, R. D.; Delaglio, F.; Tycko, R., A structural model for Alzheimer's beta -amyloid fibrils based on experimental constraints from solid state NMR., Proc. Natl. Acad. Sci. USA 99 (2002) 16742-16747.

[30] Wasmer, C.; Lange, A.; Van Melckebeke, H.; Siemer, A. B.; Riek, R.; Meier, B. H., Amyloid fibrils of the HET-s(218-289) prion form a beta solenoid with a triangular hydrophobic core, Science 319 (2008) 1523-1526.

[31] Helmus, J. J.; Surewicz, K.; Nadaud, P. S.; Surewicz, W. K.; Jaroniec, C. P., Molecular conformation and dynamics of the Y145Stop variant of human prion protein in amyloid fibrils, Proc. Natl. Acad. Sci. U. S. A. 105 (2008) 6284-6289.

[32] Cady, S. D.; Hong, M., Amantadine-Induced Conformational and Dynamical Changes of the Influenza M2 Transmembrane Proton Channel, Proc. Natl. Acad. Sci. U.S.A 105 (2008) 1483-1488.

[33] Lange, A.; Giller, K.; Hornig, S.; Martin-Eauclaire, M. F.; Pongs, O.; Becker, S.; Baldus, M., Toxin-induced conformational changes in a potassium channel revealed by solid-state NMR, Nature 440 (2006) 959-962.

[34] Hong, M., Resonance Assignment of 13C/15N Labeled Proteins by Two- and Three-Dimensional Magic-Angle-Spinning NMR, Journal of Biomolecular NMR 15 (1999) 1-14.

[35] Rienstra, C. M.; Hohwy, M.; Hong, M.; Griffin, R. G., 2D and 3D 15N-13C-13C NMR chemical shift correlation spectroscopy of solids: assignment of MAS spectra of peptides., Journal of the American Chemical Society 122 (2000) 10979-10990.

[36] Hong, M.; Gross, J. D.; Griffin, R. G., Site-resolved determination of peptide torsion angle phi from the relative orientations of backbone N-H and C-H bonds by solid-state NMR, Journal of Physical Chemistry B 101 (1997) 5869-5874.

[37] Costa, P. R.; Gross, J. D.; Hong, M.; Griffin, R. G., Solid-State NMR Measurement of psi in Peptides: a NCCN 2Q-Heteronuclear Local Field Experiment, Chem. Phys. Lett. 280 (1997) 95-103.

[38] Feng, X.; Eden, M.; Brinkmann, A.; Luthman, H.; Eriksson, L.; Graslund, A.; Antzutkin, O. N.; Levitt, M. H., Direct determination of a peptide torsion angle psi by double-quantum solid-state NMR, Journal of the American Chemical Society 119 (1997) 12006-12007.

[39] Jaroniec, C. P.; Tounge, B. A.; Rienstra, C. M.; Herzfeld, J.; Griffin, R. G., Measurement of 13C-15N distances in uniformly 13C labeled biomolecules: J-decoupled REDOR., J. Am. Chem. Soc. 121 (1999) 10237-10238.

[40] Wei, G.; de Leeuw, E.; Pazgier, M.; Yuan, W.; Zou, G.; Wang, J.; Ericksen, B.; Lu, W. Y.; Lehrer, R. I.; Lu, W., Through the looking glass: Mechanistic insights from enantiomeric human defensins, J. Biol. Chem. (2009) Epub ahead of print.

[41] Hohwy, M.; Jakobsen, H. J.; Eden, M.; Levitt, M. H.; Nielsen, N. C., Broadband dipolar recoupling in the nuclear magnetic resonance of rotating solids: a compensated C7 pulse sequence., Journal of Chemical Physics 108 (1998) 2686-2694.

[42] De Paëpe, G.; Bayro, M. J.; Lewandowski, J.; Griffin, R. G., Broadband homonuclear correlation spectroscopy at high magnetic fields and MAS frequencies, J. Am. Chem. Soc. 128 (2006) 1776-1777.

[43] Kornhaber, G. J.; Snyder, D.; Moseley, H. N.; Montelione, G. T., Identification of zinc-ligated cysteine residues based on 13Calpha and 13Cbeta chemical shift data, J. Biomol. NMR 34 (2006) 259-269.

[44] Sharma, D.; Rajarathnam, K., 13C NMR chemical shifts can predict disulfide bond formation, J. Biomol. NMR 18 (2000) 165-171.

[45] Wishart, D. S.; Sykes, B. D.; Richards, F. M., Relationship between nuclear magnetic resonance chemical shift and protein secondary structure, J. Mol. Biol. 222 (1991) 311-333.

[46] Cornilescu, G.; Delaglio, F.; Bax, A., Protein backbone angle restraints from searching a database for chemical shift and sequence homology, J. Biomol. NMR 13 (1999) 289-302.

[47] Hong, M.; Gross, J. D.; Rienstra, C. M.; Griffin, R. G.; Kumashiro, K. K.; Schmidt-Rohr, K., Coupling Amplification in 2D MAS NMR and Its Application to Torsion Angle Determination in Peptides, J. Magn. Reson. 129 (1997) 85-92.

[48] Huster, D.; Yamaguchi, S.; Hong, M., Efficient beta-sheet identification in proteins by solid-state NMR spectroscopy, J. Am. Chem. Soc. 122 (2000) 11320-11327.

[49] Zech, S.; Wand, A.; McDermott, A., Protein structure determination by high-resolution solid-state NMR spectroscopy: application to microcrystalline ubiquitin., J Am Chem Soc. 127 (2005) 8618-8626.

[50] Franks, W. T.; Wylie, B. J.; Schmidt, H. L.; Nieuwkoop, A. J.; Mayrhofer, R. M.; Shah, G. J.; Graesser, D. T.; Rienstra, C. M., Dipole tensor-based atomic-resolution structure determination of a nanocrystalline protein by solid-state NMR, Proc. Natl. Acad. Sci. U. S. A. 105 (2008) 4621-4626.

[51] Pardi, A.; Zhang, X. L.; Selsted, M. E.; Skalicky, J. J.; Yip, P. F., NMR studies of defensin antimicrobial peptides. 2. Three-dimensional structures of rabbit NP-2 and human HNP-1, Biochemistry 31 (1992) 11357-11364.

[52] Lourenzoni, M. R.; Namba, A. M.; Caseli, L.; Degrève, L.; Zaniquelli, M. E., Study of the interaction of human defensins with cell membrane models: relationships between structure and biological activity, J. Phys. Chem. B 111 (2007) 11318-11329.

[53] Takegoshi, K.; Nakamura, S.; Terao, T., ^{13}C - ^{1}H dipolar-assisted rotational resonance in magic-angle spinning NMR Chem. Phys. Lett 344 (2001) 631-637.

[54] Straus, S.; Bremi, T.; Ernst, R., Experiments and strategies for the assignment of fully 13C/15N-labelled polypeptides by solid state NMR., J. Biomol. NMR 12 (1998) 39-50.

[55] Baldus, M.; Geurts, D. G.; Hediger, S.; Meier, B. H., Efficient N-15-C-13 polarization transfer by adiabatic-passage Hartmann-Hahn cross polarization, J. M. R 118 (1996) 140-144.

[56] Bielecki, A.; Kolbert, A. C.; Levitt, M. H., Frequency-switched pulse sequences: homonuclear decoupling and dilute spin NMR in solids, Chem. Phys. Lett. 155 (1989) 341-346.

[57] Schwieters, C.; Kuszewski, J.; Tjandra, N.; Clore, G., The Xplor-NIH NMR Molecular Structure Determination Package, J. Magn. Res. 160 (2003) 66-74.

[58] Schwieters, C.; Kuszewski, J.; Clore, G., Using Xplor-NIH for NMR molecular structure determination, Progr. NMR Spectroscopy 48 (2006) 47-62.

Supporting Information

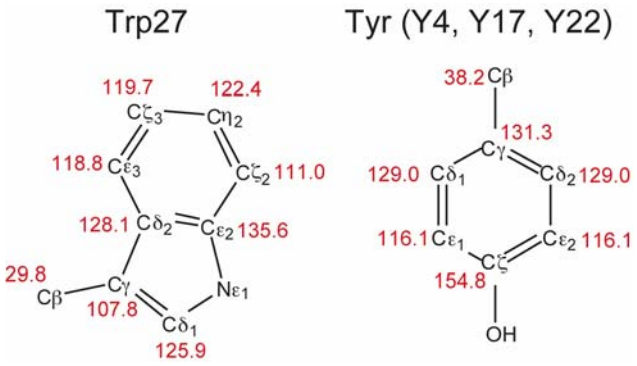

Figure S1. Summary of the ^{13}C chemical shifts of the aromatic sidechains of HNP-1.

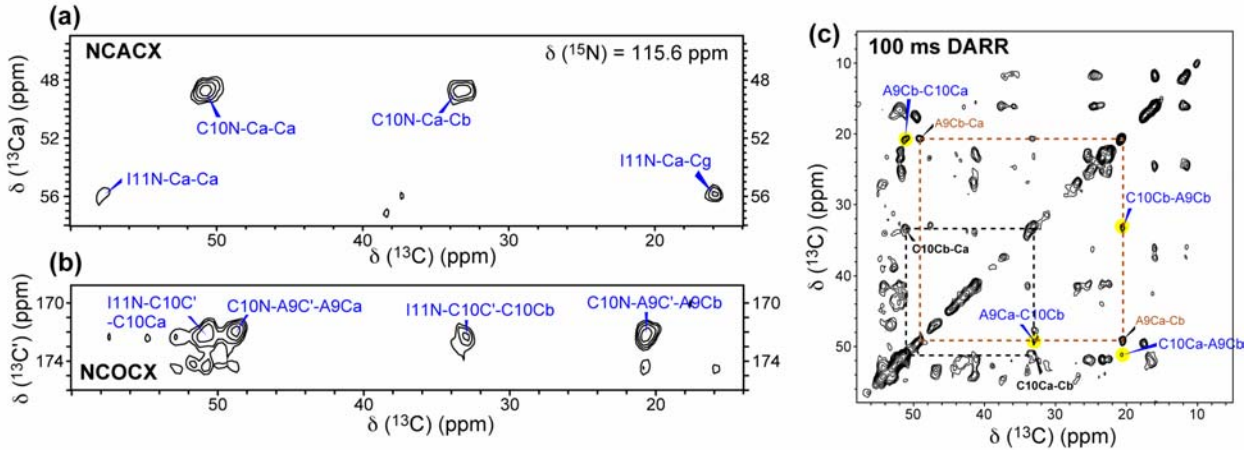

Figure S2. Assignment of C10 ^{13}C chemical shifts. (a) F2-F3 plane of the NCACX spectrum at the ^{15}N chemical shift of 115.6 ppm. The ^{15}N, ^{13}C and $^{13}C\beta$ chemical shifts of the C10 spin system are identified. (b) F2-F3 plane of the NCOCX spectrum at 115.6-ppm ^{15}N chemical shift. C10-A9 cross peaks are clearly seen. (c) 100 ms 2D ^{13}C-^{13}C DARR correlation spectrum. The C10 and A9 connectivities (dashed lines) are indicated. Sequential cross peaks between A9 and C10 are highlighted in yellow and assigned in blue, and confirm the C10 Cβ assignment to be 33.4 ppm on the TMS scale.

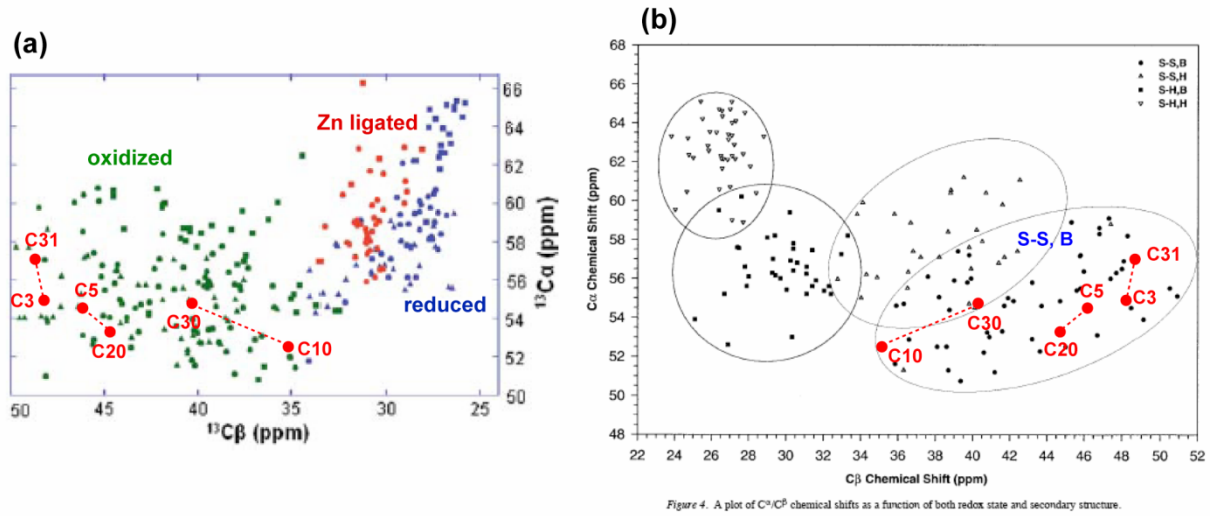

Figure S3. Cα and Cβ chemical shifts of the six cysteines in HNP-1 overlaid with literature values as a function of oxidation state. The HNP-1 cysteine chemical shifts are referenced to DSS to be consistent with the solution-NMR chemical shifts. Two literature statistical analyses of cysteine chemical shifts are shown. (a) Statistical study by Montelione and coworkers [1]. Green: oxidized cysteines. Blue: reduced cysteines. Red: Zn-ligated cysteines. The HNP-1 cysteine chemical shifts are shown as red circles along with the disulfide bonds in the native protein. (b) Statistical study by Sharma and Rajarathnam [2]. The oxidized cysteines (S-S) in the β-sheet conformation (B, filled circles) lie in the lower right corner of the figure. Both comparisons verify that the six HNP-1 cysteines, including C10, are disulfide bonded.

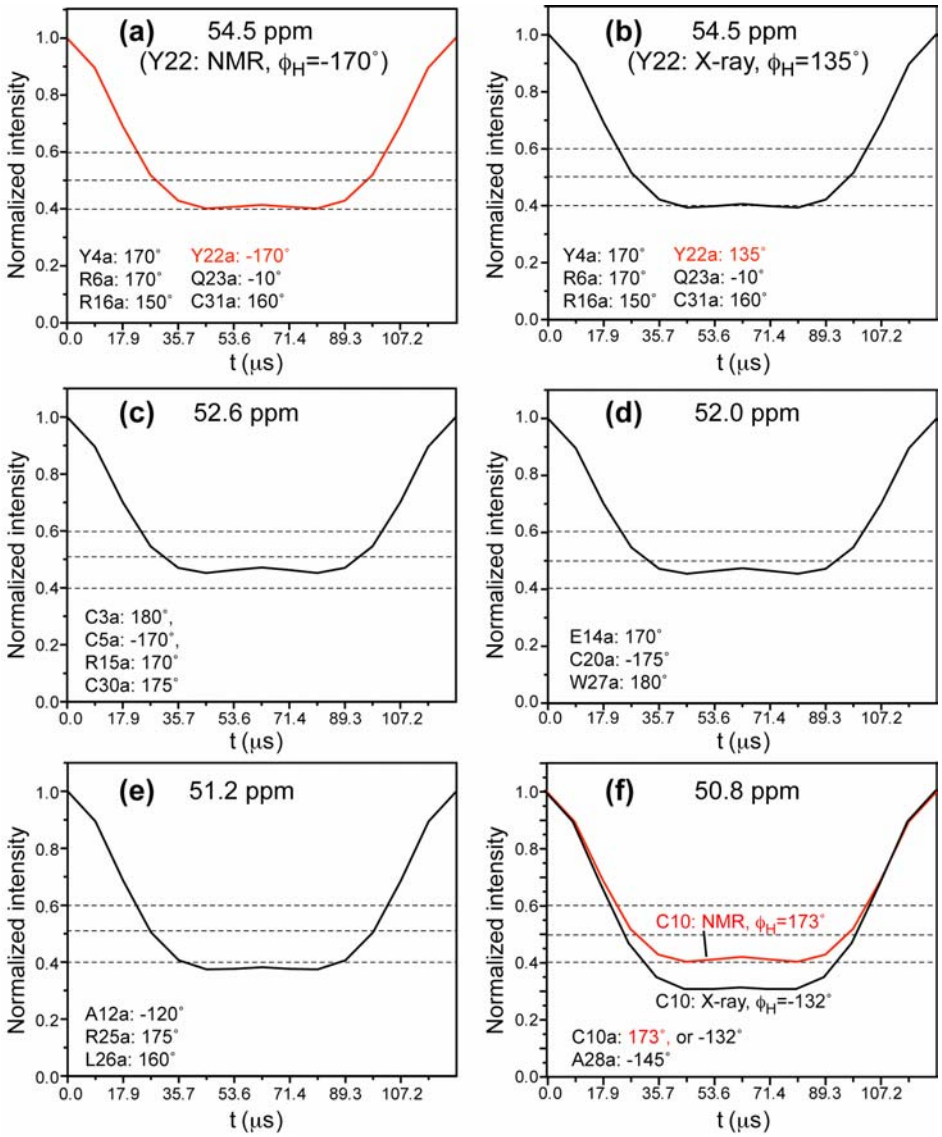

Figure S4. Simulated ϕ angle dependent HNCH curves for key backbone Cα peaks to confirm chemical-shift based torsion angles. The residues at each chemical shift frequency and their ϕ_H angles are shown. For most residues the ϕ_H angles agree well between the TALOS predictions and the crystal structure to within ± 10˚. For C10 and Y22, highlighted in red, significant disagreement exists. Simulations for both cases are shown. Simulations were carried out using the experimental condition of 8 kHz MAS, FSLG ^{1}H homonuclear decoupling, and doubling of the N-H dipolar coupling [3; 4]. (a) 54.5 ppm, using the NMR ϕ_H angle for Y22. (b) 54.5 ppm, using the crystal structure ϕ_H angle for Y22. (c) 52.6 ppm. (d) 52.0 ppm. (e) 51.2 ppm. (f) 50.8 ppm, where the C10 ϕ_H angle is 173˚ for NMR and 132˚ for X-ray.

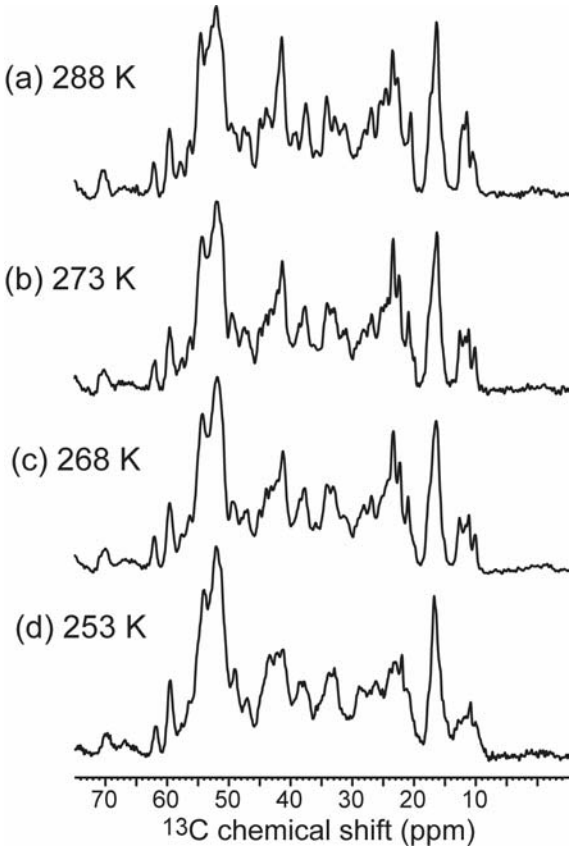

Figure S5. ^{13}C variable-temperature CP-MAS spectrum of microcrystalline HNP-1. Spectra were measured on the 4 mm MAS rotor sample from 288 K to 253 K. The resolution is not affected until 253 K, where sidechain line broadening is observed. The intensities are similarly high in this temperature range, indicating the protein is already largely immobilized at 288 K.

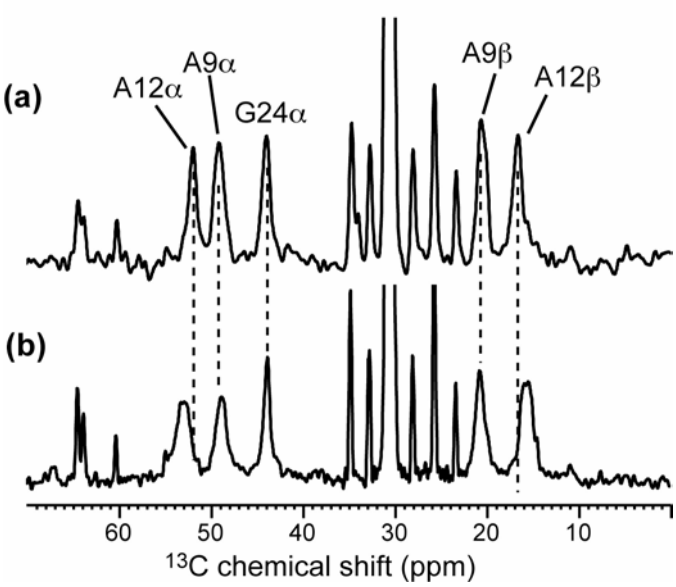

Figure S6. Conformational variability of the loop region of HNP-1 in the membrane-bound state. Site-specifically labeled HNP-1 bound to DMPC/DMPG (3 : 1) membranes was measured. (a) The Ala_{12} chemical shifts are the same as in the microcrystalline state. (b) The Ala_{12} chemical shifts are more helical than in the microcrystalline state.

Table S1: HNP-1 (ϕ, ψ) angles obtained from SSNMR chemical shifts versus crystal structure torsion angles of HNP-3. Residues with significant angular deviations between the two structures are shaded in gray.

Residues	NMR (HNP-1)		X-ray (HNP-3)		ϕ from TALOS	ψ from TALOS
	ϕ	ψ	ϕ	ψ		
A2	-	-	-	-	-	-
C3	-131.0	154.9	-112.6	148.0	19.3	16.3
Y4	-123.2	129.8	-134.1	157.9	22.7	8.7
C5	-119.7	142.7	-100.0	123.0	10.5	17.5
R6	-131.9	141.6	-133.4	150.0	18.6	11.8
I7	-135.0	147.7	-136.1	134.9	8.5	18.4
P8	-135.0	144.4	-86.7	-11.5	33.9	21.6
A9	-141.1	151.6	-163.1	173.2	14.7	10.9
C10	-127.1	150.2	-71.7	152.2	12.6	10.6
I11	-120.4	158.9	-101.6	179.7	35.6	12.2
A12	-71.8	147.0	-54.6	131.9	17.0	17.4
G13	83.2	22.6	87.2	8.9	15.1	19.2
E14	-132.1	152.3	-125.1	158.4	23.0	19.4
R15	-134.0	147.2	-130.2	150.2	12.3	19.9
R16	-99.0	124.2	-82.7	129.9	9.5	12.5
Y17	-116.2	143.2	-116.0	-6.8	22.5	20.3
G18	-120.6	134.9	-179.8	-157.7	35.2	23.2
T19	-109.5	133.8	-130.3	146.9	16.5	7.8
C20	-131.6	149.1	-117.7	152.8	17.6	20.9
I21	-98.8	127.5	-116.9	123.2	16.2	13.3
Y22	-109.4	116.6	-165.2	134.2	17.3	12.8
Q23	50.8	43.0	54.0	41.8	8.9	9
G24	79.3	3.3	66.3	20.5	8.5	12.6
R25	-123.2	151.4	-131.5	164.9	14.0	11.7
L26	-107.6	131.4	-95.3	136.6	17.5	12.1
W27	-106.0	139.2	-127.5	152.5	24.2	13.7
A28	-89.8	125.9	-81.2	138.1	7.4	16.9
F29	-111.7	134.7	-95.2	120.8	16.6	17.4
C30	-126.1	154.4	-123.3	140.3	20.5	13.2
C31	-	-	-138.8	-	-	-

Table S2. XPLOR-NIH NOE input files for microcrystalline HNP-1 from solid-state NMR data. Note the residue number starts with Ala_1 in the NOE calculation, but the rest of the paper uses the convention of Ala_2 as the first residue to align with the other HNP proteins.

```
assign ( resid 2 and name CA )  ( resid 30 and name CA ) 4.3 0.3 0.3 !
assign ( resid 2 and name CB )  ( resid 30 and name CB ) 4.1 0.3 0.3 !
assign ( resid 2 and name SG )  ( resid 30 and name SG ) 1.9 0.3 0.3 !
assign ( resid 4 and name CA )  ( resid 19 and name CA ) 6.0 0.3 0.3 !
assign ( resid 4 and name CB )  ( resid 19 and name CB ) 3.7 0.3 0.3 !
assign ( resid 4 and name SG )  ( resid 19 and name SG ) 1.9 0.3 0.3 !
assign ( resid 9 and name CA )  ( resid 29 and name CA ) 5.6 0.3 0.3 !
assign ( resid 9 and name CA )  ( resid 29 and name CA ) 3.7 0.3 0.3 !
assign ( resid 9 and name SG )  ( resid 29 and name SG ) 1.9 0.3 0.3 !
assign ( resid 1 and name CA )  ( resid 2 and name CA ) 3.8 0.3 0.3 !
assign ( resid 4 and name CA )  ( resid 5 and name CA ) 3.8 0.3 0.3 !
assign ( resid 5 and name CA )  ( resid 6 and name CA ) 3.8 0.3 0.3 !
assign ( resid 8 and name CA )  ( resid 9 and name CA ) 3.8 0.3 0.3 !
assign ( resid 11 and name CA )  ( resid 12 and name CA ) 3.8 0.3 0.3 !
assign ( resid 23 and name CA )  ( resid 24 and name CA ) 3.8 0.3 0.3 !
assign ( resid 28 and name CA )  ( resid 29 and name CA ) 3.8 0.3 0.3 !
assign ( resid 9 and name CA )  ( resid 13 and name CB ) 3.8 1.3 1.0 !
assign ( resid 13 and name CG )  ( resid 29 and name CA ) 3.8 1.3 1.0 !
assign ( resid 20 and name CG1 )  ( resid 21 and name CB ) 3.8 1.3 1.0 !
assign ( resid 24 and name CB )  ( resid 25 and name CG ) 3.8 1.3 1.0 !
assign ( resid 1 and name CA )  ( resid 29 and name CA ) 4.6 2.1 0.8 !
assign ( resid 3 and name CA )  ( resid 4 and name CB ) 4.6 2.1 0.8 !
assign ( resid 3 and name CB )  ( resid 4 and name CA ) 4.6 2.1 0.8 !
assign ( resid 3 and name CA )  ( resid 29 and name CB ) 4.6 2.1 0.8 !
```

```
assign ( resid 4 and name CA )   ( resid 5 and name CB ) 4.6 2.1 0.8 !
assign ( resid 5 and name CA )   ( resid 27 and name CA ) 4.6 2.1 0.8 !
assign ( resid 6 and name CG1 )   ( resid 25 and name CB ) 4.6 2.1 0.8 !
assign ( resid 6 and name CG1 )   ( resid 26 and name CA ) 4.6 2.1 0.8 !
assign ( resid 7 and name CB )   ( resid 8 and name CA ) 4.6 2.1 0.8 !
assign ( resid 7 and name CB )   ( resid 8 and name CB ) 4.6 2.1 0.8 !
assign ( resid 8 and name CB )   ( resid 9 and name CA ) 4.6 2.1 0.8 !
assign ( resid 9 and name CB )   ( resid 10 and name CG2 ) 4.6 2.1 0.8 !
assign ( resid 9 and name CB )   ( resid 15 and name CD ) 4.6 2.1 0.8 !
assign ( resid 11 and name CB )   ( resid 12 and name CA ) 4.6 2.1 0.8 !
assign ( resid 15 and name CA )   ( resid 27 and name CB ) 4.6 2.1 0.8 !
assign ( resid 19 and name CB )   ( resid 20 and name CG2 ) 4.6 2.1 0.8 !
assign ( resid 20 and name CA )   ( resid 25 and name CA ) 4.6 2.1 0.8 !
assign ( resid 22 and name CB )   ( resid 23 and name CA ) 4.6 2.1 0.8 !
assign ( resid 5 and name CD )   ( resid 29 and name CB ) 5.8 3.3 0.5 !
assign ( resid 10 and name CB )   ( resid 11 and name CA ) 5.8 3.3 0.5 !
assign ( resid 15 and name CB )   ( resid 28 and name CA ) 5.8 3.3 0.5 !
assign ( resid 19 and name CA )   ( resid 20 and name CD1 ) 5.8 3.3 0.5 !
assign ( resid 21 and name CB )   ( resid 22 and name CA ) 5.8 3.3 0.5 !
assign ( resid 4 and name CB )   ( resid 28 and name CA ) 7.5 5.0 0.5 !
assign ( resid 5 and name CA )   ( resid 6 and name CB ) 7.5 5.0 0.5 !
assign ( resid 5 and name CG )   ( resid 27 and name CA ) 7.5 5.0 0.5 !
assign ( resid 6 and name CA )   ( resid 7 and name CA ) 7.5 5.0 0.5 !
assign ( resid 8 and name CB )   ( resid 9 and name CA ) 7.5 5.0 0.5 !
assign ( resid 9 and name CB )   ( resid 10 and name CG1 ) 7.5 5.0 0.5 !
assign ( resid 3 and name N )   ( resid 4 and name N ) 3.5 1.0 0.5 !
assign ( resid 4 and name N )   ( resid 5 and name N ) 3.5 1.0 0.5 !
assign ( resid 6 and name N )   ( resid 7 and name N ) 3.5 1.0 0.5 !
assign ( resid 8 and name N )   ( resid 9 and name N ) 3.5 1.0 0.5 !
assign ( resid 16 and name N )   ( resid 17 and name N ) 3.5 1.0 0.5 !
assign ( resid 17 and name N )   ( resid 18 and name N ) 3.5 1.0 0.5 !
```

```
assign ( resid 21 and name N )  ( resid 22 and name N ) 3.5 1.0 0.5 !
assign ( resid 22 and name N )  ( resid 23 and name N ) 3.5 1.0 0.5 !
assign ( resid 23 and name N )  ( resid 24 and name N ) 3.5 1.0 0.5 !
assign ( resid 26 and name N )  ( resid 27 and name N ) 3.5 1.0 0.5 !
assign ( resid 4 and name N )  ( resid 18 and name N ) 6.0 3.0 0.5 !
assign ( resid 7 and name N )  ( resid 26 and name N ) 6.0 3.0 0.5 !
assign ( resid 7 and name N )  ( resid 27 and name N ) 6.0 3.0 0.5 !
assign ( resid 9 and name N )  ( resid 12 and name N ) 6.0 3.0 0.5 !
assign ( resid 16 and name N )  ( resid 29 and name N ) 6.0 3.0 0.5 !
assign ( resid 17 and name N )  ( resid 26 and name N ) 6.0 3.0 0.5 !
assign ( resid 21 and name N )  ( resid 24 and name N ) 6.0 3.0 0.5 !
assign ( resid 23 and name N )  ( resid 25 and name N ) 6.0 3.0 0.5 !
```

References

[1] Kornhaber, G. J., Snyder, D., Moseley, H. N. & Montelione, G. T. (2006). Identification of zinc-ligated cysteine residues based on $^{13}C\alpha$ and $^{13}C\beta$ chemical shift data. *J. Biomol. NMR* **34**, 259-269.

[2] Sharma, D. & Rajarathnam, K. (2000). ^{13}C NMR chemical shifts can predict disulfide bond formation. *J. Biomol. NMR* **18**, 165-171.

[3] Hong, M., Gross, J. D. & Griffin, R. G. (1997). Site-resolved determination of peptide torsion angle phi from the relative orientations of backbone N-H and C-H bonds by solid-state NMR. *J. Phys. Chem. B* **101**, 5869-5874.

[4] Hong, M., Gross, J. D., Rienstra, C. M., Griffin, R. G., Kumashiro, K. K. & Schmidt-Rohr, K. (1997). Coupling Amplification in 2D MAS NMR and Its Application to Torsion Angle Determination in Peptides. *J. Magn. Reson.* **129**, 85-92.

Chapter 4

3D ^{13}C-^{13}C-^{13}C Correlation NMR for De Novo Distance Determination of Solid Proteins and Application to a Human Alpha Defensin

A paper published in J. Magn. Reson.

2010, vol. 202, pp. 203-210

Shenhui Li, Yuan Zhang, and Mei Hong*

Abstract

The *de novo* structure of an antimicrobial protein, human α-defensin 1 (HNP-1), is determined by combining a 3D ^{13}C-^{13}C-^{13}C (CCC) magic-angle spinning (MAS) correlation experiment with standard resonance assignment experiments. Using a short spin diffusion mixing time to assign intra-residue cross peaks and a long mixing time to detect inter-residue correlation peaks, we show that the 3D CCC experiment not only reduces the ambiguity of resonance assignment, but more importantly yields two orders of magnitude more long-range distances without recourse to existing crystal structures. Most of these distance constraints could not be obtained in a *de novo* fashion from 2D correlation spectra due to significant resonance overlap. Combining the distance constraints from the 3D CCC experiment and the chemical-shift-derived torsion angles, we obtained a *de novo* high-resolution NMR structure of HNP-1, with a heavy-atom RMSD of 3.4 Å from the crystal structure of the analogous HNP-3. The average energy of the minimum-energy ensemble is less than of 40 kcal/mol. Thus, the 3D CCC experiment provides a reliable means of restraining the three-dimensional structure of insoluble proteins with unknown conformations.

Introduction

Magic-angle spinning (MAS) solid-state NMR (SSNMR) spectroscopy has become a complementary method to solution NMR and X-ray crystallography for structure determination of proteins. Techniques for measuring a large number of conformational constraints, such as chemical shifts [1-9], torsion angles [10-12], and distances [13-16], have been recently developed. For uniformly ^{13}C-labeled proteins, distance constraints are usually obtained from 2D ^{13}C-^{13}C correlation spectra such as PDSD, DARR, and CHHC [17-20]. To obtain long-distance constraints, long spin diffusion mixing times are usually required, resulting in a large number of cross peaks that are difficult to resolve and assign, since even the subset of short-range cross peaks already required 3D heteronuclear correlation experiments to fully resolve. Recently, a Proton Assisted Recoupling (PAR) experiment [21,22] was introduced to selectively enhance the intensities of weakly coupled long-range cross peaks in 2D spectra. Despite this improvement, 2D ^{13}C-^{13}C correlation approaches remain of limited utility for distance extraction, and often existing crystal structures or structural models were relied on for assigning the cross peaks in these congested 2D spectra.

Three-dimensional ^{13}C-^{13}C-^{13}C (CCC) correlation experiments have been proposed to facilitate resonance assignment [23,24]. Baldus and co-workers [23] demonstrated a CCC experiment that contains a double-quantum (DQ) indirect dimension, which avoids the cubic diagonal in the 3D spectrum and identifies the intra-residue cross peaks through the DQ signals. Rienstra and coworkers [24] proposed an alternative 3D CCC experiment that uses soft 180˚ and 90˚ pulses to selectively detect the aliphatic region of the ^{13}C spectrum in the F1 and F2 dimensions, thus shortening experimental time. However, both studies focused on increasing intra-residue resonance assignment rather than extracting long-range distances. In this work, we show that the 3D CCC experiment not only improves resonance assignment, but allows distance extraction in a *de novo* fashion, which is essential for restraining the three-dimensional fold of structurally unknown proteins.

Human neutrophil α-defensins (HNPs) are cationic antimicrobial proteins of the

human innate immune system to protect against microbial infections [25]. Six human α-defensins are known. They contain 29 - 33 amino acid residues and six conserved cysteins that form three intramolecular disulfide bonds [26-29]. HNPs kill a broad range of pathogens, including bacteria, fungi and certain enveloped viruses [25,30]. Similar to most antimicrobial peptides (AMPs), the main mode of action of HNPs is the disruption of the cell membrane of the invading pathogen [31,32]. Several crystal structures of HNPs have been reported [33-36]; however, all these structures were solved in the absence of any membranes or membrane-mimetic solvents, thus their relevance for the membrane-bound structure and mechanism of HNPs remains unknown. Understanding the detailed mechanism of human α-defensins thus requires high-resolution structures of HNPs in the lipid membrane.

We have initiated a solid-state NMR investigation of the three-dimensional structure of HNP-1 in lipid membranes. As a first step, the resonance assignment of the 30-residue HNP-1 in a microcrystalline state has been completed using various 2D ^{13}C-^{13}C and 3D ^{13}C-^{15}N correlation techniques [37]. However, the long-distance correlation peaks observed in the 2D CC spectra could not be assigned without using information from the crystal structure of the analogous HNP-3 [33]. In this work, we show that the 3D CCC experiment allows a large number of inter-residue distances to be identified, thus permitting a *de novo* structure determination of HNP-1. We also quantify the increased information content of the 3D CCC experiment compared to the 2D CC experiment.

Materials and Methods

Sample preparation

Uniformly ^{13}C, ^{15}N-labeled HNP-1 in microcrystalline form was prepared as described in a separate report [37]. Briefly, a fusion protein containing the HNP-1 sequence, GST-proHNP1, was expressed in *E. coli*, folded, and cleaved to yield the HNP-1 precursor protein proHNP-1. ProHNP-1 was purified by reversed-phase HPLC and cleaved by cyanogen bromide to give folded HNP-1. Microcrystalline HNP-1 was prepared by precipitation from a pH 6.5 polyethyleneglycol-400 solution. The hydrated

protein microcrystals were centrifuged into the MAS rotors. 3-5 mg of microcrystals were packed into a 4 mm rotor and a 2.5 mm rotor.

Solid-state NMR

Solid-state NMR experiments were carried out on a Bruker AVANCE-600 (14.1 Tesla) spectrometer. The 2D ^{13}C-^{13}C DARR spectrum with a mixing time of 100 ms was measured at 253 K under 12 kHz MAS using a 2.5 mm rotor sample. The spectral widths of the direct (F2) and indirect (F1) dimensions were 50 kHz and 27 kHz, respectively. A total of 300 t_1 slices and 96 scans per slice were measured, resulting in an experimental time of 17 hours.

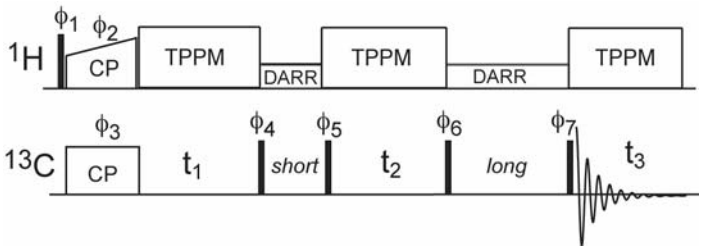

Figure 4.1. Pulse sequence for the 3D CCC MAS correlation experiment. Phase cycles are: ϕ_1 = 0 2, ϕ_2 = 1, ϕ_3= 0 0 1 1 2 2 3 3, ϕ_4 = 1 1 2 2 3 3 0 0, ϕ_5 = 3 3 0 0 1 1 2 2, ϕ_6 = 1 1 2 2 3 3 0 0, 3 3 0 0 1 1 2 2, ϕ_7 = 0 1 2 3 2 3 0 1, and receiver = 1 0 3 2 3 2 1 0, 3 2 1 0 1 0 3 2. Here 0 = +x, 1 = +y, 2 = -x, and 3 = -y.

The 3D CCC pulse sequence is shown in **Figure 4.1.** The experiment was carried out at 253 K under 8 kHz MAS using a 4 mm rotor sample. The first and second DARR mixing times were 20 ms and 100 ms, respectively. The F1 and F2 spectral widths were 13 kHz (86.7 ppm). The ^{13}C carrier was set to 39.6 ppm, thus the F1 and F2 spectral windows ranged from -3.5 to 82.7 ppm. This spectral range folded the Arg Cζ region in 157-169 ppm to 70.8-82.8 ppm, and the CO region at 170 -180 ppm to -2.4-7.6 ppm. Both folded regions avoided resonance overlap with the aliphatic carbons. The 3D spectrum was measured with 130 t_1 slices, 130 t_2 slices, and 8 scans per slice, resulting in an experimental time of 71 hours.

Typical 90° pulse lengths were 4-5 μs for both ^{1}H and ^{13}C channels. The ^{1}H-^{13}C cross polarization contact time was 700 μs and the ^{1}H decoupling field strength was 71 kHz in the experiments. The ^{13}C chemical shifts were referenced externally to the α-Gly $^{13}C'$ signal at 176.49 ppm on the TMS scale.

Structure calculation

The 2D and 3D ^{13}C correlation spectra were assigned using the program SPARKY. Structure calculation was carried out using the XPLOR-NIH program [38,39]. Distance constraints were inputted similar to that of Castellani et al [13], where sequential Cα-Cα distances were fixed to 3.8±0.5 Å, and other inter-residue distances were given the range of 2.5-7.5 Å for the 100 ms DARR mixing time used in the 3D CCC experiment [13,40]. In addition to unique distance constraints, ambiguous distances with a degeneracy of less than 5 were included in the input file. Dihedral angle constraints obtained from the assigned ^{13}C and ^{15}N chemical shifts [41] were also included [37]. Structure calculations proceeded in two stages. For the annealing process, an ensemble of 200 structures was calculated by performing molecular dynamics at 3500 K for 40 ps, followed by slow cooling from 3500 K to 25 K in 12.5 K increments, with 0.4 ps of dynamics at each temperature using a soft square NOE potential. In the second stage, each structure was refined by repeating the annealing protocol with only 10 ps of initial annealing using a hard square NOE potential with the k_{NOE} force constant held at 30 kcal. After structure refinement, the ensemble of 10 lowest energy structures was selected to represent the final structure of HNP-1. The final structure has been deposited to the Protein Data Bank (Accession code: 2KHT).

Results and Discussion

2D CC spectrum at long mixing times

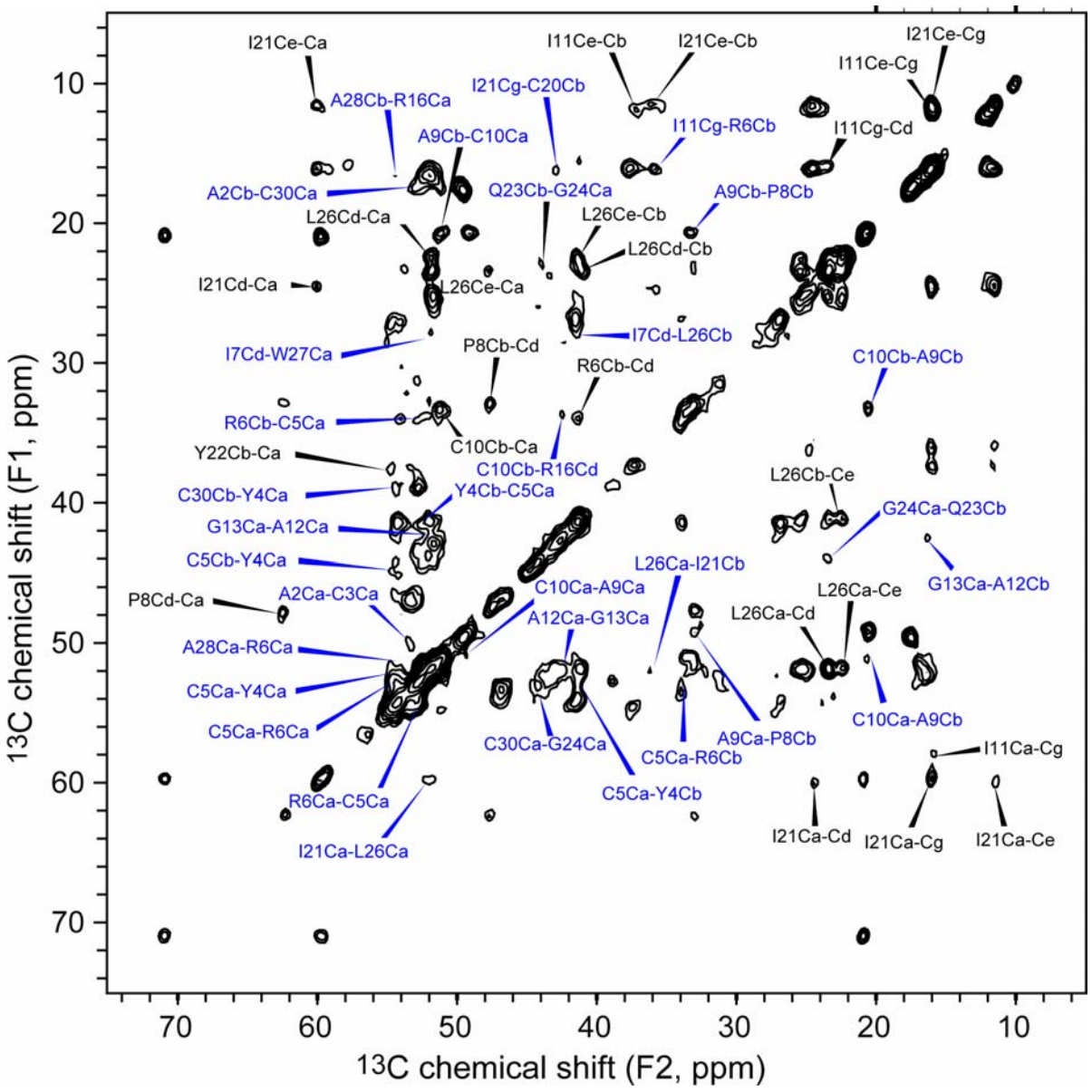

Figure 4.2. 2D ^{13}C-^{13}C correlation spectrum of microcrystalline HNP-1 at a DARR mixing time of 100 ms. The spectrum was measured under 12 kHz MAS at 253 K. Inter-residue cross peaks are annotated in blue, and some intra-residue peaks are also assigned, in black.

Before describing the analysis of the 3D CCC experiment, we first present the 100 ms 2D DARR spectrum (**Figure 4.2**), which was measured to obtain long-range correlation peaks in a conventional manner [37]. All inter-residue cross peaks in the 2D spectrum are annotated in blue, and selected intra-residue cross peaks are annotated in black. For most inter-residue cross peaks, the assignments are ambiguous, with a

degeneracy of 2 or higher. Only one of the assignment possibilities is listed in **Figure 4.2**. For example, the peak at (F1 = 33.7 ppm, F2 = 42.5 ppm) can be assigned either to R6Cβ-R16Cδ or C10Cβ-R16Cδ, corresponding to an assignment degeneracy of 2. From this 100 ms 2D CC spectrum, a total of 24 inter-residue cross peaks with an assignment degeneracy of 1 – 8 were found. Among these peaks, 15 peaks were assigned to sequential correlations (|i-j|=1), 1 peak was assigned to medium correlations (1<|i-j|≤ 4), and 8 peaks were assigned to long-range correlations (|i-j|>4).

3D CCC experiment

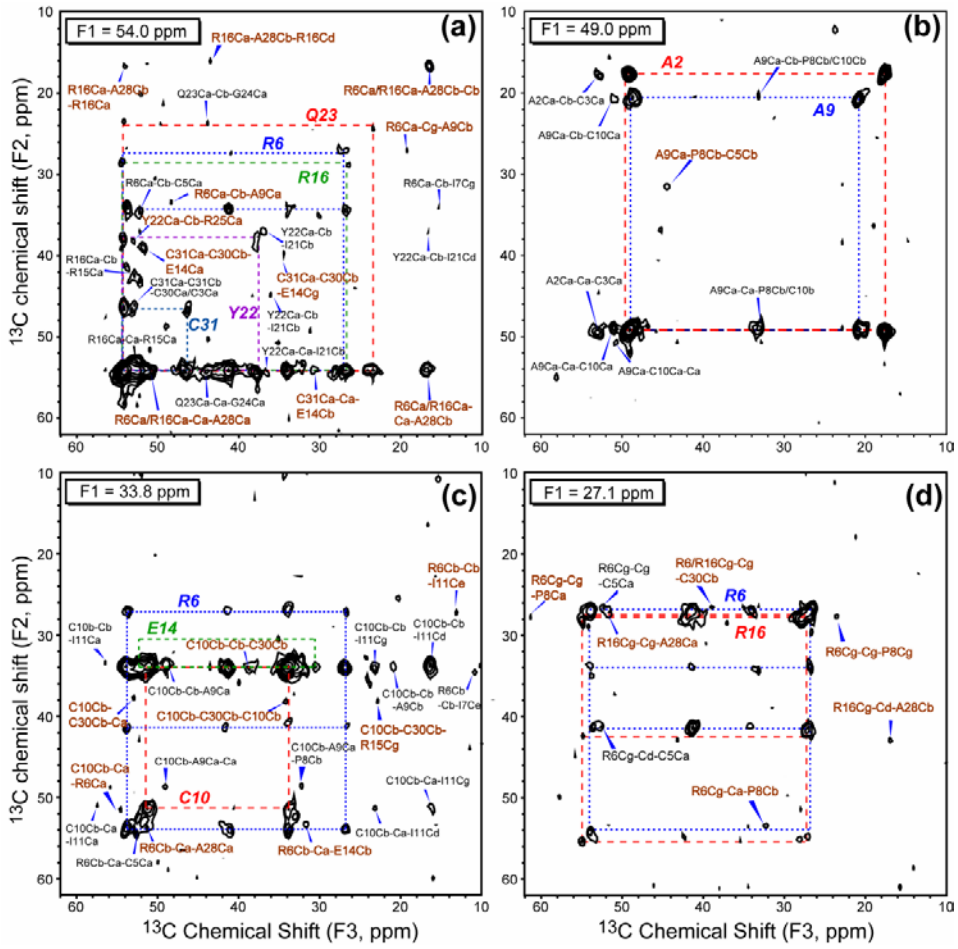

Figure 4.3. F2-F3 planes of the 3D CCC spectrum at various F1 frequencies. (a) F1=54.0 ppm, (b) F1=49.0 ppm, (c) F1=33.8 ppm, (d) F1=27.1 ppm. The amino acid spin systems are connected by dashed lines. All inter-residue cross peaks are assigned. The non-sequential inter-residue cross peaks are shown in brown while the sequential cross peaks are in black.

The 3D CCC experiment was carried out using a DARR mixing time of 20 ms between F1 and F2 and 100 ms between F2 and F3 dimensions. The short mixing time allows polarization transfer mostly within the same residue while the long mixing time establishes inter-residue correlations. **Figure 4.3** shows 4 representative 2D planes at F1 = 54.0, 49.0, 33.8, and 27.1 ppm. Compared to the 2D spectrum, each F2-F3 plane has a much smaller number of peaks, thus facilitating resonance assignment. For example, based on the previous assignment [37], the F2-F3 plane at F1 = 54.0 ppm (**Figure 4.3a**) can be attributed to five Cα sites: R6Cα (53.9 ppm), R16Cα (54.5 ppm), Y22Cα (54.2 ppm), Q23Cα (54.2 ppm) and C31Cα (54.0 ppm). Indeed, five networks of resonances indicated by dashed lines were observed, representing the spin systems of R6, R16, C31, Q23, and Y22. For example, in the R6 spin system (blue dashed lines), R6Cα (53.9 ppm), R6Cβ (33.7 ppm), and R6Cγ (26.7 ppm) are detected in the F2 dimension due to spin diffusion from R6Cα during the 20 ms mixing time. Intra-residue cross peaks such as R6Cα-Cβ-Cδ (54.0 ppm, 34.3 ppm, 41.2 ppm) and R6Cα-Cγ-Cδ (54.0 ppm, 26.9 ppm, 41.2 ppm) are readily identified in the blue square.

More important than the intra-residue cross peaks are inter-residue cross peaks in these 2D planes, which are annotated in brown for non-sequential correlation peaks and black for sequential cross peaks. In assigning these inter-residue peaks, we use the following principles. First, due to the short mixing time between the F1 and F2 dimensions the F1-F2 assignment usually does not extend beyond sequential correlations, with the exception of disulfide bonds and a few very high intensity peaks such as the Ala methyl carbons. Second, for peaks lying at diagonal planes of the 3D spectrum, where either the F1 and F2 frequencies are identical or the F1 and F3 frequencies are identical, the degenerate assignment is resolved by looking for peaks in other planes that belong to the spin systems of the degenerate sites. For example, for two spins A and A' with similar chemical shifts ω_A, the observation of a cross peak at (F1, F2, F3) = (ω_A, ω_A, ω_C) is two-fold degenerate. But if A and A' have different frequencies for their directly bonded spins B and B', then the observation of a cross peak at (ω_B, ω_A, ω_C) but not at ($\omega_{B'}$, ω_A, ω_C) justifies the assignment of (ω_A, ω_A, ω_C) to a long-range correlation between A and C and not between A' and C.

We illustrate the above principles with several examples. First, the cross peak at (F1, F2, F3) = (54.0 ppm, 33.8 ppm, 52.8 ppm), which does not lie in any diagonal plane, can be uniquely assigned to R6Cα-Cβ-C5Cα, which establishes a sequential constraint. Second, the cross peak at (54.0 ppm, 39.4 ppm, 34.2 ppm) can be uniquely assigned to C31Cα-C30Cβ-E14Cγ, indicating spatial proximity between C30 and E14. Here the other four possibilities for the F1 frequency of 54.0 ppm are ruled out because the short mixing time prohibits long-distance polarization transfer. This non-diagonal cross peak also allowed the peak at (54.0 ppm, 54.0 ppm, 31.0 ppm) to be assigned to C31Cα-C31Cα-E14Cβ with reasonable confidence, even though it appears on a diagonal plane. Another example of a peak with degenerate assignment is the peak at (54.0 ppm, 54.0 ppm, 16.7 ppm). It can be assigned to XCα-Cα-A28Cβ, where X can be one of the five Cα sites at 54.0 ppm. However, one cross peak at (33.8 ppm, 54.0 ppm, 51.3 ppm) in F1 = 33.8 ppm plane (**Figure 4.3c**) and another cross peak at (27.1 ppm, 42.5 ppm, 16.5 ppm) in **Figure 4.3d** were detected that can be uniquely assigned to R6Cβ-R6Cα-A28α and R16Cγ-R16Cδ-A28Cβ, respectively. These R6-A28 and R16-A28 correlations indicate that the (54.0 ppm, 54.0 ppm, 16.7 ppm) peak can be assigned to both R16Cα-R16Cα-A28Cβ and R6Ca-R6Ca-A28Cβ. In general, non-sequential inter-residue correlations manifest as multiple peaks in different planes of the 3D spectrum, thus increasing the confidence of assignment.

Figure 4.3b shows the F1 = 49.0 ppm plane. Two squares corresponding to the A2 (Cα at 49.5 ppm) and A9 (Cα at 48.8 ppm) spin systems are well resolved. Five sequential cross peaks between A2 and C3, A9 and C10 can be uniquely assigned. In addition, two sequential cross peaks with a degeneracy of 2 were detected that correspond to A9-P8 or A9-C10 correlations. In this spectrum, one non-sequential inter-residue cross peak is observed that indicates proximity between P8 and C5 sidechains.

Figure 4.3c shows the F2-F3 plane at F1 = 33.8 ppm, with R6, C10 and E14 spin systems, and **Figure 4.3d** displays the F1 = 27.1 ppm plane with the R6 and R16 spin systems. Most non-sequential inter-residue cross peaks fall outside the diagonal planes in these two planes, simplifying assignment. Altogether, 26 non-sequential inter-residue

constraints are identified in **Figure 4.3**, greatly exceeding the 9 non-sequential cross peaks identified in the 100 ms 2D ^{13}C-^{13}C DARR spectrum. Most importantly, the 3D assigned long-range correlations are *de novo* rather than back-confirmed with the crystal structure, thus this approach can be applied to proteins with no pre-existing structure or structural models.

Distance statistics from 3D CCC and 2D CC spectra and assignment map

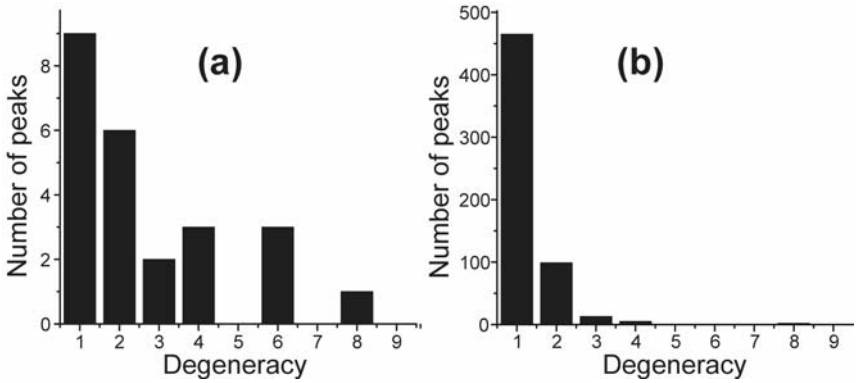

Figure 4.4. Number of assigned peaks and their degeneracies from 2D and 3D ^{13}C NMR. (a) Statistics of the 100 ms 2D CC spectrum. (b) Statistics of the 3D CCC spectrum, measured with mixing times of 20 ms and 100 ms. The 3D spectrum contains two orders of magnitude more resolved peaks than the 2D spectrum, with lower assignment degeneracies.

In the two previously published papers on the 3D CCC experiments [23,24], no analysis was given about the long-range distances that can be obtained. We now quantify the number of long-range distance constraints as well as the completeness of assignment by the 3D CCC experiment on microcrystalline HNP-1. **Figure 4.4** shows the number of assigned peaks as a function of assignment ambiguity from the 100 ms 2D CC spectrum versus the 3D CCC spectrum. A total of 24 inter-residue correlation peaks was observed in the 100 ms 2D CC spectrum, including 15 sequential, 1 medium-range and 8 long-range correlations. Among the 24 inter-residue peaks, only 9 were uniquely assigned. The average assignment degeneracy is 2.71 with a standard deviation of 0.41.

In comparison, the 3D CCC spectrum yielded 586 inter-residue correlations peaks, among which 450 were uniquely assigned. Among these unique cross peaks 220 are

sequential and 230 are non-sequential cross peaks. The average assignment degeneracy decreased to 1.30 with a standard deviation of 0.04. Therefore, the 3D CCC experiment not only increased the number of inter-residue cross peaks by two orders of magnitude but also decreased the number of ambiguous assignments significantly. Another benefit of the 3D CCC spectrum is that by having a large number of inter-residue correlations, erroneous assignment is better tolerated compared to the case when a much smaller number of constraints are available.

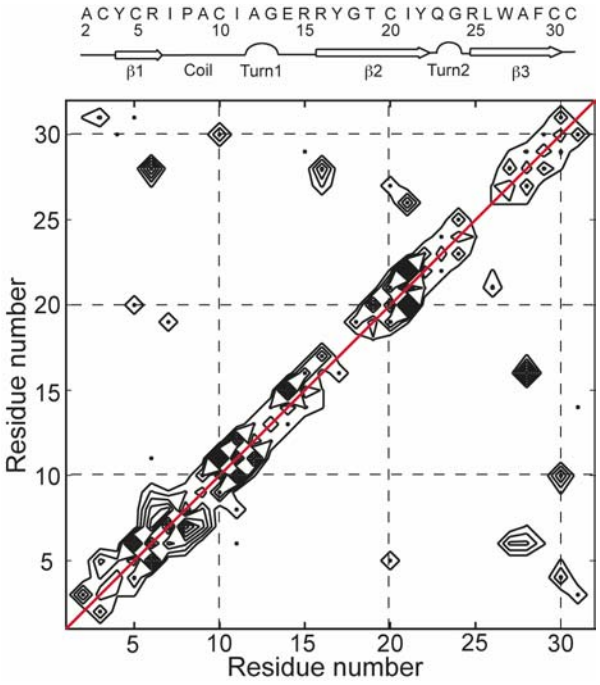

Figure 4.5. 2D contour map of the number of inter-residue cross peaks in HNP-1. A red diagonal line (red) indicating auto-correlation is drawn to distinguish from sequential correlation peaks.

Based on the 3D CCC spectrum, **Figure 4.5** plots the number of uniquely assigned inter-reside correlation peaks as a function of residue number. The number of distance constraints between two residues can be directly read off the map. For example, the numbers of correlations for the (R6, A28) pair and the (A28, R6) pair are 5 and 3, respectively, which result from eight observed cross peaks in the 3D spectrum, five of which are unique: R6Cγ-A28Cα, R6Cα-A28Cα, R6Cβ-A28Cβ, R6Cα-A28Cβ, R6Cβ-A28Cα, and A28Cα-R6Cβ, A28Cβ-R6Cβ, A28Cβ-R6Cα. These five unique constraints were inputted as NOE constraints for structure calculation. **Figure 4.5** also shows that the

correlations C3-C31, Y4-C30, and R6-A28 indicate two antiparallel β-strands β1 and β3, while the E14-C31, R15-F29, R16-A28, I21-L26, Y22-R25 cross peaks indicate another two antiparallel β-strands, β2 and β3. These antiparallel β-strands are consistent with those of the crystal structure (**Figure 4.6d**). Moreover, three disulfide bond correlations, C3-C31, C5-C20 and C10-C30, which are absent in the 2D spectrum, are now clearly identified, providing another set of important constraints for the HNP-1 structure.

Structure calculation

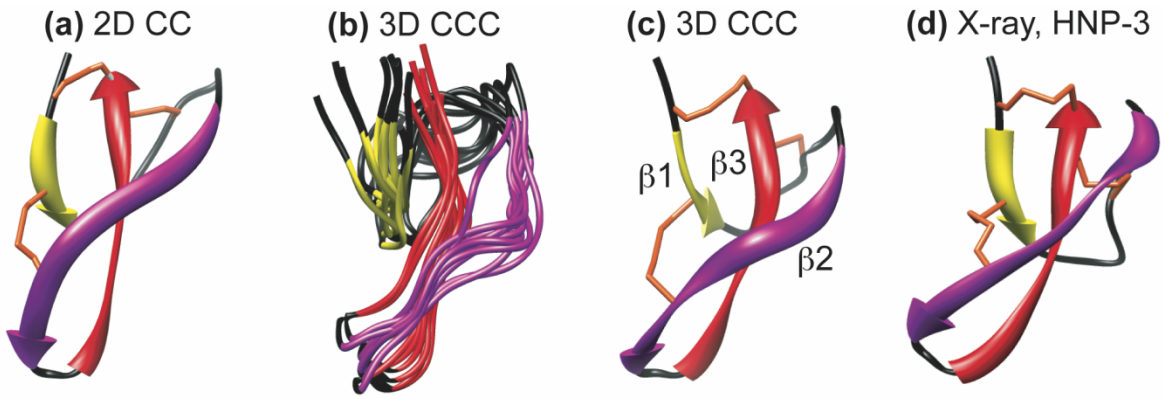

Figure 4.6. Three-dimensional structures of HNP-1 from SSNMR and HNP-3 from crystallography. (a) Average minimum-energy SSNMR structure obtained from long-distance constraints detected in the 2D CC spectrum. (b) Ensemble of 10 minimum-energy SSNMR structures obtained from long-distance constraints detected in the 3D CCC spectrum. (c) Average SSNMR structure of (b). All NMR structures shared the same torsion angle constraints obtained from chemical shifts. (d) Crystal structure of HNP-3. Yellow, purple, and red ribbons represent the three β-strands β1, β2, and β3. Black indicates loops. The three disulfide bonds are shown in orange.

Figure 4.6(a-c) shows the calculated HNP-1 structures where the long-range distance constraints were obtained from the 2D CC experiment and 3D CCC experiment. Both structures are compared with the crystal structure of HNP-3 (**Figure 4.6d**). As listed in Table 1, a total of 60 distance constraints were obtained from 2D ^{13}C-^{13}C and ^{15}N-^{15}N correlation experiments, including ^{13}C-^{13}C DARR experiments with 20 ms, 40 ms, 100 ms and 200 ms mixing, a CHHC experiment with 100 μs mixing, and a ^{15}N-^{15}N

correlation experiment with 3.0 s mixing [37]. Among these constraints, 36 were sequential (|i-j|=1), 4 were medium-range (1<|i-j|≤4), and another 20 constraints were long-range restraints (|i-j|>4). Although the long-range cross peaks were assigned by comparing with the crystal structure, due to the small number of distances, the heavy-atom RMSD of the 2D-based NMR structure from the crystal structure is still 3.8 Å (**Figure 4.6a**). These differences include 1) a bulge in the β2 strand of the NMR structure, which is absent in the crystal structure, 2) a different orientation of the β3 strand, and 3) a different orientation of the loop connecting the β1 and β2 strands. The lack of *de novo* distance determination made it difficult to assess whether the deviation between the NMR structure and the crystal structure results from the low number of distance restraints or from a true conformational distinction between HNP-1 and HNP-3.

Table 4.1 SSNMR structure statistics of HNP-1.

Distance constraints and calculation results		From 2D NMR	From 3D CCC NMR
Number of distance constraints	Sequential (|i-j| = 1)	36	129
	Medium-range (1< |i-j| ≤ 4)	4	45
	Long-range (|i-j| > 4)	20	96
	Unique	60	213
	Ambiguous	0	57
	Total	60	270
Total (ϕ, ψ) torsion angle constraints		56	56
Final energy E_{global} (kcal/mol)		264	38.5
Backbone RMSD from crystal structure (Å)		2.7	2.4
Heavy-atom RMSD from crystal structure (Å)		3.8	3.4

From the 3D CCC spectrum, we obtained a total of 213 unique distances and 57 ambiguous distances from the 450 uniquely assigned cross peaks. Some atomic pairs exhibit multiple cross peaks in the 3D spectrum, thus increasing the confidence of assignment. Among these distances, 129 are sequential, 45 are medium-range, and 96 are

long-range constraints (**Table 4.1**). As shown in **Figure 4.6b**, the ten minimum-energy structures are well clustered, and the average structure of the ensemble (**Figure 4.6c**) is more similar to the crystal structure (**Figure 4.6d**) [33] with a heavy-atom RMSD of 3.4 Å. Specifically, the β2 bulge is significantly attenuated in the new NMR structure, and the orientation of the β3 strand is also much closer to that of the HNP-3 structure. The remaining difference is the position of the I7-E14 loop, which can now be more confidently attributed to real conformational differences between the two proteins [37]. We hypothesize that this remaining conformational difference results from the sequence difference between HNP-1 and HNP-3 and is correlated with the antimicrobial activity difference between the two proteins. On average the HNP-1 antimicrobial activity is about 2-fold stronger than HNP-3 [42]. Since the three core β-strands are well constrained by the disulfide bonds and a tight turn, the only conformationally variable region of the protein is the non hydrogen-bonded loop between β1 and β2 strands. By subtly changing the conformation of the protein, this loop may thus influence the protein's interaction with the target lipid membrane and hence the antimicrobial activity [34].

How robust is the 3D CCC experiment for protein samples with limited sensitivity? If we increase the lowest contour level by a factor of 1.6, effectively removing the weakest cross peaks, then we obtain fewer (323 inter-residue) cross peaks and fewer (145) distance constraints. But even with a smaller subset of constraints, the backbone RMSD between the resulting average NMR structure and the crystal structure remains reasonably low, 2.6 Å. Thus, the information content of the 3D CCC experiment is sufficient to permit *de novo* structure determination of proteins with lower sensitivities than available here. Moreover, the present distance analysis only focuses on the correlations between aliphatic carbons. If we include carbonyl and aromatic correlations with the aliphatic carbons, then the number of long-range distance constraints will increase further and ease structure determination.

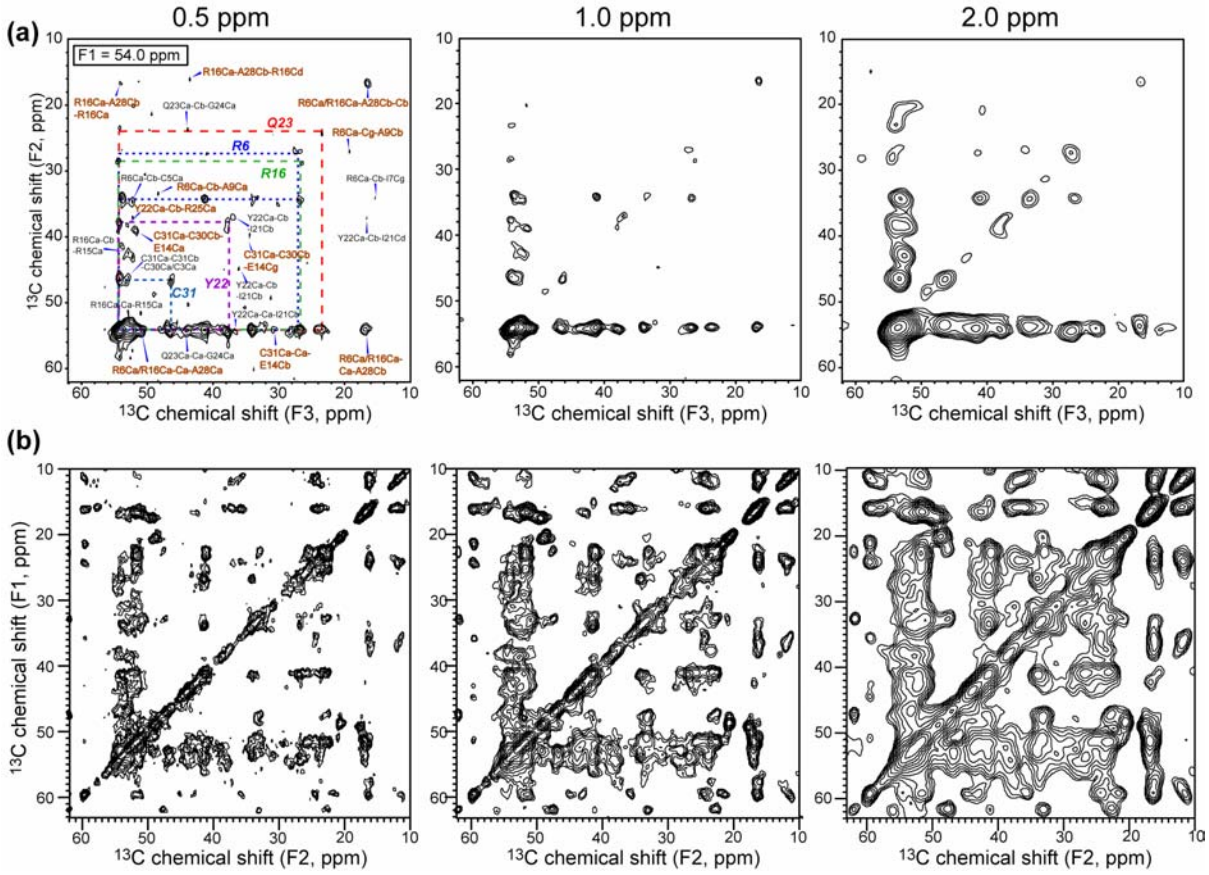

Figure 4.7. Effects of linewidths on the number of resolved cross peaks from 3D CCC and 2D DARR spectra. (a) F1=54.0 ppm plane of the 3D CCC spectrum, processed with Gaussian line broadening values of 0.5 ppm (left), 1.0 ppm (middle), and 2.0 ppm (right). The numbers of cross peaks are 47, 33, and 35, respectively. (b) 2D 100 ms DARR spectrum, processed with Gaussian line broadening values of 0.5 ppm, 1.0 ppm, and 2.0 ppm, from the left to the right. The numbers of cross peaks are 194, 126, and 84, respectively.

It is also interesting to assess how the number of distance constraints from the 3D CCC experiment is affected by linewidths, considering membrane proteins and other non-crystalline proteins typically have broader lines than microcrystalline proteins. As an example, we processed the F1 = 54.0 ppm plane of the 3D spectrum (**Figure 4.3a**) with different Gaussian line broadening values of 0.5, 1.0 and 2.0 ppm. The number of cross peaks in the aliphatic region (10 – 62 ppm) was found to be 47, 33, and 35, respectively (**Figure 4.7a**). Thus, at linewidths typical of non-crystalline proteins (1-2 ppm), the number of resolved peaks decreases only modestly, to about 75% of the maximum

number. Interestingly, the peak number does not decrease from 1.0 ppm to 2.0 ppm linewidths, suggesting that each plane of the 3D spectrum is sufficiently uncongested that it is insensitive to changes in this range of linewidths. In comparison, the number of aliphatic cross peaks in the 100 ms 2D DARR spectrum is 194, 126, and 84 for 0.5, 1.0, and 2.0 ppm line broadening (**Figure 4.7b**). Thus, the resolved peaks decreased to only 43% of the maximum value. Moreover, the peak number is significantly smaller under 2.0 ppm line broadening than under 1.0 ppm broadening, reflecting the intrinsic spectral congestion. Thus, the 3D CCC spectra are less affected by larger linewidths than 2D CC spectra, making the 3D CCC experiment also robust in terms of resolution.

Conclusion

We have shown that the 3D CCC experiment is very useful for resolving and extracting a large number of inter-residue distances that are crucial for *de novo* determination of the three-dimensional structure of proteins by solid-state NMR. By reducing peak congestion, the 3D CCC experiment reduces assignment ambiguity and significantly increases the number of long-range distance constraints. The information content is much larger than several 2D correlation experiments combined. This 3D CCC approach can be readily combined with techniques that preferentially detect long-range distances such as the PAR experiment. Similarly, one can combine the 3D CCC experiments with alternative isotopic labeling schemes to further facilitate long distance extraction.

Acknowledgment

This work is supported by an NIH grant GM66976 to M.H and an NSF instrumentation grant DBI421374 for the 600 MHz NMR at Iowa State University.

References

[1] Mielke, S. P.; Krishnan, V. V., Characterization of protein secondary structure from NMR chemical shifts, Prog. Nucl. Magn. Reson. Spect. 54 (2009) 141-165.

[2] Spera, S.; Bax, A., Empirical Correlation between Protein Backbone

Conformation and C-Alpha and C-Beta C-13 Nuclear-Magnetic-Resonance Chemical-Shifts, J. Am. Chem. Soc. 113 (1991) 5490-5492.

[3] Dedios, A. C.; Pearson, J. G.; Oldfield, E., Secondary and Tertiary Structural Effects on Protein Nmr Chemical-Shifts - an Abinitio Approach, Science 260 (1993) 1491-1496.

[4] Seidel, K.; Etzkorn, M.; Schneider, R.; Ader, C.; Baldus, M., Comparative analysis of NMR chemical shift predictions for proteins in the solid phase, Solid State Nucl. Magn. Reson. 35 (2009) 235-242.

[5] Yao, X. L.; Hong, M., Determination of Ca chemical shift tensor orientation in peptides by dipolar-modulated chemical shift recoupling NMR spectroscopy, J. Am. Chem. Soc. 124 (2002) 2730-2738.

[6] Wi, S.; Sun, H. H.; Oldfield, E.; Hong, M., Solid-state NMR and quantum chemical investigations of C-13(alpha) shielding tensor magnitudes and orientations in peptides: Determining phi and psi torsion angles, J. Am. Chem. Soc. 127 (2005) 6451-6458.

[7] Wylie, B. J.; Sperling, L. J.; Frericks, H. L.; Shah, G. J.; Franks, W. T.; Rienstra, C. M., Chemical-shift anisotropy measurements of amide and carbonyl resonances in a microcrystalline protein with slow magic-angle spinning NMR spectroscopy, J. Am. Chem. Soc. 129 (2007) 5318-5319.

[8] Wylie, B. J.; Franks, W. T.; Graesser, D. T.; Rienstra, C. M., Site-specific 13C chemical shift anisotropy measurements in a uniformly 15N,13C-labeled microcrystalline protein by 3D Magic-Angle Spinning NMR spectroscopy, J. Am. Chem. Soc. 127 (2005) 11946-11947.

[9] Wylie, B. J.; Schwieters, C. D.; Oldfield, E.; Rienstra, C. M., Protein structure refinement using 13Ca chemical shift tensors, J. Am. Chem. Soc. 131 (2009) 985-992.

[10] Hong, M.; Gross, J. D.; Hu, W.; Griffin, R. G., Determination of the peptide torsion angle phi by N-15 chemical shift and C-13(alpha)-H-1(alpha) dipolar tensor correlation in solid-state MAS NMR, J. Magn. Reson. 135 (1998) 169-177.

[11] Costa, P. R.; Gross, J. D.; Hong, M.; Griffin, R. G., Solid-state NMR measurement of Psi in peptides: a NCCN 2Q-heteronuclear local field experiment, Chemical Physics Letters 280 (1997) 95-103.

[12] Hong, M.; Gross, J. D.; Griffin, R. G., Site-resolved determination of peptide torsion angle phi from the relative orientations of backbone N-H and C-H bonds by solid-state NMR, J. Phys. Chem. B 101 (1997) 5869-5874.

[13] Castellani, F.; van Rossum, B.; Diehl, A.; Schubert, M.; Rehbein, K.; Oschkinat, H., Structure of a protein determined by solid-state magic-angle-spinning NMR spectroscopy, Nature 420 (2002) 98-102.

[14] Franks, W. T.; Wylie, B. J.; Schmidt, H. L. F.; Nieuwkoop, A. J.; Mayrhofer, R. M.; Shah, G. J.; Graesser, D. T.; Rienstra, C. M., Dipole tensor-based atomic-resolution structure determination of a nanocrystalline protein by solid-state NMR, Proc. Natl. Acad. Sci., USA 105 (2008) 4621-4626.

[15] Gardiennet, C.; Loquet, A.; Etzkorn, M.; Heise, H.; Baldus, M.; Bockmann, A., Structural constraints for the Crh protein from solid-state NMR experiments, J. Bio. NMR 40 (2008) 239-250.

[16] Loquet, A.; Bardiaux, B.; Gardiennet, C.; Blanchet, C.; Baldus, M.; Nilges, M.; Malliavin, T.; Boeckmann, A., 3D structure determination of the Crh protein from highly ambiguous solid-state NMR restraints, J. Am. Chem. Soc. 130 (2008) 3579-3589.

[17] Grommek, A.; Meier, B. H.; Ernst, M., Distance information from proton-driven spin diffusion under MAS, Chem. Phys. Lett. 427 (2006) 404-409.

[18] Crocker, E.; Patel, A. B.; Eilers, M.; Jayaraman, S.; Getmanova, E.; Reeves, P. J.; Ziliox, M.; Khorana, H. G.; Sheves, M.; Smith, S. O., Dipolar assisted rotational resonance NMR of tryptophan and tyrosine in rhodopsin, J. Biomol. NMR 29 (2004) 11-20.

[19] Lange, A.; Luca, S.; Baldus, M., Structural constraints from proton-mediated rare-spin correlation spectroscopy in rotating solids, J. Am. Chem. Soc. 124 (2002) 9704-9705.

[20] Lange, A.; Seidel, K.; Verdier, L.; Luca, S.; Baldus, M., Analysis of proton-proton transfer dynamics in rotating solids and their use for 3D structure determination, J. Am. Chem. Soc. 125 (2003) 12640-12648.

[21] De Paepe, G.; Lewandowski, J. R.; Loquet, A.; Bockmann, A.; Griffin, R. G., Proton assisted recoupling and protein structure determination, J. Chem. Phys. 129 (2008) 245101.

[22] Lewandowski, J. R.; De Paepe, G.; Eddy, M. T.; Griffin, R. G., N-15-N-15 Proton Assisted Recoupling in Magic Angle Spinning NMR, J. Am. Chem. Soc. 131 (2009) 5769-5776.

[23] Heise, H.; Seidel, K.; Etzkorn, M.; Becker, S.; Baldus, M., 3D NMR spectroscopy for resonance assignment and structure elucidation of proteins under MAS: novel pulse schemes and sensitivity considerations, J. Magn. Reson. 173 (2005) 64-74.

[24] Zhou, D. H. H.; Kloepper, K. D.; Winter, K. A.; Rienstra, C. M., Band-selective C-13 homonuclear 3D spectroscopy for solid proteins at high field with rotor-synchronized soft pulses, J. Bio. NMR 34 (2006) 245-257.

[25] Ganz, T., Defensins: Antimicrobial peptides of innate immunity, Nat. Rev. Immunol. 3 (2003) 710-720.

[26] Ganz, T.; Selsted, M. E.; Szklarek, D.; Harwig, S. S.; Daher, K.; Bainton, D. F.; Lehrer, R. I., Defensins. Natural peptide antibiotics of human neutrophils, Journal of Clinical Investigation 76 (1985) 1427-1435.

[27] Gabay, J. E.; Scott, R. W.; Campanelli, D.; Griffith, J.; Wilde, C.; Marra, M. N.; Seeger, M.; Nathan, C. F., Antibiotic proteins of human polymorphonuclear leukocytes, Proceedings of the National Academy of Sciences of the United States of America 86 (1989) 5610-5614.

[28] Jones, D. E.; Bevins, C. L., Paneth cells of the human small intestine express an antimicrobial peptide gene, Journal of Biological Chemistry 267 (1992) 23216-23225.

[29] Jones, D. E.; Bevins, C. L., Defensin-6 mRNA in human Paneth cells: implications for antimicrobial peptides in host defense of the human bowel, FEBS Letters 315 (1993) 187-192.

[30] Yang, D.; Biragyn, A.; Hoover, D. M.; Lubkowski, J.; Oppenheim, J. J., Multiple roles of antimicrobial defensins, cathelicidins, and eosinophil-derived neurotoxin in host defense, Annu. Rev. Immunol. 22 (2004) 181-215.

[31] Selsted, M. E.; Ouellette, A. J., Mammalian defensins in the antimicrobial immune response, Nature Immunol. 6 (2005) 551-557.

[32] Lehrer, R. I., Primate defensins, Nat. Rev. Microbiol. 2 (2004) 727-738.

[33] Hill, C. P.; Yee, J.; Selsted, M. E.; Eisenberg, D., Crystal-structure of defensin HNP-3, an amphiphilic dimer - mechanisms of membrane permeabilization, Science 251

(1991) 1481-1485.

[34] Szyk, A.; Wu, Z. B.; Tucker, K.; Yang, D.; Lu, W. Y.; Lubkowski, J., Crystal structures of human alpha-defensins HNP4, HD5, and HD6, Protein Sci. 15 (2006) 2749-2760.

[35] Zou, G. Z.; de Leeuw, E.; Li, C.; Pazgier, M.; Li, C. Q.; Zeng, P. Y.; Lu, W. Y.; Lubkowski, J.; Lu, W. Y., Toward understanding the cationicity of defensins - Arg and Lys versus their noncoded analogs, J. Biol. Chem. 282 (2007) 19653-19665.

[36] Xie, C.; Prahl, A.; Ericksen, B.; Wu, Z. B.; Zeng, P. Y.; Li, X. Q.; Lu, W. Y.; Lubkowski, J.; Lu, W. Y., Reconstruction of the conserved beta-bulge in mammalian defensins using D-amino acids, J. Biol. Chem. 280 (2005) 32921-32929.

[37] Zhang, Y.; Doherty, T.; Li, J.; Lu, W. Y.; Barinka, C.; Lubkowaki, J.; Hong, M., Resonance Assignment and Three-Dimensional Structure Determination of a Human alpha-Defensin, HNP-1, by Solid-State NMR, Submitted (2009).

[38] Schwieters, C. D.; Kuszewski, J. J.; Tjandra, N.; Clore, G. M., The Xplor-NIH NMR molecular structure determination package, J. Magn. Reson. 160 (2003) PII S1090-7807(1002)00014-00019.

[39] Schwieters, C. D.; Kuszewski, J. J.; Clore, G. M., Using Xplor-NIH for NMR molecular structure determination, Prog. Nucl. Magn. Reson. Spect. 48 (2006) 47-62.

[40] Castellani, F.; van Rossum, B. J.; Diehl, A.; Rehbein, K.; Oschkinat, H., Determination of solid-state NMR structures of proteins by means of three-dimensional 15N-13C-13C dipolar correlation spectroscopy and chemical shift analysis, Biochemistry 42 (2003) 11476-11483.

[41] Cornilescu, G.; Delaglio, F.; Bax, A., Protein backbone angle restraints from searching a database for chemical shift and sequence homology, J. Bio. NMR 13 (1999) 289-302.

[42] Ericksen, B.; Wu, Z.; Lu, W.; Lehrer, R. I., Antibacterial activity and specificity of the six human {alpha}-defensins, Antimicrobial Agents and Chemotherapy 49 (2005) 269-275.

Chapter 5

Membrane-Bound Structure and Topology of a Human Alpha Defensin Indicates A Dimer Pore Mechanism for Membrane Disruption

A paper published in Biochemistry

2010, vol. 49, pp. 9770-9782

Yuan Zhang, Wuyuan Lu, and Mei Hong

Abstract

Defensins are cationic and disulfide-bonded host defense proteins of many animals that target microbial cell membranes. Elucidating the three-dimensional structure, dynamics and topology of these proteins in phospholipid bilayers is important for understanding their mechanisms of action. Using solid-state NMR spectroscopy, we have now determined the conformation, dynamics, oligomeric state and topology of a human α-defensin, HNP-1, in DMPC/DMPG bilayers. 2D correlation spectra show that membrane-bound HNP-1 exhibits a similar conformation to the water-soluble state, except for the turn connecting the β2 and β3 strands, whose sidechains exhibit immobilization and conformational perturbation upon membrane binding. At high protein/lipid ratios, rapid ^{1}H spin diffusion from the lipid chains to the protein was observed, indicating that HNP-1 was well inserted into the hydrocarbon core of the bilayer. Arg Cζ - lipid ^{31}P distances indicate that only one of the four Arg residues forms tight hydrogen-bonded guanidinium-phosphate complexes. The protein is predominantly dimerized at high protein/lipid molar ratios, as shown by ^{19}F spin diffusion experiments. The presence of a small fraction of monomers and the shallower insertion at lower protein concentrations suggest that HNP-1 exhibits concentration-dependent oligomerization and membrane-bound topology. These data strongly support a "dimer pore" topology of HNP-1 in which the polar top of the dimer lines an aqueous pore while

the hydrophobic bottom faces the lipid chains. In this structure R25 lies closest to the membrane surface among the four Arg residues. The resulting pore does not have large lipid disorder, in contrast to the case of protegrin-1, a two-stranded β-hairpin antimicrobial peptide. These results provide the first glimpse into the membrane-bound structure and mechanism of action of human α-defensins.

Introduction

Defensins are host-defense antimicrobial proteins present in many animals and plants. These cationic polypeptides contain three intramolecular disulfide bonds, whose linkage patterns distinguish the α-, β-, and θ-defensins [1]. Humans have six α-defensins of about 30 residues long [2]. The human neutrophil peptides (HNP) 1-4 were found in the azurophilic granules of neutrophils [3-5], while HD-5 and HD-6 are present in intestinal epithelial cells [6,7]. Except for HD-6, the human α-defensins show wide-spectrum antimicrobial activities in the microgram per milliliter range [8,9]. Similar to many other antimicrobial peptides (AMPs), the general mechanism of antimicrobial action is believed to be permeabilization of the microbial cell membrane [10,11].

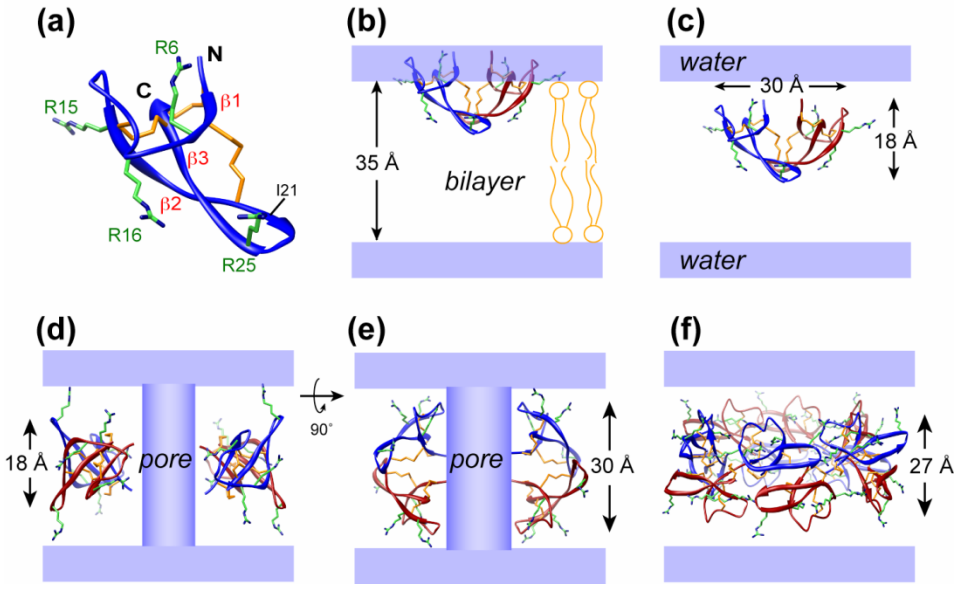

Figure 5.1. Different structural models of HNPs in lipid bilayers. The basic oligomeric state of the protein is a hydrogen-bonded dimer shaped like a basket. (a) Structure of the HNP monomer [12] with Arg residues indicated. (b) Surface-bound wedge model with the hydrophobic basket

bottom inserted into the bilayer and the polar basket top in contact with water. (c) Membrane-inserted wedge model. (d) Dimer pore model, where the hydrophobic basket bottom contacts the lipids while the polar top faces the water pore. (e) General pore model, where the dimers are rotated by 90˚ from the dimer pore orientation. (f) Multimeric pore model, where six dimers form a pore with a ~25 Å inner diameter. The height of the multimer, measured between two Pro8 residues, is 27 Å. The approximate dimensions of the various oligomeric assemblies are indicated in (b-f).

High-resolution X-ray structures of all six human α-defensins in the absence of membrane-mimetic solvents have been determined [12,13]. The structures are very similar despite significant sequence differences between HNP 1-3 and the other three defensins. The proteins consist of three antiparallel β-strands (β1, β2, β3) connected by turns and a longer loop (**Figure 5.1a**). The proteins are dimerized in the crystal through intermolecular H-bonds between the two β2 strands, thus extending the triple-stranded β-sheet to a six-stranded β-sheet. The dimer has a basket shape and is amphipathic, with a polar top and an apolar base.

Based on the crystal structure of HNP-3 [12], several mechanistic models had been proposed to account for the antimicrobial activities of HNPs. The wedge model [12] suggests that the dimer inserts into the bilayer with the hydrophobic bottom contacting the hydrocarbon region of the membrane, thus disrupting lipid packing (**Figure 5.1b, c**). The depth of the wedge is unknown, so the dimer may be partly or completely immersed in the lipid membrane. Alternatively, HNPs might form membrane-spanning pores with the hydrophobic base facing the lipids. In the so-called “dimer pore” model [12] (**Figure 5.1d**), the polar tops of two dimers are oriented to favor transmembrane (TM) orientation of a small solvent channel observed at the dimer interface in the crystal structure [12]. In the “general pore” model [12], the dimers are rotated by 90˚ around the horizontal axis (**Figure 5.1e**), so that the side view, parallel to the membrane normal, shows the basket shape of the dimer. A multimeric pore model was also proposed based on vesicle leakage and dextran permeability experiments. Here 6-8 HNP dimers may form a large pore with an inner diameter of 20-25 Å [14]. The dimers would be oriented with the long axis of the basket top at approximately 45˚ from the bilayer normal, so that the Arg residues in the

protein are located in two rings separated by about 16 Å along the bilayer normal, promoting favorable electrostatic interactions with the lipid phosphates (**Figure 5.1f**).

Despite abundant crystal structure information of HNPs, no high-resolution structure information for membrane-bound HNPs has been reported. To elucidate the mechanism of action of human defensins, we have initiated a solid-state NMR study of recombinant HNP-1 uniformly labeled with ^{13}C and ^{15}N. Since membrane-bound proteins typically have broad linewidths than proteins outside the membrane, due largely to the conformational disorder of the lipids, we found it necessary to first conduct resonance assignment of the protein in the more ordered water-soluble state, in the absence of lipids. Unlike the bactericidal channel-forming colicins [15-17], which exhibit abundant membrane-induced flexibility, HNPs cannot undergo large conformational rearrangements due to their multiple disulfide bonds. We thus first determined the NMR structure of lipid-free microcrystalline HNP-1 using 2D and 3D magic-angle-spinning (MAS) ^{13}C-^{13}C and ^{13}C-^{15}N correlation experiments [18,19]. Together with distance constraints, these chemical shifts led to the first solid-state NMR structure of a human α-defensin, which confirmed the 3D fold seen in the crystal structures (PDB code: 2KHT). This NMR structure determination yielded the complete ^{13}C and ^{15}N chemical shifts of the protein [19], with which the membrane-bound HNP-1 chemical shifts can now be compared. In this work, we investigate the conformation and dynamics of HNP-1 in the membrane, its oligomeric state [20,21], and most importantly, its interactions with lipids and with water. These results yielded the global topology of HNP-1 in the lipid membrane, enabling us to rule out most structural models and allowing us to propose the membrane-disruptive mechanism of HNP-1.

Materials and Methods

HNP-1 expression and synthesis

Recombinant ^{13}C, ^{15}N-labeled HNP-1 (ACYCRIPACIAGERRYGTCIYGQRLWAFCC) (**Figure 5.3a)** was obtained as a cleavage product from its precursor protein, proHNP1. The residues are numbered from

A2 to C31 due to sequence alignment with other mammalian defensins, many of which contain an additional N-terminal residue before A2 [12]. Using this numbering system also facilitates comparison with the structure of HNP-3, which was the first structure determined in the HNP family. Briefly, the expression protocol starts with expression of proHNP1 as a GST-fusion protein in *E. coli* using uniformly ^{13}C, ^{15}N-labeled Spectra 9 media (Cambridge Isotope Laboratories) [19,22]. GST-proHNP1 was folded and then cleaved using thrombin, producing proHNP1. ProHNP1 was purified by reversed-phase HPLC, then cleaved using cyanogen bromide to yield correctly folded HNP-1. Antimicrobial assays confirmed the activity of the protein. For example, 100% killing of *S. aureus* is reached at 64 μg/ml HNP-1 [19,22]. Crude HNP-1 was purified by reversed-phase HPLC. About 1.5 mg HNP-1 (molecular weight: 3634 Da) was purified from 1 L culture. ^{19}F-labeled HNP-1 for CODEX experiments was synthesized using t-Boc chemistry [23], where Tyr4 was replaced by 4-^{19}F-Phg. The use of phenylglycine removes the possibility of sidechain χ_1 motion that could complicate the interpretation of the CODEX data [24,25]. The choice of Tyr4 as the ^{19}F labeled site was based on the crystal structures of various HNPs, all showing close inter-subunit contact of this residue [12,13,26]. Previous studies of 4- [^{19}F]Phg mutants of the related β-hairpin antimicrobial peptide, PG-1 [24], suggest that the mutation generally does not perturb the antimicrobial activities of the peptides.

Membrane sample preparation

DMPC and DMPG lipids (Avanti Polar Lipids, Alabaster, AL) were codissolved in chloroform at a molar ratio of 3:1, dried under a stream of nitrogen gas, suspended in cyclohexane and lyophilized overnight. The resulting homogeneous lipid powder was suspended in a pH 7 phosphate buffer, vortexed and then freeze-thawed five times. The vesicle solution was sequentially extruded through polycarbonate filters with pore sizes of 400 nm and 100 nm to obtain large unilamellar vesicles. HNP-1 was dissolved in 1 mL phosphate buffer, added to the lipid vesicle solution and dialyzed overnight. The mixture was centrifuged at 200,000 g for 3 hours at 4˚C to obtain a membrane pellet. The pellet was pipette-transferred into 4 mm MAS rotors for NMR experiments.

Three samples were prepared: two U-^{13}C, ^{15}N-labeled HNP-1 samples at protein : lipid (P/L) molar ratios of 1: 18 and 1: 40, and one ^{19}F-labeled HNP-1 sample at P/L = 1: 18. The 1:18 molar ratio corresponds to a mass ratio of 1 : 3.3, thus there is sufficient lipid to ensure appropriate protein-lipid interactions.

Solid-state NMR spectroscopy

Solid-state NMR experiments were carried out on a Bruker (Karlsruhe, Germany) AVANCE-600 (14.1 Tesla) spectrometer operating at a ^{13}C Larmor frequency of 150.92 MHz for most resonance assignment experiments, and a Bruker DSX-400 (9.4 Tesla) spectrometer for ^{13}C-^{31}P REDOR experiments, ^{1}H spin diffusion and ^{13}C-^{1}H dipolar coupling measurements. Triple-resonance MAS probes with 4-mm rotors were used in all experiments. ^{13}C and ^{31}P chemical shifts were referenced externally to the α-glycine ^{13}CO signal at 176.49 ppm on the TMS scale and the hydroxyapatite ^{31}P signal at 2.73 ppm on the phosphoric acid scale, respectively. ^{15}N chemical shifts were referenced to the ^{15}N signal of N-acetyl-valine at 122.0 ppm on the liquid ammonia scale.

2D ^{13}C-^{13}C DARR correlation spectra [27] were measured at 273 K under 5 kHz MAS with a ^{13}C spin diffusion time of 40 ms. 2D N(CO)CX and N(CA)CX correlation spectra [28,29] were measured at 273 K under 7.5 kHz MAS with a ^{13}C mixing time of 40 ms for NCACX and 60 ms for NCOCX. The ^{15}N-^{13}C SPECIFIC [30] cross-polarization (CP) contact times were 3 ms. In the intra-residue NCACX experiment, ^{15}N-^{13}Cα magnetization transfer was achieved using a ^{15}N spin-lock field of 17 kHz and an on-resonance ^{13}Cα spin-lock field of 25 kHz. In the inter-residue NCOCX experiment, ^{15}N-^{13}CO magnetization transfer was accomplished with a ^{15}N on-resonance spin-lock field of 27 kHz and a tilted ^{13}CO spin-lock field strength of 35 kHz, which was the result of a 30 kHz applied pulse on resonance at Cα and an 18 kHz offset for CO.

^{13}C-^{1}H dipolar couplings were measured at 303 K using the 2D dipolar chemical-shift (DIPSHIFT) correlation experiment [31]. The sample was spun at 4.5 kHz, and the MREV-8 sequence [32] was used for ^{1}H homonuclear decoupling. The t_1-curves were fit using a Fortran program, and the fit values were divided by the MREV-8 scaling factor to

obtain the true couplings. To account for uncertainties in the MREV-8 scaling factor, we measured the rigid-limit C-H couplings using the crystalline model peptide formyl-Met-Leu-Phe (f-MLF) [33,34], where Leu Cα, Met Cβ, and Leu Cδ signals represented CH, CH_2, and CH_3 groups, respectively. The CH and CH_2 peaks gave C-H rigid-limit dipolar couplings of 11.2 kHz (fit values), which corresponded to true couplings of 23.8 kHz when the theoretical scaling factor of 0.47 for MREV-8 was used [35]. For the Leu CH_3 signal, the fit value was 3.5 kHz. The ratio of the measured HNP-1 couplings with the rigid-limit f-MLF couplings yielded the order parameter S_{CH}.

To determine the depth of insertion of HNP-1, we carried out 2D ^{13}C-detected ^{1}H spin diffusion experiments [36,37] at 303 K or 308 K under 5 kHz MAS. For the P/L = 1:18 sample, ^{1}H spin diffusion mixing times (t_m) of 2.25 – 225 ms were applied to transfer the ^{1}H magnetization of mobile lipids and water to HNP-1. For the P/L=1:40 sample, two mixing times of 100 ms and 225 ms were measured since the sensitivity was too low to measure a complete buildup curve. The ^{1}H magnetization transfer was detected through the protein ^{13}C signals. To ensure that only the mobile lipid and water polarization served as the ^{1}H magnetization source, we suppressed the ^{1}H polarization of the rigid protein by a ^{1}H T_2 filter of 0.4 x 2 ms before the t_1 evolution period. For the 2.25 ms spectrum of the 1:18 sample, the water ^{1}H cross section was extracted to analyze the water-proximal residues in the protein.

A frequency-selective rotational-echo double-resonance (REDOR) experiment [38] was used to measure protein ^{13}C distances to lipid ^{31}P. The experiments were performed at 233 K under 4.5 kHz MAS to suppress lipid motions as well as protein sidechain motions. A rotor-synchronized ^{13}C Gaussian 180° pulse of 444 μs was applied in the middle of the REDOR period to suppress ^{13}C-^{13}C J-couplings between the on-resonance ^{13}C and its directly bonded spins. ^{31}P 180° pulses of 9 μs were applied every half a rotor period to recouple the ^{13}C-^{31}P dipolar coupling. The time-dependent REDOR intensities were fit using two-spin simulations, which had been shown [39] to correspond to the vertical distance between the ^{13}C spin and the ^{31}P plane for long distances of greater than ~6 Å.

^{19}F CODEX experiments [20,40,41] for determining the oligomeric state of HNP-1 were carried out at 233 K under 7 kHz MAS. The ^{19}F chemical shift anisotropy (CSA) was recoupled by two rotor periods of 180˚ pulses. During the ^{19}F mixing time, spin diffusion changes the ^{19}F CSA and prevents complete refocusing of a stimulated echo. A z-filter after the second 180˚-pulse train allows the correction of ^{19}F T_1 relaxation effects by conducting two experiments for each t_m, a control experiment (S_0) in which the short z-filter period (10 μs) was applied between the two 180˚-pulse trains while the long t_m occurred after, and a dephasing experiment (S) where the long t_m occurs between the two 180˚-pulse trains. The intensity ratio, S/S_0, at long mixing times gives the number of ^{19}F spins in close proximity. Two mixing times, 500 ms and 1 s, were measured.

Results

Conformation and dynamics of HNP-1 in the lipid membrane

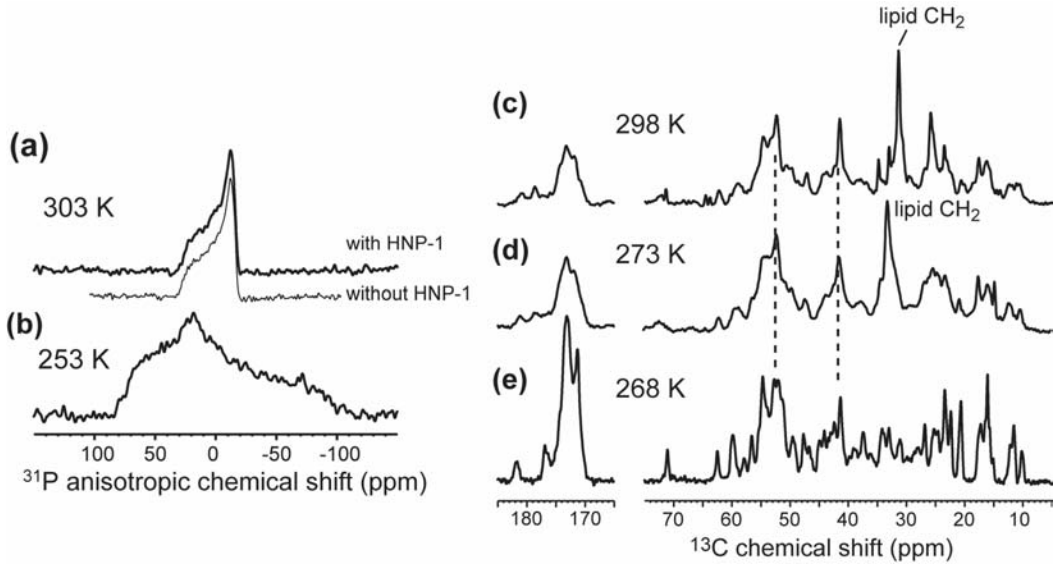

Figure 5.2. 1D ^{31}P and ^{13}C spectra of membrane-bound HNP-1. (a) ^{31}P static spectra of DMPC/DMPG membranes with HNP-1 at P/L = 1:18 at 303 K (thick line) and without the protein (thin line). The protein-bound spectrum exhibits no isotropic peak and is identical to the spectrum of the non-protein-containing membrane. (b) ^{31}P spectrum of HNP-1-bound DMPC/DMPG membrane at 253 K. (c) ^{13}C MAS spectrum of membrane-bound HNP-1 at 298 K. (d) ^{13}C spectrum of membrane-bound HNP-1 at 273 K. The protein intensities and linewidths are

little affected by temperature, suggesting that HNP-1 is immobilized in the liquid-crystalline membrane. (e) ^{13}C spectrum of microcrystalline HNP-1 without the lipids at 268 K. The intensity distribution of the membrane-bound HNP-1 is similar to that of the microcrystalline protein, indicating similar conformations.

Figure 5.2a,b shows the ^{31}P spectrum of the DMPC/DMPG (3:1) membrane with bound HNP-1 above (303 K) and below (253 K) the membrane phase transition temperature. At 303 K the ^{31}P spectrum has the classical uniaxial lineshape indicative of lamellar bilayers and is identical to the protein-free lipid spectrum, indicating that HNP-1 does not cause significant orientation disorder to the lamellar bilayer. Below the phase transition temperature (23˚C) the ^{31}P spectrum exhibited the expected broadening, with a rigid-limit span of 210 ppm at 253 K.

We examined the membrane-bound conformation of HNP-1 by comparing the ^{13}C spectra of the membrane-bound and microcrystalline states. **Figure 5.2c,d** show the 1D ^{13}C CP-MAS spectra of HNP-1 in DMPC/DMPG bilayers at 298 K and 273 K. The intensity and linewidths were largely unaffected by temperature, suggesting that HNP-1 was immobilized at ambient temperature. Compared to the microcrystalline protein spectrum (**Figure 5.2e**), the membrane-bound sample exhibited similar intensity distributions except for the additional lipid peaks. Thus, HNP-1 overall adopts a similar average conformation in the membrane as in the microcrystalline state, as expected for this disulfide-bonded protein.

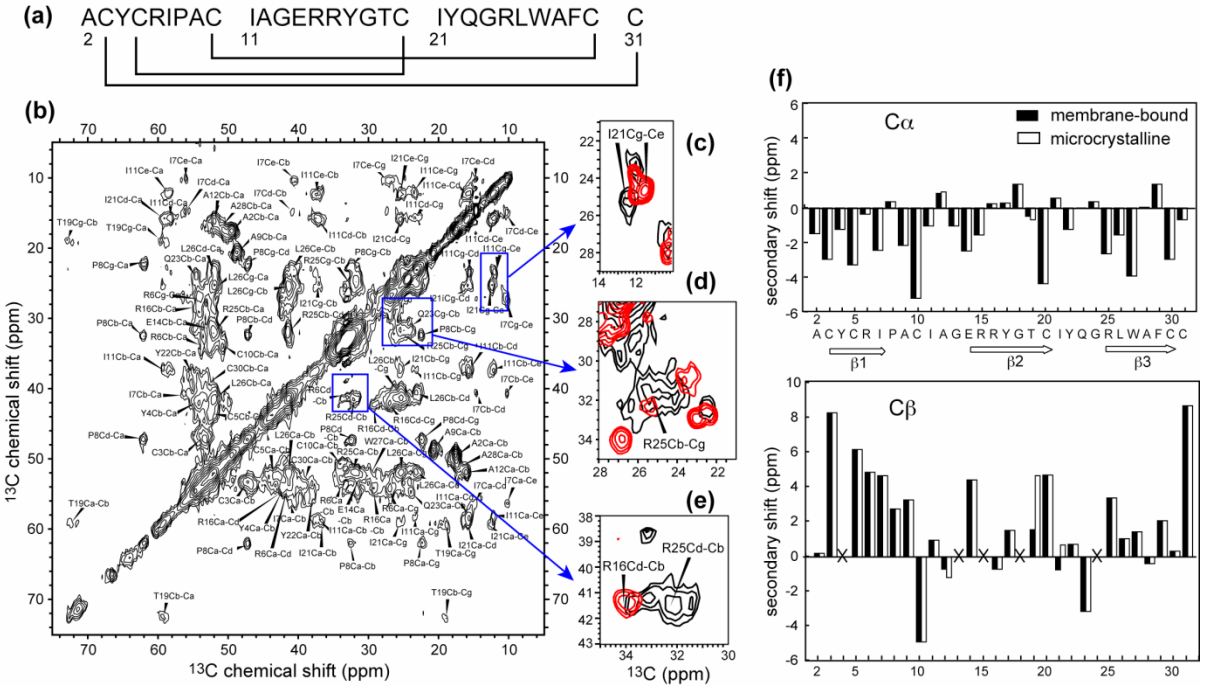

Figure 5.3. Resonance assignment of membrane-bound HNP-1 and conformational comparison with the microcrystalline protein. (a) Amino acid sequence of HNP-1. (b) 2D ^{13}C-^{13}C DARR spectrum of membrane-bound HNP-1 at 273 K with a mixing time of 40 ms. (c-e) Regions that show chemical shift changes between the membrane-bound (black) and microcrystalline (red) states. (c) I21 sidechain. (d) R25 sidechain. (e) R25 and R16 sidechains. Note the significant increase of the R25 sidechain intensities in the membrane-bound state in (d) and (e).

To better resolve the resonances, we measured 2D ^{13}C-^{13}C and ^{15}N-^{13}C correlation spectra. The 2D ^{13}C-^{13}C DARR spectrum at 40 ms mixing (**Figure 5.3b**) showed mostly intra-residue cross peaks, which could be readily assigned by comparison with the microcrystalline spectra [19]. 2D N(CO)CX and N(CA)CX spectra (**Figure S1**) further corroborated these assignments. Most residues exhibited similar chemical shifts in the membrane as in the microcrystalline form except for the sidechain peaks of I21 and R25. The I21 Cγ and Cε peaks moved downfield from the microcrystalline state: the Cγ chemical shift increased from 24.6 ppm to 25.5 ppm while the Cε peak moved from 11.5 ppm to 12.4 ppm (**Figure 5.3c**). In the microcrystalline state, the R25 sidechain resonances were not visible in the 2D ^{13}C-^{13}C spectrum and were much weaker than the

R6 and R16 signals in the 3D NCC spectra [19]. In the membrane-bound state, however, the R25 sidechain resonances became much stronger, with clear Cβ-Cγ and Cδ-Cβ cross peaks (**Figure 5.3d, e**). I21 and R25 are both located in the β2-β3 turn at the hydrophobic base of the dimer (**Figure 5.1a**). This turn was seen in the HNP-3 crystal structure to deviate significantly from crystallographic symmetry and was thought to exhibit flexing motions [12]. Thus, the membrane-induced conformational and dynamical changes of I21 and R25 sidechains are likely significant, and may reflect site-specific interactions of this β2-β3 turn with lipids (see below). **Figure 5.3f** shows the Cα and Cβ secondary chemical shifts [42] of HNP-1 for both the membrane-bound and microcrystalline states, confirming the three β-strand motifs of the protein and the similarity of the protein confirmation without and with the lipids. The Y17-G18 junction in the middle of the β2 strand deviates from the ideal β-sheet conformation, as noted before [19], and may reflect the role of G18 as a hinge for the β2-β3 hairpin [13].

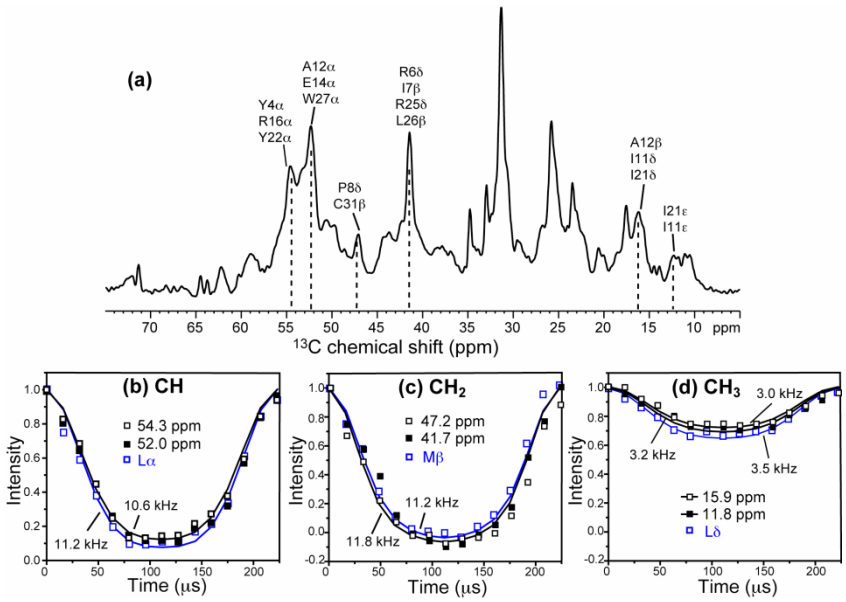

Figure 5.4. ^{13}C-^{1}H dipolar couplings of DMPC/DMPG-bound HNP-1 at 303 K under 4.5 kHz MAS. (a) ^{13}C chemical shift dimension of the 2D spectrum. (b) C-H dipolar coupling curves of two Cα cross sections and their best-fit, compared with the Leu Cα data of f-MLF. (c) C-H dipolar coupling curves of two CH_2 peaks and their best-fit, compared with the Met Cβ data of f-MLF. (d) C-H dipolar coupling curves of two CH_3 cross sections and their best-fit simulations at 3.0 and 3.2 kHz, compared to the Leu Cδ signal of f-MLF. All coupling indicated are fit values,

and convert to true couplings after they are divided by the homonuclear decoupling scaling factor.

To evaluate the mobility of membrane-bound HNP-1 more quantitatively, we measured the ^{13}C-^{1}H dipolar couplings using the 2D DIPSHIFT experiment. **Figure 5.4** shows the ^{13}C chemical shift dimension of the 2D spectrum, with partial resolution of the sites. Several dipolar cross sections representing the backbone Cα-Hα, sidechain CH_2 and CH_3 groups are shown. We found rigid-limit S_{CH}'s of 0.95–1.05 for Cα and methylene groups, while the methyl groups of Ile and Ala exhibited S_{CH} values of 0.26-0.28. Since methyl three-site jumps alone give an order parameter of 0.33, the small degree of additional scaling (0.78-0.85) indicates that other torsional degrees of freedom in the aliphatic sidechains of these residues are insignificant. Thus the DIPSHIFT data is consistent with the temperature-independent ^{13}C spectra in supporting that HNP-1 is largely immobilized in the liquid-crystalline phase of the bilayer, with only a moderate amount of sidechain motion. This finding is not only consistent with the conformational rigidity of this disulfide-bonded protein, but more importantly indicates that HNP-1 is not monomeric in the membrane. If the protein were monomeric, the small molecular weight would give rise to fast whole-body uniaxial diffusion of the protein in the membrane, as observed in many small to medium membrane proteins with molecule weights up to several tens of kDa [43-47]. Since all HNPs form dimers in the crystal [12,13,48], the immobilization suggests that when bound to the membrane, HNP-1 is at least dimeric and may form even higher-order oligomers.

Depth of insertion of HNP-1 from lipid-protein ^{1}H spin diffusion

To determine the insertion motif of HNP-1, we carried out a 2D ^{13}C-detected ^{1}H spin diffusion experiment [36]. The experiment measures inter-proton distances from the mobile water and lipid acyl chains to the rigid protein through distance-dependent ^{1}H magnetization transfer. TM proteins in contact with both the membrane surface and the hydrocarbon core exhibit fast ^{1}H spin diffusion from both lipid chains and water [37], while surface-bound proteins have much slower ^{1}H spin diffusion from the lipid chains.

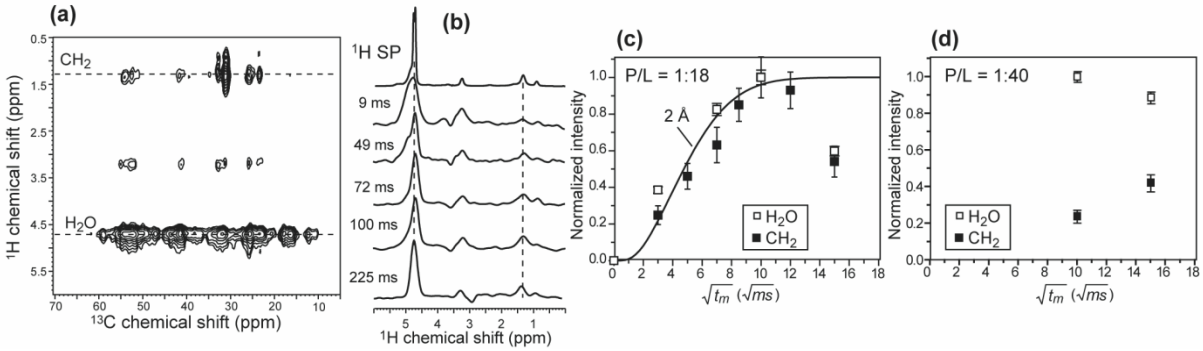

Figure 5.5. ^{1}H spin diffusion from lipid chains and water to HNP-1 in DMPC/DMPG bilayers. (a) Representative 2D spectrum for P/L = 1:18 at 303 K, at a ^{1}H mixing time of 100 ms. (b) Integrated ^{1}H cross sections from ^{13}C chemical shifts of 63 - 37 ppm as a function of ^{1}H mixing times, compared with the 1D ^{1}H spectrum at the top. (c) ^{1}H spin diffusion buildup curves for lipid CH_2 and water at P/L=1:18. (d) ^{1}H spin diffusion intensities for lipid CH_2 and water at P/L=1:40. The CH_2 buildup is much slower at the lower protein concentration.

Figure 5.5 shows the ^{1}H spin diffusion data of membrane-bound HNP-1 (P/L = 1:18) at 305 K. A representative 2D spectrum (^{1}H mixing time 100 ms) shows the characteristic cross peaks between the protein ^{13}C signals (63 – 37 ppm) and the lipid CH_2 protons at 1.3 ppm, indicating that HNP-1 is within spin diffusion reach of the acyl chains. Strong water-protein cross peaks were also observed. To quantify the distances, we measured the 2D spectra as a function of ^{1}H spin diffusion mixing time. **Figure 5.5b** shows the integrated ^{1}H cross sections for ^{13}C chemical shifts of 63–37 ppm for mixing times of 9 to 225 ms. After correcting for ^{1}H T_1 relaxation of the water and lipid CH_2 protons, we plotted the cross-peak intensities as a function of the square root of the mixing time. **Figure 5.5c** shows that both the water and lipid cross peaks with the protein reached a plateau by 100 ms, qualitatively indicating that HNP-1 is in close contact with both the hydrophobic core of the membrane and water. The equilibration allows both the water and lipid cross peaks to be normalized with respect to their own maximum intensities at 100 ms.

We simulated the CH_2 buildup curve using a 1D lattice model to obtain the minimum lipid-protein separation. In this model, ^{1}H magnetization (M_i) transfer was modeled as a discrete process along the bilayer normal [49]. The transfer rate, $\Omega = D/a^2$,

depends on the lattice spacing *a*, fixed at 2 Å, and the diffusion coefficients of the various membrane components. Based on previous calibrations we used diffusion coefficients of 0.012 nm^2/ms for lipids (D_L), 0.03 nm^2/ms for water (D_W) and 0.3 nm^2/ms for the protein (D_P) [24,36,50]. For the interfacial D_{LP} between the lipid and the protein, we used a value of 0.0025 nm^2/ms, which was within the range reported before [24,36,50]. The simulation yields the minimum lipid-protein or water-protein distances because once ^1H magnetization crosses the interface from the soft lipid matrix (or water) to the nearest protein residues, it is rapidly equilibrated within the immobilized protein. The lack of site specificity allowed us to use the integrated intensities for the protein ^{13}C signals to obtain global information about the depth of insertion of HNP-1. **Figure 5.5c** shows that the CH_2 buildup curve for the P/L=1:18 sample was best fit to a distance of 2 Å, indicating that HNP-1 was well inserted into the hydrophobic region of the DMPC/DMPG bilayer, in immediate contact with the acyl chains. This close proximity rules out the surface-bound wedge model (**Figure 5.1b**): if the basket-shaped dimer is exposed to the aqueous phase to any significant extent, for example one third of its 18 Å height, then the membrane-immersed part of the protein would be ~12 Å, which would make the protein mostly outside the hydrophobic region of the bilayer.

Some antimicrobial peptides have been found to exhibit concentration-dependent interactions with the lipid bilayer: at low concentrations they bind to the surface of the lipid membrane while at high concentrations they insert into the membrane [51,52]. To determine whether the depth of insertion of HNP-1 changes with its concentration, we measured the ^1H spin diffusion spectra of a P/L = 1:40 sample. We measured two mixing times, 100 ms and 225 ms, which were sufficiently long to give equilibrium intensities for the 1:18 sample. The lipid-protein cross peaks at 225 ms were clearly higher than at 100 ms after taking ^1H T_1 relaxation into account, indicating that the CH_2 cross peaks had not plateaued by 225 ms. To obtain the correct normalization, we scaled the CH_2 cross-peak intensities with the water cross-peak intensities in the 100 ms spectrum, since the water intensities were already equilibrated at 100 ms (**Figure 5.5d**), consistent with all membrane proteins studied so far [53-55]. This ratio was further scaled by the equilibrium intensity ratio (0.61) between the CH_2 peak and the water peak in the 1D ^1H

spectrum:

$$I_{CH_2}^{norm}(t_m) = \frac{I_{CH_2}^{obs}(t_m)\, e^{+t_m/T_{1,CH_2}}}{\left(I_{H_2O}^{obs,100ms} \cdot e^{+t_m/T_{1,H_2O}}\right)\left(I_{CH_2}^{eq} / I_{H_2O}^{eq}\right)} \quad (1)$$

The normalized CH_2 intensities at P/L = 1:40 are significantly lower than those of the 1:18 sample, indicating that HNP-1 is more shallowly inserted at lower protein concentrations. Thus, HNP-1 has similar concentration-dependent insertion motifs to several other antimicrobial peptides such as protegrin-1 [51,52].

Membrane topology of HNP-1 from ^{13}C-^{31}P distances

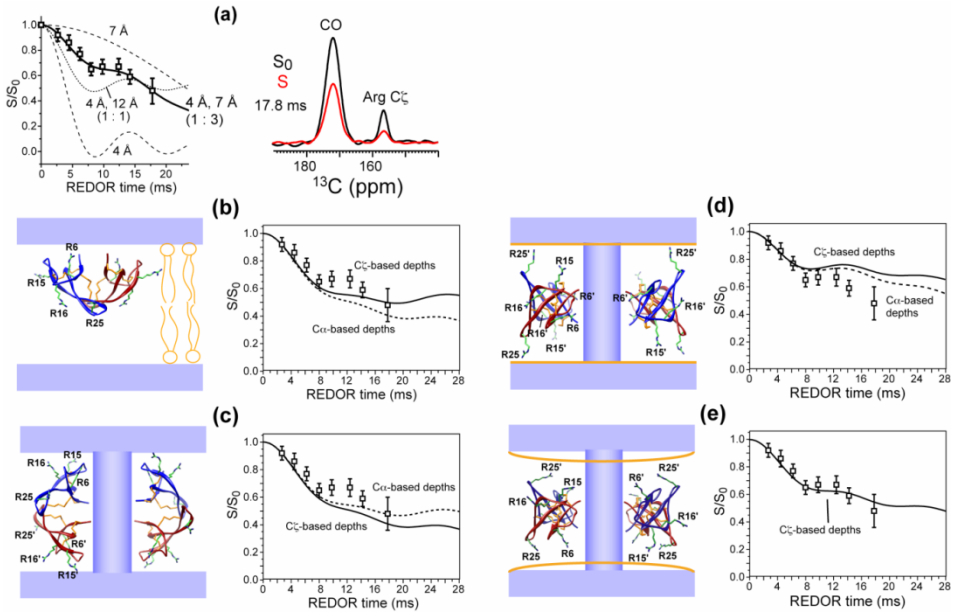

Figure 5.6. Arg Cζ-^{31}P distances of HNP-1 in DMPC/DMPG bilayers. (a) Cζ ^{13}C-^{31}P REDOR S/S_0 values as a function of mixing time and representative S_0 and S spectra. Best-fit simulation used a 1:3 combination of a 4 Å distance and a 7 Å distance. (b)-(e) Solid lines represent REDOR simulations using Cζ-P distances based on the vertical distance differences among the four Arg Cζ atoms. Dashed lines represent simulations based on the Arg Cα vertical distance differences. (b) Membrane-immersed wedge model and the best-fit Arg Cζ-P REDOR curve. Simulated curves decay faster than the experimental data. (c) General pore model and the best-fit Cζ-P curves, which decay faster than the measured data. (d-e) Simulation of the Arg Cζ-P REDOR data

using the dimer pore model. (d) Dimer pore model based on the crystal structure of HNP-3 and a 35 Å bilayer thickness. The simulated Cζ-P REDOR curves decay slower than the experimental data. (e) Dimer pore model after adjusting the Arg sidechain rotameric states (Table 1) and using a 30-Å membrane thickness. The calculated Cζ-P curve fits the data very well.

We also investigated the membrane topology of HNP-1 by measuring ^{13}C-^{31}P distances between the Arg residues and the lipid headgroups. The well resolved Arg Cζ signal at 157 ppm provides a site-specific probe of the interaction of the four Arg's with the lipid phosphates. **Figure 5.6a** shows the normalized Cζ intensities, S/S_0, as a function of REDOR mixing time. The intensities decayed quickly to 0.67 in the first 10 ms, then more slowly to ~0.5 by 18 ms. The bimodal decay cannot be fit to a single distance, but to a short distance of 4 Å for the initial fast regime and three longer distances of ~7 Å for the long-time regime. The weighting factor of 1 : 3 reflects the intensity plateau at 0.67 between 8 ms and 14 ms. Thus, the data suggests that one out of four guanidinium ions forms tight H-bonded complexes with the lipid phosphates, while the other Arg's are more distant.

Table 5.1. Arg Cζ distances to lipid ^{31}P (R_{CP}, Å) in various topology models of HNPs in lipid bilayers.

Residue[1]	Original HNP-3 structure [2] 35 Å bilayer thickness				Arg-modified structure, 30 Å bilayer thickness	
	Rotamer	R_{CP}, wedge	R_{CP}, general pore	R_{CP}, dimer pore	Rotamer	R_{CP}, dimer pore
R6	mmt180 [3] mtt-85	4	7	15	tpt180	9
R15	mtt180	6	4	8	mtt85	6.5
R16	ttt180	16	6	16	ptt85	10
R25	mtt-85	18	15	4	ttt180	4

[1.] Each residue in principle has four distances to the membrane surfaces due to the dimer state and two bilayer surfaces. Tabulated here is the shortest distance, which is the one relevant for the ^{13}C-^{31}P distance experiment.

[2.] The crystal structure of HNP-3 was used to model the dimer pore [12], since the NMR structure is for the HNP-1 monomer and has lower resolution for the sidechains.

[3.] The symbols m, t, p indicate -60˚, 180˚, and +60˚, respectively, for the consecutive χ torsion angles from the backbone [56].

We now consider the compatibility of the various membrane topological models of HNP-1 with the Arg Cζ-P distances. In the fully immersed wedge model (**Figure 5.6b, 1c**), R6 and R15 are closest to the membrane surface, with their Cζ depths differing by only ~2 Å when the axis of the basket-shaped dimer is oriented parallel to the bilayer normal (**Table 5.1**) [12]. Thus, if R6 Cζ is 4 Å away from ^{31}P, then R15 Cζ should be about 6 Å away. Using this approach, we estimated all four Cζ-P distances for the immersed wedge model (**Table 5.1**) and simulated the resulting REDOR curve. **Figure 5.6b** shows that the simulated REDOR curve decays faster than the experimental intensities, especially in the 8 – 14 ms regime.

Since Arg residues have multiple rotameric states with similar energetic stabilities [56] and the lipid bilayer is expected to exert a strong influence to Arg sidechain conformation through salt bridge interaction [39,57], the Arg sidechains may adopt different conformations in the membrane than found in the crystal. However, any rotamer differences should shorten the Cζ-P distances and speed up the dipolar dephasing, rather than slowing down the dephasing, which would be required to fit the experimental data. When the four Cζ-P distances were estimated based on the relative positions of the four Arg backbone Cα atoms to eliminate sidechain conformational effects, the simulated REDOR curve (dashed line) (**Figure 5.6b**) still decayed too fast compared to the observed data.

In the general pore model (**Figure 5.6c, Figure 5.1e**), more than one Arg sidechain was close to the ^{31}P atoms. Specifically, R6, R15, and R16, all have similar Cζ depths based on the crystal structure (**Table 5.1**) [12]. Keeping the least inserted R15 Cζ-P distance at 4 Å, as constrained by the REDOR data, we obtain R16 and R6 Cζ-P distances of ~6 and 7 Å. The resulting REDOR curve again decays faster than the measured data, and cannot be remedied by changing the sidechain conformation.

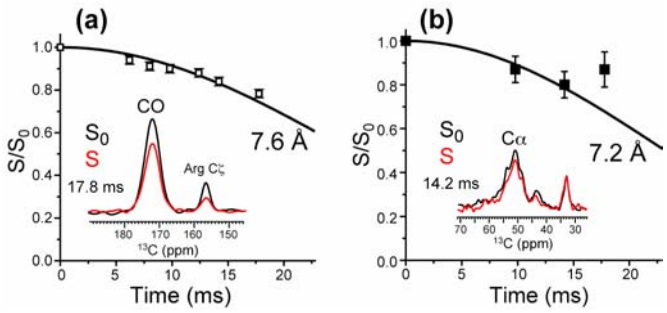

Figure 5.7. ^{13}C-^{31}P REDOR dephasing of backbone CO and Cα of membrane-bound HNP-1. (a) CO peak. (b) Cα peak. Best-fit curves represent average two-spin distances.

Finally, we considered the dimer pore model, where the dimer orientation was rotated by 90˚ from that of the general pore model (**Figure 5.6d, Figure 5.1d**). Here the situation is qualitatively different: R25 is now closest to the membrane surface, with the next nearest Arg, R15 in the other monomer, ~4 Å deeper in the membrane. Using the rotamers in the HNP-3 structure, we found the simulated curve to now decay more slowly than the measured data (**Figure 5.6d**), thus allowing us to modify the sidechain conformations to minimize the Cζ-P distances. In addition, ^{13}CO-^{31}P and $^{13}C\alpha$-^{31}P REDOR data suggested a slight membrane thinning from 35 Å to 30 Å (**Figure 5.7**). Combining these two changes, we obtained Arg rotamers that gave Cζ-P distances of 4, 6.5, 9, and 10 Å (**Table 5.1)**, which gave excellent fit to the experimental data (**Figure 5.6e**). Moreover, R25, the residue with the shortest Cζ-P distance, is also the residue showing significant immobilization upon membrane binding (**Figure 5.3**). Thus, the conformational changes also support the dimer pore topology of HNP-1.

Backbone CO and Cα distances to ^{31}P are consistent with the Arg Cζ REDOR data. Both signals decay slowly, with average S/S_0 values of ~0.8 at 14 ms. Simulations yielded best-fit average distances of 7.6 Å for CO and 7.2 Å for Cα. Since no site resolution was attempted, we added the REDOR dephasing of every CO and Cα atoms in each structural model based on their distances to the membrane surface. **Figure S2** shows the distance distribution for the dimer pore model, where the shortest distance to ^{31}P was fixed at 4 Å. The simulated REDOR curves fit the measured dephasing well. In reaching this agreement, it was necessary to thin the membrane to 30 Å, suggesting that HNP-1

insertion slightly reduces the bilayer thickness. Although the backbone ^{13}C-^{31}P REDOR did not exclude the other structural models, it was consistent with the dimer pore structure. In addition, the ^{13}CO-^{31}P REDOR data verified that HNP-1 was inserted into the gel-phase membrane, since simulations using a surface-bound wedge model were inconsistent with the experimental result (**Figure S3**).

Residue-specific water-protein distances

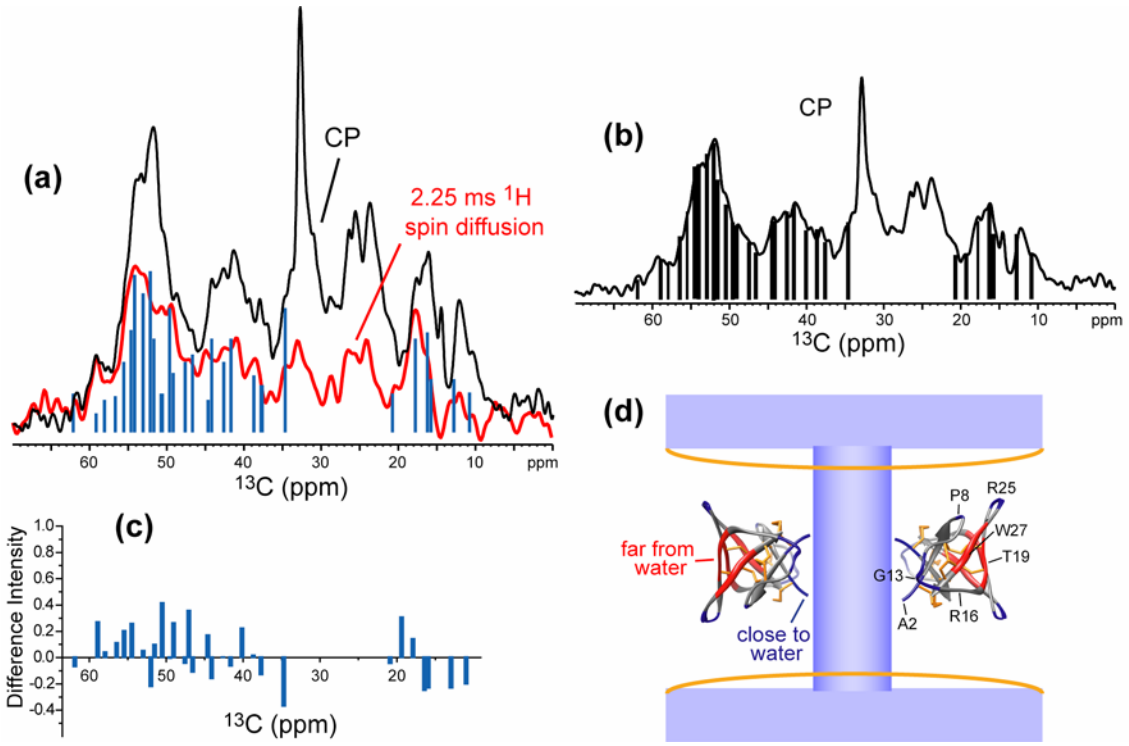

Figure 5.8. Water-protein ^{1}H spin diffusion to determine the membrane topology of HNP-1. (a) ^{13}C spectrum after 2.25 ms ^{1}H spin diffusion from water (red), superimposed with the ^{13}C CP spectrum (black). Simulated stick spectrum based on the dimer pore model is shown in blue. (b) ^{13}C CP spectrum and simulation to fix the CP weighting factors. (c) Difference between the experimental and simulated water-edited spectrum from (a). (d) Dimer pore model, where residues close to water are shown in blue, interfacial residues in gray, and residues far from water in red. The respective intensity weighting factors are 1, 0.55 and 0.1.

To complement the topology information from the lipid-to-protein spin diffusion experiment, we examined the water-to-protein ^{1}H spin diffusion profile at the short

mixing time of 2.2 ms, when the ^{1}H spin diffusion from water to the protein has not fully equilibrated in the protein, thus giving site-specific information about residue distances to water. **Figure 5.8a** shows the water-edited ^{13}C spectrum (red) extracted from the water ^{1}H cross section of the 2D spectrum. This water-edited spectrum was superimposed with the ^{13}C CP spectrum, which reflects the equilibrium ^{13}C magnetization. The two spectra were scaled such that the water-edited spectral intensities at most equaled but not exceeded the CP intensities. It can be seen that the intensity distribution of the water-edited spectrum is clearly different from that of the CP spectrum due to the selectivity of the water-to-protein spin diffusion at this short time. For example, the lipid chain signals from 32.5 ppm to 22 ppm were much attenuated, as expected because of the immiscibility of water with the hydrocarbon core. The protein signals in the 53-40 ppm region, which mainly result from Cα and Cβ, were also reduced relative to the Cα intensities in the 60-55 ppm range.

To simulate the water-edited ^{13}C spectrum, we first reproduced the equilibrium CP spectrum by using appropriate weighting factors for each carbon. These weighting factors accounted for different CP dynamics of CH_n (n=1, 2,3) groups and the different mobilities between the backbone and sidechains (**Figure 5.8b**). Next, we assigned each carbon a spin-diffusion weighting factor based on the proximity of each site to water on the membrane surface and water in the pore. Both the crystal structure of HNP-3 [12] and the solid-state NMR structure of HNP-1 [19] were considered in estimating the carbon-water distances, and the simulation was insensitive to the exact starting structure. Three categories of spin diffusion weighting factors were used. Carbons close to water were given a weighting factor of 1, while those far from water a weighting factor of 0.1. Residues in the middle were assigned a weighting factor of 0.55. Combining the water-proximity weighting factors with the CP weighting factors, we simulated the water-edited spectrum expected for the dimer pore topology. **Figure 5.8a** shows that the simulated stick spectrum is in good agreement with the measured spectrum. The RMSD difference between the two was 0.22 as normalized to the 54-ppm peak intensity (**Figure 5.8c**), comparable to the experimental noise of 0.18, indicating that the measured spectrum is consistent with the dimer pore topology. We did not consider the 33 – 22 ppm region in

the simulation due to significant overlap between the lipid and protein signals in this region. The use of the solid-state NMR structure for the choice of spin diffusion weighting factors did not affect the good fit (**Figure S4**).

Oligomeric structure of HNP-1 in the lipid membrane

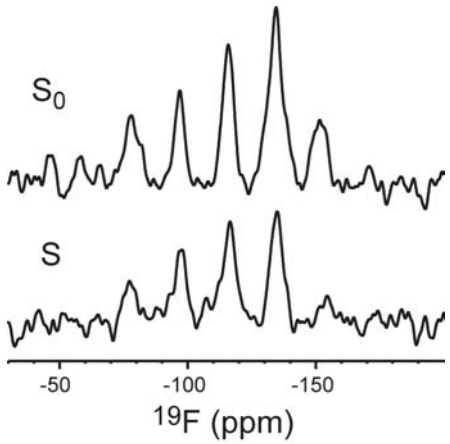

Figure 5.9. ^{19}F CODEX control (S_0) and dephased (S) spectra of 4-^{19}F-Phg$_4$-labeled HNP-1 in DMPC/DMPG (3:1) membranes at P/L=1:18. The mixing time was 1 s. The S/S_0 value was 0.66 ±0.06.

So far we have assumed that HNP-1 assembles into a basic unit of dimers in the membrane, upon which loose higher-order oligomers may form. Although the immobilization result supports this assumption, we further verified this hypothesis using the ^{19}F CODEX experiment. The experiment detects ^{19}F magnetization exchange between orientationally different singly fluorinated proteins. The oligomeric number *n* is obtained from the CODEX echo intensity at long mixing times, which is 1/*n*. We substituted Tyr4 in the β1 strand by 4-^{19}F-Phg, since crystal structures suggest this residue to lie in the dimer interface, with inter-monomer distances of less than 10 Å (PDB codes: 1DFN, 3HJ2). **Figure 5.9** shows the ^{19}F CODEX control (S_0) and exchange (S) spectra of HNP-1 in DMPC/DMPG membranes (P/L = 1:18) at a mixing time of 1 s. The S/S_0 value was 0.66 ± 0.06 and was the same between 1 s and 500 ms within experimental uncertainty, indicating that intermolecular spin diffusion has equilibrated. The slightly larger than 0.5 final value indicates that the majority (66%) of ^{19}F-labeled Tyr$_4$ exists in a dimer state (*n*

= 2) while the rest (33%) has ^{19}F-^{19}F distances greater than ~15 Å. Thus, at a protein concentration of about 5 mol% in the membrane, the majority of HNP-1 is tightly dimerized, while the rest either exists in a monomer state or forms loose dimers with Tyr4 separations greater than the upper limit of this ^{19}F spin diffusion technique.

Discussion

Evidence of pore formation by HNPs in lipid membranes from biochemical data

Since the discovery of human α-defensins [3,4], many antimicrobial assays, lipid vesicle experiments, and high-resolution structures have been reported to understand the mechanisms of action of these host-defense proteins [1,58]. Similar to smaller β-hairpin antimicrobial peptides, bactericidal activity by HNPs followed inner membrane permeabilization [59]. Dye release and fluorescence spectroscopy experiments found that HNP-1 caused both fusion and lysis of negatively charged lipid vesicles through electrostatic interactions [60]. For rabbit neutrophil defensins, vesicle leakage depends on the membrane composition: it is all-or-none for whole *E. coli* lipids but graded for POPG vesicles [61]. Electron micrographs of human parasite cells *Trypanosoma cruzi* in the presence of micromolar concentrations of HNP-1 showed distinct 25-nm sized pores in the cellular and flagellar membranes [62], through which HNP-1 appears to enter the trypanosome cells, causing subsequent DNA fragmentation and cell destruction. Vesicle leakage experiments also showed that HNP-induced pores increase with the concentration of the anionic lipid [63]. These biochemical studies all indicated that human α-defensins cause pore formation in anionic lipid membranes. However, the molecular structure and topology of HNP-1 at the pore and the type of lipid disorder has remained elusive.

Structural constraints on HNP-1-induced pores in anionic lipid membranes

The ^{1}H spin diffusion, ^{13}C-^{31}P REDOR, and ^{19}F CODEX results combined to give the following constraints to HNP-1 structure in the anionic lipid membrane. At high protein concentrations of P/L = 1:18, HNP-1 fully spans the membrane and contacts the hydrophobic chains. Among the four Arg's, one Arg forms hydrogen-bonded complexes with the lipid phosphates. This Arg is most likely R25 in the β2-β3 turn, because its

signal was enhanced in the 2D correlation spectra by lipid-induced immobilization. The DMPC/DMPG bilayer is thinned slightly upon HNP-1 binding. Seen at Tyr_4, the majority of the protein is at least dimerized at P/L = 1:18. These observations support the dimer pore model for HNP-1 in the membrane. The fully immersed wedge model and the general pore model would place R25 to be the furthest Arg residue from the membrane surface, which is inconsistent with the 2D ^{13}C spectra, because the center of the hydrocarbon region is the most fluid region of the bilayer and should not immobilize R25. The depth distribution of the four Arg sidechains in the fully immersed wedge model and general pore model also do not agree with the stoichiometry that only one Arg Cζ is H-bonded to the lipid phosphates. The data also rule out a surface-bound wedge model where the polar basket top is significantly exposed to water, since it does not agree with the fast ^{1}H spin diffusion from the lipid chains to the protein. In the multimeric pore model, the Arg backbones lie at roughly the same depths in each lipid leaflet, with the two Cα rings separated by ~16 Å. Thus, the Cζ atoms are expected to be similarly close to the membrane surface ^{31}P, which does not agree well with the distance distribution of the Cζ-P REDOR data. At lower protein concentrations (P/L=1:40), HNP-1 is less inserted into the membrane, as seen in the slower lipid-protein ^{1}H spin diffusion. Although sensitivity limitations preclude the determination of the exact topology, it is reasonable to expect the surface-bound wedge model to be the most likely scenario.

In model-specific fitting of the various experimental data, we primarily used the crystal structure of HNP-3 (PDB: 1DFN) because the solid-state NMR structure [19] (PDB: 2KHT) is that of the monomer, with no direct intermolecular constraints for the dimer. Nevertheless, **Figure S4** shows that the hypothetical dimer NMR structure would give similar conclusions as the HNP-3 crystal structure for the water-edited ^{13}C spectrum, suggesting that the exact input structure does not affect the conclusion of the global topology of HNP-1.

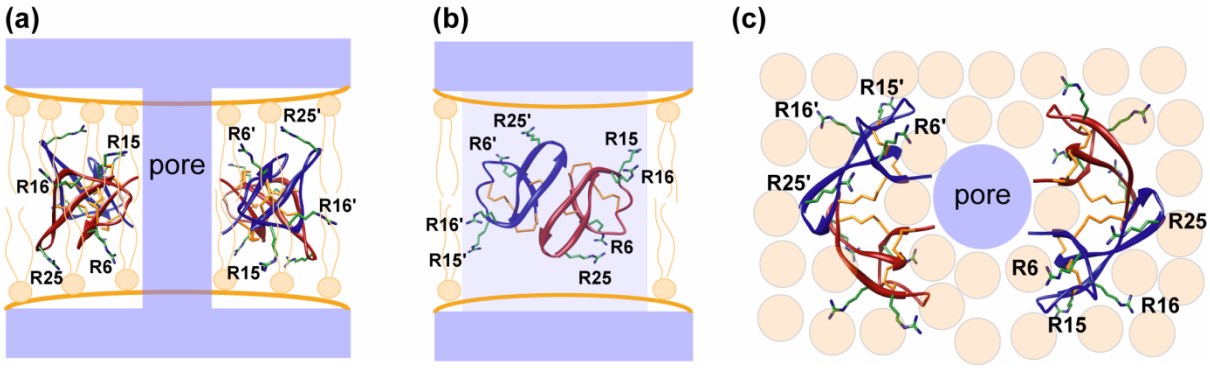

Figure 5.10. Membrane topology of HNP-1 in anionic lipid bilayers. At high protein concentrations HNP-1 is mostly dimerized and spans the membrane, lining a central water pore. The R25 sidechain lies closest to the membrane surface interacting with the phosphate groups. The lipid chains near the pore do not exhibit significant orientational disorder. (a) Side view. (b) Side view with the pore behind one dimer. (c) Top view. The distances between the two dimers and the total oligomeric number of the assembly are not probed by the experiments reported here.

Taken together, the solid-state NMR data support the dimer pore topology, where HNP-1 dimers span the membrane with the R25-containing β2- β3 turn pointing at the membrane surfaces (**Figure 5.10**). When water on the membrane surface and in the pore is both considered, the dimer pore topology reproduces the observed water-edited protein ^{13}C spectrum. The orientation and depth of each dimer is well constrained by the NMR data, and the ^{19}F CODEX data supports the dimerization of the majority of the protein. The small fraction of monomers is likely related to the observed shallower insertion of the protein at lower concentrations, and suggests that concentration-dependent oligomerization may be important for the membrane-disruptive activity of HNP-1.

Does the dimer pore mechanism of HNP-1 apply to other human α-defensins? Comparisons of the activities and specificities of the six human α-defensins indicate that their interactions with lipid membranes are diverse. Against Gram-positive *S. aureus,* the relative potencies were HNP-2 > HNP-1 > HNP-3 > HNP-4, while the relative potencies against the Gram-negative *E. coli* were HNP-4 > HNP-2 > HNP-1 = HNP-3 [8]. Among HNP 1, 2, and 3, whose amino acid sequences differ only in their N-terminal residue, HNP-3, which possesses an N-terminal polar residue Asp, has weaker activities than

HNP-1 and HNP-2, which have a hydrophobic residue at the N-terminus [5,8]. Consistently, acetylation and amidation of HNP-2 to remove the terminal charges modulated the protein's antimicrobial activity and vesicle leakage [64]. Thus, the positive charge density and charge distribution have a significant effect on the membrane interaction of HNPs. In comparison, HD5 and HD6, which are found in intestinal epithelial cells, have much lower sequence homologies to HNPs [6,7]. HD6 has nearly two orders of magnitude weaker activities than the HNPs [8], while HD5, while localized on the cell membrane, was suggested to possibly interact with the cells in a receptor-mediated fashion [65]. Based on the high sequence homology and functional similarity between HNP-1 and HNP-2, we speculate that the dimer pore mechanism may apply to HNP-2 and should be relevant to HNP-3 as well, but the other defensins in this family may adopt different orientations and depths of insertion in the lipid membrane.

Comparison of HNP-1 with small β-hairpin antimicrobial peptides

Our previous studies of the two-stranded disulfide-bonded β-hairpin antimicrobial peptide, PG-1, indicated that the strong interactions between Arg guanidinium ions and the lipid phosphate groups drove the formation of toroidal pore defects in the membrane, where PG-1 lines the pore as a TM β-barrel [24,39,55]. When the guanidinium ions were dimethylated, the mutant showed 3-fold weaker antimicrobial activities and no longer formed large β-barrels in the membrane [66]. A PG-1 mutant with only half the number of Arg residues inserted only partially into the anionic membrane and exhibited much weaker interactions with the lipid headgroups [50]. Guanidinium-phosphate interactions were also observed in Arg-rich cell-penetrating peptides, penetratin [67] and the HIV TAT peptide [68]. In HNP-1, although only one guanidinium group is within H-bonding distance to the lipid phosphates, the average distance for the other three Arg residues is 7 Å, which is short compared to the bilayer thickness (**Figure 5.6a**). Lu and coworkers have shown by mutagenesis that when three of the four Arg's were converted to Lys, HNP-1 activity was significantly weakened, and the effect was more pronounced against the Gram-positive *S. aureus* than the Gram-negative *E. coli* [69].

It is interesting that no isotropic peak was observed in the ^{31}P NMR spectra,

indicating that high-curvature defects such as micelles or toroidal pores were absent in the HNP-bound DMPC/DMPG membrane (**Figure 5.2**). Thus, in the DMPC/DMPG membrane, the HNP-1 dimer pores exist in regular lamellar bilayers, consistent with the classical barrel-stave model. The retention of the bilayer integrity contrasts with the behavior of PG-1, which caused substantial membrane disorder to phosphocholine (PC)/phosphatidylglycerol (PG) membranes as well as phosphatidylethanolamine (PE)/PG membranes. The HNP-1 interaction with the DMPC/DMPG membrane is more akin to that of tachyplesins [70] and a synthetic antimicrobial arylamide [71], which did not disrupt PC/PG membranes. However, tachyplesin-1 caused clear disruption to the PE/PG membrane [70]. The extent of membrane disorder depends on both the distribution of Arg residues in the protein sequence and the composition of the lipid membrane. It is possible that HNP-lipid interactions are sensitive to the membrane composition, similar to tachyplesins, so that while HNP-1 does not disrupt PC/PG membranes, it may disrupt PE/PG membranes. Similarly, an increased percentage of the negatively charged PG lipids may cause a large amount of membrane disorder. A study of rabbit neutrophil defensins suggested that the presence of PE and cardiolipin lipids increased the membrane disruption [61]. Given the increased complexity of HNPs over two-stranded β-hairpin antimicrobial peptides, structural investigations as a function of membrane composition will be useful to further elucidate the membrane interaction and mechanism of action of this class of defensins. Finally, the precise antimicrobial mechanism of HNP-1 in vivo may depend on factors other than HNP-phospholipid interaction. It was recently reported that HNP-1 activity correlates with the amount of lipid II, a bacterial cell wall precursor [63]: inhibition of lipid II synthesis weakened the HNP-1 antibacterial activity. This result suggests that interaction of cell wall components with HNP to be involved in the antimicrobial action of HNPs, and may explain why D-amino-acid analogs of HNPs were found to have weaker bactericidal activities but similar membrane-disruptive abilities compared to their L-amino acid counterparts. Thus, the mechanism of action of HNPs, similar to nisin [72], may involve multiple targets in the bacteria. The dual mechanisms may also contribute to the lack of significant membrane disorder seen in the ^{31}P NMR spectra.

References

[1] Ganz, T., Defensins: antimicrobial peptides of innate immunity, Nat. Rev. Immunol. 3 (2003) 710-720.

[2] Xie, C.; Prahl, A.; Ericksen, B.; Wu, Z.; Zeng, P.; Li, X.; Lu, W.-Y.; Lubkowski, J.; Lu, W., Reconstruction of the Conserved Beta-Bulge in Mammalian Defensins Using D-Amino Acids, J. Biol. Chem. 280 (2005) 32921-32929.

[3] Selsted, M. E.; Harwig, S. S.; Ganz, T.; Schilling, J. W.; Lehrer, R. I., Primary structures of three human neutrophil defensins, J. Clin. Invest. 76 (1985) 1436-1439.

[4] Gabay, J. E.; Scott, R. W.; Campanelli, D.; Griffith, J.; Wilde, C.; Marra, M. N.; Seeger, M.; Nathan, C. F., Antibiotic proteins of human polymorphonuclear leukocytes, Proc. Natl. Acad. Sci. U. S. A. 86 (1989) 5610-5614.

[5] Ganz, T.; Selsted, M. E.; Szklarek, D.; Harwig, S. S.; Daher, K.; Bainton, D. F.; Lehrer, R. I., Defensins. Natural peptide antibiotics of human neutrophils, J. Clin. Invest. 76 (1985) 1427-1435.

[6] Jones, D. E.; Bevins, C. L., Defensin-6 mRNA in human Paneth cells: implications for antimicrobial peptides in host defense of the human bowel, FEBS Lett. 315 (1993) 187-192.

[7] Jones, D. E.; Bevins, C. L., Paneth cells of the human small intestine express an antimicrobial peptide gene, J. Biol. Chem. 267 (1992) 23216-23225.

[8] Ericksen, B.; Wu, Z.; Lu, W.; Lehrer, R. I., Antibacterial activity and specificity of the six human {alpha}-defensins, Antimicrob. Agents Chemother. 49 (2005) 269-275.

[9] Wu, Z.; Ericksen, B.; Tucker, K.; Lubkowski, J.; Lu, W., Synthesis and characterization of human alpha-defensins 4-6., J. Pept. Res. 64 (2004) 118-125.

[10] Lehrer, R. I., Ganz, T, Antimicrobial peptides in mammalian and insect host defence, Curr. Opin. Immunol. 11 (1999) 23.

[11] Kagan, B. L.; Selsted, M. E.; Ganz, T.; Lehrer, R. I., Antimicrobial defensin peptides form voltage-dependent ion-permeable channels in planar lipid bilayer membranes, Proc. Natl. Acad. Sci. U. S. A. 87 (1990) 210-214.

[12] Hill, C. P.; Yee, J.; Selsted, M. E.; Eisenberg, D., Crystal structure of defensin

HNP-3, an amphiphilic dimer: mechanisms of membrane permeabilization., Science 251 (1991) 1481-1485.

[13] Szyk, A.; Wu, Z.; Tucker, K.; Yang, D.; Lu, W.; Lubkowski, J., Crystal structures of human alpha-defensins HNP4, HD5, and HD6., Protein Sci. 15 (2006) 2749-2760.

[14] Wimley, W. C.; Selsted, M. E.; White, S. H., Interactions between human defensins and lipid bilayers: evidence for formation of multimeric pores, Protein Sci. 3 (1994) 1362-1373.

[15] Luo, W.; Yao, X. L.; Hong, M., Large Structure Rearrangement of Colicin Ia Channel Domain After Membrane Binding from 2D 13C Spin Diffusion NMR, J. Am. Chem. Soc. 127 (2005) 6402-6408.

[16] Huster, D.; Xiao, L. S.; Hong, M., Solid-State NMR Investigation of the dynamics of colicin Ia channel-forming domain, Biochemistry 40 (2001) 7662-7674.

[17] Huster, D.; Yao, X.; Jakes, K.; Hong, M., Conformational changes of colicin Ia channel-forming domain upon membrane binding: a solid-state NMR study, Biochim. Biophys. Acta 1561 (2002) 159-170.

[18] Li, S.; Zhang, Y.; Hong, M., 3D 13C-13C-13C correlation NMR for de novo distance determination of solid proteins and application to a human alpha defensin, J. Magn. Reson. 202 (2010) 203-210.

[19] Zhang, Y.; Doherty, T.; Li, J.; Lu, W.; Barinka, C.; Lubkowski, J.; Hong, M., Resonance assignment and three-dimensional structure determination of a human a-defensin, HNP-1, by solid-state NMR, J. Mol. Biol. 397 (2010) 408-422.

[20] Luo, W.; Hong, M., Determination of the oligomeric number and intermolecular distances of membrane protein assemblies by anisotropic 1H-driven spin diffusion NMR spectroscopy, J. Am. Chem. Soc. 128 (2006) 7242-7251.

[21] Luo, W.; Mani, R.; Hong, M., Sidechain conformation and gating of the M2 transmembrane peptide proton channel of influenza A virus from solid-state NMR, J. Phys. Chem. 111 (2007) 10825-10832.

[22] Pazgier, M., Lubkowski, J, Expression and purification of recombinant human alpha-defensins in Escherichia coli, Protein Expr. Purif. 49 (2006) 1-8.

[23] Wu, Z.; Powell, R.; Lu, W., Productive folding of human neutrophil alpha-defensins in vitro without the pro-peptide, J. Am. Chem. Soc. 125 (2003) 2402-2403.

[24] Mani, R.; Cady, S. D.; Tang, M.; Waring, A. J.; Lehrer, R. I.; Hong, M., Membrane-dependent oligomeric structure and pore formation of a b-hairpin antimicrobial peptide in lipid bilayers from solid-state NMR, Proc. Natl. Acad. Sci. USA 103 (2006) 16242-16247.

[25] Afonin, S.; Glaser, R. W.; Berditchevskaia, M.; Wadhwani, P.; Guhrs, K. H.; Mollmann, U.; Perner, A.; Ulrich, A. S., 4-fluorophenylglycine as a label for 19F NMR structure analysis of membrane-associated peptides, Chembiochem 4 (2003) 1151-1163.

[26] Zou, G.; de Leeuw, E.; Lubkowski, J.; Lu, W., Molecular determinants for the interaction of human neutrophil alpha defensin 1 with its propeptide, J. Mol. Biol. 381 (2008) 1281-1291.

[27] Takegoshi, K.; Nakamura, S.; Terao, T., ^{13}C - ^{1}H dipolar-assisted rotational resonance in magic-angle spinning NMR Chem. Phys. Lett 344 (2001) 631-637.

[28] Rienstra, C. M.; Hohwy, M.; Hong, M.; Griffin, R. G., 2D and 3D 15N-13C-13C NMR chemical shift correlation spectroscopy of solids: assignment of MAS spectra of peptides., Journal of the American Chemical Society 122 (2000) 10979-10990.

[29] Hong, M., Resonance Assignment of 13C/15N Labeled Proteins by Two- and Three-Dimensional Magic-Angle-Spinning NMR, Journal of Biomolecular NMR 15 (1999) 1-14.

[30] Baldus, M.; Petkova, A. T.; Herzfeld, J.; Griffin, R. G., Cross polarization in the tilted frame: assignment and spectral simplification in heteronuclear spin systems., Molecular Physics 95 (1998) 1197-1207.

[31] Munowitz, M. G.; Griffin, R. G.; Bodenhausen, G.; Huang, T. H., Two-dimensional rotational spin-echo NMR in solids: correlation of chemical shift and dipolar interactions, J. Am. Chem. Soc. 103 (1981) 2529-2533.

[32] Rhim, W.-K.; Elleman, D. D.; Vaughan, R. W., Analysis of multiple-pulse NMR in solids., J. Chem. Phys. 59 (1973) 3740-3749.

[33] Hong, M.; Griffin, R. G., Resonance Assignment for Solid Peptides by Dipolar-Mediated 13C/15N Correlation Solid-State NMR, J. Am. Chem. Soc. 120 (1998) 7113-7114.

[34] Rienstra, C.; Tucker-Kellogg, L.; Jaroniec, C.; Hohg, M.; Reif, B.; McMahon, M.; Tidor, B.; Lozano-Pérez, T.; Griffin, R., De novo determination of peptide structure with

solid-state magic-angle spinning NMR spectroscopy., Proc Natl Acad Sci U S A. 99 (2002) 10260-10265.

[35] Mehring, M. High Resolution NMR in Solids; Springer-Verlag: New York, 1983.

[36] Huster, D.; Yao, X. L.; Hong, M., Membrane protein topology probed by 1H spin diffusion from lipids using solid-state NMR spectroscopy, J. Am. Chem. Soc 124 (2002) 874-883.

[37] Kumashiro, K. K.; Schmidt-Rohr, K.; Murphy, O. J.; Ouellette, K. L.; Cramer, W. A.; Thompson, L. K., A novel tool for probing membrane protein structure: solid-state NMR with proton spin diffusion and X-nucleus detection, J. Am. Chem. Soc. 120 (1998) 5043-5051.

[38] Jaroniec, C. P.; Tounge, B. A.; Rienstra, C. M.; Herzfeld, J.; Griffin, R. G., Measurement of 13C-15N distances in uniformly 13C labeled biomolecules: J-decoupled REDOR, J. Am. Chem. Soc. 121 (1999) 10237-10238.

[39] Tang, M.; Waring, A. J.; Hong, M., Phosphate-Mediated Arginine Insertion into Lipid Membranes and Pore Formation by a Cationic Membrane Peptide from Solid-State NMR, J. Am. Chem. Soc 129 (2007) 11438-11446.

[40] deAzevedo, E. R.; Bonagamba, T. J.; Hu, W.; Schmidt-Rohr, K., Centerband-only detection of exchange: efficient analysis of dynamics in solids by NMR, J. Am. Chem. Soc. 121 (1999) 8411-8412.

[41] Buffy, J. J.; Waring, A. J.; Hong, M., Determination of Peptide Oligomerization in Lipid Membranes with Magic-Angle Spinning Spin Diffusion NMR, Journal of the American Chemical Society 127 (2005) 4477-4483.

[42] Wang, Y.; Jardetzky, O., Probability-based protein secondary structure identification using combined NMR chemical-shift data., Protein Sci. 11 (2002) 852-861.

[43] Cady, S. D.; Goodman, C.; C.Tatko; DeGrado, W. F.; Hong, M., Determining the orientation of uniaxially rotating membrane proteins using unoriented samples: a 2H, 13C, and 15N solid-state NMR investigation of the dynamics and orientation of a transmembrane helical bundle, J. Am. Chem. Soc. 129 (2007) 5719-5729.

[44] Hong, M.; Doherty, T., Orientation determination of membrane-disruptive proteins using powder samples and rotational diffusion: a simple solid-state NMR approach, Chem. Phys. Lett. 432 (2006) 296-300.

[45] Aisenbrey, C.; Bechinger, B., Investigations of polypeptide rotational diffusion in aligned membranes by 2H and 15N solid-state NMR spectroscopy, J. Am. Chem. Soc. 126 (2004) 16676-16683.

[46] Lewis, B. A.; Harbison, G. S.; Herzfeld, J.; Griffin, R. G., NMR structural analysis of a membrane protein: bacteriorhodopsin peptide backbone orientation and motion, Biochemistry 24 (1985) 4671-4679.

[47] Fares, C.; Qian, J.; Davis, J. H., Magic angle spinning and static oriented sample NMR studies of the relaxation in the rotating frame of membrane peptides, J. Chem. Phys. 122 (2005) 194908.

[48] Hoover, D.; R.K.; Blumenthal, R.; Puri, A.; Oppenheim, J.; Chertov, O.; Lubkowski, J., The structure of human beta-defensin-2 shows evidence of higher order oligomerization, J. Biol. Chem. 275 (2000) 32911-32918.

[49] Schmidt-Rohr, K.; Spiess, H. W. Multidimensional Solid-State NMR and Polymers; 1st ed.; Academic Press: San Diego, 1994.

[50] Tang, M.; Waring, A. J.; Hong, M., Effects of arginine density on the membrane-bound structure of a cationic antimicrobial peptide from solid-state NMR, Biochim. Biophys. Acta 1788 (2009) 514-521.

[51] Huang, H. W., Action of antimicrobial peptides: two-state model., Biochemistry 39 (2000) 8347-8352.

[52] Glaser, R. W.; Sachse, C.; Durr, U. H.; Wadhwani, P.; Afonin, S.; Strandberg, E.; Ulrich, A. S., Concentration-Dependent Realignment of the Antimicrobial Peptide PGLa in Lipid Membranes Observed by Solid-State 19F-NMR., Biophys. J. 88 (2005) 3392-3397.

[53] Hong, M., Structure, topology, and dynamics of membrane peptides and proteins from solid-state NMR spectroscopy, J. Phys. Chem. B. 111 (2007) 10340-10351.

[54] Hong, M., Oligomeric structure, dynamics, and orientation of membrane proteins from solid-state NMR, Structure 14 (2006) 1731-1740.

[55] Tang, M.; Hong, M., Structure and mechanism of beta-hairpin antimicrobial peptides in lipid bilayers from solid-state NMR spectroscopy, Mol. Biosyst. 5 (2009) 317-322.

[56] Lovell, S. C.; Word, J. M.; Richardson, J. S.; Richardson, D. C., The penultimate

rotamer library, Proteins: Structure, Function, and Genetics 40 (2000).

[57] Schug, K. A.; Lindner, W., Noncovalent binding between guanidinium and anionic groups: focus on biological- and synthetic-based arginine/guanidinium interactions with phosph [on]ate and sulf [on]ate residues, Chem Rev. 105 (2005) 67-114.

[58] Lehrer, R. I.; Lichtenstein, A. K.; Ganz, T., Defensins: antimicrobial and cytotoxic peptides of mammalian cells, Annu. Rev. Immunol. 11 (1993) 105-128.

[59] Lehrer, R. I.; Barton, A.; Daher, K. A.; Harwig, S. S.; Ganz, T.; Selsted, M. E., Interaction of human defensins with Escherichia coli. Mechanism of bactericidal activity, J. Clin. Invest. 84 (1989) 553-561.

[60] Fujii, G.; Selsted, M. E.; Eisenberg, D., Defensins promote fusion and lysis of negatively charged membranes., Prot. Sci. 2 (1993) 1301-1312.

[61] Hristova, K.; Selsted, M. E.; White, S. H., Critical role of lipid composition in membrane permeabilization by rabbit neutrophil defensins, J. Biol. Chem. 272 (1997) 24224-24233.

[62] Madison, M. N.; Kleshchenko, Y. Y.; Nde, P. N.; Simmons, K. J.; Lima, M. F.; Villalta, F., Human Defensin alpha-1 Causes Trypanosoma cruzi Membrane Pore Formation and Induces DNA Fragmentation, Which Leads to Trypanosome Destruction, Infect. Immun. 75 (2007) 4780-4791.

[63] de Leeuw, E.; Li, C.; Zeng, P.; Li, C.; Diepeveen-de Buin, M.; Lu, W. Y.; Breukink, E.; Lu, W., Functional interaction of human neutrophil peptide-1 with the cell wall precursor lipid II, FEBS Lett. 584 (2010) 1543-1548.

[64] Xie, C.; Zeng, P.; Ericksen, B.; Wu, Z.; Lu, W.-Y.; Lu, W., Effects of the Terminal Charges in Human Neutrophil alpha-defensin 2 on its Bactericidal and Membrane Activity, Peptides 26 (2005) 2377-2383.

[65] de Leeuw, E.; Rajabi, M.; Zou, G.; Pazgier, M.; Lu, W., Selective Arginines are Important for the Antibaterial Activity and Host Cell Interaction of Human alpha-defensin 5, FEBS Letters 583 (2009) 2507-2512.

[66] Tang, M.; Waring, A. J.; Lehrer, R. I.; Hong, M., Effects of Guanidinium-Phosphate Hydrogen Bonding on the Membrane-Bound Structure and Activity of an Arginine-Rich Membrane Peptide from Solid-State NMR, Angew. Chem. Int. Ed. Engl.

47 (2008) 3202-3205.

[67] Su, Y.; Doherty, T.; Waring, A. J.; Ruchala, P.; Hong, M., Roles of Arginine and Lysine Residues in the Translocation of a Cell-Penetrating from 13C, 31P and 19F Solid-State NMR, Biochemistry 48 (2009) 4587-4595.

[68] Su, Y.; Waring, A. J.; Ruchala, P.; Hong, M., Membrane-Bound Dynamic Structure of an Arginine-Rich Cell-Penetrating Peptide, the Protein Transduction Domain of HIV TAT, from Solid-State NMR, Biochemistry 49 (2010) 6009-6020.

[69] Zou, G.; de Leeuw, E.; Li, C.; Pazgier, M.; Li, C.; Zeng, P.; Lu, W.; Lubkowski, J.; Lu, W., Toward understanding the cationicity of defensins. Arg and Lys versus their noncoded analogs., J. Biol. Chem. 282 (2007) 19653-19665.

[70] Doherty, T.; Waring, A. J.; Hong, M., Peptide-lipid interactions of the beta-hairpin antimicrobial peptide tachyplesin and its linear derivatives from solid-state NMR, Biochim. Biophys. Acta 1758 (2006) 1285-1291.

[71] Su, Y.; DeGrado, W. F.; Hong, M., Orientation, dynamics, and lipid interaction of an antimicrobial arylamide investigated by 19F and 31P solid-state NMR spectroscopy, J. Am. Chem. Soc. 132 (2010) 9197-9205.

[72] Christ, K.; Wiedemann, I.; Bakowsky, U.; Sahl, H. G.; Bendas, G., The role of lipid II in membrane binding of and pore formation by nisin analyzed by two combined biosensor techniques, Biochim. Biophys. Acta 1768 (2007) 694-704.

Supporting Information

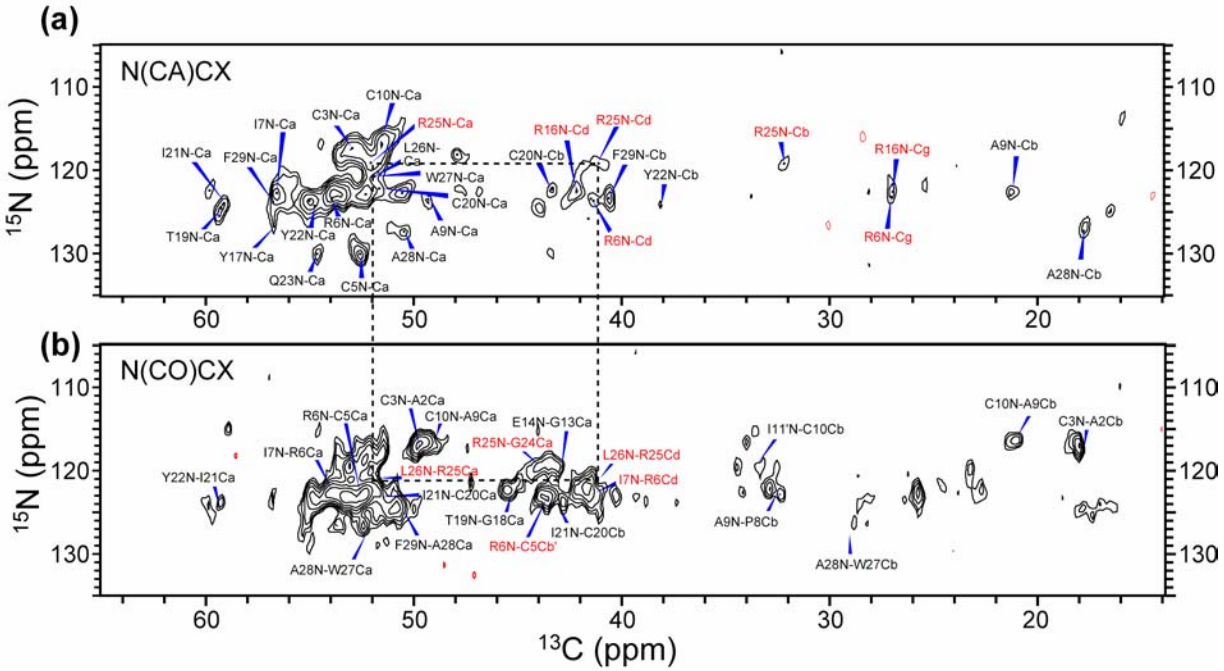

Figure S1. 2D ^{15}N-^{13}C correlation spectra of HNP-1 bound to DMPC/DMPG membranes to confirm resonance assignment. The Arg and L26 resonances are shown in red. (a) N(CA)CX spectrum. (b) N(CO)CX spectrum. R15 signals are not observed in these spectra, indicating it is dynamically disordered at the temperature of the experiment, 273 K.

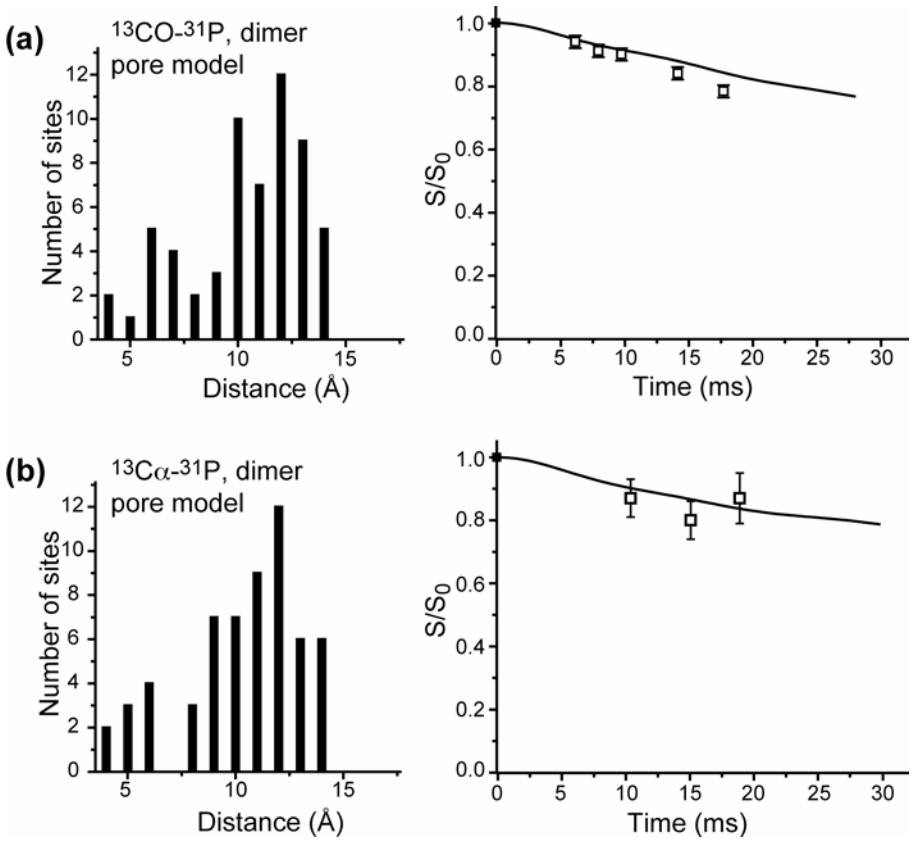

Figure S2. REDOR distance simulations using the dimer pore model. (a) ^{13}CO-^{31}P distance distribution and the resulting REDOR curve, superimposed with the experimental data. (b) ^{13}Cα-^{31}P distance distribution and the resulting REDOR curve, superimposed with the experimental data.

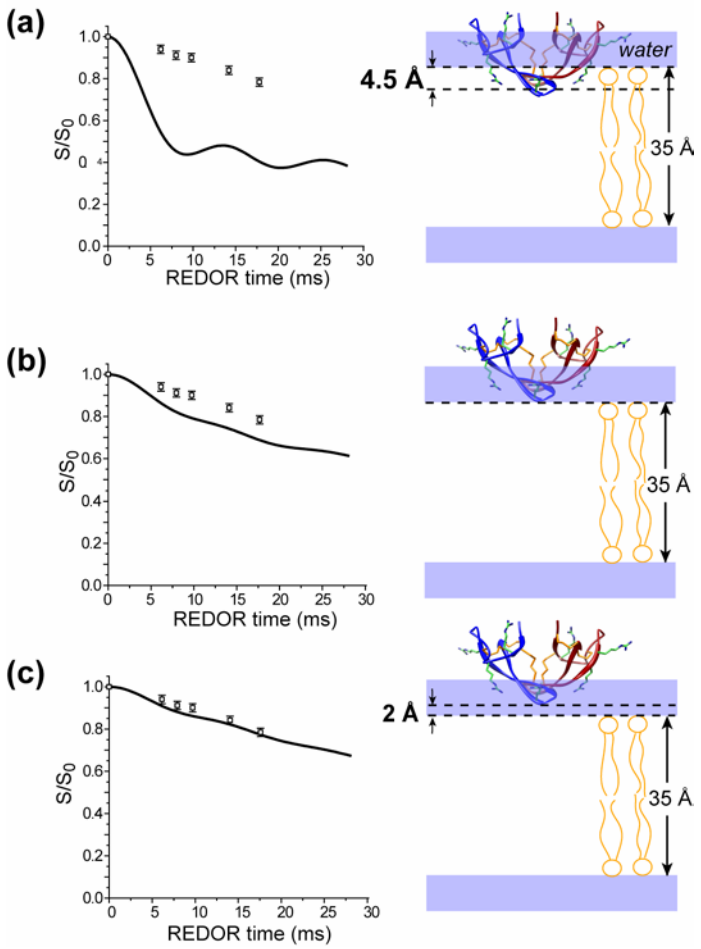

Figure S3. Simulations of the ^{13}CO-^{31}P REDOR distances for the surface-bound wedge model to verify that HNP-1 is inserted into the membrane at low temperature. (a) If the HNP-1 wedge is partly immersed into the membrane with a quarter of its full height (4.5 Å), then the simulated CO-P REDOR dephasing disagrees completely with the measured data. (b) If the wedge has its bottom on the membrane surface, then the simulated dephasing still contradicts with the data. (c) If the protein is 2 Å above the membrane surface, then the simulated dephasing will agree with the data. However, this scenario of the protein "floating" above the membrane surface contradicts the Arg Cζ-P REDOR data. Therefore, HNP-1 is well inserted into the membrane at low temperature.

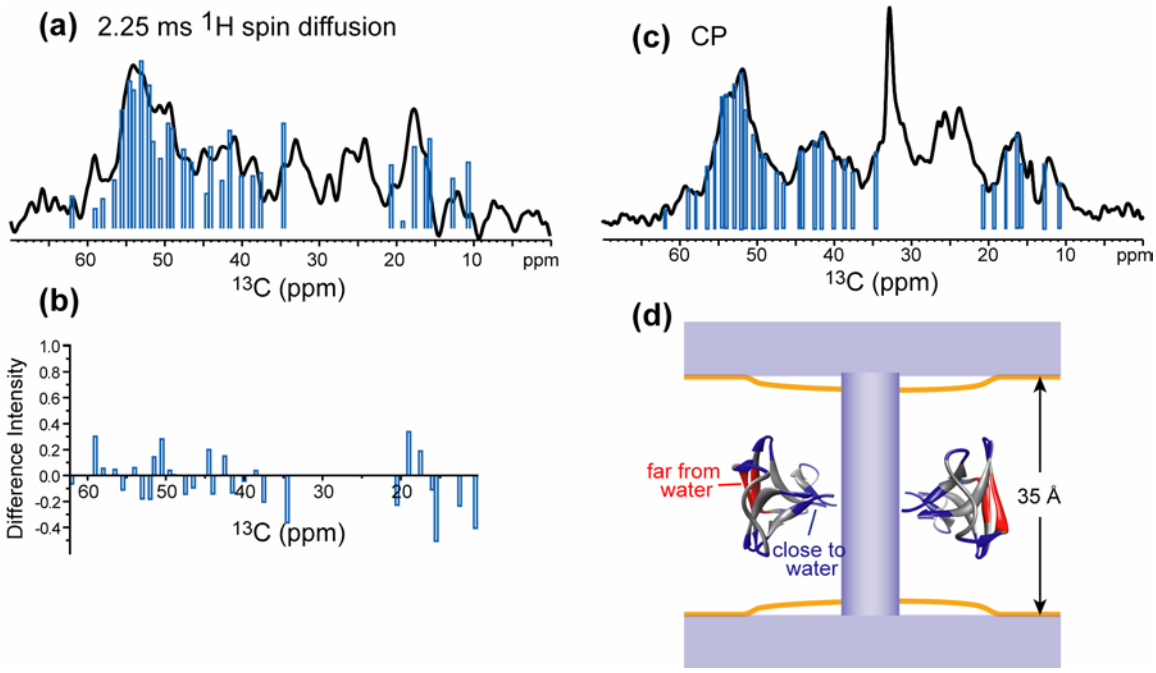

Figure S4. Simulation of the water-to-protein ^{1}H spin diffusion spectrum at 2.25 ms mixing using a dimer pore model where the solid-state NMR-determined HNP-1 structure was used as input [1]. (a) Experimental ^{13}C spectrum superimposed with the stick spectrum (blue) simulated based on the proximity of residues to water in the dimer pore model. (b) Difference between the experimental and simulated spectra in (a). (c) Simulation (blue) of the experimental ^{13}C CP spectrum. (d) Dimer pore model, where residues close to water are shown in blue, residues far from water shown in red, and the interface residues in gray.

Reference

[1] Zhang, Y., Doherty, T., Li, J., Lu, W., Barinka, C., Lubkowski, J. & Hong, M. (2010). Resonance assignment and three-dimensional structure determination of a human a-defensin, HNP-1, by solid-state NMR. *J. Mol. Biol.* **397** 408-422.

Chapter 6

Bicelle Alignment and Orientation Simulation of HNP-1 in Bicelle Systems

Introduction

In solid-state NMR of membrane proteins, aligned membrane samples are often used to obtain information about peptide orientation in the lipid membrane and membrane disruption by the peptide. In the presence of water, different lipids and combination of lipids self-assemble to form phospholipid bilayers that enable the proteins to maintain their native structures and functions. The proteins can be uniaxially aligned along with the phospholipids in the magnetic field of the NMR spectrometer [1]. Two of the most common oriented lipid systems are lipids mechanically aligned on glass plates [2,3] and lipid bicelles aligned magnetically [4-7]. Mechanically aligned lipid bilayers have the advantage that they allow wider choices of lipid combinations. However, they suffer from low sample stability due to the difficulty of maintaining sample hydration in the presence of high-power radiofrequency irradiations [8]. Bicelle samples have the disadvantage of limited choices of lipid compositions, since not all lipids will align in a magnetic field, and restricted temperature range for each lipid composition. But they have the benefit of being easier and quicker to make and allowing measurements in an MAS probe.

The bicelle membrane is intermediate between micelles and bilayers [9,10]. It consists of a mixture of long-chain phosphatidylcholine (PC) lipids (between 12 and 18 carbons) and short chain PC lipids (6 to 8 carbons). The long-chain lipids form the planar bilayer region of the bicelle while the short-chain lipids 'cap' the rim of the bilayer [11]. Bicelles are characterized by q, the molar ratio of long- to short-chain lipids. Small 'isotropic' bicelles ($q<0.5$) reorient rapidly with no preferred direction of alignment

[7].We are interested in larger bicelles with q>2.5, which are aligned by the strong magnetic field, forming a liquid crystalline phase with the bilayer normal perpendicular to the direction of the magnetic field [12]. This orientation is driven by the cooperative diamagnetic susceptibilities of the lipid molecules. A glycerophospholipid with saturated chains has the parallel diamagnetic susceptibility, $\chi_{\parallel}$, (along the lipid long axis) smaller than the perpendicular $\chi_{\perp}$, resulting in a negative anisotropy, $\Delta\chi = \chi_{\parallel} - \chi_{\perp}$ [13]. Bicelles can also be 'flipped' 90º by the addition of lanthanide ions [14]. Because such lanthanides possess a strong positive $\Delta\chi$, they can turn the bilayer normal to be uniaxially aligned parallel to the magnetic field [15]. Protein structures can be determined in either perpendicular or parallel bicelles [1,16].

The common short-chain lipids used for bicelles are DHPC, 6-O-PC, and DCPC (Yuan, include any other before the introduction of Triton). Recently Opella and coworkers reported bicelles with enhanced alignment order and improved stability [17]. This system consists of long-chain phosphatidylcholine lipids mixed with the short-chain lipid Triton X-100 with a molar ratio of 5:1 (q = 5). They prepare the sample by adding a solution containing Triton X-100 to the proteoliposome pellet with a lipid concentration of 20% (w/v). Upon formation of the magnetically aligned bilayer phase, the translucent proteoliposome pellet turns into a clear, non-viscous solution when placed in ice. This bicelle sample exhibits narrow line widths of ~0.5 ppm and remains well-aligned over a broad range of temperature. It is also stable for long periods of time (months).

In this chapter, we study the alignment of bicelles with different lipid combinations, long- to short-chain lipid ratios and hydration levels. The alignment of bicelles with peptides was also studied and a phase diagram was generated. We show that the orientation of HNP-1, a dimeric protein with 3 β-strands in each monomer, can determined in principle by 2D correlation spectra of ^{15}N anisotropic chemical shift and N-H dipolar coupling. We show simulated 2D spectra employing site-specifically labeled residues.

Procedure for preparing bicelles

This procedure roughly follows the protocol described by De Angelis and Opella [11], while additional papers are referenced for comparing the sample preparation conditions [18-20]. First, the desired amount of the short-chain lipid such as 6-O-PC is weighed out. It is important for the short-chain lipid to be non-hydrolyzable to increase the long-term stability of the sample. In addition, the lipid mass needs to be accurate to obtain the desired q. Thus, it is a good practice to dry the lipid in a lyopholizer for 2-4 hours and then reweigh to confirm the mass. The dry mass is then used to calculate the appropriate amount of DMPC (the long-chain lipid) required to reach the desired q value. We usually use q = 3.2. Dissolve 6-O-PC in sufficient water or buffer to give a lipid/water ratio of 35% (w/v). The micelle solution should be clear and homogeneous at this stage. Add this micelle solution to the long-chain lipid powder. The resulting mixture at this step is heterogeneous, with water on top of the lipid. To create a homogeneous mixture, the sample is heated to 42 ºC with hot water, and cooled to 0 ºC in an ice bath, then vortexed for 30 seconds. Repeat the cool-thaw cycle three more times until the solution becomes homogeneous and the entire amount of long-chain lipid is dissolved. Even if there are no visible particles floating in the solution, the sample should be to placed in a 4ºC refrigerator overnight to allow the lipid to dissolve and the sample to equilibrate.

The next day, the bicelle solution should be viscous at room temperature and become non-viscous and fluidic at 0ºC. If this viscosity test is passed, then the bicelle sample can be checked by ^{31}P NMR for degree of alignment. To transfer the sample into the rotor, we place it in the refrigerator for ~5 minutes to cool it to the solution phase, together with the pipet tip we are going to use. Once the sample becomes fluid, we use the pipet tip to take out the solution and transfer it into the rotor. This step needs to be done quickly to avoid the sample returning to the gel phase at room temperature in the pipet tip. The ^{31}P single-pulse experiment is carried out on the 600 MHz NMR spectrometer (14.1 T) using a static ^{31}P probe containing a solenoid coil whose axis is perpendicular to the magnetic field. ^{31}P chemical shifts are referenced to 85% H_3PO_4 at 0 ppm. The temperature of alignment can be different from expected, since it depends

sensitively on the the long- to short-chain lipid ratio and hydration level. Thus a range of temperatures (298-320 K) should be scanned before identifying the temperature for the best bicelle alignment. Normally a 3 K difference is sufficient to cause a different lineshape.

After a well aligned bicelle sample is prepared and characterized, it can be added directly to the peptide using a precooled pipet tip. At the beginning, the peptide may not be completely dissolved. This problem can be overcome by the cool-and-thaw cycles. A clean needle is also useful to physically stir the mixture and speed up dissolution. After the peptide is added to the bicelle solution, the resulting mixture should be allowed to sit overnight to equilibrate. With a high peptide concentration, the solution can be viscous at all temperatures. The sample is now ready for ^{31}P NMR.

Factors Affecting Bicelle Alignment

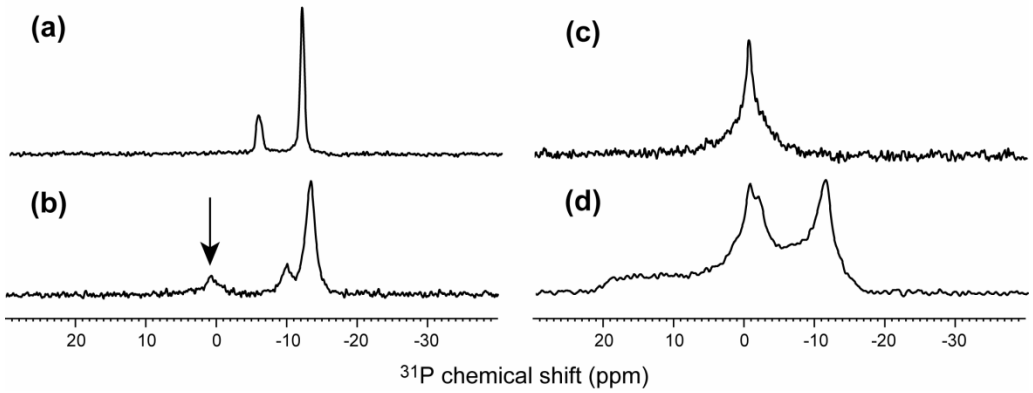

Figure 5.1. ^{31}P spectra of different phases of lipids. (a) Magnetically-oriented bicelle phase. The sample is DMPC/6-O-PC with 65% hydration at 310 K. (b) Aligned bicelle coexisting with isotropic bicelles (arrow). The sample is DMPC/6-O-PC in the presence of RC100b with 65% hydration at 314 K. (c) Isotropic bicelles. The sample here is DMPC/6-O-PC containing RC100b, with 70% hydration at 314 K after pulsing overnight. (d) Unoriented bilayers mixed with isotropic bicelles. The sample here is DMPC/6-O-PC with 70% hydration at 303 K and the spectra is collected right after the sample was put into the magnetic field.

Static ^{31}P spectra are used to characterize the phase of the bicelle lipid mixture. The lipid mixtures can form different phases under different temperature-composition-

hydration conditions, resulting in different static ^{31}P lineshapes (Figure 5.1). For the successfully oriented bicelle, the ^{31}P spectrum shows two single sharp peaks for the long-chain lipids and short-chain lipids at anisotropic chemical shift frequencies. The intensities of the two peaks should reflect the q value. For oriented bicelles coexisting with isotropic bicelles or micelles, the spectrum shows a sharp peak at 0 ppm representing the isotropic phase, in addition to the two anisotropic chemical shift peaks for the oriented bicelles. When the lipids are fully in the isotropic phase, the spectrum will have only one peak at 0 ppm and the two bicelle peaks disappear. When the lipids are unaligned but do not form small isotropic vesicles, then a uniaxial powder pattern is observed, representing unoriented lamellar bilayers.

Lipid Ratio

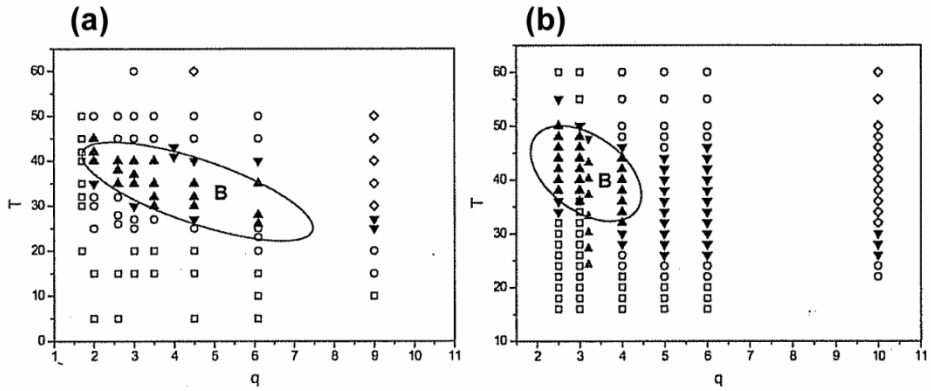

Figure 5.2. Phase diagrams of two bicelles as a function of temperature and q value. (a) Phase diagram of DMPC/DCPC with 80% hydration [21]. (b) Phase diagram of DMPC/DCPC with 75% hydration [22]. The phase diagrams are summarized based on ^{31}P NMR spectra reported in the literature. The upward triangle represents a single phase of bicelles oriented along the magnetic field. The downward triangle stands for oriented bicelles coexisting with isotropic or unoriented phases. The opened circle denotes unoriented and isotropic phases. The open rectangle denotes the isotropic phase. The open diamond stands for the lamellar phase. [21] [22]

The lipid ratio q, which is defined as the molar ratio of long- to short-chain lipids, is one of the major factors affecting bicelle alignment. Raffard et al. [21] and Triba et al. [22] have examined the bicelle alignment with different q ratios at fixed hydration levels by ^{31}P NMR (Figure 5.2). For the DMPC (14:0 chains) /DCPC (1,2-dicaproyl-sn-glycero-

3-phosphocholine, 6:0 chains) system [21] with q ratios less than 2, the lipids exhibit a single sharp line centered at -0.4 ppm, which is the isotropic chemical shift of phosphatidylcholines. This reflects the formation of micelles or small isotropic bicelles at all temperatures. When the q ratio is larger than 9, the spectrum is composed of a single axially symmetric powder pattern, reflecting an unoriented lamellar phase at all temperatures. The region in which bicelles self-orient in the magnetic field is roughly delineated by q = 2.5-7 and T = 298 – 318 K. Similarly, for DMPC/DHPC (1,2-diheptanoyl-sn-glycero-3-phosphocholine, 7:0 chains) systems [22], aligned bicelle phase occurs between q = 2-5 and T = 308 – 323 K. Thus, for our DMPC/6-O-PC sample, we choose the q ratio of 3.2, which is in the middle of the q range that is supposed to give oriented bicelles in the magnetic field.

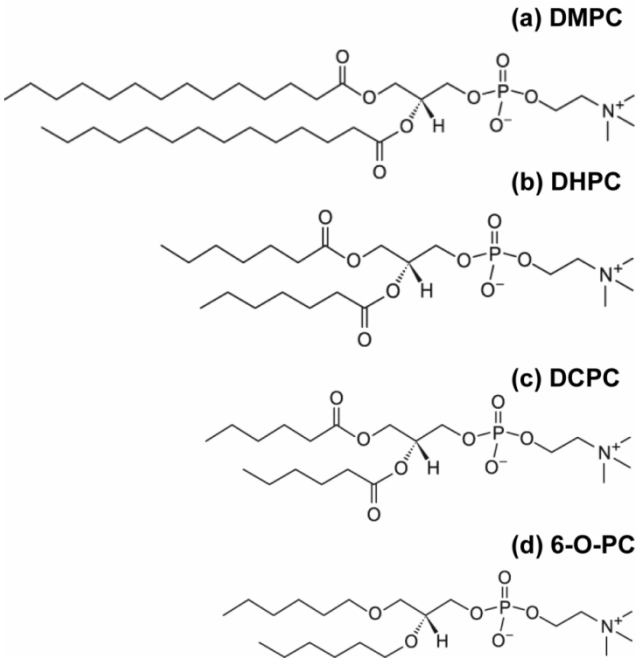

Figure 5.3. Chemical structures of DMPC, DHPC, DCPC and 6-O-PC.

People have found that increasing the chain length of the short-chain and long-chain lipids shrinks the zone where the oriented bicelles are observed [22]. For instance, the DMPC/DCPC system has a bicelle phase ranges from q = 2 to q = 7, while the DMPC/DHPC system's bicelle phase shrinks to q = 2-5. We have measured the ^{31}P spectra for both DMPC/6-O-PC and DMPC/DHPC systems at different temperatures.

The sample containing 6-O-PC, which has a shorter aliphatic chain, gives the narrowest FWHM of 0.9 ppm and the line shape is narrow from 297 K to 316 K. In contrast, for the DMPC/DHPC system the narrowest line width is 1.2 ppm and the lines start to broaden significantly (~2.5 ppm) below 297 K.

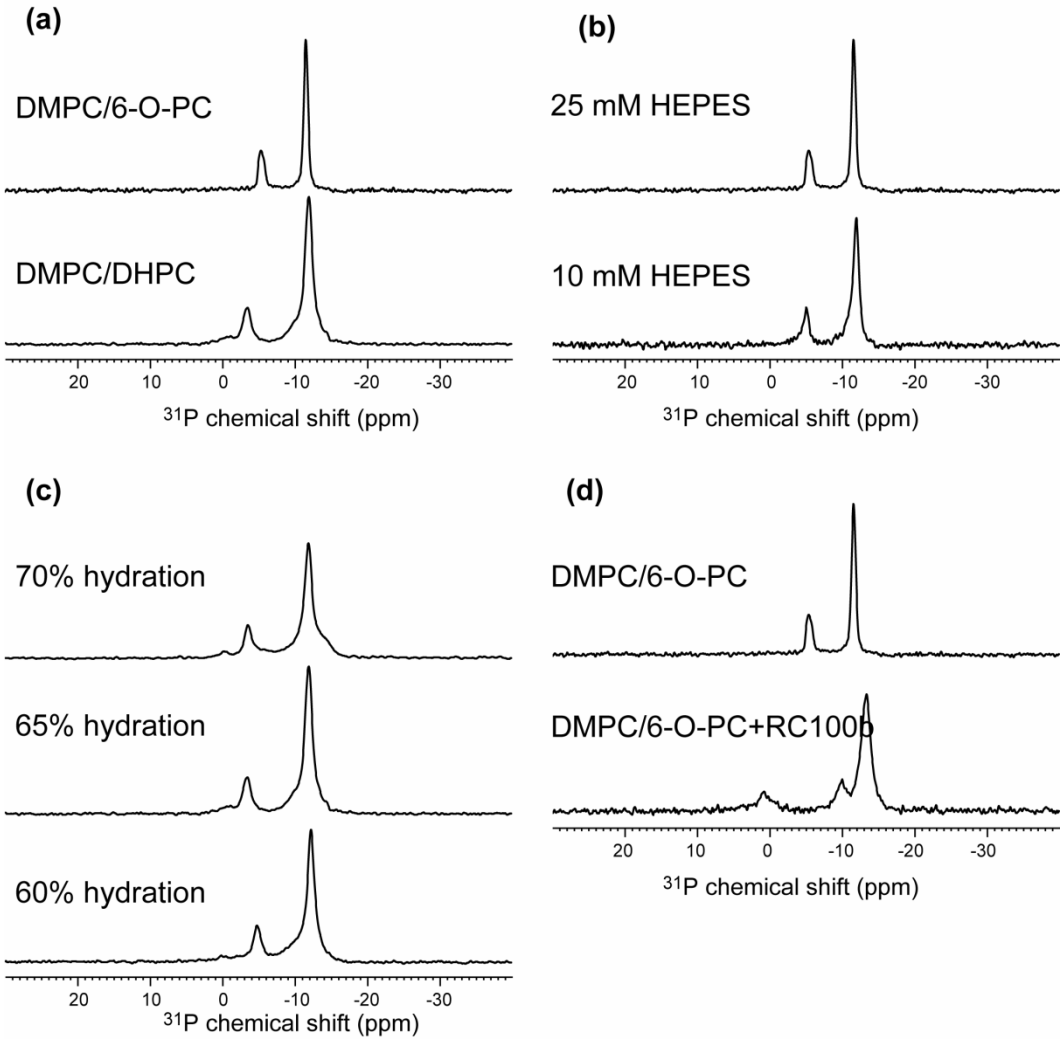

Figure 5.4. Factors affecting bicelle alignment. For all samples shown here, q = 3.2. (a) DMPC/6-O-PC at 310 K with 65% hydration (top) and DMPC/DHPC at 300 K with 65% hydration (bottom). (b) DMPC/6-O-PC with 65% hydration. The top spectrum is prepared in 25 mM HEPES buffer and aligned at 310 K and the lower one is prepared in 10 mM HEPES buffer and aligned at 306 K. (c) DMPC/DHPC mixture with different hydration levels: 70% at 310 K, 65% at 300 K and 60% at 320 K. (d) ^{31}P spectra of DMPC/6-O-PC with (at 310 K) and without the peptide RC100b (at 314 K).

Bicelle Alignment in the presence of salt

Previously, people have found that the temperature range and the center of the bicellar domain do not change with the addition of salt (ref??). In other words the salt does not appear to be necessary for bicelle formation. However, it did shift the bicellar domain in the direction of increasing short-chain lipids, in other words the bicelles form at lower q in the presence of salt than in the absence of salt [23].

We measured the ^{31}P spectra of DMPC/6-O-PC with different concentrations of HEPES buffer, 10 mM and 25 mM. The line width of the sample prepared with 10 mM HEPES buffer is broader than at 25 mM, indicating that salt facilitates the alignment of the bicelle in the magnetic field. The reason for this better alignment may be that the addition of ions may increase the absolute value of $\Delta\chi$, thereby influencing the lipid alignment with respect to the bilayer normal.

Bicelle Alignment as a Function of Hydration

Hydration level is another factor that affects bicelle alignment. We have prepared several DMPC/DHPC samples with hydration levels of 60%, 65% and 70%. Among them, the 65% hydrated sample gave the narrowest line width (0.9 ppm). From the literature, people have found that the sample with lower hydration level tends to be more stable over a wider temperature range and aligns in the field more easily [21]. This is probably because of tighter packing of the bicelle, which leads to less swelling. Our later investigation of bicelles with peptides also shows that DMPC/6-O-PC containing retrocyclin has a better alignment at 65% hydration than at 70% hydration. This result further supports the statement that moderate dehydration leads to better bicelle alignment. The reason why 60% hydration has a broader FWHM than the 65% is probably because the bicelles are too crowded to have the free space to orient.

Bicelle with Peptides

Addition of peptides to bicelles can interfere with alignment and lead to broader line widths. For example, the best FWHM we can obtain for DMPC/6-O-PC bicelle alone is 0.9 ppm at 65% hydration. After adding the retrocyclin into the bicelle at a

peptide/lipid molar ratio of 1/40, the ^{31}P line width increased to 1.5 ppm. The alignment temperature range also changes by the addition of peptide. Without retrocyclin , the alignment temperature range is 300 K – 310 K. With retrocyclin, the best alignment temperature increased to 315 K. Decreasing the peptide concentration should help the bicelle alignment.

In conclusion, the alignment of bicelles is sensitive to several factors such as lipid composition, temperature and hydration levels. The bicellar domains are found for lipid molar composition between 63% and 85% for long-chain lipid (q = 2-5), for a temperature range of 25-45 ºC and for hydration levels from 40% to 95% (w/w). Increasing the chain length for both short-chain and long-chain lipids, for example, going from DMPC/DCPC to DPPC/DHPC, reduces the zone where the oriented discs are observed. The presence of salts can increase the bicelle domain and sometimes improves the bicelle orientation in the magnetic field. Moderate dehydration can also favor alignment due to tighter packing of the bicelles [21].

Orientation Simulation of HNP-1

The orientation of a membrane protein can be determined from the two-dimensional spectra correlating ^{1}H-^{15}N dipolar coupling and ^{15}N chemical shift. A common method for measuring such spectra is PISEMA [24,25]. Previous studies showed that the PISEMA spectra of membrane proteins in oriented lipid bilayers are an sensitive indicator of the α-helical structure and topology. The resonance frequencies in the PISEMA spectra depend on the helix orientation, as well as backbone dihedral angles, the magnitudes and orientations of the principal element of the amide ^{15}N chemical shift tensor. Because the ^{15}N chemical shift tensor is reasonably well characterized for protein backbone amides, it is possible to calculate solid-state NMR spectra for specific structural models of proteins.

For helical proteins, the characteristic ‘wheel-like’ patterns of resonances observed in these spectra reflect the helical wheel projections of residues and therefore provide direct information on the secondary structure and topology of membrane proteins in phospholipid bilayers. These patterns are referred as PISA (Polarity Index Slant Angle)

wheels [24,25]. In this study, we calculate the 2D ^{15}N-^{1}H/^{15}N correlation spectra for ideal α-helices and β-sheets using a FORTRAN program, then simulate the spectrum expected for the β-strand rich HNP-1. The Fortran program defines a molecule-fixed coordinate system that reflects the α-helix axis and geometry and calculates the anisotropic frequencies based on the orientation of the magnetic field (B_0) in this coordinate system. For α-helices, the z axis of this reference system is the α-helix axis, and is obtained as the average orientation of an even number of consecutive N-H bonds in the helix. The x-y plane is defined as the plane perpendicular to the α-helix axis. There are two parameters to define the orientation of the helices: the tilt angle τ, which is between the α-helix axis and the B_0 field, and the rotation angle ρ, which is defined as the angle between the projection of B_0 onto the x-y plane and the radial axis of the helix on the x-y plane that passes through the Cα carbon of the second residue. The z axis of the ^{15}N chemical shift tensor is 17º from the N-H bond, whereas the x axis is 25º from the peptide plane. The rigid limit N-H dipolar coupling is 10 kHz, corresponding to a bond length of 1.07 Å. Literature ^{15}N chemical shift principal values of (64, 77, 217) ppm were used to simulate the orientation dependent spectra. The ^{15}N anisotropic chemical shift frequencies $\delta_{\|}$, which is the frequency when the protein is uniformly aligned and the alignment axis parallel to the magnetic field (0º -aligned sample), can be calculated by

$$\delta_{\|} = \omega_{0°aligned} = \frac{1}{2}\delta(3cos^2\tau - 1 - \eta sin^2\tau cos2\rho) + \omega_{iso}$$

Here $\delta = \delta_{zz} - \delta_{iso}$ and $\eta = (\delta_{yy} - \delta_{xx})/\delta$ are the anisotropy and asymmetry parameters, respectively, of the rigid-limit interaction tensor. The N-H dipolar coupling can be derived by the equation below:

$$\omega_{NH} = \frac{1}{2}(3cos^2\tau - 1)\omega_{NH,rigid}$$

Here $\omega_{NH,rigid}$ is the rigid limit N-H dipolar coupling.

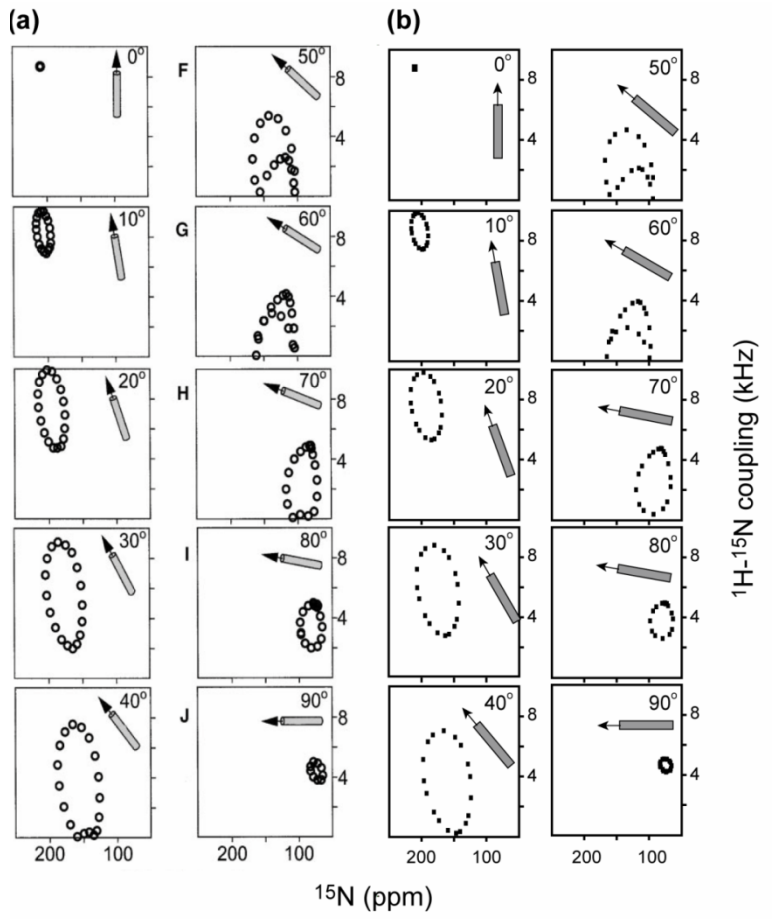

Figure 5.5. Simulated PISEMA spectra for the full range of possible orientations of an ideal α-helix (ϕ = -65º, ψ = -40º) aligned by glass plates (b). (a) Literature reported simulations [25]. (b) Our own simulations using the Fortran program. The two sets of simulations show perfect agreement.

Figure 5.5 shows the calculated PISEMA spectra for the full range of possible orientations of an ideal α-helix with identical backbone dihedral angles of (ϕ = -65º, ψ = -40º) for all residues. The peptide is assumed to align with the bilayer normal parallel to the B_0 field, as applicable for glass-plate aligned samples. When the helix axis is parallel to the bilayer normal ($\tau = 0^\circ$), all the amides have the same orientation relative to the magnetic field, therefore all the sites give the same N-H dipolar coupling and ^{15}N chemical shift frequencies. Since the amide backbone N-H bonds in the α-helix are nearly, but not exactly, parallel to the helix axis, the resonance frequencies approach, but do not reach, their maximum values of 10 kHz. Tilting the helix away from the

membrane normal breaks the symmetry, inducing variations in the orientations of the amide N-H bond vectors relative to the field. For all helix orientations other than parallel to the field direction, the PISEMA spectra have characteristic wheel-like patterns whose frequency breadths reflect the extent of the helix tilt. When the helices are tilted to be parallel to the membrane surface, their amide N-H bonds and $_{33}$ of the ^{15}N chemical shift tensor are nearly orthogonal to the magnetic field and give highly overlapped PISEMA spectra with all resonance frequencies around 5 kHz and 75 ppm. The N-H dipolar coupling values indicated here are not scaled by the homonuclear decoupling scaling factor.

β-strand peptides have very different geometries and are defined in the following way. The z axis of the reference system is the β-strand axis, and is calculated as the average orientation of an even number of consecutive C'_{i-1}-N_i bonds. The y-z plane, which is the local β-sheet plane, is defined as the common plane containing the z axis and a specific C=O vector. We used the C=O bond of the second residue to define the y-z plane. The tilt angle τ is defined as the angle between the β-strand axis and the B_0 field, which is the bilayer normal if the sample is aligned by glass plates. The rotation angle ρ is defined as the angle between the y axis and the projection of B_0 onto the x-y plane.

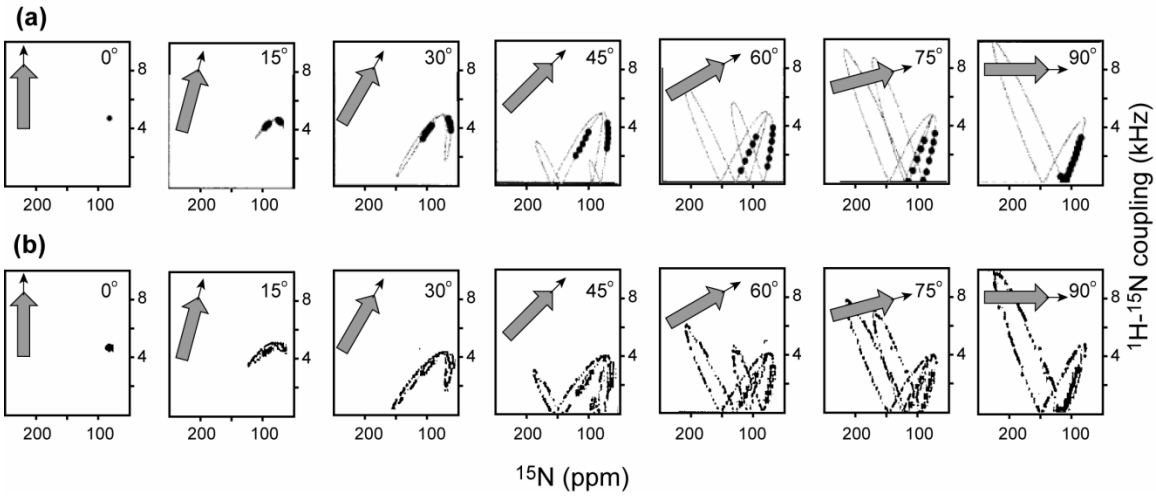

Figure 5.6. Simulated PISEMA spectra of β-strands (ϕ = -140º, ψ = -135º) with different orientations relative to the magnetic field aligned by glass plates (b). (a) Literature reported

simulations [26]. (b) Our own simulations using the Fortran program. For each τ angle, we did several simulations for ρ from 0º to 360º. And the ρ = 0º points were shown in filled circles.

Figure 5.6 shows the calculated PISEMA spectra of β-strands with several τ values relative to the magnetic field. The (ϕ, ψ) torsion angles for the strands residues are (-140º, 135º). Same as the α-helix, when the strand long axis is oriented parallel to the bilayer normal, all amides have identical orientation relative to the magnetic field, thus all resonances overlap at a single N-H dipolar coupling and ^{15}N chemical shift value. However, unlike the α-helix, of which the resonance frequencies approach the maximum attainable values of 10 kHz, the N-H dipolar couplings of β-strands approach, but do not reach, a value of 5 kHz. This is because the amide N-H bonds in β-strands are nearly perpendicular to the strand axis. Therefore, the maximum attainable value is only half of the α-helix

$$\omega_{NH} = \frac{1}{2}(3cos^2 90^\circ - 1) * \frac{1}{2}(3cos^2\tau - 1)\omega_{NH,rigid} = \left(-\frac{1}{2}\right)\frac{1}{2}(3cos^2\tau - 1)\omega_{NH,rigid}.$$

When the β-strand is tilted away from the bilayer normal, the PISEMA spectra trace out butterfly-like resonance patterns. Because β-strands lack cylindrical symmetry around the main molecular axis, their 2D spectra depend characteristically on both the tilt angle of the strand axis and the rotation angle of the β-sheet plane, while the PISA wheel patterns of α-helix are distinguished mostly by the tilt angle of the helical axis and not by the helix rotation angle.

What we were discussing above is the orientation simulation for proteins in glass-plate oriented bilayers. The bicelle sample is a different case because it is aligned with bilayer normal perpendicular to the magnetic field, while that of the glass-plate sample is parallel to the magnetic field. This difference introduces a scaling factor for both the N-H dipolar coupling and ^{15}N chemical shift frequencies. For the N-H dipolar coupling:

$$\omega_{NH,bicelle} = \frac{1}{2}(3cos^2\theta - 1) * \frac{1}{2}(3cos^2\tau - 1)\omega_{NH,rigid}$$
$$= \frac{1}{2}(3cos^2\theta - 1)\omega_{NH,glass-plate}$$

Here θ = 90º because of the different orientation between bicelle and glass plate. Hence:

$$\omega_{NH,bicelle} = -\frac{1}{2}\omega_{NH,glass-plate}$$

For the ^{15}N chemical shift frequencies:

$$\delta_{\|,bicelle} = \frac{1}{2}(3cos^2\theta - 1) * \frac{1}{2}\delta(3cos^2\tau - 1 - \eta sin^2\tau cos2\phi) + \omega_{iso}$$
$$= \frac{1}{2}(3cos^2\theta - 1) * \delta_{ani,glass-plate} + \omega_{iso}$$

Again, with θ = 90º:

$$\delta_{\|,bicelle} = \left(-\frac{1}{2}\right) * \delta_{ani,glass-plate} + \omega_{iso}$$

Therefore, the F1 dimension of the PISEMA spectra (N-H dipolar coupling) of the bicelle sample is half of that of the glass plate. The F2 dimension (^{15}N chemical shift) of the bicelle is generated by first scaling down the glass plate spectra by a factor of 2 and then taking the mirror image around the ω_{iso} (120 ppm). As a result, when τ = 0º, the PISEMA spectrum of α-helix in bicelles is a single point at (71 ppm, 5 kHz) and the β-sheet peak is at (148 ppm, 2.5 kHz).

For a real protein with non-ideal secondary structures, the expected 2D spectra become more complex. The human α-defensin HNP-1 consists of three antiparallel β-strands connected by turns and a long loop. The protein is dimerized through intermolecular H-bonds between the two β2 strands. The dimer has a basket shape with a polar top and an apolar base Since the three β-strands in this protein are not completely parallel to each other and the relatively long loop region and the dimerization make the structure more complex, we cannot easily calculate the PISEMA spectrum of this protein by simulating the orientation of the three β-strands separately and then combining them together. Thus we used a different strategy to calculate the PISEMA spectra. We defined a Cartesian coordinate system with x, y, z axes and added the coordinates into the PDB file of the protein. Thus when we rotate these axes, we also rotate the whole body of the

protein. Then we read out the coordinates of the protein and obtain the orientation of the N-H bond vectors and the ^{15}N chemical shift vectors. We place the z axis of the reference coordinate system to be perpendicular to the plane of the top of the basket, the x axis to be parallel to the axis connecting the two R25 Cα sites in the two monomers, and the y axis to be perpendicular to the x-z plane. The tilt angle τ is defined as the angle between the z axis and the bilayer normal. The rotation angle ρ is defined to be the angle between the projection of the bilayer normal onto the x-y plane and the y axis.

Previously people have proposed several mechanistic models to explain the antimicrobial activity of HNPs [27,28]. The wedge model suggests that the dimer inserts into the bilayer with the hydrophobic bottom contacting the hydrocarbon region of the membrane, which makes the $\tau = 0^{o}$. The dimer pore model suggests that the polar top of the dimer is oriented to favor the transmembrane orientation of the solvent channel at the dimer interface, which has (τ, ρ) angles of (90^{o}, 90^{o}). In the general pore model, the dimer is rotated by 90^{o} around the z axis of the dimer pore model. Thus the (τ, ρ) angle is (90^{o}, 0^{o}) for the general pore model.

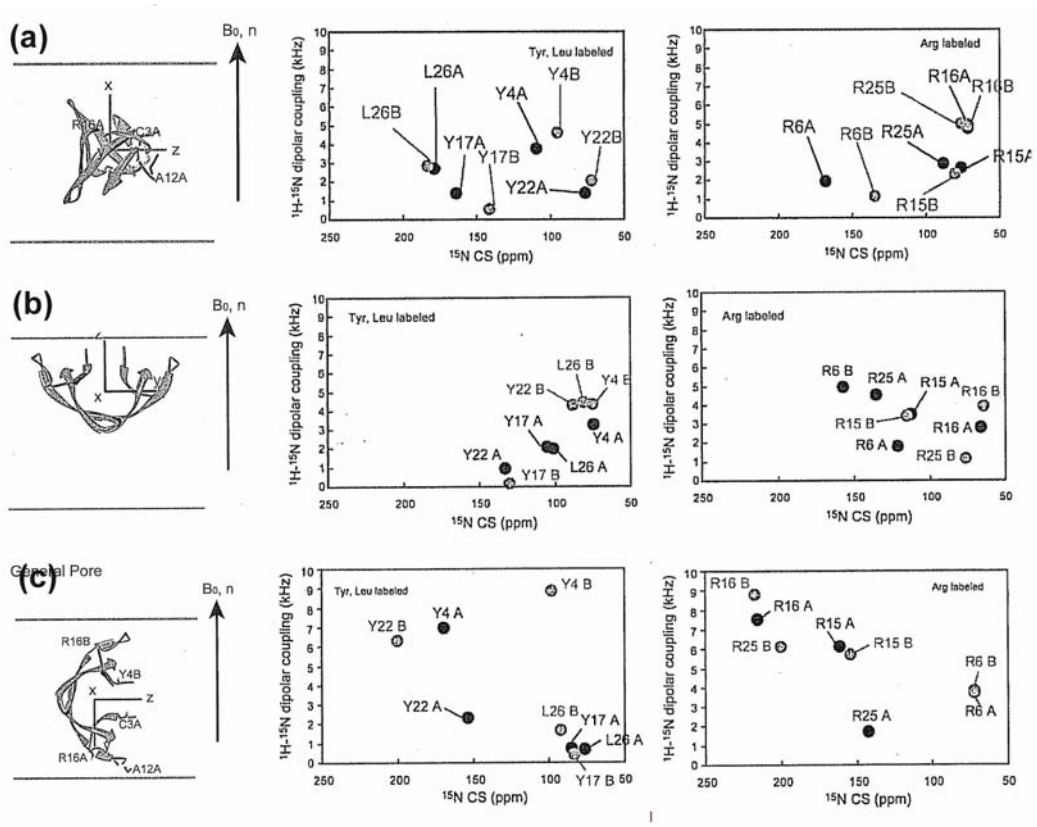

Figure 5.7. Simulated ^{15}N chemical shift – ^{1}H-^{15}N dipolar coupling 2D correlation spectra for three orientations of HNP-1 in the lipid membrane. (a) Dimer pore model, with $\tau = 90^{\circ}$ and $\rho = 90^{\circ}$. (b) Wedge model, with $\tau = 0^{\circ}$. (c) General pore model, with $\tau = 90^{\circ}$ and $\rho = 0^{\circ}$.

We chose three residue types, leucine (Leu26), tyrosine (Tyr4, Tyr17, Tyr22) and arginine (Arg5, Arg15, Arg16, Arg25), as the proposed labeled sites. Figure 5.7 shows the simulated 2D spectra for the three orientational models. In addition to the labeled sites, several residues were also calculated to verify the validity of the simulation. For example, in the dimer pore model, the N-H vector of A12 is almost parallel to the x axis, thus parallel to the bilayer normal. Therefore, the N-H dipolar coupling of A12 should be close to the maximum value 10 kHz. The simulated A12 value is 8.8 kHz, which is close to 10 kHz. In the general pore model, the N-H vector of I7 is parallel to the z axis, which means it is perpendicular to the bilayer normal. As a result, the N-H dipolar coupling of I7 should be around 5 kHz. And in the calculated spectrum, the I7 N-H dipolar coupling is 4.1 kHz, in agree with the prediction.

The calculated spectra above are for glass-plate samples with the bilayer normal 0º with B_0. For bicelle samples, we need to consider the $(-\frac{1}{2})$ scaling factor because of the different orientation between the bicelle axis and the glass plate alignment axis. As we discussed above, the N-H dipolar coupling of the bicelle sample is half of that of the glass plate. The ^{15}N chemical shift of the bicelle is generated by first scaling down the glass plate spectra by a factor of 2 and then taking a mirror image around the ω_{iso} (120 ppm). Therefore, we can determine the orientation of the HNP-1 in the lipid bilayers by comparing the experimental PISEMA spectra with the calculated 2D spectra for the proposed models.

Reference

[1] De Angelis, A.; Jones, D.; Grant, C.; Park, S.; Mesleh, M.; Opella, S., NMR experiments on aligned samples of membrane proteins, Methods. Enzymol. 394 (2005) 350-382.

[2] Opella, S.; Ma, C.; Marassi, F., Nuclear magnetic resonance of membrane-associated peptides and proteins, Methods. Enzymol. 338 (2001) 285-313.

[3] Kechem, R.; Roux, B.; Cross, T., High-resolution polypeptide structure in a lamellar phase lipid environment from solid state NMR derived orientational constraints, Structure. 5 (1997) 1655-1669.

[4] Ram, P.; Prestegard, J., Magnetic field induced ordering of bile salt/phospholipid micelles: new media for NMR structural investigations, Biochim. Biophys. Acta. 940 (1988) 289-294.

[5] Sanders, C. I.; Prestegard, J., Magnetically orientable phospholipid bilayers containing small amounts of a bile salt analogue, CHAPSO, Biophys. J. 58 (1990) 447-460.

[6] Sanders, C. I.; Schwonek, J., Characterization of magnetically orientable bilayers in mixtures of dihexanoylphosphatidylcholine and dimyristoylphosphatidylcholine by solid-state NMR, Biochemistry. 31 (1992) 8898-8905.

[7] Sanders, C.; Hare, B.; Howard, K.; Prestegard, J., Magnetically-oriented phospholipids micelles as a tool for the study of membrane associated molecules, Prog. NMR Spectrosc. 26 (1994) 421-444.

[8] Hallock, K.; Henzler Wildman, K.; Lee, D.-K.; Ramamoorthy, A., An innovative procedure using a sublimable solid to align lipid bilayers for solid-state NMR studies, Biophys. J. 82 (2002) 2499-2503.

[9] Gabriel, N.; Roberts, M., Spontaneous formation of stable unilamellar vesicles, Biochemistry. 23 (1984) 4011-4015.

[10] Sanders, C.; Landis, G., Reconstitution of membrane proteins into lipid-rich bilayered mixed micelles for NMR studies, Biochemistry. 34 (1995) 4030-4040.

[11] De Angelis, A.; Opella, S., Bicelle samples for solid-state NMR of membrane proteins, Nat. Protoc. 2 (2007) 2332-2338.

[12] Thomas, B.; Cardon, T.; Dave, P.; Lorigan, G., Magnetically aligned phospholipid bilayers with large q ratios stabilize magnetic alignment with high order in the gel and L phases, Langmuir 21 (2005) 4291-4298.

[13] Boroske, E.; Helfrich, W., Magnetic anisotropy of egg lecithin membranes, Biophys. J. 24 (1978) 863-868.

[14] Prosser, R.; Bryant, H.; Bryant, R.; Vold, R., Lanthanide chelates as bilayer alignment tools in NMR studies of membrane-associated peptides, J. Magn. Res. 141 (1999) 256-260.

[15] Prosser, R.; Hunt, S.; DiNatale, J.; RR, V., Magnetically aligned membrane model systems with positive order parameter: switching the sign of Szz with paramagnetic ions, J. Am. Chem. Soc. 118 (1996) 269-270.

[16] De Angelis, A.; Nevzorov, A.; Park, S.; Howell, S.; Mrse, A.; Opella, S., High-Resolution NMR Spectroscopy of Membrane Proteins in Aligned Bicelles, J. Am. Chem. Soc. 126 (2004) 15340-15341.

[17] Park, S.; Opella, S., Triton X-100 as the "short-chain lipid" improves the magnetic alignment and stability of membrane proteins in phosphatidylcholine bilayers for oriented-sample solid-state NMR spectroscopy, J. Am. Chem. Soc. 132 (2010) 12552-12553.

[18] Aussenac, F.; Lavigne, B.; Dufourc, E., Toward bicelle stability with ether-linked phospholipids: temperature, composition, and hydration diagrams by 2H and 31P solid-state NMR, Langmuir 21 (2005) 7129-7135.

[19] Dvinskikh, S.; Yamamoto, K.; UH, D.; Ramamoorthy, A., Sensitivity and resolution enhancement in solid-state NMR spectroscopy of bicelles, J. Magn. Res. 184 (2007) 228-235.

[20] Doherty, T.; Su, Y.; Hong, M., High-Resolution Orientation and Depth of Insertion of the Voltage-Sensing S4 Helix of a Potassium Channel in Lipid Bilayers, J. Mol. Biol. 401 (2010) 642-652.

[21] Raffard, G.; Steinbruckner, S.; Arnold, A.; Davis, J.; Dufourc, E., Temperature-composition diagram of dimyristoyl-dicaproyl phosphatidylcholine "bicelles" self-orienting in the magnetic field: a solid state 2H- and 31P-NMR study, Langmuir. 16 (2000) 7655-7662.

[22] Triba, M.; Devaux, P.; Warschawski, D., Effects of Lipid Chain Length and Unsaturation on Bicelles Stability A Phosphorus NMR Study, Biophys. J. 91 (2006) 1357-1367.

[23] Arnold, A.; Labrot, T.; Oda, R.; Dufourc, E., Cation Modulation of Bicelle Size and Magnetic Alignment as Revealed by Solid-State NMR and Electron Microscopy, Biophys. J. 83 (2002) 2667-2680.

[24] Wang, J.; Denny, J.; Tian, C.; Kovacs, F.; Song, Z.; Fu, R.; Quine, J.; Cross, T.; Kim, S.; Mo, Y.; Nishimura, K.; Gan, Z., Imaging Membrane Protein Helical Wheels, J. Magn. Res. 144 (2000) 162-167.

[25] Marassi, F.; Opella, S., A solid-state NMR index of helical membrane protein structure and topology, J. Magn. Res. 144 (2000) 150-155.

[26] Marassi, F., A simple approach to membrane protein secondary structure and topology based on NMR spectroscopy, Biophys. J. 80 (2001) 994-1003.

[27] Hill, C. P.; Yee, J.; Selsted, M. E.; Eisenberg, D., Crystal structure of defensin HNP-3, an amphiphilic dimer: mechanisms of membrane permeabilization., Science 251 (1991) 1481-1485.

[28] Wimley, W. C.; Selsted, M. E.; White, S. H., Interactions between human defensins and lipid bilayers: evidence for formation of multimeric pores, Protein Sci. 3 (1994) 1362-1373.

Appendix A

Protocol for purification of ^{15}N, ^{13}C labeled HNP-1

1. Pasteurize

Prepare four 1 L flask, use tin to seal. Put the flasks into autoclave, set the temperature to be 121 °C, solution 30 min, dry 40 min. After the autoclave complete, take out the flasks and put them onto a clean table (with tin).

Dissolve LB Agar into deionized water (35 g/L), add kanamycin with final concentration of 50 μg/ml (1000 times dilution). Put the solution into autoclave (121 °C, solution 30 min). Then transfer the solution onto several culture dishes. After it cools down, use parafilm to seal and store in 4 °C freezer.

Prepare 1 M IPTG solution (2.38 g for 10 ml), use 0.22 μm membrane to filter the solution into ten 1.5 ml eppendorf tube. Use parafilm to seal, store in -20 °C freezer.

2. Cell culture and protein expression

Take out the E. coli bacteria from 80 °C freezer (using seeding tool). Use flame to burn the seeding tool for half minute, let it sit for half minute for cooling. Take out some bacteria using the seeding tool (just slightly touch). Inoculate the bacteria onto the solid media. Put the culture dish into the 4 °C freezer. Let it sit overnight. (Plasmid : pGEX-2T-Kana + GST_ProHNP-1; Host cell: Ecoli BL21L (pLysS DE3)

Next morning, near the flame, add 250 ml Spectra9 CN media into one 1 L flask. Add 250μl 50 mg/ml kanamycin solution using 1 ml pipet. Use flame to burn the seeding tool for half a minute, let it sit for half a minute for cooling. Take out the culture dish. Pick one separate clone (~2 mm diameter) using the seeding tool. Put the seeding tool into the media to inoculate the cell. Then use flame to burn the tool. Use tin to seal the flask and shake the cell at 250 rpm, 37 °C overnight (from 4 pm to 10 am). Also put the remaining 750 ml media into 37 °C room overnight to warm up.

Next morning, add 750 µl 50 mg/ml kanamycin solution into the remaining 750 ml Spectra9 CN media. Mix the overnight 250ml media with the rest media. Transfer it into 4 x 1 L flasks (250ml each). Continue to shake cell at 250 rpm, 27 °C for 1.5 hr (from 10 am to 11:30 am). Use 1 ml pipet to suck out 750 µl culture and measure the UV-vis. Continue shaking until the UV-vis reaches 1.2 OD (600 nm). Induce cells with final concentration of 3mM IPTG (750 µl to 250 ml media). Continue shaking for 2 hr (from 12 pm to 2 pm).

Spin cells at 7000 g rpm for 15 min at 4 °C in four 500ml spin tubes. Then pour out the supernatant and use 4 x 10 ml PBS buffer to wash the cells and transfer it into 2 x 50 ml tubes by 5ml pipet. Spin the cell at 7000 rpm for 10 min and pour out the supernatant. Get the wet weight of the cells (2 x 2 g). Completely suspend the cell in 2 x 10 ml (5 ml/g) Bugbuster solution. Add 2 x 5 µl Bioprecessing reagent into the two tubes. Shake for 20 min. Centrifuge at 10000 g rpm for 20 min. Pour out the supernatant and wash the inclusion bodies with 2 x 20 ml PBS + 2M urea solution. Spin at 10000 g rpm for 10 min. Pour out the supernatant. Add 1.5 g DTT (in total for the two bottles) and dissolve the inclusion bodies with 200 ml 8 M urea solution.

Use 0.45 µm membrane to filter the solution. Adjust pH to 4~6 before loading into the HPLC column for desalting (column: C18, 10-15 µm). Use 10% B (acetonitrile) for washing (~20 min) and 65% B for elution (the first peak should appear in ~10 min after changing to 65% B). The flow rate is 40ml/min and insert rate is 20 ml/min. The detector is at 214 nm and 280 nm. A is water + 1% TFA. Get ~200 ml solution and freeze it in 1 L round flask with liquid nitrogen. Lyophilize overnight (usually need 2~3 days).

3. Protein refolding and digestion

Get ~300 mg lyophilized inclusion body. Dissolve it with 250 ml 8 M urea solution (~1 mg/ml). Add 364 mg cystein (for 1 L) into the solution (final concentration is 3 mM). Stir after the solid is completely dissolved. Dilute the solution with 750 ml 0.2 M $NaHCO_3$ (three times volume, 16.8 g in 750 ml H_2O). Start the refolding process with adding 72 mg cystine into the solution and stir slowly at room temperature overnight.

The next morning, prepare the cleavage buffer. Dissolve 67.8 g Tris-HCl (20 mM), 245.4 g NaCl (150 mM), 10.3 g $CaCl_2$ (1.5 mM) into 4 L water. Adjust the pH to be 8.4 (using 37% HCl). Dilute this solution 7 times within the 30 L tank. Transfer the 1 L folded protein solution into four 250 ml dialysis tubes (MWCO=10000). Dialyze the protein solution against the cleavage buffer. Change buffer twice within 24 hr (Start at 10:30 am, change buffer at 6:00 pm).

The next morning, transfer the protein solution into a 1 L bottle. Use dionized water to rinse the tube. Add 33 μl bovine α-thrombin into the 1 L solution and stir slowly overnight.

4. Purification of labeled proHNP-1

The thrombin digestion product needs to be adjust to pH 4~6 (using acetic acid, usually ~4.5) and filtered with 0.45 μm filtration membrane. Set the linear gradient acetonitrile from 25 to 45% within 1 hr. Collect target elution peaks and lyophilize the proHNP-1. The volume is ~30 ml (3~4 tubes).

5. Cleavage of proHNP-1 with CNBr

The CNBr is already prepared as 50 mg/ml solution containing 5% TFA and stored in 4 C fridge. Dissolve the 5 mg proHNP-1 with 10 ml water. Put the solution into the hood. Add 10ml CNBr solution into the peptide with gloves. Stir at room temperature overnight.

Adjust the pH of the solution to be 4~6. Set the linear gradient acetonitrile from 25 to 45% within 1 hr. Collect target elution peaks and lyophilize the HNP-1. The volume is ~30 ml (3~4 tubes).

After lyophilization, we can get 2-3 mg HNP-1 powder for 1 L media.

6. Crystallization of HNP-1

The crystalized HNP-1 was prepared by precipitation of protein with poly(ethylene glycol)400 (PEG-400). A solution of PEG-400 containing 30 mM Cacodylate and 60 mM Li_2SO_4, with pH = 6.5 was slowly added to the stock solution. The final concentration of PEG-400 is ~30%. Two batches were precipitated with stock

solution concentration of 36 mg/ml and 30 mg/ml. The high-concentration stock solution (36 mg/ml) yields microcrystals one hour after mixing with PEG. Figure B.1 shows the picture of the peptide solution after mixing with PEG.

After half an hour:

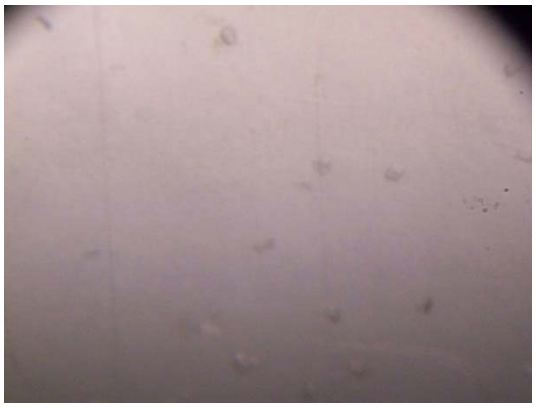

After 1 hour:

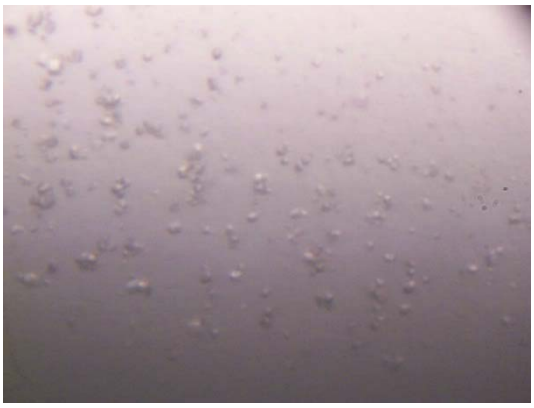

After 1 day:

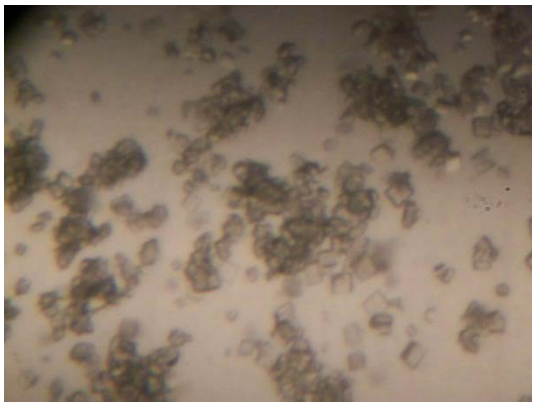

After 2 days:

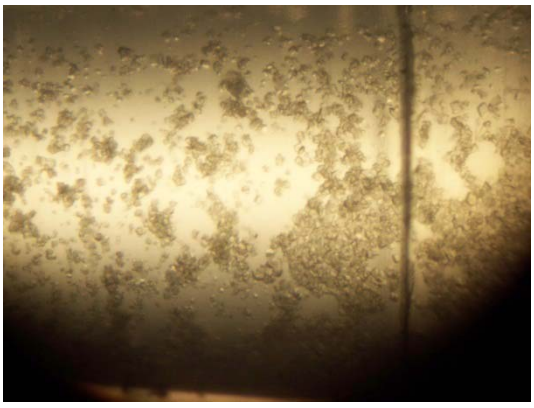

Figure B.1. Crystal picture of HNP-1 after mixing with PEG as a function of time.

The low-concentration stock solution (30 mg/ml) produced microcrystals gradually in a 4-day period, with ~80% of the protein eventually precipitating from the supernatant, which is estimated by the residual absorbance of the supernatant at 280 nm. The hydrated precipitate was centrifuged and transferred to the rotor after removal of supernatant.

Appendix B

Input code for protein structure determination by Xplor-NIH

1. anneal.py

```
xplor.requireVersion("2.14.4")


#
# slow cooling protocol in torsion angle
space for protein G. Uses
# NOE, RDC, J-coupling restraints.
#
# this script performs annealing from an
extended structure
#
# CDS 2005/05/10
#

# this checks for typos on the command-line.
User-customized arguments can
# also be specified.
#
(opts,args) =
xplor.parseArguments(["quick"])

quick=False
for opt in opts:
   if opt[0]=="quick":  #specify -quick to
just test that the script runs
      quick=True
      pass
   pass


# filename for output structures. This string
must contain the STRUCTURE
# literal so that each calculated structure has
a unique name. The SCRIPT
# literal is replaced by this filename (or stdin
if redirected using <),
# but it is optional.
#
outFilename = "SCRIPT_STRUCTURE.sa"
numberOfStructures=20   #usually you want
to create at least 20

if quick:
   numberOfStructures=3
   pass

# protocol module has many high-level
helper functions.
#
import protocol

protocol.initRandomSeed()   #set random
seed - by time

command = xplor.command

# generate PSF data from sequence and
initialize the correct parameters.
#
from psfGen import seqToPSF
seqToPSF('HNP1.seq')

# generate random extended initial structure
with correct covalent geometry
#
protocol.genExtendedStructure()

#
```

```
# a PotList contains a list of potential terms.
This is used to specify which
# terms are active during refinement.
#
from potList import PotList
potList = PotList()

# parameters to ramp up during the
simulated annealing protocol
#
from simulationTools import MultRamp,
StaticRamp, InitialParams

rampedParams=[]
highTempParams=[]

# compare atomic Cartesian rmsd with a
reference structure
#  backbone and heavy atom RMSDs will be
printed in the output
#  structure files
#
from posDiffPotTools import
create_PosDiffPot
refRMSD =
create_PosDiffPot("refRMSD","name CA or
name C or name N",
                  pdbFile='1DFN.pdb',
#                   cmpSel="not name H*")

# orientation Tensor - used with the dipolar
coupling term
#  one for each medium
#   For each medium, specify a name, and
initial values of Da, Rh.
#
from varTensorTools import
create_VarTensor
media={}
#                 medium  Da   rhombicity
#for (medium,Da,Rh) in [ ('t',   -6.5, 0.62),
#                 ('b',   -9.9, 0.23) ]:
#    oTensor = create_VarTensor(medium)
#    oTensor.setDa(Da)
#    oTensor.setRh(Rh)
#    media[medium] = oTensor
#    pass


# dipolar coupling restraints for protein
amide NH.
#
# collect all RDCs in the rdcs PotList
#
# RDC scaling. Three possible contributions.
#   1) gamma_A * gamma_B / r_AB^3
prefactor. So that the same Da can be used
#      for different expts. in the same medium.
Sometimes the data is
#      prescaled so that this is not needed.
scale_toNH() is used for this.
#      Note that if the expt. data has been
prescaled, the values for rdc rmsd
#      reported in the output will relative to
the scaled values- not the expt.
#      values.
#   2) expt. error scaling. Used here. A scale
factor equal to 1/err^2
#      (relative to that for NH) is used.
#   3) sometimes the reciprocal of the Da^2
is used if there is a large
#      spread in Da values. Not used here.
#
from rdcPotTools import create_RDCPot,
scale_toNH
rdcs = PotList('rdc')
#for (medium,expt,file,              scale) in \
#    [('t','NH' ,'tmv107_nh.tbl'       ,1),
#     ('t','NCO','tmv107_nc.tbl'       ,.05),
#     ('t','HNC','tmv107_hnc.tbl'      ,.108),
#     ('b','NH' ,'bicelles_new_nh.tbl' ,1),
#     ('b','NCO','bicelles_new_nc.tbl' ,.05),
#     ('b','HNC','bicelles_new_hnc.tbl',.108)
#     ]:
#    rdc =
create_RDCPot("%s_%s"%(medium,expt),fi
le,media[medium])
```

```
   #1) scale prefactor relative to NH
   #   see python/rdcPotTools.py for exact
calculation
   # scale_toNH(rdc) - not needed for these
datasets -
   #                  but non-NH reported
rmsd values will be wrong.

   #3) Da rescaling factor (separate
multiplicative factor)
   # scale *= ( 9.9 / rdc.oTensor.Da(0) )**2
#    rdc.setScale(scale)
#    rdcs.append(rdc)
#    pass
#potList.append(rdcs)
#rampedParams.append( MultRamp(0.01,1.
0, "rdcs.setScale( VALUE )") )


# set up NOE potential
noe=PotList('noe')
potList.append(noe)
from noePotTools import create_NOEPot
for (name,scale,file) in
[('all',1,"HNP1_NOE.tbl"),
                  #add entries for additional
tables
                  ]:
   pot = create_NOEPot(name,file)
   # pot.setPotType("soft") # if you think
there may be bad NOEs
   pot.setScale(scale)
   noe.append(pot)
rampedParams.append( MultRamp(2,30,
"noe.setScale( VALUE )") )

# set up J coupling - with Karplus
coefficients
#from jCoupPotTools import
create_JCoupPot
#jCoup =
create_JCoupPot("jcoup","jna_coup.tbl",
#                  A=6.98,B=-
1.38,C=1.72,phase=-60.0)
#potList.append(jCoup)

# Set up dihedral angles
from xplorPot import XplorPot
protocol.initDihedrals("HNP1_dihe.tbl",
                  useDefaults=0)
potList.append( XplorPot('CDIH') )
highTempParams.append( StaticRamp("pot
List['CDIH'].setScale(10)") )
rampedParams.append( StaticRamp("potList
['CDIH'].setScale(200)") )
# set custom values of threshold values for
violation calculation
#
potList['CDIH'].setThreshold( 5 )



# radius of gyration term
#
protocol.initCollapse("resid 1:56",
                  Rtarget=10.16)
potList.append( XplorPot('COLL') )

# hbda - distance/angle bb hbond term
#
#protocol.initHBDA('hbda.tbl')
#potList.append( XplorPot('HBDA') )

#Rama torsion angle database
#
protocol.initRamaDatabase()
potList.append( XplorPot('RAMA') )
rampedParams.append( MultRamp(.002,1,"p
otList['RAMA'].setScale(VALUE)") )

#
# setup parameters for atom-atom repulsive
term. (van der Waals-like term)
#
potList.append( XplorPot('VDW') )
rampedParams.append( StaticRamp("protoc
ol.initNBond()") )
rampedParams.append( MultRamp(0.9,0.8,
```

```
                    "command('param
nbonds repel VALUE end end')") )
rampedParams.append( MultRamp(.004,4,
                    "command('param
nbonds rcon VALUE end end')") )
# nonbonded interaction only between CA
atoms
highTempParams.append( StaticRamp("""pr
otocol.initNBond(cutnb=100,

tolerance=45,
                                repel=1.2,

onlyCA=1)""") )


potList.append( XplorPot("BOND") )
potList.append( XplorPot("ANGL") )
potList['ANGL'].setThreshold( 5 )
rampedParams.append( MultRamp(0.4,1,"po
tList['ANGL'].setScale(VALUE)") )
potList.append( XplorPot("IMPR") )
potList['IMPR'].setThreshold( 5 )
rampedParams.append( MultRamp(0.1,1,"po
tList['IMPR'].setScale(VALUE)") )



# Give atoms uniform weights, except for
the anisotropy axis
#
from atomAction import SetProperty
import varTensorTools
AtomSel("not resname
ANI").apply( SetProperty("mass",100.) )
varTensorTools.massSetup(media.values(),3
00)
AtomSel("all
").apply( SetProperty("fric",10.) )


# IVM setup
#   the IVM is used for performing dynamics
and minimization in torsion-angle
#   space, and in Cartesian space.
#
from ivm import IVM
dyn = IVM()

# initialize ivm topology for torsion-angle
dynamics

for m in media.values():
   m.setFreedom("fixDa, fixRh")       #fix
tensor Rh, Da, vary orientation
#    m.setFreedom("varyDa, varyRh")
#vary tensor Rh, Da, vary orientation
protocol.torsionTopology(dyn,oTensors=me
dia.values())

# minc used for final cartesian minimization
#
minc = IVM()
protocol.initMinimize(minc)

for m in media.values():
   m.setFreedom("varyDa, varyRh")
#allow all tensor parameters float here
   pass
protocol.cartesianTopology(minc,oTensors=
media.values())



# object which performs simulated
annealing
#
from simulationTools import AnnealIVM
init_t  = 3500.     # Need high temp and slow
annealing to converge
cool = AnnealIVM(initTemp =init_t,
            finalTemp=25,
            tempStep =12.5,
            ivm=dyn,
            rampedParams = rampedParams)

#cart_cool is for optional cartesian-space
cooling
```

```
cart_cool = AnnealIVM(initTemp =init_t,
                      finalTemp=25,
                         tempStep =12.5,
                   ivm=minc,
                   rampedParams =
rampedParams)

def calcOneStructure(loopInfo):
   """ this function calculates a single
structure, performs analysis on the
   structure, and then writes out a pdb file,
with remarks.
   """

   # generate a new structure with
randomized torsion angles
   #
   from monteCarlo import
randomizeTorsions
   randomizeTorsions(dyn)

   # calc. initial tensor orientation
   #
   from varTensorTools import
calcTensorOrientation
   for medium in media.values():
      calcTensorOrientation(medium)
      pass

   # initialize parameters for high temp
dynamics.
   InitialParams( rampedParams )
   # high-temp dynamics setup - only need
to specify parameters which
   #   differfrom initial values in
rampedParams
   InitialParams( highTempParams )

   # high temp dynamics
   #
   protocol.initDynamics(dyn,
                   potList=potList, # potential
terms to use
                   bathTemp=init_t,
                   initVelocities=1,
                   finalTime=800,   # stops at
800ps or 8000 steps
                   numSteps=8000,   #
whichever comes first
                   printInterval=100)

   dyn.setETolerance( init_t/100 )  #used to
det. stepsize. default: t/1000
   dyn.run()

   # initialize parameters for cooling loop
   InitialParams( rampedParams )


   # initialize integrator for simulated
annealing
   #
   protocol.initDynamics(dyn,
                   potList=potList,
                   numSteps=100,      #at each
temp: 100 steps or
                   finalTime=.2 ,      # .2ps,
whichever is less
                   printInterval=100)

   # perform simulated annealing
   #
   cool.run()


   # final torsion angle minimization
   #
   protocol.initMinimize(dyn,
                   printInterval=50)
   dyn.run()

   # optional cooling in Cartesian
coordinates
   #
   protocol.initDynamics(minc,
                   potList=potList,
                   numSteps=100,      #at each
temp: 100 steps or
```

```
                finalTime=.4 ,      # .2ps,
whichever is less
                printInterval=100)
   #cart_cool.run()
   # final all- atom minimization
   #
   protocol.initMinimize(minc,
                potList=potList,
                dEPred=10)
   minc.run()

   #do analysis and write structure
   loopInfo.writeStructure(potList)
   pass



from simulationTools import StructureLoop,
FinalParams
```

2. refine.py

```
xplor.requireVersion("2.18")

#
# slow cooling protocol in torsion angle
space for protein G. Uses
# NOE, RDC, J-coupling restraints.
#
# this version refines from a reasonable
model structure.
#
# CDS 2005/05/10
#

xplor.parseArguments() # check for typos on
the command-line

outFilename = "SCRIPT_STRUCTURE.sa"
numberOfStructures=3

StructureLoop(numStructures=numberOfStr
uctures,
        pdbTemplate=outFilename,

structLoopAction=calcOneStructure,
        genViolationStats=1,
        averageTopFraction=0.5, #report
stats on best 50% of structs

averageContext=FinalParams(rampedParam
s),
        averageCrossTerms=refRMSD,

averageSortPots=[potList['BOND'],potList['
ANGL'],potList['IMPR'],
                noe,rdcs,potList['CDIH']],
        averagePotList=potList).run()

# protocol module has many high-level
helper functions.
#
import protocol
protocol.initRandomSeed(3421)   #explicitly
set random seed

#
# annealing settings
#

command = xplor.command

protocol.initParams("protein")

# generate PSF data from sequence and
initialize the correct parameters.
#
#from psfGen import seqToPSF
seqToPSF('HNP1.seq')
```

```
protocol.initStruct("HNP1.psf") # - or from
file

# generate a random extended structure with
correct covalent geometry
#  saves the generated structure in the
indicated file for faster startup
#  next time.
#
protocol.genExtendedStructure("HNP1_exte
nded.pdb" %

protocol.initialRandomSeed())

# or read an existing model
#
protocol.loadPDB("1DFN.pdb")
xplor.simulation.deleteAtoms("not known")

protocol.fixupCovalentGeom(maxIters=100,
useVDW=1)

#
# a PotList contains a list of potential terms.
This is used to specify which
# terms are active during refinement.
#
from potList import PotList
potList = PotList()

# parameters to ramp up during the
simulated annealing protocol
#
from simulationTools import MultRamp,
StaticRamp, InitialParams

rampedParams=[]
highTempParams=[]

# compare atomic Cartesian rmsd with a
reference structure
#  backbone and heavy atom RMSDs will be
printed in the output
#  structure files
#
from posDiffPotTools import
create_PosDiffPot
refRMSD =
create_PosDiffPot("refRMSD","name CA or
name C or name N",
                  pdbFile='1DFN.pdb',
                  cmpSel="not name H*")

# orientation Tensor - used with the dipolar
coupling term
#  one for each medium
#   For each medium, specify a name, and
initial values of Da, Rh.
#
from varTensorTools import
create_VarTensor
media={}
#                  medium  Da   rhombicity
for (medium,Da,Rh) in [ ('t',   -6.5, 0.62),
                ('b',   -9.9, 0.23) ]:
   oTensor = create_VarTensor(medium)
   oTensor.setDa(Da)
   oTensor.setRh(Rh)
   media[medium] = oTensor
   pass


# dipolar coupling restraints for protein
amide NH.
#
# collect all RDCs in the rdcs PotList
#
# RDC scaling. Three possible contributions.
#   1) gamma_A * gamma_B / r_AB^3
prefactor. So that the same Da can be used
#      for different expts. in the same medium.
Sometimes the data is
#      prescaled so that this is not needed.
scale_toNH() is used for this.
#      Note that if the expt. data has been
prescaled, the values for rdc rmsd
#      reported in the output will relative to
the scaled values- not the expt.
```

```
#      values.
#   2) expt. error scaling. Used here. A scale
factor equal to 1/err^2
#      (relative to that for NH) is used.
#   3) sometimes the reciprocal of the Da^2
is used if there is a large
#      spread in Da values. Not used here.
#
#from rdcPotTools import create_RDCPot,
scale_toNH
#rdcs = PotList('rdc')
#for (medium,expt,file,                scale) in \
#    [('t','NH' ,'tmv107_nh.tbl'      ,1),
#     ('t','NCO','tmv107_nc.tbl'      ,.05),
#     ('t','HNC','tmv107_hnc.tbl'     ,.108),
#     ('b','NH' ,'bicelles_new_nh.tbl' ,1),
#     ('b','NCO','bicelles_new_nc.tbl' ,.05),
#     ('b','HNC','bicelles_new_hnc.tbl',.108)
#     ]:
#    rdc =
create_RDCPot("%s_%s"%(medium,expt),fi
le,media[medium])

   #1) scale prefactor relative to NH
   #   see python/rdcPotTools.py for exact
calculation
   # scale_toNH(rdc) - not needed for these
datasets -
   #                  but non-NH reported
rmsd values will be wrong.

   #3) Da rescaling factor (separate
multiplicative factor)
   # scale *= ( 1. / rdc.oTensor.Da(0) )**2
#    rdc.setScale(scale)
#    rdc.setShowAllRestraints(1) #all
restraints are printed during #analysis
#    rdc.setThreshold(1.5)       # in Hz
#    rdcs.append(rdc)
#    pass
#potList.append(rdcs)
#rampedParams.append( MultRamp(0.05,5.
0, "rdcs.setScale( VALUE )") )

# calc. initial tensor orientation
#
#from varTensorTools import
calcTensorOrientation
#for medium in media.values():
#    calcTensorOrientation(medium)
#    pass

# set up NOE potential
noe=PotList('noe')
potList.append(noe)
from noePotTools import create_NOEPot
for (name,scale,file) in
[('all',1,"HNP1_NOE.tbl"),
                  #add entries for additional
tables
                  ]:
   pot = create_NOEPot(name,file)
   # pot.setPotType("soft") - if you think
there may be bad NOEs
   pot.setScale(scale)
   noe.append(pot)
rampedParams.append( MultRamp(2,30,
"noe.setScale( VALUE )") )

# set up J coupling - with Karplus
coefficients
#from jCoupPotTools import
create_JCoupPot
#jCoup =
create_JCoupPot("jcoup","jna_coup.tbl",
#                  A=6.98,B=-
1.38,C=1.72,phase=-60.0)
#potList.append(jCoup)

# Set up dihedral angles
from xplorPot import XplorPot
protocol.initDihedrals("HNP1_dihe.tbl",
                 useDefaults=0)
potList.append( XplorPot('CDIH') )
highTempParams.append( StaticRamp("pot
List['CDIH'].setScale(10)") )
rampedParams.append( StaticRamp("potList
['CDIH'].setScale(200)") )
```

```
# set custom values of threshold values for
violation calculation
#
potList['CDIH'].setThreshold( 5 ) #5 degrees
is the default value, though



# gyration volume term
#
# gyration volume term
#
from gyrPotTools import create_GyrPot
gyr = create_GyrPot("Vgyr",
                    "resid 1:56") # selection should
exclude disordered tails
potList.append(gyr)
#rampedParams.append( MultRamp(.002,1,"
gyr.setScale(VALUE)") )

# hbda - distance/angle bb hbond term
#
protocol.initHBDA('hbda.tbl')
potList.append( XplorPot('HBDA') )

#Rama torsion angle database
#
#protocol.initRamaDatabase()
#potList.append( XplorPot('RAMA') )
#rampedParams.append( MultRamp(.002,1,"
potList['RAMA'].setScale(VALUE)") )

#
# setup parameters for atom-atom repulsive
term. (van der Waals-like term)
#
potList.append( XplorPot('VDW') )
rampedParams.append( StaticRamp("protoc
ol.initNBond()") )
rampedParams.append( MultRamp(0.9,0.8,
                              "command('param
nbonds repel VALUE end end')") )
rampedParams.append( MultRamp(.004,4,
                              "command('param
nbonds rcon VALUE end end')") )
# nonbonded interaction only between CA
atoms
highTempParams.append( StaticRamp("""pr
otocol.initNBond(cutnb=100,

tolerance=45,
                                  repel=1.2,

onlyCA=1)""") )


potList.append( XplorPot("BOND") )
potList.append( XplorPot("ANGL") )
potList['ANGL'].setThreshold( 5 )
rampedParams.append( MultRamp(0.4,1,"po
tList['ANGL'].setScale(VALUE)") )
potList.append( XplorPot("IMPR") )
potList['IMPR'].setThreshold( 5 )
rampedParams.append( MultRamp(0.1,1,"po
tList['IMPR'].setScale(VALUE)") )



# Give atoms uniform weights, except for
the anisotropy axis
#
from atomAction import SetProperty
import varTensorTools
AtomSel("not resname
ANI").apply( SetProperty("mass",100.) )
varTensorTools.massSetup(media.values(),3
00)
AtomSel("all
").apply( SetProperty("fric",10.) )


# IVM setup
#   the IVM is used for performing dynamics
and minimization in torsion-angle
#   space, and in Cartesian space.
#
from ivm import IVM
```

```
dyn = IVM()

# initially minimize in Cartesian space with
only the covalent constraints.
#   Note that bonds, angles and many
impropers can't change with the
#   internal torsion-angle dynamics
#   breaks bonds topologically - doesn't
change force field
#
#dyn.potList().add( XplorPot("BOND") )
#dyn.potList().add( XplorPot("ANGL") )
#dyn.potList().add( XplorPot("IMPR") )
#
#dyn.breakAllBondsIn("not resname ANI")
#import varTensorTools
#for m in media.values():
#    m.setFreedom("fix")              #fix
tensor parameters
#    varTensorTools.topologySetup(dyn,m)
#setup tensor topology
#
#protocol.initMinimize(dyn,numSteps=1000)
#dyn.run()

# reset ivm topology for torsion-angle
dynamics
#
dyn.reset()

for m in media.values():
#    m.setFreedom("fixDa, fixRh")       #fix
tensor Rh, Da, vary orientation
   m.setFreedom("varyDa, varyRh")
#vary tensor Rh, Da, vary orientation
protocol.torsionTopology(dyn,oTensors=me
dia.values())

# minc used for final cartesian minimization
#
minc = IVM()
protocol.initMinimize(minc)

for m in media.values():
   m.setFreedom("varyDa, varyRh")
#allow all tensor parameters float here
   pass
protocol.cartesianTopology(minc,oTensors=
media.values())



# object which performs simulated
annealing
#
from simulationTools import AnnealIVM
init_t  = 3000.     # Need high temp and slow
annealing to converge
cool = AnnealIVM(initTemp =init_t,
             finalTemp=25,
             tempStep =12.5,
             ivm=dyn,
             rampedParams = rampedParams)

def accept(potList):
   """
   return True if current structure meets
acceptance criteria
   """
   if potList['noe'].violations()>0:
      return False
   if potList['rdc'].rms()>1.2: #this might be
tightened some
      return False
   if potList['CDIH'].violations()>0:
      return False
   if potList['BOND'].violations()>1:
      return False
   if potList['ANGL'].violations()>0:
      return False
   if potList['IMPR'].violations()>1:
      return False

   return True

def calcOneStructure(loopInfo):
   """ this function calculates a single
structure, performs analysis on the
```

```
   structure, and then writes out a pdb file,
with remarks.
   """

   # initialize parameters for high temp
dynamics.
   InitialParams( rampedParams )
   # high-temp dynamics setup - only need
to specify parameters which
   #   differfrom initial values in
rampedParams
   InitialParams( highTempParams )

   # high temp dynamics
   #
   protocol.initDynamics(dyn,
                  potList=potList, # potential
terms to use
                  bathTemp=init_t,
                  initVelocities=1,
                  finalTime=10,    # stops at
10ps or 5000 steps
                  numSteps=5000,   #
whichever comes first
                  printInterval=100)

   dyn.setETolerance( init_t/100 )  #used to
det. stepsize. default: t/1000
   dyn.run()

   # initialize parameters for cooling loop
   InitialParams( rampedParams )



   # initialize integrator for simulated
annealing
   #
   protocol.initDynamics(dyn,
                  potList=potList,
                  numSteps=100,      #at each
temp: 100 steps or
                  finalTime=.2 ,      # .2ps,
whichever is less
                  printInterval=100)

   # perform simulated annealing
   #
   cool.run()



   # final torsion angle minimization
   #
   protocol.initMinimize(dyn,
                  printInterval=50)
   dyn.run()

   # final all- atom minimization
   #
   protocol.initMinimize(minc,
                  potList=potList,
                  dEPred=10)
   minc.run()

   #do analysis and write structure
   loopInfo.writeStructure(potList)
   pass



from simulationTools import StructureLoop,
FinalParams
StructureLoop(numStructures=numberOfStr
uctures,
          pdbTemplate=outFilename,

structLoopAction=calcOneStructure,
          genViolationStats=1,
          averagePotList=potList,

averageSortPots=[potList['BOND'],potList['
ANGL'],potList['IMPR'],
                     noe,rdcs,potList['CDIH']],
          averageCrossTerms=refRMSD,
          averageTopFraction=0.5, #report
only on best 50% of structs
          averageAccept=accept,   #only use
structures which pass accept()
```

```
averageContext=FinalParams(rampedParam
s),

averageFilename="SCRIPT_ave.pdb",
#generate regularized ave structure
        averageFitSel="name CA",
                averageCompSel="not resname
ANI and not name H*"    ).run()
```